CITY UNIVERSITY LONDON

In vivo investigations of photoplethysmograms and arterial oxygen saturation from the auditory canal in conditions of compromised peripheral perfusion

by

Karthik Budidha

A thesis submitted in partial fulfillment for the degree of Doctor of Philosophy

in the

Research Centre for Biomedical Engineering

School of Mathematics, Computer Science & Engineering

Northampton Square, London, EC1V 0HB

July 2016

City, University of London
Northampton Square
London
EC1V 0HB
United Kingdom

T +44 (0)20 7040 5060

THE FOLLOWING PARTS OF THIS THESIS HAVE BEEN REDACTED FOR COPYRIGHT REASONS:

p. 6: **Fig. 2.1.** Inspiratory and expiratory stages of pulmonary ventilation**.**
p. 7: **Fig. 2.2.** Gas exchange between alveoli and capillaries.
p. 10: **Fig. 2.4.** Stages in cardiac cycle and circulatory routes.
p. 17: **Fig. 3.3.** Block diagram of a single beam spectrophotometer.
p. 21: **Fig. 3.5.** Catheter in the pulmonary artery of the heart and Venus oxygen saturation measurement system.
p. 31: **Fig. 4.3.** The Nihon Kohden OLV-5100.
p. 49: **Fig. 5.2.** Thermogram of the hand.
p. 68: **Fig. 6.4.** Branches of common carotid artery.
p. 69: **Fig. 6.5.** Thermogram of the ear.
p. 154: **Quote**: From The emperor's old clothes, C.A.R. Hoare.

Declaration of Authorship

I, Karthik Budidha, declare that this thesis titled, '*In vivo* investigations of photoplethysmograms and arterial oxygen saturation from the auditory canal in conditions of compromised peripheral perfusion' and the work presented in it are my own. I confirm that:

- This work was done wholly or mainly while in candidature for a research degree at this University.
- Where I have consulted the published work of others, this is always clearly attributed.
- Where I have quoted from the work of others, the source is always given. With the exception of such quotations, this thesis is entirely my own work.
- I have acknowledged all main sources of help.
- Where the thesis is based on work done by myself jointly with others, I have made clear exactly what was done by others and what I have contributed myself.

Signed: _____

Date: _____

"A man is like a fraction whose numerator is what he is and whose denominator is what he thinks of himself. The larger the denominator, the smaller the fraction"

— Leo Tolstoy

Abstract

Pulse oximeters rely on the technique of photoplethysmography (PPG) to estimate arterial oxygen saturation (SpO_2). In conditions of poor peripheral perfusion such as hypotension, hypothermia, and vasoconstriction, the PPG signals detected are often small and noisy, or in some cases unobtainable. Hence, pulse oximeters produce erroneous SpO_2 readings in these circumstances. The problem arises as most commercial pulse oximeter probes are designed to be attached to peripheral sites such as the finger or toes, which are easily affected by vasoconstriction. In order to overcome this problem, the ear canal was investigated as an alternative site for measuring reliable SpO_2 on the hypothesis that blood flow to this central site is preferentially preserved. Novel miniature ear canal PPG sensors were developed along with a state of the art PPG processing unit and a data acquisition system to allow for PPG measurements from different depths and surfaces of the ear canal. A preliminary *in vivo* investigation on seven healthy volunteers has revealed that good quality PPG signals with high amplitude can be obtained from the *posterior* surface of the *outer ear canal*. Based on these observations, a second prototype probe suitable for acquisition of PPGs from the posterior surface of the outer ear canal was developed. A pilot study was then carried out on 15 healthy volunteers to validate the feasibility of measuring PPGs and SpO_2 from the ear canal in conditions of induced local peripheral vasoconstriction (right hand immersion in ice water). The PPG signals acquired from the ear canal probe were compared with those obtained simultaneously from finger probes attached to the left and the right index fingers. Significant drop ($p< 0.05$) in amplitude was observed in the PPG signals acquired from the left ($> 45\%$) and right ($> 50\%$) index fingers during the ice water immersion, while good quality PPG signals with relatively constant amplitude were obtained from the ear canal. Also, the SpO_2 values showed that the ear canal pulse oximeter performed better than the two finger pulse oximeters (mean failure rate 30%). A second *in vivo* investigation was carried out in 15 healthy volunteers, where hypoperfusion was induced more naturally by exposing the volunteer to cold temperatures of 10°C for 10 min. Normalised Pulse Amplitude (NPA) and SpO_2 was calculated from the PPG signals acquired from the ear canal, the finger and the earlobe. By the end of the cold exposure, a mean drop of $> 80\%$ was found in the NPA of finger PPGs. The % drop in the NPA of red and infrared earlobe PPG signals was 20% and 26% respectively. Contrarily to both these sites, the NPA of the ear canal PPGs had only dropped by 0.2% and 13% respectively. The SpO_2 estimated from the finger sensor was below 90% in 5 volunteers (failure) by the end of the cold exposure. The earlobe pulse oximeter failed in 3 volunteers. The ear canal sensor on the other hand had only failed in 1 volunteer. These results strongly suggest that the ear canal may be used as a suitable alternative site for reliable monitoring of PPGs and SpO_2 in cases of compromised peripheral perfusion.

Acknowledgements

This thesis is a result of my research work at City University London where I have been accompanied and supported by many people. It is a pleasure that I now have the chance to express my appreciation to all, who gave me the inspiration and motivation to finish this thesis. First of all, I am indebted to my supervisor Prof P A Kyriacou for all the guidance and support through each and every step of my PhD. His eagerness towards this project and insightful thinking have been of great value to me.

Secondly, I wish to express my special thanks to Dr Victor Rybynok, who has been an inspiration, guide and a great friend during the period of my research.

I thank all my collegues in the Research Centre for Biomedical Engineering and all the staff at City University London. In particular, i would like to thank Mr Tomas Abay, Dr Meha Qassem and Dr Carolina Gama whose friendship and advice has supported me throughout my work.

I would like to acknowledge the support of the City University Graduate School, City future fund and Institute of Physics and Engineering in Medicine (IPEM) for the financial contribution towards attending international conferences.

Lastly, and most importantly, I wish to thank my parents for their unconditional love and support through all the highs and lows of my life.

Contents

List of Figures

List of Tables

Abbreviations

Hb	**H**aemoglobin
HbO_2	**O**xy**H**aemoglobin
MetHb	**MetH**aemoglobin
COHb	**C**arb**O**xy**H**aemoglobin
CytOx	**Cyto**chrome C **Ox**idase
P_{O_2}	Partial **P**ressure of **O**xygen
P_{CO_2}	Partial **P**ressure of **C**arbon di**O**xide
SO_2	**O**xygen **S**aturation
SaO_2	**A**rterial **O**xygen **S**aturation
StO_2	**T**issue **O**xygen **S**aturation
SpO_2	**A**rterial **O**xygen **S**aturation by **P**ulse oximetry
SvO_2	**V**enous **O**xygen **S**aturation
TOI	**T**issue **O**xygenation **I**ndex
PPG	**P**hoto**P**lethysmo**G**raph
NIRS	**N**ear **I**nfrared **S**pectroscopy
CW-NIRS	**C**ontinuous **W**ave **N**ear **I**nfrared **S**pectroscopy
DPF	**D**ifferential **P**athlength **F**actor
RECAP	**R**eflectance **E**ar **CA**nal **P**robe
SNR	**S**ignal–to–**N**oise **R**atio
R_{OS}	**R**atio of **R**atios
EMI	**E**lectro**m**agnetic **I**nterference
PI	**P**erfusion **I**ndex
PVI	**P**leth **V**ariability **I**ndex
HRV	**H**eart **R**ate **V**ariability
PRV	**P**ulse **R**ate **V**ariability
PTT	**P**ulse **T**ransit **T**ime
PPD	**P**ulse **P**ropagation **D**istance
PCB	**P**rinted **C**ircuit **B**oard
STL	**ST**ereo**L**ithography
SD	**S**tandard **D**eviation

SEM	**S**tandard **E**rror of the **M**ean
TIA	**T**rans**i**mpedance **A**mplifier
SHA	**S**ample and **H**old **A**mplifier
CS	**C**urrent **S**ource
RCV	**R**eference **C**ontrol **V**oltage
MCU	**M**icro-**C**ontroller **U**nit
PM	**P**hase **M**argin
pk-pk	**P**ea**k**–to–**P**ea**k**
LSB	**L**east **S**ignificant **B**it
VI	**V**irtual **I**nstrument
HR	**H**eart **R**ate
LIF	**L**eft **I**ndex **F**inger
LIF	**R**ight **I**ndex **F**inger
EC	**E**ar **C**anal
LDF	**L**aser **D**oppler **F**lowmetry
NPA	**N**ormalised **P**ulse **A**mplitude
HF	**H**igh **F**requency
LF	**L**ow **F**requency
nTHI	**n**ormalised **T**issue **H**aemoglobin **I**ndex
ECG	**E**lectro**c**ardio**g**ram
BP	**B**lood **P**ressure
NIBP	**N**on **I**nvasive **B**lood **P**ressure

List of Publications

- K Budidha and P A Kyriacou, "Devepopment of an optical probe to investigate the suitability of measuring photoplethysmographs and blood oxygen saturation from the human auditory canal", in *2013 35th Annual International Conference of the IEEE Engineering in Medicine and Biology Society (EMBC)*, Jul. 2013, pp. 1736–1739.
- K Budidha and P A Kyriacou, "The Human ear canal: investigation of its suitability for monitoring photoplethysmographs and arterial oxygen saturation", *Physiological Measurement*, vol. 35, no.2, pp.111–128, Feb. 2014.
- K Budidha and P A Kyriacou, "Investigation of pulse transit times utilizing multisite reflectance photoplethysmography under conditions of artificially induced peripheral vasoconstriction, in *2014 36th Annual International Conference of the IEEE Engineering in Medicine and Biology Society (EMBC)*, Chicago, Illinois, USA: IEEE, 2014.
- K Budidha, T Y Abay, and P A Kyriacou, "Investigation of photoplethysmography, laser doppler flowmetry and near infrared spectroscopy during induced thermal stress", in *Engineering in Medicine and Biology Society (EMBC), 2015 37th Annual International Conference of the IEEE*. IEEE, 2015, pp. 6417–6420.
- K Budidha and P A Kyriacou, "Investigation of photoplethysmography and arterial blood oxygen saturation from the ear-canal and the finger under conditions of artificially induced hypothermia", in *Engineering in Medicine and Biology Society (EMBC), 2015 37th Annual International Conference of the IEEE*. IEEE, 2015, pp. 7954–7957.
- K Budidha, T Y Abay and P A Kyriacou, "Comparison of cerebral with peripheral blood flow autoregulation using photoplethysmography", in *Innovations and Applications of Monitoring Perfusion, Oxygenation and Ventilation (I.A.M.P.O.V.)*, 2015. Tokyo, Japan, Oct 2015, pp. 45–46.
- P A Kyriacou, K Budidha and H Njoum, "Investigation of pulse transit times using multisite reflectance photoplethysmography under conditions of artificially induced peripheral vasoconstriction" in *7th World Congress of Biomechanics (WCB 2014)*, Boston, Massachusetts, USA, 2014.
- V Rybynok, J M May, K Budidha, and P A Kyriacou, "Design and development of a novel multichannel photoplethysmographic research system", in *2013 IEEE Point-of-Care Healthcare Technologies (PHT)*, Jan. 2013, pp. 267–270.
- V Rybynok, J M May, K Budidha, H Njoum, J P Phillips, and P A Kyriacou, "ZenPPG: a modular multi-channel photoplethysmography system", in *Innovations and Applications of Monitoring Perfusion, Oxygenation and Ventilation (I.A.M.P.O.V.)*, 2012. Yale University, New Haven, CT, USA: Yale University, Jul. 2012, pp. 54–55.
- T Y Abay, K Budidha and P A Kyriacou, "Assessment of blood flow, blood volume and haemoglobin concentrations by photoplethymography during induced hypothermia", in *Innovations and Applications of Monitoring Perfusion, Oxygenation and Ventilation (I.A.M.P.O.V.)*, 2015. Tokyo, Japan, Oct 2015, pp. 37–38.

1

Introduction

A pulse oximeter is a non-invasive optical device used to provide a continuous and robust measure of arterial oxygen saturation (SpO_2). The device measures SpO_2 by shining light at two different wavelengths into the vascular tissue (such as the finger or the ear lobe) and sensing the changes in light absorption of the oxygenated and deoxygenated haemoglobin produced during arterial pulsations [1]. The device has since its invention in the 1980's revolutionised anaesthesia and critical care. Pulse oximeters are now one of the most commonly used medical devices in health care; in fact they are now a standard of practice for the administration of general anaesthesia. The oximetry measurements provided by the instrument are often referred to as the "fifth vital sign" [2].

The popularity of the device and its increased clinical use in recent years has driven the manufacturers and researchers to consistently develop its hardware, software and signal processing algorithms. However, there still remain a few unsolved problems that limit its performance. Possibly, the most important limitation of the device in its current state is the inability to estimate accurate SpO_2 in conditions of poor peripheral perfusion. Poor perfusion can result from various clinical conditions such as hypotension, hypothermia, vasoconstriction, low cardiac output, hypovolemia, and peripheral vascular disease [3–15]. These clinical situations, can occur in patients undergoing major surgical procedures such as cardiopulmonary bypass surgery or in patients with chronic cardiovascular complications and renal failure [16]. The SpO_2 readings in these conditions become very inaccurate or

cease altogether. The failure of the device in these circumstances is directly associated with the inability of the pulse oximeter probe, placed at the periphery, to detect adequate photoplethysmographic signals which are necessary for the estimation of SpO_2 by pulse oximetry. Most commercial probes are attached to the extremities such as the finger, earlobe or toe, where the pulsatile flow is very easily withdrawn and diverted to more vital organs. Many attempts were made previously to minimise or eliminate this limitation by the application of vasodilation creams [11], administration of intra-arterial vasodilators [17], digital nerve blockers [18–20], and applications of sensors on better perfused areas such as the forehead [13], nose [21], and oesophagus [22]. However, these attempts were either impractical for use in critically ill patients or gave no improvement in poorly perfused states. Thus, SpO_2 readings are still unobtainable or inaccurate at just the time when they will be most necessary.

In an effort to address this limitation of pulse oximeters, the outer auditory canal was proposed as an alternative site for monitoring photoplethysmograms (PPG) and SpO_2. The hypothesis underlying the proposal was that the ear canal being closer to the trunk, and being supplied by the arteries that supply blood to the brain, would remain adequately perfused during low perfusion states. This thesis describes in detail the incremental design, and development of a novel ear canal electro-optic PPG sensor and a state of the art PPG processing system used to acquire PPGs from the ear canal. The *in vivo* investigations carried out to test the hypothesis are also described in this thesis.

A brief summary of each of the chapters contained in this thesis is as follows:

Chapter 2 describes the anatomy and physiology of the respiratory and cardiovascular system of the human body with emphasis on the method of oxygen transport from surrounding air to each cell in the body. An overview on the significance of adequate oxygen supply and the pathologies resulting from deficient oxygen supply are also discussed.

Chapter 3 lists the chemical, optical and calorimetric techniques used to measure oxygenation in both blood and tissue. The chapter provides a brief review on the principle of operation and the physiological basis through which oxygenation is measured by some of the modalities currently being used in clinical practice. The basic principles of spectrophotometry and oximetry such as the Beer-Lambert law for the absorption of light in a solution are also described in this chapter.

Chapter 4 describes the principle of photoplethysmography and the way in which it is applied in pulse oximetry. The chapter provides a brief history of pulse oximetry and the choice of wavelengths commonly used in the device. Following this, the equations required (manipulation of Beer-Lambert law) for converting the measured light transmission through tissue to values of haemoglobin oxygen saturation are developed. The modern

methods for calibrating pulse oximeters are also briefly pointed out. The two probe configurations commonly used in pulse oximetry and the instrumentation used to detect the PPG signals and estimate SpO_2 are then discussed.

Chapter 5 provides an in-depth review of the technological and physiological limitations of pulse oximeters. Following the limitations, the recent advancements in the field of pulse oximetry and photoplethysmography, and the need for further development of pulse oximeters to improve their performance, especially in conditions of poor peripheral perfusion are discussed. A possible solution i.e., the ear canal as a site for uninterrupted monitoring of PPGs and SpO_2 in such circumstances is also proposed.

Chapter 6 describes the anatomy and the physiology of the human ear. A detailed description of the blood supply to the ear canal and its surrounding tissue is provided in this chapter since the ear canal is the main area of investigation in this project. The chapter then focuses on the physiological advantages of the ear canal over other sensor locations for monitoring PPGs. Finally, the chapter presents previous work carried out by other researchers in developing an in-ear PPG sensor, the drawbacks associated with their developments, further gaps in knowledge, and how the proposed technology aims to achieve this new knowledge.

Chapter 7 details the incremental design and development of the reflectance ear canal PPG (RECAP) probe. The design considerations, components used in the fabrication of the probe, their specifications and the manufacturing procedures are reported in this chapter. In addition, the preliminary tests carried out to find the optimal depth and surface within the ear canal from which high quality PPGs are obtained are presented in this chapter. The design and development of two optically identical finger PPG probes are also described.

Chapter 8 covers the development of a modular dual channel, dual wavelength PPG processing system. The chapter begins with the design brief and specifications of the system, followed by the top-level and circuit level design architecture. The system is used to drive the emitters, and precondition the acquired PPG signals (the ear canal and finger PPGs). The last sections of the chapter provide a comprehensive description of the manufacturing process and the system's performance.

Chapter 9 presents the developed virtual instrument (VI) which is used in conjunction with the developed sensors, Lead I ECG and the PPG instrumentation system. The chapter describes the various algorithms used in the VI to acquire, display and analyse the acquired PPG signals.

Chapter 10 describes the first *in vivo* investigation of PPG signals and SpO_2 values in healthy volunteers undergoing induced local hypoperfusion by means of a cold pressor

test (CPT). The motivation for the investigation is first presented here followed by the materials and methods of the study. The data acquired and the statistical analysis that was undertaken are presented, and the reasons for any particular trends in the data was discussed. Preliminary estimates of the ear canal SpO_2 were compared to those obtained from the peripheral finger probe during CPT.

Chapter 11 details the second *in vivo* investigation of PPG signals acquired from the ear canal and the finger of healthy volunteers undergoing peripheral vasoconstriction by hypothermia. The aims and objects of the investigation, the measurement setup, the protocol, the data analysis and materials used are described. Data and statistical analysis of all acquired PPG signals undertaken are presented and discussed. Comparisons are made of the AC and DC PPG amplitudes measured from the ear canal and the finger. The reliability of measuring accurate SpO_2 by the ear canal and the finger pulse oximeters under conditions of cold stress is assessed.

Chapter 12 presents the conclusions along with suggestions for future work.

— Oxygen is addicting and toxic. It rusts a person in a century or less. With oxygen came the danger, and the blessing, of fire. If introduced today, this gas might have difficulty getting approved by the Food and Drug Administration.

John W. Severinghaus - J Clin Monit 1986; 270-288

2

Tissue perfusion - Anatomy, physiology and pathology

The human body is composed of trillions (approx - 75) of cells. Each of these cells requires continuous oxygen (O_2) supply and excretion of carbon dioxide (CO_2) for metabolism. Metabolism is a set of diverse chemical reactions continuously proceeding in every living cell [23]. Oxygen starvation leads to improper metabolism, which in turn may lead to cell death. Thus, oxygen is known to be the most vital element for life [24]. Oxygen is delivered to each cell in the body with the help of the respiratory and circulatory systems. The respiratory system provides gaseous exchange i.e. intake of oxygen and removal of carbon dioxide, and the cardiovascular system transports blood containing gases from the lungs to every cell in the body [25]. The percentage level of oxygen present in the bloodstream indicates how well the cells are perfused and is called oxygen saturation [26]. Failure to either system upsets metabolism and allows waste product build-up. This may contribute to the development of multiple organ failures and increase chances of mortality. Thus, oxygen saturation measure is an important indicator of patients health. Several invasive and non-invasive techniques are used for measuring oxygen saturation in clinical environments with pulse oximetry being the most commonly used non-invasive technique [26]. This thesis proposes a new application of pulse oximetry which estimates arterial blood oxygen saturation from the external auditory canal. Before continuing, it is

essential to understand the mechanism of oxygen transport and underlying physiology of the respiratory and cardiovascular systems, which is the content of this chapter.

2.1 Respiratory system

A respiratory system is a group of organs that includes the lungs and the air passages (nose, pharynx, larynx, trachea and bronchi). Together these organs are responsible for carrying O_2 from the atmosphere into the bloodstream and for expelling the waste product CO_2. This process of gaseous exchange is known as respiration. The respiratory cycle in the human body is split into three main steps: pulmonary ventilation, external respiration and internal respiration.

2.1.1 Pulmonary ventilation

Pulmonary ventilation is the mechanical process by which gases are exchanged between the atmosphere and the lungs alveoli [28]. This process is controlled by the respiratory and motor neurones in the brain and spinal cord. The respiratory neurones in the brain are controlled by chemoreceptors (provide feedback on O_2, CO_2, and hydrogen ions in the blood) and mechanoreceptors (provide feedback on mechanical aspects of breathing) [29]. Depending on the feedback given by these receptors, the respiratory neurones excite the motor neurone in the spinal cord which causes the contraction of the diaphragm, the pectoral muscles and the external intercostal muscles [26]. This contraction results in the enlargement of the anteroposterior and lateral diameter of the chest cavity. The expansion of the chest cavity lowers pressure within the lungs triggering a pressure difference between the air inside the body and air outside the body. Thus, allowing air to flow into the lungs

FIGURE 2.1: The inspiratory and expiratory stages of pulmonary ventilation [27].

known as inspiration [30]. The inspired air flows from the nose into the pharynx, larynx, trachea, bronchi and finally, into the lungs alveoli, where the gases exchange. This gas exchange occurs through the process of diffusion (Section 2.1.2).

During normal breathing, the elastic recoil of the external intercostal muscles and the diaphragm causes a decrease in the diameter of the chest cavity and an increase in alveolar pressure. This creates a pressure gradient resulting in the flow of air out of the lungs [24]. However during forced breathing, the respiratory neurones cyclically excite the motor neurones in the spinal cord, resulting in contraction of the abdominal muscles and the internal intercostal muscles [26], causing a reduction in the diameter of the chest cavity and increasing the pressure inside the lungs as shown in Figure 2.1. This creates a pressure gradient resulting in the flow of air out of the lungs and is known as expiration.

2.1.2 External respiration

External respiration is the exchange of gases between the air in the alveoli and the blood in the pulmonary capillaries surrounding the walls of alveoli [24]. Alveoli are microscopic balloon-like structures made up of collagen and elastic fibres [31]. The elastic fibres help alveoli to stretch as they are filled with air during inhalation. Each alveolus is surrounded by a network of pulmonary capillaries as shown in Figure 2.2. The capillaries are made of simple squamous epithelium, so there are only two cells between the air in the alveoli and the blood in the pulmonary capillaries, which permits the efficient exchange of gases [32]. The gas exchange takes place by the process of passive diffusion.

Diffusion through tissue is described by Fick's law, which states that the rate of transfer of gas through a sheet of tissue is proportional to the tissue area and the difference in gas

FIGURE 2.2: Gas exchange occurs between alveoli and capillaries surrounding alveoli [33].

partial pressure between both sides, and inversely proportional to the tissue thickness [32]. Air in the alveoli has a higher partial pressure of oxygen (P_{O_2}) and lower partial pressure of carbon dioxide (P_{CO_2}). Blood being carried by the capillary network has higher P_{CO_2} and lower P_{O_2} [24]. This pressure gradient causes diffusion of O_2 from alveoli into blood and CO_2 from the blood into alveoli. However, external respiration cannot be carried out by diffusion in blood plasma alone, as gases are not particularly soluble in blood, which is composed mostly of water. Thus, for efficient oxygen transport, a secondary transport mechanism is required [34].

The compound "haemoglobin" (Hb) present in the red blood cells provides the necessary binding mechanism that allows oxygen to be transported through the blood. Haemoglobin (Heme = blood, Globin = polypeptide chain) molecules have a tetrahedral structure. Each haemoglobin molecule consists of four iron (heme) atoms which can bind with four atoms of oxygen accordingly [34]. In the oxygenated state, the molecule is called oxyhaemoglobin (HbO_2) and is bright red in colour, and in the reduced state, it is purplish blue and referred to as deoxyhaemoglobin. Haemoglobins that are unable to bind to oxygen or interfere with the ability of oxyhaemoglobin to release oxygen to the tissue are called dysfunctional haemoglobins. The three most common dysfunctional haemoglobins are methaemoglobin, carboxyhaemoglobin, and sulfhaemoglobin [26]

2.1.3 Internal respiration

Internal respiration refers to the exchange of gases between the blood in the systemic capillaries and the tissue cells. The oxygenated blood from the lungs returns to the heart via the pulmonary vein during external respiration. The heart pumps the oxygenated blood to the rest of the body through systemic capillaries. The tissue surrounding the systemic capillaries usually has lower P_{O_2} and higher P_{CO_2}, when compared to the oxygenated blood [31]. Hence, oxygen diffuses into the surrounding tissue and carbon dioxide diffuses into the blood. Once inside the cell, the oxygen is used for producing energy in the form of adenosine triphosphate (ATP).

2.2 The Oxyhaemoglobin dissociation curve

The oxyhaemoglobin dissociation curve as shown in Figure 2.3 is an important tool for understanding how readily haemoglobin acquires and releases oxygen molecules to the surrounding tissue. The oxyhaemoglobin dissociation curve illustrates the equilibrium of oxyhaemoglobin and deoxyhaemoglobin at various partial pressures [35]. The sigmoid shape of the curve is due to the cooperative binding nature of haemoglobin. When haemoglobin

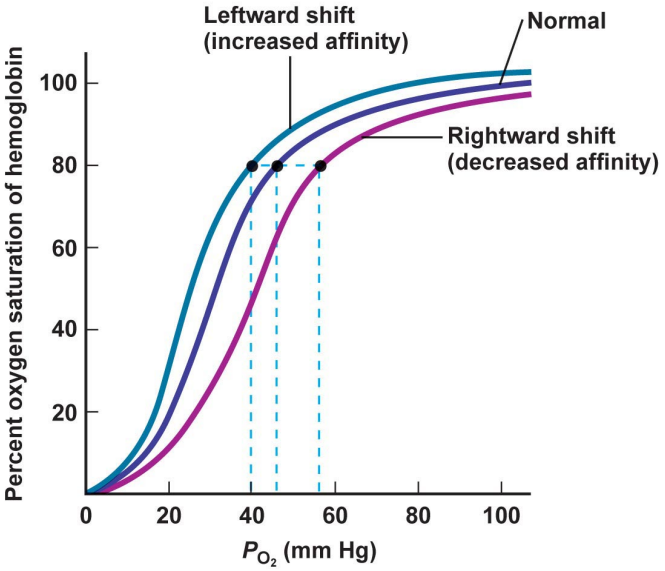

FIGURE 2.3: Oxyhaemoglobin disassociation curve [37].

binds with one oxygen molecule, it has a greater affinity to bind with another oxygen molecule. Consequently, when oxyhaemoglobin releases one oxygen molecule in the tissue, it has higher propensity to lose another oxygen molecule. Hence, at high partial pressures of oxygen, usually in the lungs, the red blood cells are saturated with oxygen (oxyhaemoglobin). At areas of low partial pressures of oxygen such as tissue the oxyhaemoglobin releases oxygen and becomes haemoglobin [26]. Factors such as decreased carbon dioxide concentration, increased pH and decreased temperature will shift the curve to the left. The left shifted curve indicates that haemoglobin molecules will be highly saturated at a lower partial pressure of oxygen. A right shifted curve means there is a reduced affinity between the haemoglobin and the oxygen [36].

2.3 Circulatory system

The circulatory system is a vast network of organs and vessels that is responsible for, (1) efficient delivery of oxygen and vital nutrients required by the cells, (2) removal of carbon dioxide and other waste products produced by the cells during cellular respiration. For efficient delivery of oxygen, blood must travel through a series of vessels with enough pressure. This is facilitated by the heart which acts as a pump [26]. Together, the heart and the blood vessels form circulatory routes through which blood is carried around the body. These routes are parallel and in most cases a portion of the cardiac output flows separately to each tissue of the body so that each organ receives it's own supply of freshly oxygenated blood. The two main circulatory routes are the systemic circulation and the pulmonary circulation [24].

2.3.1 Heart

The heart is a dual muscular pump which supplies oxygen-rich blood to the whole body and returns the deoxygenated blood to the lungs [38]. The heart consists of four hollow chambers; the upper two chambers are called atria and the lower two are ventricles. Internal valves present between the chambers help blood flow in one direction, preventing backwards flow of blood. The closing and the opening of these valves make a thumping sound - the 'heart beat' [23]. The sequence of events that occur when the heart beats is known as a cardiac cycle as shown in Figure 2.4(b). This sequence is initiated by a series of electrical impulses, originating from the sinoatrial node triggering the atria to contract. This contraction causes the opening of atrioventricular (AV) valves and rushing of blood into ventricles. These electrical impulses then pass through the atrioventricular node into ventricular walls, stimulating ventricular contraction [31]. As the ventricular contraction increases, the ventricular pressure causes the AV valves to close and opens the semi-lunar valves. The closing of AV valves at this stage results in producing the first heart sound 'LUB'. The opening of the semi-lunar valves allows the blood to flow into the pulmonary artery and the aorta. Once the ventricles start to relax the ventricular pressure falls causing the semilunar valves to shut. This produces the second heart sound 'DUB'.

FIGURE 2.4: (a) Stages in cardiac cycle. 1: relaxed heart, 2: atrial contraction, 3: ventricular contraction, [39] (b) Circulatory routes that deliver blood to tissues of the body [40].

2.3.2 Blood circulation

When the heart contracts during the cardiac cycle, the blood from the heart flows to the rest of the body through a network of blood vessels arranged in specific circulatory routes. The two main circulatory routes are the systemic circulation and pulmonary circulation [24]. The pulmonary circulation is the part of the circulatory system that transports blood to and from the lungs for the uptake of oxygen and removal of carbon dioxide. Deoxygenated blood from the right atrium is pumped into the right ventricle during atrial contraction. From the right ventricle of the heart, the blood is then pumped out into the pulmonary artery. The blood from the pulmonary artery travels through smaller arterioles and eventually into arterial capillaries in the lungs, where the gas exchange takes place between the alveoli and the capillaries [38]. The oxygenated blood from the lungs is then returned to the left atrium, and to the body through the systemic circulation (Figure 2.4(a)).

In the systemic circulation, the oxygenated blood from the left atrium is pumped into the left ventricle during atrial contraction. The blood from the left ventricle then enters the aorta during ventricular contraction. The aorta is the single systemic artery emerging from the heart. By successive branching, the aorta gives rise to hundreds of arteries taking oxygenated blood to all regions of the body [30]. Following the branching, the arteries divide into numerous arterioles. In the target organs, they produce many capillaries. A similar number of venules converge into each other forming veins of increasingly larger size. Finally, only the two veins, the superior and the inferior vena cava return the blood to the right atrium [30]. This unimpeded flow of blood to the body via the circulatory networks is referred as *perfusion*, and the volume of blood that flows through a target tissue is known as *Tissue perfusion*.

2.4 Significance of oxygen in human body

Oxygen is the key element for the survival of cells in the human body. Cells obtain energy by oxidation of glucose to carbon dioxide and water in cellular respiration. This energy is used in the regulation of tissue repair, growth, immune functions, and hormone synthesis [41]. In the absence of oxygen, cells cease to function and eventually die leading to malfunctioning of organs. At times when dead and degenerative cells cannot be replaced with new cells, the toxins from dead cells poison surrounding cells [42]. This causes them to mutate forming abnormal growths and increased susceptibility to infectious diseases. Restriction of oxygen supply in the blood is known as hypoxemia [1]. This condition can be caused by blockage of airways, intake of narcotics, stress, high altitudes, and diseases such as anaemia, pulmonary oedema, sleep apnoea, and pneumonia. The primary symptoms

of hypoxemia include shortness of breath, fatigue, confusion, pain in muscles and joints, short term memory loss, etc., [43]. Also, chronic restriction of oxygen transport in the body caused by a build-up of plaque in the arteries can lead to stroke and heart failure. With increased amount of oxygen consumption, our bodies can reverse degeneration, stimulate the immune system and promote healing. Thus, oxygen is essential for healthy function of living organisms.

2.5 Pathologies due to impaired perfusion

Adequate perfusion is required for life. If an organ is not adequately perfused with sufficient oxygenated blood, it cannot create enough energy to maintain its health and function. This section describes some of the pathologies resulting from inadequate perfusion.

2.5.1 Circulatory shock

Circulatory shock represents a state of collapse and failure of the cardiovascular system in which blood circulation decreases and eventually ceases [44]. Shock results from the inadequate cardiac output. Therefore, any condition that reduces the cardiac output far below normal will likely lead to circulatory shock. The two factors that severely reduce cardiac output are (1) decreased ability of the heart to pump blood due to cardiac abnormalities and (2) decreased venous return. The circulatory shock that results from diminished cardiac pumping ability is called *cardiogenic shock*. Shock resulting from heavy loss (20% or $1/5^{th}$) of the body's blood is called hypovolemic shock or haemorrhagic shock [45]. One of the key dangers of shock is that it progresses by a positive feedback mechanism. Once shock begins, it tends to make itself worse, so immediate treatment of shock is critical to the survival of the sufferer [46]. Almost 70% of the people who develop cardiogenic shock do not survive.

2.5.2 Ischaemia

Ischaemia can also be described as an inadequate flow of blood to a part of the body, caused by constriction or blockage of the blood vessels supplying it. It is an absolute or relative shortage of the blood supply to an organ that can be caused due to conditions such as tachycardia, atherosclerosis, hypotension, thromboembolism and foreign body embolism [47]. Ischaemia may result in irreversible damage to highly aerobic tissues of the heart and brain, in as little as 3-4 minutes at body temperature. Tissues with slower metabolic rates may undergo irreversible damage after 20 minutes [48]. Without immediate intervention, ischaemia may progress quickly to tissue necrosis and gangrene within a few hours.

Restoration of blood supply to ischaemic tissues causes the production of free radicals and reactive oxygen species that cause additional damage to the cells known as reperfusion injury. This can be more damaging than the initial ischaemia. The restored blood flow also exaggerates the inflammation response of damaged tissues, causing white blood cells to destroy damaged cells that may otherwise still be viable [49].

2.5.3 Hypoxia

Hypoxia is defined as the deficiency in the amount of oxygen reaching body tissues. Hypoxia can be caused due to inadequate transport and delivery of oxygen, inadequate tissue capabilities of using oxygen, venous to arterial shunts and hypoventilation [50]. Hypoxia, if severe enough, can cause the death of the cells, but in less severe degrees it results principally in depressed mental activity, sometimes culminating in a coma, and reduced work capacity of the muscles [51].

2.6 Summary

The ability of the body to utilise oxygen has a direct impact on health. Oxygen present in the air is inspired into the lungs during breathing. The inspired oxygen is diffused into the blood with the help of haemoglobin. The blood then supplies oxygen to every cell in the body with the help of the cardiovascular system. The cells receive oxygen and convert it into the energy required to carry on processes essential for living. Failure in any of these processes can lead to cell death and may eventually cause organ failure and death. Oxygen saturation levels in the human body is a direct indicator of good health. Oxygen starvation in the human body leads to build up of acids in muscles, poor digestion, and dizziness. Hence, it is imperative to measure oxygen levels in critically ill patients with low blood flow states. There are several techniques for measuring oxygen levels in the body and these are discussed in the next chapter.

— For life, nothing is more important than oxygen supply. Thus, one might argue that nothing is more important to monitor the care of the unconscious or disabled patient than the colour of the arterial blood.

John W. Severinghaus, and Poul B. Astrup - J Clin Monit 1986; 270-288

3

A review of oxygen measurement technologies

Adequate oxygen supply to the body's tissues is required for normal body function. Knowledge of oxygen level in the blood could help assess a person's health and overall well-being. Blood oxygenation is the measure of oxygen present in arterial or venous blood. Tissue oxygenation is the measure of oxygen present in the vascular tissue (i.e. measuring O_2 in microvascular bed). Blood oxygenation assesses how well oxygen binds to haemoglobin, indicating adequacy of pulmonary gas exchange. Tissue oxygenation indicates adequacy of tissue perfusion and is primarily determined by local oxygen delivery, particularly blood flow.

Oxygen levels in the blood or tissue can be measured using chemical, optical or colorimetric techniques. Some methods determine blood oxygenation by measuring the partial pressure of oxygen (P_{O_2}) in blood and others by measuring oxygen saturation (SO_2) [26]. 'Oximetry' is the general term used to refer to optical methods of measuring oxygen levels, and is most often used in clinical environments. In oximetry, the level of oxygen in arterial and venous blood is indirectly determined by measuring the arterial oxygen saturation (SaO_2) and the venous oxygen saturation (SvO_2) [43]. Oxygen levels measured in tissue are determined by measuring the tissue oxygen saturation (StO_2) or the tissue oxygenation index (TOI). Figure 3.1 shows the taxonomy of oxygenation measurement in blood and tissue. It is not within the scope of the thesis to explain all the methods used to measure

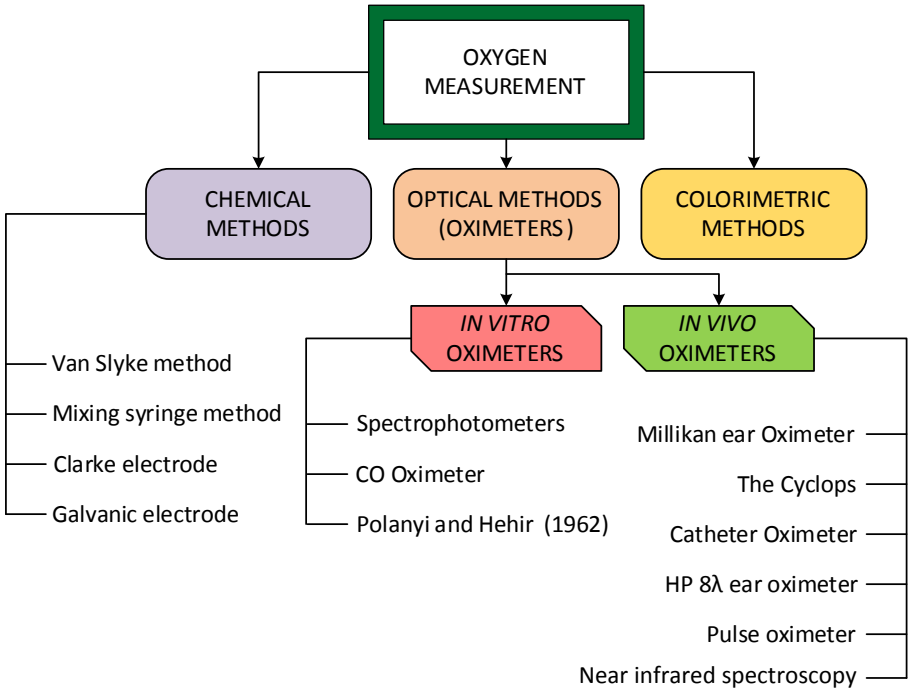

FIGURE 3.1: Taxonomy of the field of oxygenation measurement (Redrawn from [52]).

oxygen in the body. Hence, a few key methods that are commonly used in clinical environments are described in the chapter. The first section of the chapter describes one of the most commonly used chemical methods of determining tissue oxygenation, and the rest of the chapter discusses, optical techniques used to determine blood and tissue oxygenation.

3.1 Clark's electrode

Clark's electrode is an electrochemical oxygen sensor most commonly used to determine the partial pressure of oxygen in arterial blood. It is widely used in blood gas analysers, which use a variety of electrodes to measure pH, P_{O_2} and P_{CO_2} in small samples of blood [26]. Clark's electrode uses the basic principles of oxidation and reduction to measure P_{O_2} in a solution. This sensor is categorised as an amperometric sensor and requires an external polarising bias voltage source of about 0.6 V. As shown in Figure 3.2, the sensor consists of silver (anode) and platinum (cathode) electrodes connected to the positive and negative side of a voltage source, immersed in potassium chloride electrolyte. The cathode is made from noble metals such as platinum or gold so that the electrode surface does not participate in the chemical reactions. When oxygen is dissolved in the potassium chloride

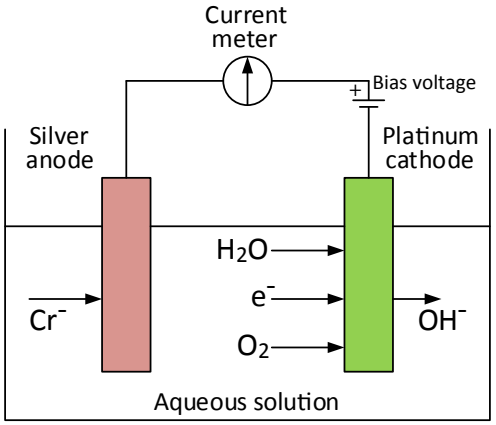

FIGURE 3.2: Principle of operation of Clark electrode (inspired from [56]).

solution and exposed to the bias voltage, the following reaction occurs,

$$At\ the\ cathode: O_2 + 2H_2O + 4e^- = 4OH^- \tag{3.1}$$

$$At\ the\ anode: Ag + Cl^- = AgCl + e^- \tag{3.2}$$

$$In\ the\ electrolyte: NaCl + OH^- = NaOH + Cl^- \tag{3.3}$$

Electrons are taken up at the cathode and the current generated is directly proportional to the O_2 molecules reduced at the surface of the cathode (i.e., the amount of P_{O_2} in the solution) [53],[54],[55]. The actual sensor is arranged in a cylindrical fashion, and is used to measure P_{O_2} of blood solutions in vitro, and when miniaturised, can be attached to the end of the catheter and placed inside an artery to provide in vivo measurement [55].

3.2 Spectrophotometry

Spectrophotometry is an optical technique used to measure the concentration of any transparent substance in a solution. It is the basis for all oximetry techniques. A spectrophotometer usually consists of a light source, a monochromator, a cuvette, a photodetector and an amplifier as shown in Figure 3.3. Wide bandwidth incandescent light is passed through the monochromator to produce a single-wavelength beam of choice [57]. The monochromator can consist of either a prism, a diffraction grating, or a narrow-bandwidth filter. Monochromatic light is then passed through a cuvette of known path length containing the substance under test. A portion of this light is transmitted through the sample and the rest is absorbed by the sample. The transmitted light is detected by the photodetector on the other end of the cuvette [1]. The photodetector converts detected light into an electrical current proportional to the intensity of the light detected. The concentration

FIGURE 3.3: Block diagram of a single beam spectrophotometer [58].

of a light-absorbing substance in a solution is then determined by the spectrophotometer using the Beer-Lambert law [57]. According to Beers's law, when a monochromatic light of intensity I_0 enters a sample, a part of the light is transmitted through the sample while another part is absorbed. The intensity I of light transmitting through the medium decreases exponentially with distance. This relationship is given as

$$I = I_0 \; e^{-\varepsilon(\lambda).c.d} \tag{3.4}$$

Where '$\varepsilon(\lambda)$' is the extinction coefficient of the absorbing substance at a specific wavelength, 'c' is the concentration of the absorbing substance which is constant in the medium, and d is the optical path length through the medium. The transmittance of light travelling through the medium is defined as the ratio of transmitted light (I) to incident light (I_0) [1].

$$Transmittance\ (T) = \frac{I}{I_0} = e^{-\varepsilon(\lambda).c.d} \tag{3.5}$$

As each molecule in the solution absorbs light equally, the absorbance of the substance is linearly related to the concentration of substance in the sample and is defined as the negative logarithm of transmittance

$$Absorbance\ (A) = -\ln(T) = \varepsilon(\lambda).c.d \tag{3.6}$$

Beer's law can be applied to a medium containing more than one absorbing substance. The total absorbance of the sample is given by the sum of n independent absorbances.

$$A_t = \varepsilon_1(\lambda).c_1.d_1 + \varepsilon_2(\lambda).c_2.d_2 + ... + \varepsilon_n(\lambda).c_n.d_n \tag{3.7}$$

As mentioned earlier, spectrophotometers are used for determining the concentration of any transparent substance in a solution. However, in a clinical setting, they are used to measure the concentration of oxygen in the blood. The concentration of oxygen in the blood can only be measured if the chemical and light absorbance properties of blood are known [26]. The chemical and light absorbance characteristics of blood depend on haemoglobin present in red blood cells. The absorbance properties of haemoglobin change

with its chemical binding and the wavelength of the incident light. The following subsections describe how haemoglobin binds with different chemicals in blood and also explains how each of these different haemoglobins absorb incident light at different wavelengths.

3.2.1 Chemical binding of haemoglobin

As described in Section 2.1.2, haemoglobin binds with oxygen in the alveoli during external respiration. In the oxygenated state the molecule is called oxyhaemoglobin (HbO_2) and is bright red in colour. In the reduced state (i.e., when the oxygen in the blood is diffused to the cells) the molecule is referred to as deoxyhaemoglobin (Hb). These haemoglobins that can bind reversibly with molecular oxygen are called functional haemoglobins. Although oxygenated and reduced haemoglobin make up most of the blood content in the body, they do not represent the only haemoglobin species present in human blood [59]. Haemoglobin may also combine with other substances such as carbon monoxide or hydrogen sulphide as well. Haemoglobins that are unable to bind to oxygen or interfere with the ability of oxyhaemoglobin to release oxygen to the tissue are called Dysfunctional haemoglobins [1]. The two most common dysfunctional haemoglobins are:

- **Methaemoglobin (MetHb)**: Methaemoglobin is oxidised haemoglobin and is the result of oxidation of a free heme ion (Fe^{2+}). MetHb levels may be high congenitally or as a result of exposure to a number of agents, most notably anaesthetics, sulpha drugs, and nitrites. In healthy individuals, the amount of methaemoglobin remains under 0.6% [1].

- **Carboxyhaemoglobin (COHb)**: This is formed when haemoglobin combines with carbon monoxide (CO). The affinity of Hb binding with CO is approximately 210 times larger than that of oxygen [60]. Therefore, the presence of a high level of CO will reduce the amount of oxygenated Hb significantly. Smoking increases the level of COHb, but normal levels are below 2%. Inhalation of CO from fires can cause a dangerous or fatal rise in COHb concentration [61].

3.2.2 Haemoglobin absorption spectra

Haemoglobin and its variants have specific characteristics for light absorption. Each has its own pattern of absorption over a range of wavelengths. This is due to different chemical bonding characteristics of haemoglobin. Figure 3.4 shows the extinction coefficients of oxyhaemoglobin, reduced haemoglobin, methaemoglobin and carboxyhaemoglobin in the red and near-infrared region. The absorbance of light in the red region of the spectrum is much higher for reduced haemoglobin than for oxyhaemoglobin. The extinction coefficients

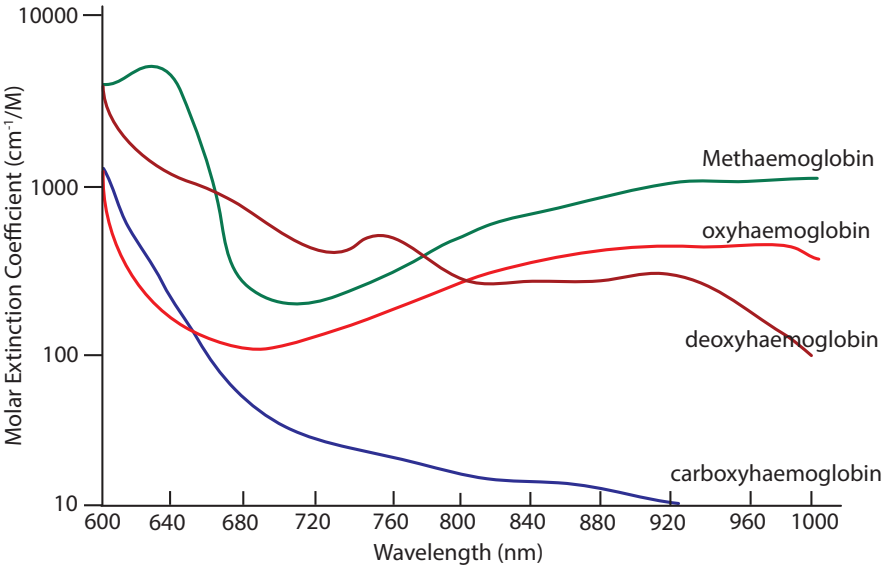

FIGURE 3.4: Extinction coefficients of the four most common haemoglobin species - oxyhaemoglobin, deoxyhaemoglobin, carboxyhaemoglobin and methaemoglobin - in the visible and near-infrared regions [26].

of both haemoglobin species are equal at the isobestic point (805 nm) [62]. The reduced haemoglobin is more transparent to light in the infrared region of the spectrum than the oxyhaemoglobin. The extinction coefficient of carboxyhaemoglobin is about the same as that of oxyhaemoglobin in the red region while it is almost transparent in the infrared band. Methaemoglobin absorbs much light in the red region of the spectrum and its extinction coefficient remains higher than that of oxyhaemoglobin in the infrared region [63]. Using these optical properties of blood, the concentration of all the haemoglobin species in a sample of blood can be determined using a spectrophotometer. If the absolute concentrations of different haemoglobin species in a sample of blood are known then, the functional and fractional oxygen saturation of the sample can be calculated easily. The functional oxygen saturation is measured as a percentage and is defined as the ratio of oxyhaemoglobin (C_{HbO_2}) concentration to the sum of concentrations of oxygenated and reduced haemoglobin (C_{Hb}) [64],[63].

$$Functional\ SO_2 = \frac{C_{HbO_2}}{C_{Hb} + C_{HbO_2}} \times 100\% \tag{3.8}$$

The fractional oxygen saturation is the measured as a ratio of the concentration of oxygenated haemoglobin to the concentration of total haemoglobin [1].

$$Fractional\ SO_2 = \frac{C_{HbO_2}}{C_{Hb} + C_{HbO_2} + C_{COHb} + C_{MetHb}} \times 100\% \tag{3.9}$$

3.3 CO-Oximeters

CO-oximeters are spectrophotometers specially designed to analyse the concentrations of four most common species of haemoglobin in blood; oxyhaemoglobin, reduced haemoglobin, carboxyhaemoglobin, and methaemoglobin. CO-oximeters are very accurate and are considered the "gold standard" method for measuring haemoglobin species [1]. A CO-oximeter analyse small samples of arterial blood collected in a heparinized syringe. Samples are collected in a heparinized syringe to prevent clotting of the blood. The blood sample is inserted into the sample port of a CO-oximeter and then transported into a cuvette which is regulated at 37° C. The blood sample is then haemolysed (red blood cell membranes removed) to reduce the amount of light scattering. This is to increase the accuracy of the measurement [26]. Scattering is reduced in a haemolysed sample as the haemoglobin molecules are distributed evenly throughout the blood sample instead of being localised in red blood cells.

Light from a halogen lamp is transmitted by two different pathways within the instrument, and two measurements sensors are used. One pathway is the transmission of light directly from the source to the detector. This measurement provides a reference value for the intensity of light transmitted. The second light pathway is from the source, through the blood sample, and into the sensor. This pathway is used to measure the intensity of unabsorbed light by the sample. In modern CO-oximeters, the unabsorbed light before reaching the photodiode is split into 128 different wavelengths using a concave diffraction grating [65]. However, in the most basic mode, the instrument uses data from four wavelengths to calculate the concentrations of the four most common Hb species:

$$C_{Hb} = K[\varepsilon_{Hb}(\lambda_1)A_1 \ + \ \varepsilon_{Hb}(\lambda_2)A_2 \ + \ \varepsilon_{Hb}(\lambda_3)A_3 \ + \ \varepsilon_{Hb}(\lambda_4)A_4] \tag{3.10}$$

$$C_{HbO_2} = K[\varepsilon_{HbO_2}(\lambda_1)A_1 \ + \ \varepsilon_{HbO_2}(\lambda_2)A_2 \ + \ \varepsilon_{HbO_2}(\lambda_3)A_3 \ + \ \varepsilon_{HbO_2}(\lambda_4)A_4] \tag{3.11}$$

$$C_{COHb} = K[\varepsilon_{COHb}(\lambda_1)A_1 \ + \ \varepsilon_{COHb}(\lambda_2)A_2 \ + \ \varepsilon_{COHb}(\lambda_3)A_3 \ + \ \varepsilon_{COHb}(\lambda_4)A_4] \tag{3.12}$$

$$C_{MetHb} = K[\varepsilon_{MetHb}(\lambda_1)A_1 \ + \ \varepsilon_{MetHb}(\lambda_2)A_2 \ + \ \varepsilon_{MetHb}(\lambda_3)A_3 \ + \ \varepsilon_{MetHb}(\lambda_4)A_4] \tag{3.13}$$

Where C_x is the concentration of Hb species 'x'. $\varepsilon_x(\lambda_1)$ is the extinction coefficient of haemoglobin type x at the first wavelength, A_1 is the absorbance value of blood at the first wavelength and K is a constant set by the calibration procedure. Total haemoglobin concentration, fractional oxygen saturation and functional oxygen saturation of blood sample are measured by the instrument using the measured haemoglobin concentration values [1]. Although CO-oximeters provide a very accurate *in vitro* measurement, they have the disadvantage that every time a measurement is required, a blood sample must be taken and the readings obtained apply only to the instant in time in which the blood is withdrawn.

3.4 Optical fibre venous oximetry

Fibre optic venous oximetry is an *in vivo*, catheter-based oximetry technique used to measure continuous blood oxygen saturation in critically ill patients. This technique measures oxygen levels in venous blood instead of arterial blood. Oxygen saturation measured from the arterial blood indicates how well the body is perfused with oxygenated blood. While oxygen saturation measured from mixed venous blood reflects the amount of O_2 left over in the blood, after the uptake of O_2 by tissue [66]. Hence by measuring venous oxygen saturation (SvO_2) of a hemodynamically unstable patient in ICU, the balance between oxygen delivery and consumption at the tissue level, can be monitored. The normal range for SvO_2 is 60 - 80 %. If the SvO_2 value is normal, there is sufficient oxygen supply available to the tissues. However, if the SvO_2 value is low, then either the oxygen supply is insufficient or the oxygen demand is elevated. Regardless of the cause, a decrease in SvO_2 indicates that the body has called upon its last line of defence to preserve oxygen balance and in these cases therapeutic interventions may be appropriate [67].

$$SvO_2 = \text{Oxygen Delivery } (SaO_2) - \text{Oxygen Consumed } (vO_2) \tag{3.14}$$

SvO_2 values are usually only measured in the pulmonary artery. This is to allow for adequate mixing of venous blood returning to the right side of the heart from the superior and inferior vena cavae and the coronary sinus [68].

SvO_2 is measured by a multi-lumen tube (catheter), made of flexible plastic with a number of channels. The distal end of the catheter consists of a small inflatable balloon and a thermistor, used to measure cardiac output. Running along the distal end of the catheter

(a) Catheter in the pulmonary artery of the heart (b) Venous oxygen saturation measurement system

FIGURE 3.5: Venous oxygen saturation is measured from the pulmonary artery of the heart using reflection spectroscopy [68].

is a pair of optical fibres, used for venous oxygen saturation measurements (Figure 3.5(a)). The technology used to measure SvO_2 is based on reflection spectrophotometry [69]. This involves transmitting light of selected wavelength through one of the fiber-optic filaments to the blood flowing past the catheter tip and detecting the reflected light back using the other fiber-optic filament. The detected light is converted into an electrical signal using the photodetector located in the optical module (Figure 3.5(b)). Since haemoglobin and oxyhaemoglobin absorb light differently at the selected wavelengths, the reflected light can be analysed to determine the percent SvO_2. Although continuous oxygen measurement is possible using optical fibre venous oximetry, it requires the placement of a pulmonary artery catheter, which is an invasive procedure with the possibility of numerous complications [68].

3.5 Pulse Oximetry

Pulse oximetry is a non-invasive optical technique used to monitor continuous arterial oxygen saturation in human vascular tissue. There is no doubt that pulse oximetry represents the greatest advancement in patient monitoring in recent years. By virtue of its ability to quickly detect hypoxaemia, it has become the standard of care during anaesthesia as well as in the recovery room and intensive care units. It was invented by Takuo Aoyagi in 1974 [26]. Pulse oximeters determine the oxygen saturation of arterial blood by measuring the light absorbance of living tissue at two different wavelengths and use the arterial pulsation to differentiate between the absorbance of arterial blood and other absorbers such as skin, melanin, venous blood, etc., [70]. The two wavelengths typically used are 660 nm and 940 nm, but other wavelengths could be used. The absorbance of light by tissue at both wavelengths is recorded as a voltage signal known as the photoplethysmograph (PPG) [71]. The photoplethysmograph consists of two main components, an AC pulsating component

FIGURE 3.6: A portable fingertip pulse oximeter [26].

(refers to absorption during arterial pulsation) and a DC component (refers to the absorption of venous blood and other absorbers). The saturation values obtained *in-vivo* by the pulse oximeter is often abbreviated SpO_2 to differentiate it from the saturation value obtained *in-vitro* from haemolysed arterial blood by a CO-oximeter (SaO_2). SpO_2 values in healthy individuals are between 95% and 100% [72]. Pulse oximeters are empirically calibrated by the manufacturers using data obtained from a large group of healthy human volunteers. Pulse oximeters possess many advantages over previous technologies. They are non-invasive, continuous, does not require calibration, are accurate, relatively mobile and convenient to use [73]. A detailed description of the technology and its application is described in Chapter 4.

3.6 Near infrared spectroscopy

Diverse optical systems used for measuring blood oxygenation have been discussed in this chapter so far, this section depicts a non-invasive method for measuring tissue oxygenation in the body. Near-infrared spectroscopy (NIRS) is one of the commonly used optical techniques to provide a regional quantification of tissue oxygenation in the body. NIRS was first invented by F.F Jobsis in 1977 and since then many groups around the world have refined and amended the technique [74]. NIRS systems can be connected to any vascular part of the body for instance on the muscles to gauge the oxygen uptake. However, the technique is predominantly utilised in quantifying the oxygenation status of the brain tissue [75].

The basis of NIRS relies upon two main principles: (1) that tissue is relatively transparent to light in the near infrared region (i.e., 700 - 1100nm) and (2) that there are compounds in the tissues whose absorption of light varies with oxygenation (e.g. HbO_2, Hb, CytOx) and have characteristic absorption spectra (Figure 3.4). The concentrations of these compounds are likely to change rapidly during alterations in tissue perfusion and oxygenation [76].

3.6.1 Modified Beer-Lambert law as used in NIRS

NIRS provides tissue oxygenation measure by monitoring *in-vivo* changes of the oxygen saturation of haemoglobin molecules in the body, based on the absorbance of near-infrared light by haemoglobin [77]. The concentrations of haemoglobin variants are then determined using the Beer-Lambert law (Equation 3.6). However attenuation of light energy in tissue due to absorption (20%) is relatively low compared to the scattering of light (80%), and it is the scattering effect which causes the light to travel further than the straight line

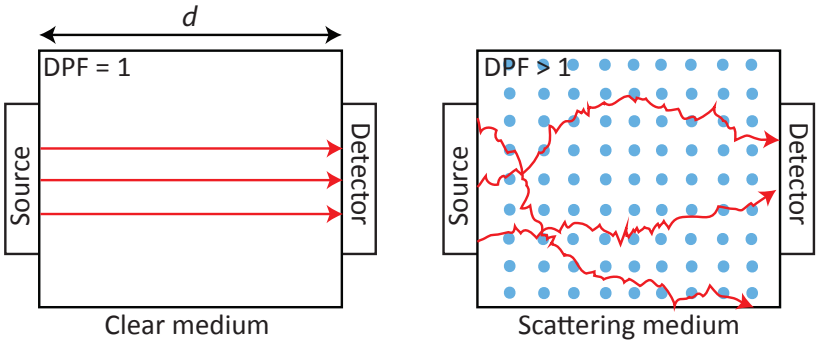

FIGURE 3.7: Illustration showing the path length of light photons in a clear and scattering medium. The actual light path of photons increases due to scattering (inspired from [76]).

between the source and the detector as shown in Figure 3.7 [78]. Besides being the major cause of light attenuation in tissues, Beer's law does not take into account scattering while deriving the concentration of different chromophores. The increase in the distance travelled by each photon because of scattering introduces an additional factor known as differential pathlength factor (DPF) to Beer's law [79].

$$A = \varepsilon(\lambda).c.d.DPF + G \quad \left(DPF = \frac{\text{Mean optical path length}}{\text{Inter-optode spacing (d)}}\right) \tag{3.15}$$

Where DPF is the ratio of mean optical path length to the straight line distance between the source and the detector, and G expresses the attenuation due to scattering. DPF is generally derived from studies in healthy adults and is assumed to be constant. In reality, the value varies from individual to individual. Values for DPF in different tissues and patient age groups are in the public domain [80–82].

3.6.2 Deriving tissue oxygenation using NIRS

The algorithms used by NIRS systems to derive tissue oxygenation vary from manufacturer to manufacturer but the essential features and the physical principles are common across all commercially available NIRS systems [74]. Near infrared light generated at two or more wavelengths by laser diodes is directed into vascular tissue and the attenuated light is detected by a silicon photodiode placed several cm away from the light source. The wavelengths used are a mix of wavelengths around the isobestic point of the haemoglobin absorption spectrum (Figure 3.4), such as 770/830, 760/840 and 690/900 nm [83]. The changes in light attenuation are converted into chromophore concentrations by an inbuilt computer. Two distinct methods are commonly used in handling the data conversion. The two methods are the relative quantification method or continuous wave method and the absolute concentration quantification method.

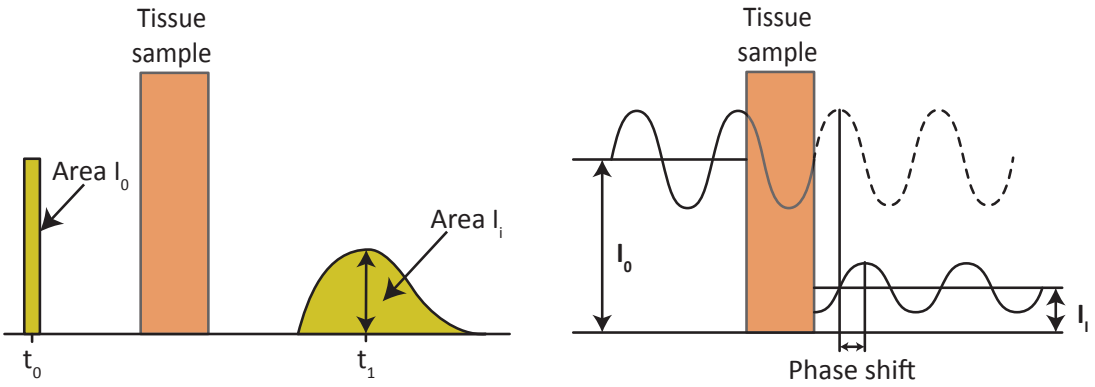

(a) Time domain NIRS

(b) Frequency domain NIRS

FIGURE 3.8: Schematic presentation of the two main categories of quantitative NIRS (inspired from [76]).

Continuous wave (CW) NIRS instruments are the earliest and the most common commercial NIRS devices. In the continuous wave method, the absolute concentrations of haemoglobin are not measured, as the loss of light due to tissue scattering (G) is not known [79]. The scattering factor 'G' is dependent upon the measurement geometry and the scattering coefficient of the tissue. Therefore, CW-NIRS assumes that G does not change during the measurement period and determines the change in concentration of a chromophore (Δc) from the change in attenuation (ΔA) [78]. The change in absorption of haemoglobin variants is given by

$$(\Delta A) = (\Delta c).\varepsilon(\lambda).d.DPF + \Delta G; \quad \text{where } \Delta G = 0 \tag{3.16}$$

A ratio of light absorption by oxyhaemoglobin and haemoglobin is then used to calculate the mean tissue oxygen saturation. Thus avoiding quantification of change in haemoglobin concentrations. CW-NIRS is only fit to do oxygenation trend monitoring. However, over the years several methods to quantify the changes in concentrations of chromophores were investigated. One such method regularly used by commercial NIRS devices is spatially resolved spectroscopy (SRS) [84].

The second category of NIRS equipment allows full quantification of changes in chromophore concentration and maximises the potential of tissue spectroscopy. The NIRS devices using the absolute quantification technique can be classified into two main groups - (1) Time domain NIRS instruments, (2) Frequency domain NIRS devices. In time-domain NIRS measurements, the tissue is illuminated with ultrashort light pulses (2ps), and variations in received light intensity are measured with respect to time (as shown in Figure 3.8) [79]. From these variations, the actual distance travelled by the light photons is calculated. Since the absorption of the light, the distance and the extinction coefficient are known, the concentration of oxyhaemoglobin and haemoglobin can be calculated. For

known concentrations of HbO_2 and Hb, the tissue oxygenation index TOI is given by

$$TOI\ or\ StO_2 = \frac{HbO_2}{HbO_2 + Hb} \times 100\% \tag{3.17}$$

In frequency domain NIRS measurements, the light source is modulated to a frequency of 100-200 MHz, and the relationship between the amplitude and the phase of the incident and the detected light (the optical frequency response of the tissue) is measured [85]. Using the measured phase shift, the actual path length is calculated. From these measurements, the concentration of haemoglobin variants and the tissue oxygenation is measured.

3.7 Summary

Oxygen levels in the human body can be measured using chemical, optical and calorimetric techniques. Oximetry is the general term used to refer to optical measurement techniques. Spectrophotometry is the basis of all the oximetry techniques. CO-oximeters are specially designed spectrophotometers used to determine the concentrations of Hb species in blood. Tissue oxygenation can be measured by near infrared spectroscopy. Other optical techniques for monitoring blood oxygen level include optical fibre venous oximetry, pulse oximetry, etc. Pulse oximetry is the safest, efficient, and reasonably accurate method for measuring arterial oxygen saturation. A detailed description of this technique is given in next chapter.

— The clinical applications of pulse oximetry in medicine are as important as oxygen is to life. This may seem an overstatement, but as more and more pulse-oximeters are coming into use, more and more hypoxaemic events are being seen as precursors of pathological events

John TB Moyle - Pulse oximetry, 1994

4

Theory of Pulse Oximetry

Blood oxygenation is determined by measuring the partial pressure of oxygen (PO_2) in blood or by measuring oxygen saturation (SaO_2). There are various methods for measuring oxygen levels in the body as discussed in Chapter 3. Pulse oximetry is one of the most convenient non-invasive and accurate techniques for measuring arterial oxygen saturation. The fact that this non-invasive technology measures SpO_2 continuously without the need for calibration has made it a standard for monitoring blood oxygenation status in critical care. Takuo Aoyagi first developed the pulse oximeter in 1974 using a combination of transmission oximetry and photoplethysmography [86]. Pulse oximeters provide a robust measure of SpO_2 by shining light into the vascular tissue, and measuring the changes in light absorbance produced during arterial pulsations. These changes in light absorbance during arterial pulsations are measured as a voltage signal known as a photoplethysmograph.

This chapter describes the theoretical background of the principle of pulse oximetry. The principle of photoplethysmography and its application in pulse oximetry are also discussed in this chapter to highlight how the pulsatile arterial blood can be differentiated from venous blood and miscellaneous tissue. The light absorbance properties of blood and the modified Beer-Lambert law as used in pulse oximetry are also explained in this chapter, before discussing how current commercial pulse oximeters are calibrated for estimating

SpO_2. Finally, a brief review of the type of optical components used in modern pulse oximeter sensors, and the sensor design configurations are discussed in the chapter.

4.1 Photoplethysmography

Photoplethysmography is a non-invasive optical technique widely used in the study and monitoring of pulsations associated with changes in blood volume in the peripheral vascular bed [87]. It has a widespread clinical application, with the technology being utilised in commercially available medical devices, for example in pulse oximeters, vascular diagnostics and digital beat-to-beat blood pressure measurement systems [88]. Although this technique has been used for many years, there are still disagreements about how the information collected arises in the photoplethysmographic signal and there are some doubts and fundamental misconceptions associated with the method [87]. It is generally accepted, however, that PPGs can provide valuable information about the cardiovascular system [89].

4.1.1 Principle of photoplethysmography

When light transilluminates vascular tissue, the emitted light is reflected, scattered and absorbed in the tissue and blood. The intensity of light absorbed or reflected varies with arterial pulsations (heart's pulsations). These variations are due to the transmitted light intensity corresponding directly to the cardiac cycle and can be detected using a photodetector. This is the principle on which photoplethysmography is based [90].

It is possible for the tissue to directly transilluminate vascular tissue by placing the light source on one side of the skin and the photodiode on the other. This mode known as the transmission mode is limited to areas such as the finger, the ear lobe or the toe [26]. However, when the light is directed down into the skin, a proportion of the light is backscattered so that it emerges from the skin adjacent to the light source. This reflected light can be detected by placing the photodetector next to the light source. This mode is called the reflection mode which, allows measurements on virtually any vascular tissue [64], [90]. The intensity of the reflected and backscattered light which reaches the photodetector in either reflection or transmission mode is measured and the variations in the photodetector current are assumed to be related to blood volume changes underneath the probe. These variations are electrically amplified and recorded as a voltage signal called the photoplethysmograph (PPG) (Figure 4.1) [91].

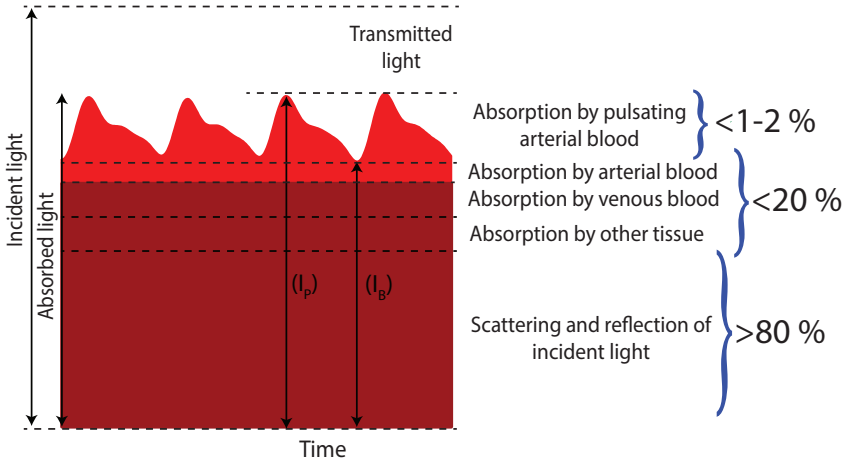

FIGURE 4.1: Absorbed and transmitted light in living tissue. The amount of absorbed light correlates with the pulsation of arterial blood (illustration inspired from [92])

4.1.2 Photoplethysmographic waveform

The photoplethysmographic waveform is divided into two components. A pulsatile AC component synchronous with the cardiac cycle and a slowly varying DC component with a magnitude that is determined by the nature of the material through which the light passes (skin, cartilage, venous blood, etc.) (Figure 4.1). The amplitude of the pulsatile component varies with the pumping action of the heart. As the volume of blood in arteries and the arterioles starts to increase during systole, the proportion of incident light absorbed also increases. Conversely during diastole, the light absorption decreases with a decrease in blood volume, creating a rapidly alternating signal. These excursions in light absorption typically account for 1-2% of the total light absorption [93]. However, this is not entirely due to the increase in blood volume during systole, if it were, then the variation in absorption during the cardiac cycle would be very much less [1].

Examination of fluid mechanics of blood by D'Agrosa and Hertzmen in 1967 has shown that the orientation of red blood cells in blood changes during the cardiac cycle, thereby

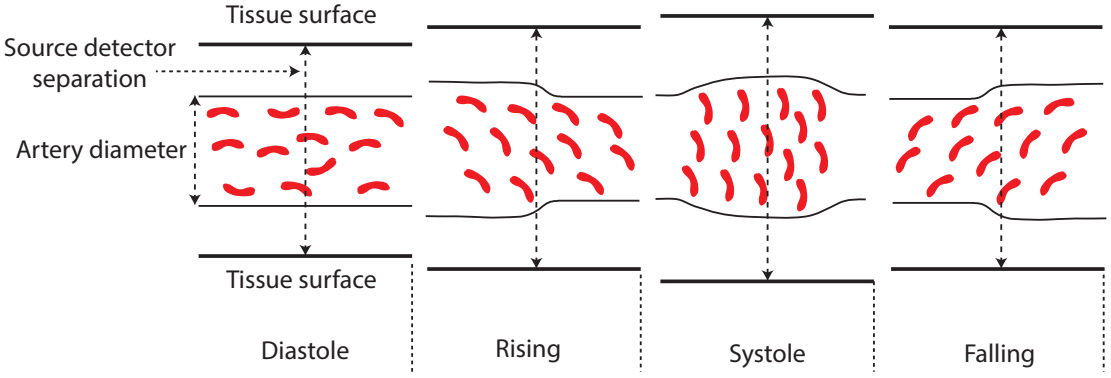

FIGURE 4.2: Erythrocytes changing their axis during cardiac cycle (inspired from [52])

presenting a greater absorption path length [94]. As shown in Figure 4.2, during diastole, the cells are less densely grouped and are rotated such that their long axes are parallel to the direction of flow. At systole, the cells are packed tightly together and are orientated such that their long axes are perpendicular to the direction of flow, hence increasing the optical path length and thereby absorption [95]. The AC PPG signal can be extracted using a band-pass filter (typical bandwidth 0.5 Hz to 20 Hz) [87]. The AC PPG pulse shapes are indicative of vessel compliance and cardiac performance. The DC component includes the absorption due to still arterial blood, venous blood, and other tissues and constitutes up to 99% of the total light absorption. The DC component varies slowly due to respiration, vasomotor activity and vasoconstrictor waves, and thermoregulation. This DC component may be extracted using a low pass filter (typical bandwidth DC 0.5 Hz) [70].

4.1.3 Photoplethysmography in pulse oximetry

Pulse oximetry is the most recognised application of photoplethysmography. Pulse oximeters measure SpO_2 using PPG signals obtained at two different wavelengths in living tissue [96]. The two wavelengths typically used are 660 nm (in the red part of the visible spectrum) and 940 nm (in the infrared part of the spectrum) but other wavelengths could be used. The light absorbance of oxygenated haemoglobin and deoxygenated haemoglobin at these two wavelengths is different. Therefore, the amplitudes of the red and infrared AC PPG signals are different and are sensitive to changes in arterial oxygen saturation. From the ratios of these amplitudes and the corresponding DC photoplethysmographic components, SpO_2 is estimated. Hence, the technique of pulse oximetry relies on the presence of adequate peripheral pulsations, which are detected as photoplethysmographic signals [93]. Therefore, for pulse oximeters to accurately estimate SpO_2, PPG signals of high quality and high signal to noise ratio (SNR) are required.

4.2 Pulse oximetry

Pulse oximeters can measure arterial oxygen saturation from any vascular tissue in the body. It is based on two physical principles:

- The light absorbance of oxygenated haemoglobin is different from that of reduced haemoglobin, at the two wavelengths used in pulse oximetry.
- The pulsatile nature of arterial blood results in a waveform in the transmitted signal that allows the absorbance effects of arterial blood to be identified from those of non-pulsatile venous blood and other body tissue.

FIGURE 4.3: The Nihon Kohden OLV-5100, the first commercially available pulse oximeter, with ear-probe [68].

4.2.1 Evolution of Pulse oximetry

The oxygen-carrying blood pigment - 'haemoglobin' (Hb), was first discovered by a German chemist known as Friedrich Ludwig Hünefeld in the early nineteenth century. The evolution of pulse oximetry has begun when this pigment was first reported to change colour when mixed with oxygen by Hoppe-Seyler and George Gabriel Stokes. This discovery led to the development of the first tissue oximeter. Ludwig Nicolai and Kurt Kramer made the first steps towards modern oxygen saturation measurement in 1931 [97]. Using an incandescent light and a barrier photocell they made the first report of precise oxygen saturation measurement of blood both in cuvettes and flowing blood in 1934. Using Kramers work, a German physician known as Karl Matthes produced the first oximeter to measure continuous oxygen saturation in humans, by transillumination of the ear [86].

The next significant development came during the Second World War in 1939 when Glenn Millikan a British scientist designed the first lightweight and practical aviation ear oximeter for aircraft pilots and incidentally coined the term 'Oximeter' [98]. Building on the work done by Millikan, a surgeon and inventor Robert Shaw developed an eight wavelength ear oximeter in 1964. Eight wavelengths of light were passed through tissue and the oxygen content was calculated from the differential absorption of the various wavelengths during the experiment conducted by him. It was later observed that there was a pulsatile change in light absorption in tissues during each cardiac cycle, attributable to the arrival of arterial blood in the capillaries. This marked the evolution from tissue oximetry to pulse oximetry. However due to its expense and the large size of the ear piece, it was seldom used for clinical monitoring [99].

Aoyagi and co-workers achieved the next breakthrough in 1974 with the development of the non-invasive pulse oximeter (Figure 4.3). Aoyagi found that arterial oxygen saturation, rather than tissue oxygen saturation, could now be obtained by measuring light absorption at the peak and trough of a pulse and cancelling that which was common to both, leaving the pulsatile arterial component [100]. This new device developed by Nihon Kohden

used filtered light sources similar to Millikans ear oximeter. The device was evaluated clinically in the mid-1970s and marketed with little success. A competing pulse oximeter was introduced by the Minolta Co, marketed in the United States as the Oximet MET-1471 in 1977 with a fingertip probe which was connected to the instrument using optical fibres. This device was found to overestimate oxygen saturation during clinical testing [99].

The first clinically approved pulse oximeter was developed by Biox Corporation of Boulder, Colorado [100]. Their device used light emitting diodes (LEDs) as light sources and photodiodes as photodetector instead of optical fibres. The saturation estimates were also improved by using a digital microprocessor to store a complex calibration algorithm based on human volunteer data. This device immediately became popular with neonatologists and anaesthetists achieving widespread use in these fields by the 1980s. Non-invasive pulse oximetry is now an indispensable and mandatory tool for the monitoring of patients in these clinical areas, as practitioners may be considered negligent if they fail to use it, by the American Society of Anesthesiologists [101].

4.2.2 Choice of wavelengths in pulse oximetry

Pulse oximeters determine arterial oxygen saturation from the ratio of the absorption (R_{OS}) of the light energy at two wavelengths. The two most commonly used wavelengths are 660 nm and 940 nm [103]. The choice of wavelengths is based on three main criteria. First, at chosen wavelengths (λ_1 and λ_2) the difference in absorption between Hb and HbO_2 should be the greatest. Second, one of the chosen wavelengths should mostly be

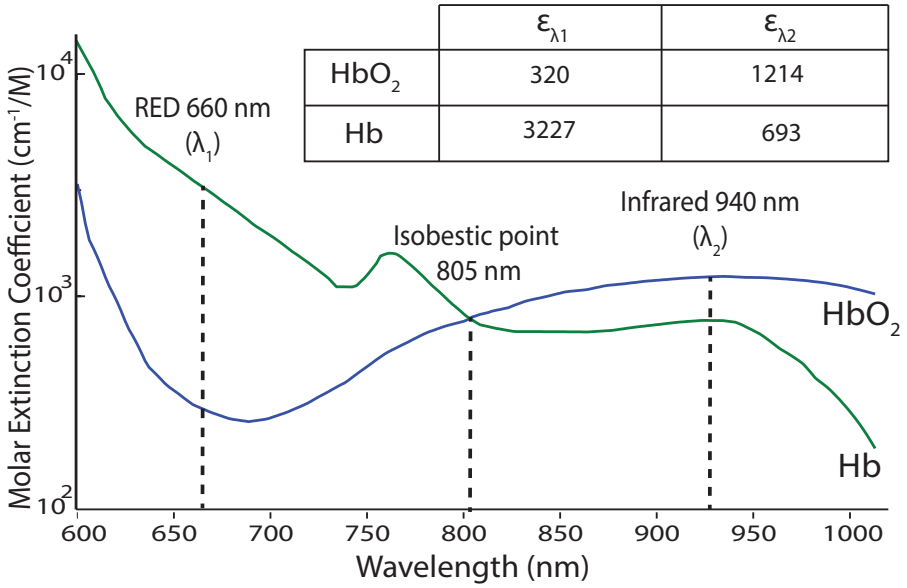

FIGURE 4.4: Absorption spectra of Hb and HbO_2 at the wavelengths of interest in pulse oximetry (plotted using data acquired from [102])

absorbed by HbO_2 and the other by Hb. Finally, the absorption spectra around the chosen wavelengths should be relatively flat [104].

Figure 4.4 depicts the absorption of Hb and HbO_2 across a portion of the visible and near infrared electromagnetic spectrum. It can be seen in Figure 4.4 that Hb and HbO_2 have different absorption across the entire portion of the spectrum except at 805 nm, termed the isobestic point. Below the isobestic point, absorption is principally due to Hb, while above the isobestic point most absorption is due to HbO_2 [105]. The absorption between Hb and HbO_2 is greatest at 660 nm below the isobestic point, thus, absorption measured at this wavelength will be largely proportional to the concentration of Hb. At any wavelengths below 600nm, skin pigment melanin absorbs light sharply. Above the isobestic point, the difference is greatest above 970 nm, however from 950nm and upwards the water in the tissue absorbs light, making use of these wavelengths unviable. At 940 nm, absorption by water is sufficiently low, and both the Hb and HbO_2 absorption curves are relatively flat [106]. Another compelling reason for the choice of 660nm and 940nm is the common availability of LEDs at these wavelengths.

4.2.3 Manipulating Beer-Lamberts law for use in pulse oximetry

As mentioned in Section 3.2, the absorption of light at any given wavelength in tissue can be determined by using Beer-Lambert Law. According to Beers Law, the absorbance of a substance in a medium is linearly proportional to the concentration of the substance, extinction coefficient and the optical path length. For the absorbance to be linearly related to the concentration, optical distance and absorptivity, the medium must be homogeneous. However, when determining the absorption of blood using pulse oximetry, this is not a good assumption, as blood is not homogeneous [107]. Recalling Equation 3.6 and 3.7, the relation between absorption, transmittance and the original intensity (I_0) is given by

$$A = -ln(T) = \frac{I}{I_0} \tag{4.1}$$

Where absorbance of the tissue can only be determined if the intensity of the detected light and the original intensities of transmitted light are known. But the intensity of the original incident light is very difficult to determine accurately as not all the LEDs in a single batch from a factory emit the same intensity. Moreover, LEDs are not monochromatic as their intensity is spread over a spectrum of wavelengths. Hence to make 'I_0' become irrelevant in the estimation of arterial oxygen saturation, pulse oximeters take advantage of the pulsating properties of arteries. The arteries contain more blood during systole (contraction of the heart) than diastole (relaxation of the heart). Their diameter, therefore, increases due to increased pressure (the walls of the arteries are fairly elastic). This effect occurs in the arteries and arterioles (small arteries that feed the capillaries) but not in

the veins (or the capillaries themselves). This can be seen as a change in the optical path distance (d) in the Beer-Lamberts Law [108]. Beer's Law can be modified to provide the intensity of absorption during systole (I_P) and diastole (I_B) (Figure 4.1). Baseline intensity (I_B) can be written as,

$$I_B = I_0 \; e^{-\varepsilon_B(\lambda).c_B.d} = I_0 \; e^{-\alpha_B(\lambda).d} \tag{4.2}$$

Where α_B is the absorptivity of baseline absorption and is equivalent to $\varepsilon_B(\lambda).c_B$ and d is the optical path length. The light emerging from the pulsatile component can be written as

$$I_P = I_B \; e^{-\alpha_P(\lambda)\Delta d} = I_0 \; e^{-\alpha_B(\lambda)d \; -\alpha_P(\lambda)\Delta d} \tag{4.3}$$

Where α_P is the absorptivity of the pulsatile arterial blood. A change in transmittance (ΔT) can now be defined as the ratio of the pulse intensity over the baseline intensity [103]

$$\Delta T = \frac{I_P}{I_B} = \frac{I_0 \; e^{-\alpha_B(\lambda)d \; -\alpha_P(\lambda)\Delta d}}{I_0 \; e^{-\alpha_B(\lambda)d}} = \Delta T = e^{-\alpha_P(\lambda)\Delta d} \tag{4.4}$$

The I_0 terms cancel out leaving the arterial transmittance as a function of the pulsatile components absorptivity and path length only [109]. The unscattered absorbance of light at each wavelength can be calculated by taking the natural log of Equation 4.4.

$$\Delta A = -\ln\left(\frac{I_P}{I_B}\right) = -\ln(e^{-\alpha_P(\lambda)\Delta d}) = \alpha_P(\lambda)\Delta d \tag{4.5}$$

Now by comparing the ratio of the unscattered absorbance measured at two wavelengths used in pulse oximetry (i.e., red (R) and infrared(IR)), a ratio R_{OS} can be calculated such that,

$$R_{OS} = \frac{\Delta A(\lambda_R)}{\Delta A(\lambda_{IR})} = \frac{\alpha_P(\lambda_R)\Delta d_R}{\alpha_P(\lambda_{IR})\Delta d_{IR}} \tag{4.6}$$

Note that the change in optical path length (Δd) is, however, impossible to measure [109]. By assuming that the geometrical distance between the source and the detector is the same at each wavelength, and number of scattering events per millimetre of tissue is similar, variable distance Δd (the optical path length over which arterial absorption takes place) can be eliminated as follows

$$R_{OS} = \frac{\Delta A(\lambda_R)}{\Delta A(\lambda_{IR})} = \frac{\alpha_P(\lambda_R)}{\alpha_P(\lambda_{IR})} \tag{4.7}$$

This ratio is used in calculating the oxygen saturation level of the patients' blood. Before describing the conventional way of measuring SpO_2, it is important to understand what is physically being measured here in Equation 4.7

4.2.4 Ratio of ratios

In pulse oximetry, two diodes emit red and infrared signals that are transmitted through a spot in the body and detected in their attenuated form by a photodetector. Figure 4.5 shows the red and infrared PPG signal obtained by monitoring the intensity of light emerging from the tissue by the photodetector. Note that the PPG signals appear inverted compared to the absorption-derived waveform depicted in Figure 4.1. The change in absorption at red (R) and infrared (IR) wavelengths is given by

$$\Delta A(\lambda_R) = \ln\left(\frac{I_d(\lambda_R)}{I_s(\lambda_R)}\right) \tag{4.8}$$
$$\Delta A(\lambda_{IR}) = \ln\left(\frac{I_d(\lambda_{IR})}{I_s(\lambda_{IR})}\right)$$

Where, $I_d(\lambda_R)$ and $I_d(\lambda_{IR})$ represent the baseline transmittance at the R and IR wavelengths, and $I_s(\lambda_R)$ and $I_s(\lambda_{IR})$ represent the pulsatile transmittance at respective wavelengths. The difference between $I_d(\lambda_R)$ and $I_s(\lambda_R)$, represents the reduction in transmittance due to the pulsation of the arterial blood. This variation in transmitted signal is referred to as the AC component of the PPG signal, where $\mathrm{AC}_R = I_d(\lambda_R)$ - $I_s(\lambda_R)$. Since AC is very small, the Equation 4.8 can be rewritten as [110]

$$\Delta A(\lambda_R) = \ln\left(\frac{I_s(\lambda_R) + AC_R}{I_s(\lambda_R)}\right) = \ln\left(1 + \frac{AC_R}{I_s(\lambda_R)}\right) \simeq \left(\frac{AC_R}{I_s(\lambda_R)}\right) \tag{4.9}$$
$$\Delta A(\lambda_{IR}) = \ln\left(\frac{I_s(\lambda_{IR}) + AC_{IR}}{I_s(\lambda_{IR})}\right) = \ln\left(1 + \frac{AC_{IR}}{I_s(\lambda_{IR})}\right) \simeq \left(\frac{AC_{IR}}{I_s(\lambda_{IR})}\right)$$

Another consequence of AC being small is that the slowly varying (DC) component of the signal may be considered roughly equal to $I_s(\lambda_R)$ or $I_d(\lambda_R)$, so

$$\Delta A(\lambda_R) = \left(\frac{AC_R}{DC_R}\right) \quad and \quad \Delta A(\lambda_{IR}) = \left(\frac{AC_{IR}}{DC_{IR}}\right) \tag{4.10}$$

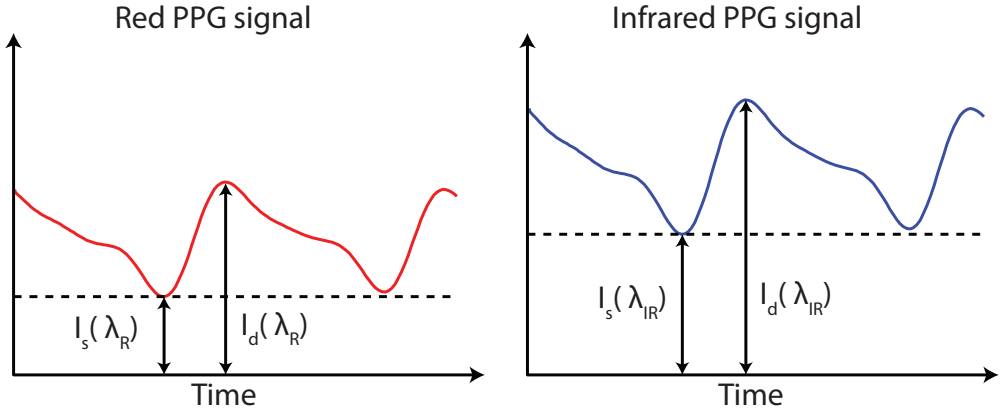

FIGURE 4.5: Received light intensity from the red (R) and infrared (IR) LEDs over time

Substituting Equation 4.10 into Equation 4.7, the ratio of ratios can be calculated, where

$$R_{OS} = \frac{\Delta A(\lambda_R)}{\Delta A(\lambda_{IR})} = \frac{(^{AC}/_{DC})_R}{(^{AC}/_{DC})_{IR}} \tag{4.11}$$

4.2.5 Deriving arterial oxygen saturation using the ratio of ratios

As mentioned in Section 3.2.2, arterial oxygen saturation (SaO_2) is defined as the percentage concentration of the oxygenated haemoglobin divided by the sum of concentrations of oxygenated and reduced haemoglobin [111]

$$SaO_2 = \frac{C_{HbO_2}}{C_{HbO_2} + C_{Hb}} \times 100\% \tag{4.12}$$

As the optical path is assumed to be the same for each medium in pulse oximetry, the concentrations for HbO_2 and Hb can be related to the functional oxygen saturation

$$\begin{aligned} C_{HbO_2} &= SaO_2(C_{HbO_2} + C_{Hb}) \\ C_{Hb} &= (1 - SaO_2)(C_{HbO_2} + C_{Hb}) \end{aligned} \tag{4.13}$$

Going back to Beer-Lamberts Law for multiple media in Equation 3.7 and combining it with Equation 4.13, the total absorbance at red and infrared wavelengths can be written as

$$\begin{aligned} A_t(\lambda_R) &= [\varepsilon_{Hb}(\lambda_R) + SaO_2(\varepsilon_{HbO_2}(\lambda_R) - \varepsilon_{Hb}(\lambda_R))] \times (C_{HbO_2} + C_{Hb})d \\ A_t(\lambda_{IR}) &= [\varepsilon_{Hb}(\lambda_{IR}) + SaO_2(\varepsilon_{HbO_2}(\lambda_{IR}) - \varepsilon_{Hb}(\lambda_{IR}))] \times (C_{HbO_2} + C_{Hb})d \end{aligned} \tag{4.14}$$

Just as in computing the Ratio of Ratios in Equation 4.7, the ratio of absorbance at the red wavelength over the absorbance at the infrared wavelength is given by

$$R_{OS} = \frac{A_t(\lambda_R)}{A_t(\lambda_{IR})} = \frac{[\varepsilon_{Hb}(\lambda_R) + SaO_2(\varepsilon_{HbO_2}(\lambda_R) - \varepsilon_{Hb}(\lambda_R))] \times (C_{HbO_2} + C_{Hb})d}{[\varepsilon_{Hb}(\lambda_{IR}) + SaO_2(\varepsilon_{HbO_2}(\lambda_{IR}) - \varepsilon_{Hb}(\lambda_{IR}))] \times (C_{HbO_2} + C_{Hb})d} \tag{4.15}$$

$$R_{OS} = \frac{\varepsilon_{Hb}(\lambda_R) + SaO_2(\varepsilon_{HbO_2}(\lambda_R) - \varepsilon_{Hb}(\lambda_R))}{\varepsilon_{Hb}(\lambda_{IR}) + SaO_2(\varepsilon_{HbO_2}(\lambda_{IR}) - \varepsilon_{Hb}(\lambda_{IR}))}$$

The above equation can now be simplified to the form where functional oxygen saturation is a function of the ratio of ratios. Note that SaO_2 is referred as SpO_2; indicating arterial blood oxygen saturation measured by pulse oximetry

$$SpO_2 = \frac{R_{OS}.\ \varepsilon_{Hb}(\lambda_{IR}) - \varepsilon_{Hb}(\lambda_R)}{R_{OS}[\varepsilon_{Hb}(\lambda_{IR}) - \varepsilon_{HbO_2}(\lambda_{IR})] + \varepsilon_{HbO_2}(\lambda_R) - \varepsilon_{Hb}(\lambda_R)} \times 100\% \tag{4.16}$$

Note that Equation 4.16 is composed of all measurable and known values. The value of R_{OS} is calculated from the four parameters derived in Equation 4.11 and the values of the molar extinction coefficients of oxygenated and de-oxygenated haemoglobin are known and given as a function of wavelength in Figure 4.4 [112]. By substituting these values from Figure 4.4 into Equation 4.16, produces the following equation

$$SpO_2 = \frac{R_{OS} \times 693 - 3227}{R_{OS} \times (693 - 1214) + 320 - 3227} = \frac{693.R_{OS} - 3227}{-521.R_{OS} - 2907} \tag{4.17}$$

and approximating Equation 4.17 with a linear function produces the following equation

$$SpO_2 = 116 - 41(R_{OS}) \tag{4.18}$$

However, a more accurate empirically derived linear equation that is commonly used by those who had any experience with pulse oximetry technology is

$$SpO_2 = 110 - 25(R_{OS}) \tag{4.19}$$

4.2.6 Calibration of pulse oximeters

Since, SpO_2 is calculated using a ration (R_{OS}) rather than absolute value, there is no need for any calibration. However, most modern pulse oximetry manufactures build experimental calibration curves instead of relying on the theoretically obtained equations such as

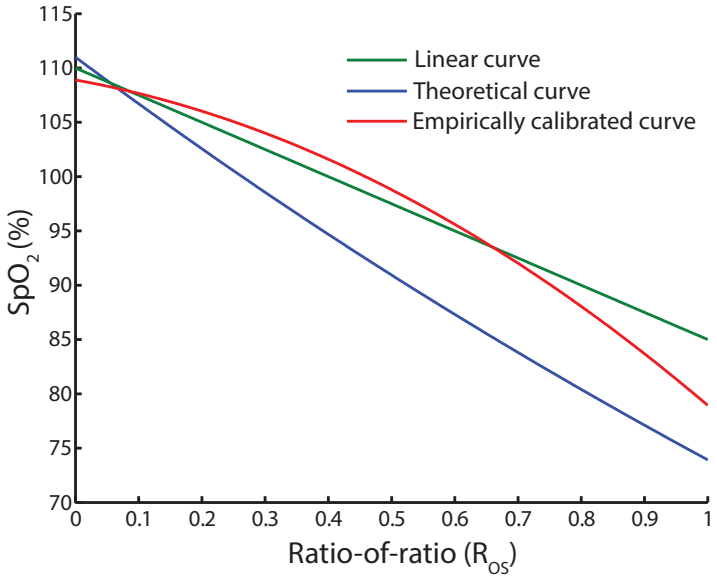

FIGURE 4.6: Calibration curves for pulse oximeters: Functions plotted in green and blue are theoretically obtained curves using Equation 4.17 and 4.18, red line is the experimentally obtained calibration curve used in commercial Pulse Oximeter

Equation 4.17 and 4.18. One of such calibration curves is plotted together with functions from Equation 4.17 and 4.18 in Figure 4.6.

Manufacturers calibrate pulse oximeters empirically by correlating the measured ratio of AC/DC PPG signals to SaO_2 values measured from *in-vitro* oximeters such as CO-oximeters [101]. The calibration procedure involves desaturating the subjects by asking them to breathe hypoxic gas mixtures and collecting optical measurements of blood samples at different steady-state oxygenation levels. At each oxygenation level, the measured SaO_2 value is correlated to the R_{OS} value measured by the pulse oximeter. In most studies the volunteers are desaturated to a SaO_2 of up to 80%. As a result, the accuracy of pulse oximetry deteriorates when SaO_2 falls to 80% or less. The calibration curve programmed into the software also varies from manufacturer to manufacturer and can be different in various pulse oximeters of the same manufacturer [1]. For these reasons, the same pulse oximeter and probe should be used for all saturation determination in a given patient. One of the limitations of this calibration method is the limited range of oxygen saturation that can be acquired. Ethical issues prevent intentional desaturation of healthy subjects below a certain point due to the risk of hypoxic brain damage.

4.3 Pulse Oximetry Probes

The pulse oximeter probes are widely used in clinical settings for the monitoring of arterial blood oxygen saturation. A conventional pulse oximetry sensor consists of a pair of light emitters and a highly sensitive photodetector, mounted inside a reusable spring loaded clip. The most commonly used light sources are the Light Emitting Diodes (LED). LEDs are ideal for pulse oximeters as they are cheap, compact and possess excellent drive characteristics, along with large light output over a narrow bandwidth [113]. The photodetectors usually used in pulse oximetry probes are silicon photodiodes, but other devices such as photocells and phototransistors are also used. Silicon photodiodes are a good choice for light detection, as they possess good linearity to detected light and produce minimum noise. The two main configurations used in the design of pulse oximetry probes are discussed below:

4.3.1 Transmittance probes

As the name suggests, in transmittance probes, light emitters transmit light through one side of the vascular tissue to the photodiode on the other side, as shown in Figure 4.7. Transmittance probes were the first pulse oximetry probes to be developed and remain the most commonly used probes in clinical environments [57]. The probe consists of

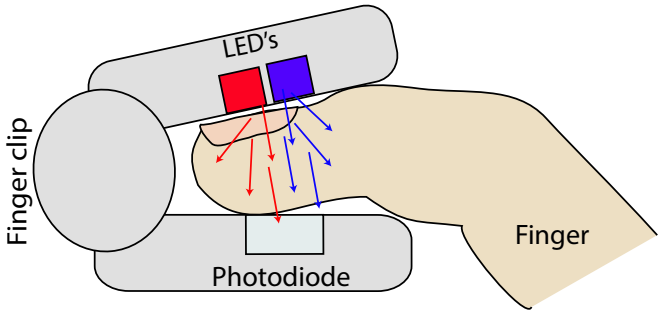

FIGURE 4.7: Transmission pulse oximetry configuration - illustrating the relative positions of the emitters and photodetector (drawing inspired from [116])

two emitters, with wavelengths at 660nm in the red region and at 940 nm in the near infrared region. LEDs are mounted on the pulse oximeter probe so their output is directed perpendicularly through the finger to the photodetector, which is located opposite the LEDs. The intensity of light emerging from the tissue is attenuated by the blood present in the tissue. This varies with the arterial pulse and is used to measure SpO_2 and heart rate [70]. The probe is designed to fit comfortably on the finger and is spring loaded, applying constant light pressure on the tissues. The whole assembly is shielded to prevent ambient light from entering the detector. Normally transmission probes are placed on the patients finger, earlobe or toe and are available in different reusable packaging [114]. A disadvantage of transmission-mode pulse oximetry is the limited measurement sites. For this sensor to be effective, it must be placed somewhere on the body where transmitted light can be readily detected. Placement of the sensor on the ear or fingertip may result in inaccuracies when peripheral circulation is impaired [115].

4.3.2 Reflectance pulse oximetry probe

Incident light from the emitters is known to be absorbed, transmitted and reflected when travelling through biological tissue. Reflectance probes make use of the reflection property

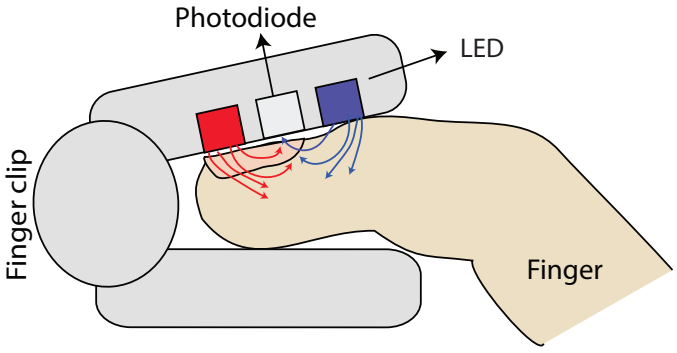

FIGURE 4.8: Reflectance pulse oximetry configuration - illustrating the relative positions of the emitters and photodetector

of light to acquire arterial oxygen saturation. Reflectance probes consist of two LEDs, with wavelengths at 660nm in the red region and at 940 nm in the near infrared region and a photodiode aligned next to the emitters. The light from the emitters transilluminates the tissue and the backscattered light is detected as a pulsating photoplethysmograph by the photodiode next to the emitters (Figure 4.8). These signals are then analysed by the pulse oximeters to estimate arterial oxygen saturation [93].

As the emitters and photodetectors are placed adjacent to each other, reflection pulse oximetry probes can be used to measure arterial oxygen saturation at virtually any place on the skin. This solves the sensor placement problems associated with transmission-mode pulse oximetry. It has been found that the separation between the emitters and photodetector affects the quality of the photoplethysmographic signals received in reflection pulse oximetry. A separation of 4 to 5 mm between the emitter and the photodetector is usually recommended [117]. The most common surfaces for monitoring oxygen saturation with a reflectance pulse oximetry probe are the forehead and temple [115].

4.4 Instrumentation used in pulse oximetry

This section describes briefly the main electronic blocks comprising the pulse oximeter system (Figure 4.9)

Emitter driver - In the pulse oximeter, the red and infrared emitters are driven by a current driver circuit consisting of a current source and a multiplexer. Emitter drive currents may vary between 60 mA to 120 mA. As there is only one photodiode to take samples of light at both wavelengths, the signals need to be multiplexed. Therefore, only one LED can be on at any instant [26]. The multiplexer, driven by timing signals

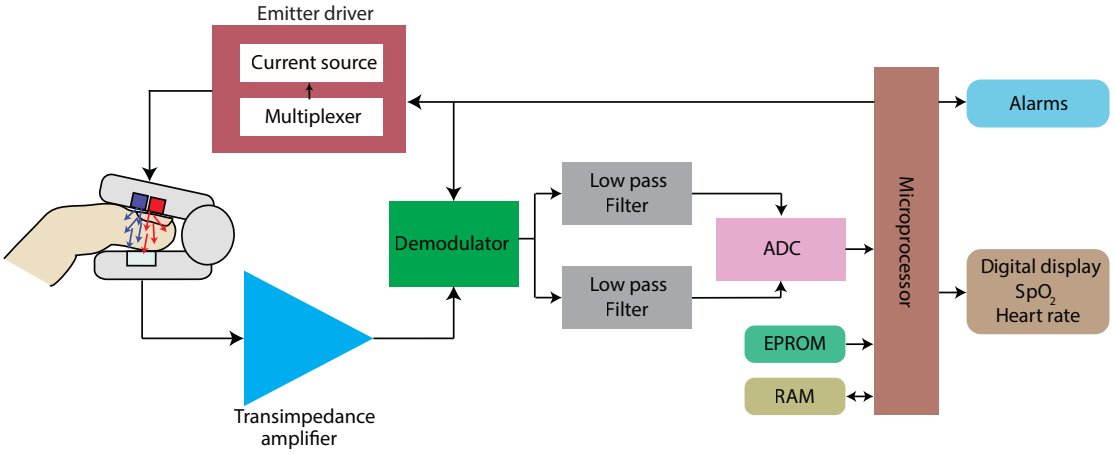

FIGURE 4.9: Block diagram of a commercial pulse oximetry showing the major electronics components (Drawing inspired from [1])

generated by the microprocessor, turns the red and infrared emitters on and off at a rate of approximately 500 Hz in sequence.

Transimpedance amplifier - The transimpedance amplifier converts and amplifies the photocurrents generated by the photodetector into a mixed voltage signal. The strength of the signal from the amplifier depends on the intensity of light detected by the photodiode and the gain resistor of the transimpedance amplifier.

Demodulator and filtering - The inputs to this circuit are the mixed PPG signal output of the transimpedance amplifier and the timing signal from the microprocessor. The microprocessor along with the information stored in the EPROM calculates the time period each signal component is present in the photodetector output [118]. Switching at the right time results in the two PPG components (red and infrared) getting separated.

Analogue-to-Digital Converter (ADC) - This is the point in the system where digital electronics take over. The PPG signals are converted by an analogue-to-digital converter to a form suitable for manipulation by the microprocessor. In most of the commercial pulse oximeters, the analogue-to-digital conversion is accomplished by using a sample and hold circuit, which holds a voltage until it is sampled by the ADC controlled by a routine written in the memory of the microprocessor [105].

Microprocessor - The most important component of the pulse oximeter system is the microprocessor. The digitised information at the output of the ADC is processed by the microprocessor to compute the blood oxygen saturation from the ratio (R_{OS}) derived from the signal at the red wavelength compared with the signal at the infrared wavelength.

Displays and Status Messages - Apart from displays of blood oxygen saturation, heart rate, and photoplethysmograph, most pulse oximeters also display messages such as: no probe connected, battery low, noisy signal, probe off the patient, searching for a pulse, insufficient signal [119].

Alarms - All pulse oximeters must have alarms for low oxygen saturation and for low and high heart rate. These alarms have to be both in audio and visual form. Comparators, power amplifiers, drivers and speakers constitute the audio alarm section. LCD bar graphs and blinkers are used for the visual section [108].

Power supply - The internal power supply requirements of the pulse oximeter may be considered in three sections: the light emitting diodes; the electronics; and the display. The power supply present in most pulse oximetry boards is switched mode power supply with an optically isolated power transformer, isolating the mains input from the rest of the pulse oximetry system, therefore preventing any form of electric shock to the patient.

4.5 Applications of Pulse Oximetry

Pulse oximetry has become one of the most commonly used tools in the clinical environment for assessing patients blood oxygenation status. The pulse oximeter provides an indicator of arterial oxygen saturation, a quantity that is extremely simple to interpret, thus providing a rapidly responding indicator of hypoxaemic events [110]. They are non-invasive, easy to use, and readily available. Pulse oximeters are now a monitoring standard equipment in anaesthetic rooms, operating theatres, intensive care units, ambulances, etc. Pulse oximeters are used to provide useful clinical information in many different settings, including physiological monitoring, vascular assessment and autonomic function [87].

In physiological monitoring, pulse oximeters are now used to measure parameters beyond SpO_2 and heart rate. Recent advancements include measurement of blood pressure [120], venous oxygen saturation [121], and respiration [122]. However, these new parameters are not currently available in clinical monitors and are confined to research systems. In vascular assessment the technology is used to assess microcirculation [123], arterial compliance and ageing [124], and endothelial function [125]. Pulse oximeters are also used in the assessment of vasomotor function [126]. Assessment of vasculature and vasomotor function by pulse oximetry is however, still in an early research stage.

4.6 Summary

Pulse oximetry is an optical technique used in the monitoring of tissue perfusion and is essentially a combination of oximetry and photoplethysmography. By shining light at two wavelengths (red and infrared) onto a tissue and receiving either the transmitted light or reflected light, oxygen saturation levels can be estimated. Pulse oximetry takes Beers law as its basis, and although this does not effectively account for scattering effects when used in conjunction with empirical calibration, it provides a reliable estimation of saturation. The pulse oximeter sensor is the heart of pulse oximeter, as the accurate functioning of the device depends on the probe. Pulse oximeter sensors are available in reflectance and transmittance configurations. Most commercial devices use transmittance finger sensors.

— The reputation of the technique of pulse oximetry can be maintained only if its limitations are always borne in mind. Currently, this is not the situation, and the indicated value of SpO_2 is relied on totally by most users.

John TB Moyle, Pulse oximetry, 1994

5

Limitations and recent advancements in Pulse Oximetry technology

In recent years, continuous assessment of arterial oxygen saturation during anaesthesia and surgery has become increasingly dependent on pulse oximetry, as the technique has proved to be accurate and capable of detecting hypoxic changes in sedated patients. In fact, pulse oximetry has been made a standard of practice for the administration of general anaesthetic in the USA [1]. Many publications have reported the durability of the technique for measuring arterial oxygen saturation. However, the technique has also been reported to fail in some circumstances [59].

The limitations by which pulse oximeters fail to estimate accurate SpO_2 can be classified into technical and physiological. Some of these limitations are harmless where the device is unable to measure SpO_2 but makes the observer aware that it is not functioning properly, but others can be dangerous and can cause false sensing of patients wellbeing. One of the well-known scenarios in which pulse oximeters fail to produce an accurate estimate of SpO_2 is under conditions of compromised peripheral perfusion, where the detected peripheral pulse is very weak. This chapter briefly discusses the technical and physiological limitations of pulse oximetry before describing the recent advancements made in the technique to avoid such limitations. The last section of the chapter presents a possible solution for monitoring arterial oxygen saturation in conditions of poor peripheral perfusion.

5.1 Technical limitations

Numerous factors have been shown to affect the absorbance characteristics or signal-to-noise ratio of pulse oximetry negatively. These limitations include motion artefacts, calibration assumptions, electromagnetic interference, nail polish, time-lag due to over averaging, skin pigmentation, centre wavelength variability of LEDs and probe positioning. Some of these limitations are more likely to have an effect on the pulse oximeter than others. Nonetheless all these confinements introduce a certain degree of error in the estimated SpO_2 value measured by the pulse oximeter. This section describes some of the main technical limitations.

5.1.1 Motion Artifacts

One of the most commonly occurring and clinically troublesome limitation of pulse oximetry is motion artefact. Mechanical disturbances between the probe and the anatomy of the patient should be avoided as much as possible while using pulse oximeters as it may lead to inaccurate results. The change in absorption of energy during the cardiac cycle accounts for only 1-2 % of the total absorption, any motion that alters the remaining fraction of absorption (especially when due to venous blood) will drive the absorbance ratio (R_{OS}) near 1 and SpO_2 to a value close to 85 % [127, 128]. Most modern pulse oximeters are equipped with microprocessors which attempt to limit these issues by longer averaging, holding data, or alarm delays. However, rhythmic motions or vibrations with a frequency similar to the heart rate ($0.5 - 3.5\ Hz$) can be accounted as the normal signal, and this would lead to inaccurate SpO_2 readings [129, 130].

5.1.2 Calibration assumptions

As mentioned earlier in Section 4.2.6, arterial oxygen saturation derived from the absorbance ratio was initially based on the Beer-Lambert law, but the results obtained led to a gross overestimation of oxygen saturation as the light reflecting and scattering properties are ignored in Beer's Law [129]. The accuracy of the results was improved using the empirically derived calibration curves (Section 4.2.6). These calibration curves are obtained by correlating the measured absorbance ratio (R_{OS}) with arterial SaO_2 values obtained from a large group of healthy volunteers over a range of desaturation values [127]. However, the results produced by CO-Oximeters typically have an inaccuracy of ± 0.5 % [1]. Hence, the value of SpO_2 obtained from pulse oximeters can only be as accurate as their empirical calibration curves. It is also unethical to desaturate volunteers below SaO_2 levels of 80 %, therefore lower SpO_2 values are derived by extrapolation and, hence,

are less accurate. Moreover, because the subjects recruited for calibration purposes are healthy young adults, the applicability of calibration data to patients at the age extremes has been questioned [131, 132].

5.1.3 Electromagnetic interference

The likelihood of electromagnetic interference (EMI) corrupting the pulse oximeter's performance is usually low. However, they can be sensitive to EMI at times due to the microelectronic circuitry and many microprocessors used. Pulse oximeters are prone to EMI from both radio and visible regions of the electromagnetic spectrum. One of the most powerful sources of EMI that is likely to be encountered by a pulse oximeter in a clinical setting is from the radio-frequency produced by a surgical diathermy unit. These electrosurgical units used in operating theatres produce radio-frequency energy up to 400 W at mixed frequencies, which can interfere with pulse oximeters to produce erroneous SpO_2 readings [1].

Intense visible or infrared light also might interfere with pulse oximeters [133]. The excessive increase of light energy reaching the photodiode from ambient light or other light sources can saturate the photodiode and drive the R_{OS} value towards unity which corresponds to a SpO_2 of 85%. This phenomenon, known as the flooding effect is far worse if the light source is pulsatile. The new-generation sensors avoid this by insulating the sensors from any ambient light entering the photodiode. Health care professionals, particularly those who handle neonates exposed to phototherapy, must be aware of this potential limitation [127].

5.1.4 Time lag in detecting hypoxic events

While most conventional pulse oximeters present fast response times, there may be a clinically significant delay between a sudden change in alveolar oxygen tension and the related change in the oxygen saturation readings. It is possible for arterial oxygenation to reach dangerous levels before the pulse oximeter alarm is activated. This time, lag is primarily associated with the sensor location [133, 134]. Desaturation could be detected earlier if the sensor was to be placed on a more central site, other than finger or toes. The other source of time delay is the complexity of the algorithms used in the modern pulse oximeters (i.e. the time over which the pulse signals are averaged) and this might exceed 15 to 20 seconds [127]. Verhoeff and Sykes found that a delay of 1 min between a change in alveolar oxygen tension and an indication on the pulse oximeter could potentially result in damaging hypoxia [135, 136].

5.1.5 Other technical limitations

One of the other limitations in the design of pulse oximeters is the type of light source used. Although LEDs are reliable sources of narrow wavelength light, the peak wavelength of different emitters of the same type is known to vary [26]. There might be a variation of up to 15 nm in the centre wavelength between any two LEDs of the same type. From the absorption spectra of Hb and HbO_2 in Figure 4.4, it is evident that any shift in wavelength of light source leaves the oximeter working with a different set of extinction coefficients, therefore leading to an error in the estimation of SpO_2. This is why it is critical to choose wavelengths in the flatter region of the absorption spectrum. Modern sensors are equipped with a coding resistor with a specific value in the probe connector. This resistor helps the pulse oximeter to choose an appropriate calibration curve to be used for calculating SpO_2 [1].

Skin pigmentation has shown variable effects on pulse oximetry. Although according to the theory, the constant level of absorption presented by skin pigmentation is subtracted in the calculation of SpO_2, dark skin pigmentation has been implicated for erroneous SpO_2 readings, especially at SpO_2 values of < 80 % [129]. The mechanism of such artefact, if present, is unclear, and could arise from optical interference, low signal-to-noise effects, or as a reflection of the relative lack of darkly pigmented subjects in calibration trials [137, 138].

Probe placement also plays an important role in the estimation of accurate SpO_2 by a pulse oximeter. Inappropriate probe placement leads to errors readings, especially on the small fingers of neonates and infants [131]. In this case, the emitted light can be projected tangentially to the detector, sometimes without crossing an arterial bed, leading to optical shunting. This pitfall can be avoided by positioning the emitter and the detector exactly opposite to each other and by using probes of appropriate size for neonates and infants [139].

5.2 Physiological Limitations

Along with the technical limitations, pulse oximeters additionally suffers from few physiological limitations (i.e., errors resulting from physiological conditions). These constraints include intravenous dyes, anaemia, abnormal haemoglobin molecules, venous pulsations, morbidity and reduced perfusion.

5.2.1 Intravenous dyes

Dyes such as methylene blue, indocyanine green, patent blue, nitrobenzene and indigo carmine are commonly injected intravenously or intra-arterially into the uterine cavity or lymphatics during surgical procedures. Usage of pulse oximeters during or shortly after the induction of these dyes has shown to have resulted in falsely low SpO_2 values without actual desaturation [141–144]. These errors occur as the pulse oximeter cannot distinguish between the absorption of light by intravenous dye and the absorption by haemoglobin species [140]. For example, methylene blue has its peak spectral absorption at 668nm, hence it absorbers most of the light emitted by the red emitter (Figure 5.1). This absorption is interpreted by the pulse oximeter as the presence of reduced haemoglobin, leading to inaccurate estimation of SpO_2. With methylene blue administrations as little as 5ml in human subjects, a drop in SpO_2 by 1% was seen [141].

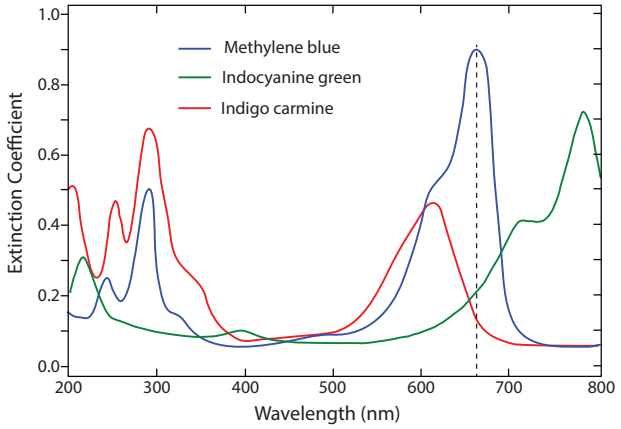

FIGURE 5.1: Absorbance spectra of three commonly used intravenous dyes, dashed line at 668 nm corresponds to the peak absorption of methylene blue and one of the wavelengths emitted and sensed by most pulse oximeters (Redrawn from [140])

5.2.2 Abnormal Haemoglobin molecules

Pulse oximeters provide a measure of arterial oxygen saturation by quantifying the absorption of light at two wavelengths, using the assumption that the light is only absorbed by oxyhaemoglobin and deoxyhaemoglobin. However, unfortunately, this is not true; the transmitted light is also absorbed by other haemoglobin species and would interfere with pulse oximetry readings. The two most significant false absorbers are Carboxyhaemoglobin (COHb) and methaemoglobin (MetHb).

Absorption due to COHb causes the pulse oximeter to overestimate arterial oxygenation [145]. This effect is caused by the specific absorption characteristics of COHb, which exhibits red light absorption similar to that of oxyhaemoglobin. Therefore increased COHb

causes the pulse oximeter to overestimate SpO_2. Pulse oximeter overestimates SpO_2 by 1 % for every 1 % increase of circulating COHb [146, 147]. Methaemoglobin absorbs approximately equal amounts of energy in the red region as deoxyhaemoglobin, and in the infrared region, it absorbs more than the other haemoglobin species. Hence, an increase in MetHb causes the SpO_2 reading to be low when SaO_2 is above 85 % and high when SaO_2 is below 85 %, thus underestimating high saturation values and overestimating severe hypoxaemia [146, 148].

5.2.3 Anaemia

Patients suffering from anaemia are known to have a reduced number of red blood cells or haemoglobin in the body. The condition usually causes tissue hypoxia as the oxygen binding capacity of blood is reduced [149]. In principle, anaemia should not affect pulse oximetry at all, as changes in total haemoglobin concentration inside a specimen does not impact the proportion of relative absorbances [129]. However, severe anaemia has shown an adverse effect on the accuracy of the pulse oximeter [150, 151]. Though in non-hypoxic patients with acute anaemia from haemorrhage, pulse oximeters have shown good accuracy [152]. This suggests that the effect of anaemia on pulse oximetry is profound only in patients suffering from hypoxia.

5.2.4 Venous pulsations

Pulse oximeters assume that the pulsatile component of the light absorbance is due to the arterial blood. However, this assumption is not entirely true in all circumstances. Conditions such as arteriovenous anastomoses, glomuses and tricuspid incompetence with regurgitation may cause peripheral veins to become sufficiently pulsatile. In these cases, the pulse oximeter would not be able to distinguish between the absorption due to pulsatile veins and arteries, leading to inaccurate estimation of SpO_2 [153, 154]. A study conducted by Sami et al. on a patient with ischaemic cardiomyopathy has shown marked central venous pulsations and a pulse oximeter bias of -18 % [155]. The error may be worst when the sensors are utilised on the forehead compared to when the sensor is placed on the finger [156].

5.2.5 Morbidity

Although pulse oximeters are noninvasive and considered very safe, morbidity has been associated with its use [133]. Skin ischaemia and necrosis have been reported due to the pressure exerted by the sensor, especially under conditions of low perfusion [157]. In

the intensive care situation, digital injury from pulse oximetry may have an incidence as high as 5 %, with the highest incidence being in very sick patients with noradrenaline (norepinephrine) infusions reducing the peripheral perfusion [158]. There have also been reports of burns on fingers in children [159]. The Medicines and Healthcare products Regulatory Agency (MHRA), a UK government-run body, has issued a safety notice to healthcare facilities warning that the site of application of pulse oximeter probe should be regularly inspected in accordance with the manufacturer's instructions [160].

5.2.6 Inadequate peripheral perfusion

Compromised peripheral perfusion is presumably the most common cause of pulse oximetry failure after motion artefacts [127]. Pulse oximeters rely on the presence of adequate arterial pulsations to distinguish between the light absorbed by the arterial blood from that absorbed by the venous blood and other tissues. With the loss or diminution of the peripheral arterial pulse, the estimated SpO_2 reading quickly becomes very inaccurate or non-existent. These inaccuracies occur due to the inability of the pulse oximeter to distinguish between light absorbed by arterial blood from that of venous blood, in the absence of arterial pulse [73]. Poor peripheral pulsation can result from hypotension, hypothermia, low cardiac output, hypovolemia, peripheral vascular disease, infusion of vasoactive drugs, proximal blood pressure cuff inflation, leaning on an extremity, Raynaud's phenomenon (Figure 5.2) and from performing a Valsalva manoeuvre [9, 162]. Under these conditions most pulse oximeters do not produce a reading, some modern pulse oximeters, however, display a message such as "Low Quality Signal" or "Poor Perfusion" on the screen to make the user aware of the situation.

FIGURE 5.2: Thermograms of a healthy hand (left) and the hand of a person with Raynauds disease (right) after 2 minutes immersion in cold water. Hotter areas are shown in yellow and orange, while colder areas are in blue, black and purple. These hands are from two different people, one male and one female. ([161])

Other factors reported to contribute to low perfusion and pulse oximeter failure includes the very young and very elderly patients, ASA III and IV patients, prolonged duration of the intraoperative procedure and chronic renal failure [16]. The failure rates of pulse oximeters under conditions of poor peripheral perfusion have been investigated before by many researchers, some of the results from their studies are listed here.

- A study by Moller and co-workers from their hand-kept anaesthesia records, reported a total failure rate of 2.5 % in 10,802 patients, but it increased to 7.2 % in patients who were American Society of Anaesthesiologists (ASA) physical status IV [163, 164].
- Freund and colleagues reviewed 11,046 cases from four University of Washington Hospitals and reported an overall failure rate of 1.24 %, but it increased to 4.24 % at the Veterans Hospital, where ASA physical status tended to be greater. They had also reported that, when the device did fail in a patient, it did not function for 32 % of the mean anaesthesia time [165, 166].
- Reich and co-workers studied predictors of pulse oximetry data failure by reviewing 9203 electronic medical records and reported a failure rate of 9.18 % [16]. Another study by Reich suggested that the pulse oximeters are more likely to fail in patients undergoing cardiopulmonary bypass surgery than in other anaesthetised patients [167].
- Shafique et al. has investigated the failure rates in transmittance and transreflectance pulse oximeters in conditions of artificially induced hypothermia, in 20 healthy volunteers. The results show that at low-temperature ranges, from 13 to 21^0C, the failure rate of the trans-reflectance pulse oximeter was 2.4 % as compared to the transmittance commercial pulse oximeter with a failure rate of 70 % [168].
- Hummler et al. has examined the accuracy of pulse oximetry measurements in 37 adult anaesthetized, ventilated rabbits, during sepsis. The results show that modern pulse oximeters have a bias beyond $\pm$ 3 when compared to SaO_2 values, in more than 21 % of the subjects [169].

Other interesting studies evaluating the performance of pulse oximeters in conditions of compromised peripheral perfusion are described in [3–15]. The failure rates discussed in these studies are directly associated with the application of pulse oximeter sensors to extremities such as the finger or toe, where the pulsatile flow is very easily compromised. Many attempts were made previously to improve the signal detection such as application of vasodilation creams [11], administration of intra-arterial vasodilators [17], digital nerve blockers [18–20], and applications of sensors on better perfused areas such as forehead [13] and the nose [21]. However, it is not always possible to use vasodilators and nerve blockers in critically ill patients. Moreover, the actual failure rate has increased when pulse oximeter

sensors were used on nose and forehead [156, 170, 171]. Thus, SpO_2 readings are often unobtainable or inaccurate at just the time when they would be most valuable. To curb this limitation, many researchers have successfully developed pulse oximeter sensors to measure SpO_2 from more centrally perfused sites such as the oesophagus [22], the pharynx [172], the anterior fontanel [173], and other splanchnic organs [174]. These technologies and other advancements in pulse oximetry in the recent past are discussed in the following sections.

5.3 Recent advancements in pulse oximetry

Since the introduction of pulse oximeters into clinical practice in the 1980's most amendments to pulse oximeter technology have been largely cosmetic modifications, such as the size of the device, user interface, and size and colour of the readout. These modifications have made the device a less expensive and effective means for health monitoring in clinical setting and in home care. In recent years, however, manufacturers and researchers have developed oximeters that are better able to distinguish between motion artefact, electronic noise, and authentic patient events [175].

Advancements in pulse oximeter technology have particularly been in four main streams. (1) Analysis of the photoplethysmographic waveform (2) Multi-wavelength analysis to quantify chemical component fractions in blood, (3) Advancements in algorithms to improve signal detection and (4) development of novel reflectance pulse oximeter sensors.

5.3.1 Advancements in analysis of the photoplethysmographic waveform

Despite its simple appearance, the PPG waveform is a highly intricate signal that contains far more information in its shape, height, and timing than just pulse rate. The raw PPG waveforms are considered to be a true projection of the haemodynamic output of the entire cardiovascular system [176]. Various algorithms were developed by researchers in recent years to analyse the PPG waveform in both the time and frequency domain [177]. Parameters such as respiration rate, sympathetic tone, pulse transit time, perfusion index and path variability index can be estimated from the developed algorithms. However, some of the developed algorithms are not yet in clinical use.

5.3.1.1 PPG signal amplitude analysis

The auto-scale function in the pulse oximeter usually conceals the amplitude changes of the PPG signal. However if this was to be turned off, relative changes in the amplitude

of the PPG signal could be observed [177]. The changes in the amplitude of PPG signals can be linked to significant changes in arterial blood pressure (BP) and vascular tone. For example, during episodes of increased sympathetic tone, the amplitude of the PPG signal decreases due to the resultant vasoconstriction. Conversely, with vasodilation the PPG signal amplitude increases. This is particularly true in patients who are critically ill, or who are anaesthetised, undergoing surgery, or in labour [176]. Currently, none of the commercially available pulse oximeters display not auto-scaled PPG signals over a large duration of time. However, a new variable providing similar information known as Perfusion index (PI) was introduced by Masimo *(Masimo Corp., Irvine, CA, USA)* in their pulse oximeters (Rad-8, Rad-5, ISpO$_2$Rx etc.) [178]. PI is defined as the ratio of pulsatile (AC) and non-pulsatile (DC) components of the infrared photoplethysmographic waveform as shown in Figure 5.3.

$$\text{Perfusion Index (PI)} = \frac{AC}{DC} \times 100\ \% \tag{5.1}$$

PI is used to assess peripheral perfusion and circulatory strength of the peripheral measurement site. PI values usually range from 0.02 % for a frail pulse (suggesting peripheral vasoconstriction) to 20 % for an extremely strong pulse (suggesting vasodilation) [179]. PI has been shown to be useful in assessing the severity of illness in newborns, to determine the effectiveness of epidural blocks, and to quantify peripheral perfusion for diagnosis of congenital heart disease in newborns [180–184].

5.3.1.2 Analysis of amplitude variability due to respiration

Both the baseline (DC) and pulsatile (AC) components of the PPG signal are known to oscillate with spontaneous and positive pressure ventilation [177]. The ability to detect

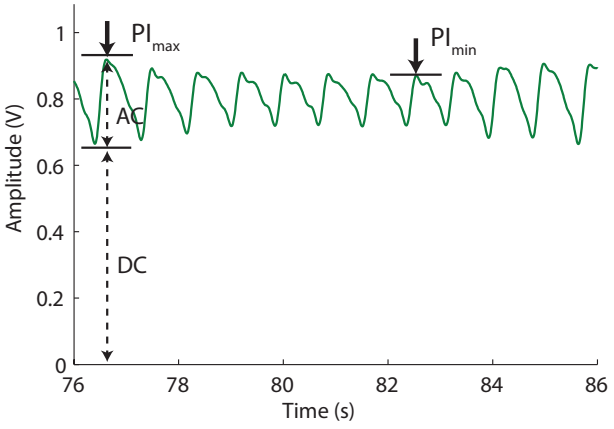

FIGURE 5.3: Computation of Perfusion Index (PI) and Pleth Variability Index PVI from the pulsatile AC and non-pulsatile DC components of the photoplethysmographic waveform

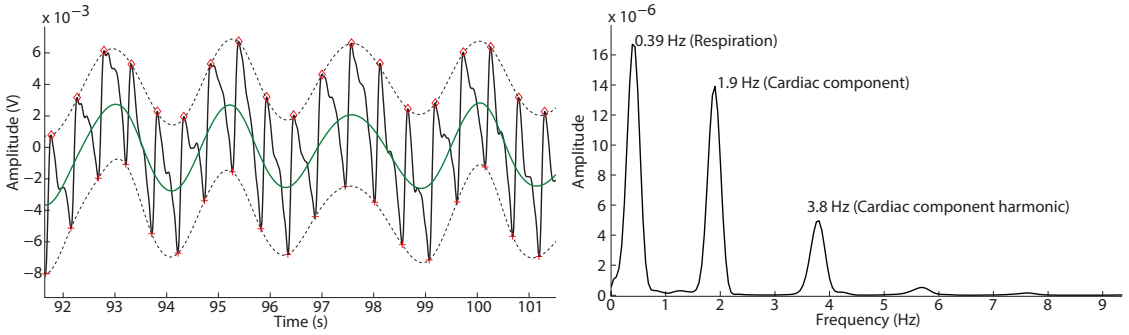

(a) Peak, trough detection (red markers) and mean envelope detection (green signal) using cubic spline interpolation

(b) Fast Fourier Transform of the PPG signal showing the respiration and cardiac components

FIGURE 5.4: Extraction of respiration component using time domain and frequency domain methods

these oscillations enables whole new possibilities. At the very least, respiratory rate can be reliably determined using the PPG signals. Several methods are used to extract respiration rate from the PPG signals, one of the common methods is to filter the raw PPG signals using a band pass filter with cut-off frequencies of 0.1 Hz and 0.5 Hz and then calculating the respiration rate from the resulting signal [122, 185–190]. The accuracy of this method is low, mainly during shallow breathing. In a more accurate time domain method, the respiration signal is extracted by detecting the peaks and troughs of the PPG signal and by constructing the upper and lower envelopes using cubic spline interpolation [191, 192]. The mean envelope of the upper and lower envelopes shows the respiratory modulation as shown in Figure 5.4(a). Spectral analysis techniques such as Fast Fourier Transformation (FFT) based on Welchs averaged periodogram can also be used to characterise respiratory oscillations as shown in Figure 5.4(b) [186, 188, 193].

The variability in PPG signal amplitude due to respiration has recently been used as a dynamic parameter in functional haemodynamic monitoring. This new parameter called the Pleth Variability Index (PVI) was first introduced by Masimo *(Masimo Corp., Irvine, CA, USA)* in their new pulse oximeters [194]. Masimo defines PVI as a measure of the dynamic changes in the perfusion index that occur during one or more complete respiratory cycles (Figure 5.3).

$$\text{Pleth Variability Index (PVI)} = \frac{PI_{max} - PI_{min}}{PI_{max}} \times 100\ \% \tag{5.2}$$

Numerous clinical studies have shown PVI to detect occult haemorrhage and its resulting hypovolemia and to assess fluid responsiveness in surgical and intensive care patients [195–198]. The greater the PVI, the more likely the patient will respond to fluid administration.

5.3.1.3 Time variability analysis of PPG signals

The variations in the time interval between arterial pulsations (heartbeats) can reveal further information regarding the heart's function and its association with the autonomic nervous system. The variability in time duration between consecutive heart beats is known as Heart rate variability (HRV) [199, 200]. HRV is traditionally measured from the QRS complex of the electrocardiogram (ECG). Since PPG also reflects the cardiac rhythm, variability in heart rate can also be estimated from the PPG signal. HRV measured from PPG is referred to as Pulse Rate Variability (PRV) [201]. PRV is measured as the time difference between the peaks (PP - peak to peak) of consecutive pulses (as shown in Figure 5.5). A high PRV usually indicates good health, whereas low PRV is associated with higher risk of death, mainly in patients with coronary heart disease.

The autonomic nervous systems control over the heart's function can be determined by analysing the PRV signal (black trace in Figure 5.5) in the time and frequency domains. Standard indices such as SDPP (standard deviation of all PP intervals), RMSSD (the square root of the mean of the sum of the squares of adjacent PP intervals), and nPP50 (percentage of pairs of adjacent PP intervals differing by more than 50 ms) can be estimated in time domains. Frequency domain parameters such as P_{LF} (power of low frequency component [Range: 0.003 - 0.04 Hz]), P_{HF} (power of high frequency components [Range: 0.15 - 0.4 Hz]), and the ratio between P_{LF} and P_{HF} can also be estimated [202, 203]. From the measured indices the influence of parasympathetic and sympathetic activity is determined.

The main difference between HRV and PRV is the time the pulse wave takes to travel from the heart to the finger [201]. This time called the pulse transit time (PTT) is measured as the time difference between the R-wave of the ECG and the corresponding foot of the PPG signal (Figure 5.6) [204]. PTT is an effective parameter for estimating arterial stiffness and local vascular resistance and hence can be used as a potential diagnostic tool

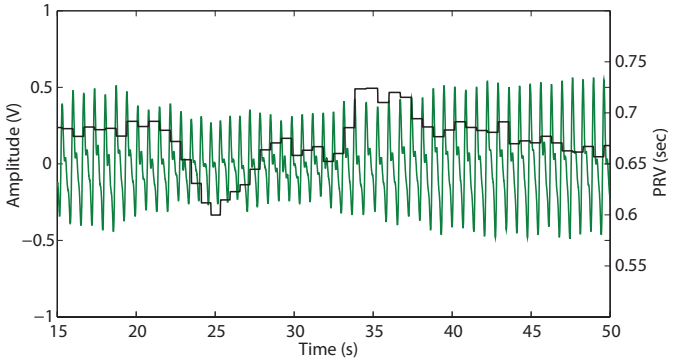

FIGURE 5.5: Computation of PRV from the AC photoplethysmographic waveform. Black trace shows the changes in times interval between consecutive pulses for 35 seconds.

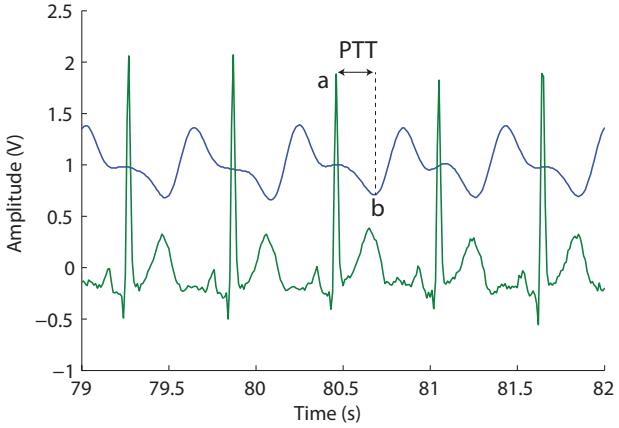

FIGURE 5.6: Computation of PTT from ECG and PPG signals. PTT is the time difference between points 'a' and 'b' (illustration inspired from [204])

for cardiovascular diseases [205]. However, PTT measurements require the use of ECG in conjunction with the PPG signal. Also, large variability in PTT may affect the PRV measurements. Nonetheless, if the distance from the pulse measurement site to the heart and PTT are known, then the velocity of the pulse can also be measured

$$\text{Pulse Wave Velocity (PWV)} = \frac{Pulse\ Propagation\ Distance\ (PPD)}{Pulse\ Transit\ Time\ (PTT)} \tag{5.3}$$

"Just as with SpO_2 measurements, PI, PVI, PTT, and respiration measurements are subjected to measurement sites. In conditions of compromised peripheral perfusion, none of these parameters can be estimated accurately due to the absence of the peripheral pulse. Hence, the advancements in the analysis of the PPG signal are truly only possible if the peripheral pulse is detectable".

5.3.2 Advancements in multi-wavelength analysis

Pulse oximeters estimate arterial oxygen saturation based on the 'assumption' that when light is shone on vascular tissue, it is only absorbed or attenuated by oxygenated and deoxygenated haemoglobin. However, this assumption is not true, as dysfunctional haemoglobins such as carboxyhaemoglobin and methaemoglobin also absorb transmitted light (Section 5.2.2). The presence of these dysfunctional haemoglobins can interfere with pulse oximeters performance. Besides, pulse oximeters have for long been limited to the use of just two wavelengths in determining SpO_2 [146, 206].

The possibility of multi-wavelength pulse oximetry has been a topic of research for many years. However, a commercial pulse oximeter with such technology was not available till 2006, when Masimo Corp. *(Irvine, CA, USA)* introduced their new 'Rainbow Technology' pulse oximeters [207]. Before this, Aoyagi, who invented the pulse oximeter has developed a

three wavelength sensor to improve the accuracy of the estimated SpO_2 in 2002 [208, 209]. Another noteworthy development is the four wavelength pulse oximeter that estimated total Haemoglobin (Hbt) by Noiri et al. However, this device never made it into the commercial market [210]. Masimo's 'Rainbow SET' pulse CO-Oximeter (Models: Rad-57, Rainbow-7 etc.) uses 8 wavelengths of light to measure SpO_2 as well as SpCO (estimate of COHb %) and SpMet (estimate of MetHb %). This technology has enabled continuous monitoring of haemoglobin species, which was not possible before, and now stands as an alternative to the time and labour consuming invasive blood tests, done in hospitals with laboratory CO-Oximeters [207, 211]. In an attempt to test the reliability of the Pulse CO-Oximeter in victims of carbon monoxide poisoning, Coulange *et al.* conducted a study in 12 patients. The results of the study have shown an overestimation of COHb by 1.5 %, compared to the results obtained using a CO-Oximeter [212]. Layne *et al.* measured SpCO and COHb % in 130 patients, they also found a bias of 0.65 % and a precision of 1.8 %, in a COHb range from zero to 31 % [213].

Although the pulse CO-oximeters work reasonably well, they have two main limitations.

- The SpO_2 calculation algorithm does not make use of the light absorbances from 8-wavelengths, instead sticks to the conventional red and infrared wavelengths. Hence, the estimated SpO_2 values are still subjected to inaccuracies under the presence of significant levels of COHb or MetHb.
- The device has also been reported to have 'crosstalk' between the MetHb and COHb measurement channels. In 2008, the Masimo Radical 7 pulse oximeter were also equipped with algorithms to measure Hbt as well [214].

5.3.3 Advancements in signal processing algorithms

As mentioned earlier in Section 5.1, motion, low perfusion, and optical shunting can induce considerable errors into pulse oximeter accuracy, resulting in loss of data, erroneous readings, and false alarms. These technical difficulties were in the past dealt with by longer averaging, holding data, or by inducing alarm delays. In recent years, however, researchers have developed many intelligent signal processing algorithms for analysing motion affected PPG signals in both off-line and on-line modes. There have been numerous publications describing the developed algorithms and their effectiveness [215–220]. Although at the present moment, this motion resistant technology is only available in pulse oximeters manufactured by Masimo Corp., Nellcor™ and Phillips Healthcare. The fundamentally distinct method of acquiring, processing and reporting arterial oxygen saturation and pulse rate in Masimo pulse oximeters is called the Signal Extraction Technology® (SET) [221]. Nellcor and Phillips refer to their motion tolerant technology as OxiMax™ Technology [222] and Fourier Artifact Suppression Technology (FAST-SpO_2) [223] respectively.

Masimo SET technology uses a highly sophisticated adaptive filter with Discrete Saturation Transform (DST) and four other parallel engines, to distinguish between venous and arterial pulsations, and remove noise produced by movements. Thus, enabling the direct calculation of arterial oxygen saturation and pulse rate [221].

It has been publicised over the years, that the Masimo's SET is far superior in its performance over other motion tolerant technologies. A study comparing six "motion resistant" pulse oximeters by Baker found that the Masimo SET was the only product with no drop outs, high sensitivity and specificity under challenging motion and low perfusion conditions [224]. More than 100 such studies describe Masimo SET technology to provide the most reliable SpO_2 and pulse rate measurements [225]. However, an article by Giuliano *et al.* explains that none of the new-generation oximeters differ from each other in clinical performance. In this article, Giuliano *et al.* reviewed 17 published studies comparing the performance of different motion resistant pulse oximeters from 1995 to 2003. They found that there is a lack of consistency among study variables and techniques and discrepancies between the results of the studies, making it difficult to make any overall recommendations about which of the new-generation motion-tolerant devices are best suited for use in critical care [226].

Masimo SET pulse oximeters have also been shown to fail in patients experiencing 'low perfusion states' [227–230]. Frode *et al.* found the system to be misleading in patients experiencing profound bradycardia [228], as the pulse oximeter was producing pulse tone measurements when the patient's heart stopped. To further investigate this incident, Frode *et al.* conducted experiments by occluding the measurement hand of a volunteer using a non-invasive blood pressure cuff and found the pulse oximeter to produce tone measurements for 8 seconds after the plethysmograph is flat and there is no palpable pulse. Hummler *et al.* conducted a study on anaesthetised and ventilated rabbits, to evaluate the effect of deteriorating perfusion caused by sepsis on the accuracy of pulse oximetry measurements [169, 231]. The results showed a bias beyond ± 3 % in 22.6 % of the measurements made with Masimo SET pulse oximeter. Nonetheless, the developments in this area have resulted in pulse oximeters with better capability to acquire and display PPGs and calculate SpO_2, compared to conventional oximeters.

5.3.4 Advancements in novel reflectance PPG sensors

Pulse oximeters rely on the presence of adequate arterial pulsations to distinguish between the light absorbed by the arterial blood from that by other absorbers. With the loss or diminution of the peripheral arterial pulse, as in the case of hypothermia or peripheral vascular disease, the device ceases to function. The problem arises as the majority if not all clinically used pulse oximeter sensors operate in transmission mode. Hence limiting

the sensors applicability or usage to extremities such as the finger, toe, or earlobe, where perfusion is easily compromised.

In order to overcome this limitation plus enable the investigation of SpO_2 in specific organs and or tissues, researchers have developed novel reflection based sensors utilising either miniaturised optoelectronic components or optical fibres. These sensors were used to measure PPGs directly from more central organs such as the oesophagus [22], larynx [172], liver, Kidney, bowel [174], brain [110], and other vascular areas such as the forehead, anterior fontanelle [232] and free flaps [233]. These new sensors have been shown to estimate SpO_2 reliably in the presence of compromised peripheral perfusion and have responded well to changes in blood oxygenation. Some of the recent sensor developments, their advantages and disadvantages are discussed here.

Forehead reflectance sensor – The only reflectance pulse oximeter sensor which is currently commercially available from most major pulse oximeter manufacturers is the forehead pulse oximeter sensor. The hypothesis behind this sensor development is that the forehead is more central than the finger and hence should register changes in saturation faster than the finger or other peripheral sites. The perfusion at this site is also preserved at times when the periphery fails, as it is essentially supplied by the internal carotid artery. Numerous studies have examined the efficacy of this sensor site and found conflicting results in different clinical settings [234–238]. Sugino *et al.* conducted a study to compare the sensitivity of forehead sensors and finger sensors in 18 patients receiving general anaesthesia [171]. They concluded that forehead SpO_2 monitoring (in the range SpO_2 = 90 % - 100 %), has a sensitivity similar to conventional finger monitoring under normal conditions during general anaesthesia. Barker *et al.* conducted studies on a mixed group of surgical and intensive care paediatric patients, to test the accuracy of forehead pulse oximeter probes. These studies revealed that the arterial saturation estimated by forehead reflectance pulse oximetry has an error greater than 7 % for 28 % of the monitoring time when compared to earlobe and blood gas analyser [170]. Another study comparing the finger and forehead sensors by Cheng *et at.* found the forehead pulse oximeter sensor works well on healthy, well-oxygenated volunteers, but experienced difficulties when used in critically ill patients [237].

Although the forehead sensor is non-invasive and offers fast response time, signal strength is usually low and thus the potential for artefacts is high. Forehead sensors also suffer from attachment problems, a loose-fitted sensor using medical tape introduces inaccuracies due to motion and venous pulsations [156, 239]. If the sensor was to be applied using a headband, then the pressure applied on the sensor will occlude the vascular bed of the forehead. There have also been reports of patients developing tissue necrosis due to prolonged application of a forehead pulse oximeter sensor under a headband [240]. A very

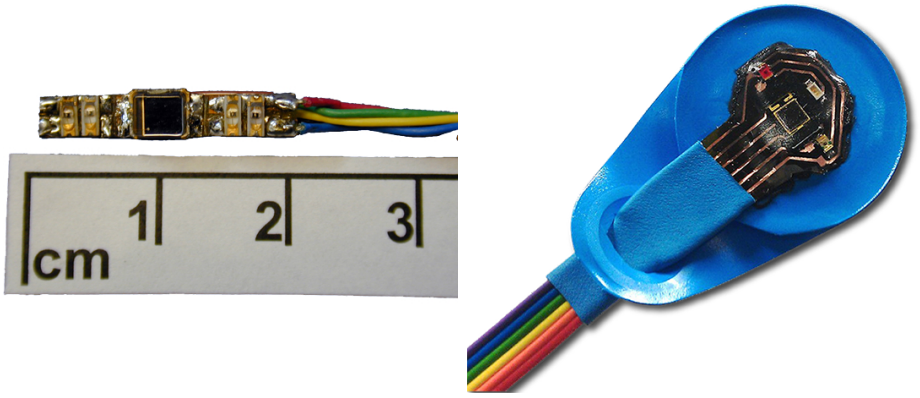

(a) Oesophageal reflectance sensor (b) anterior fontanelle sensor

FIGURE 5.7: New optoelectronic reflectance sensors for measuring PPG directly from (a) The oesophagus and (b) The anterior fontanelle

slight pressure of 4 - 5 mmHg on the probe, however, seems to correct the attachment problem.

Faisst *et al.* and May *et al* have explored the possibility of applying the forehead sensor on other scalp locations where SpO_2 monitoring may be unaffected. Faisst *et al.* explored the possibility of measuring SpO_2s from the forehead, cheek, and back of the head of thirty-one neonates using a forehead reflectance sensor [241]. May *et al.* developed a reflectance, 3-wavelength sensor to investigate the possibility of measuring SpO_2 from the anterior fontanelle of 16 neonates (Figure 5.7(b)) [173]. The SpO_2s estimated from the fontanelle sensor have a mean difference of 2.2 % to the SpO_2 estimated by commercial finger pulse oximeter and a 1.7 % difference to the blood gas results.

Oesophageal sensor -One of the well known optoelectronic sensors developed in the recent past is the oesophageal pulse oximeter sensor by Kyriacou *et al.* In this work, the oesophagus was proposed as an alternative site for measuring PPGs and SpO_2s, on the hypothesis that this central site will remain adequately perfused in conditions leading to peripheral shut down [108]. Kyriacou *et al.* developed the oesophageal sensor using four surface mount emitters and a photodetector to detect blood volume changes at red and infrared wavelengths from the oesophagus (Figure 5.7(a)). The developed sensor was fitted inside a disposable and sterilised stomach tube (size 20-Fr), prior to its usage. The performance of the oesophageal probe was evaluated in 49 patients undergoing hypothermic cardiothoracic bypass surgery [242]. The results from the study demonstrated that reliable acquisition of PPGs and SpO_2 values is possible from the oesophagus. Of the 49 participants in the study, the finger pulse oximeter has failed to record pulsatile PPG signals and display SpO_2 values in 5 (10.2 %) patients for at least 10 min, where the oesophageal readings remained reliable [243–246].

Similar developments and studies were carried by Chen et al. in 45 patients undergoing controlled hypoxemia, and the results from his study showed accurate and earlier detection of hypoxemia when compared to conventional pulse oximetry [247]. Kyriacou *et al.* also developed a miniaturised oesophageal sensor for use in neonates [248]. Although the oesophageal sensor has shown promising results, there are a few limitations associated with the technology. Firstly, the developed technology is semi-invasive, hence is only suitable for patients who are anaesthetized, as it would cause discomfort if inserted in conscious patients. The use of the sensor also requires the patient to be administered with muscle relaxants to suppress the cough reflex, as coughing would inevitably induce unwanted motion artefact. The sensor requires it to be inserted in the oesophagus initially at various depths, to find an optimum depth at which the patient has good quality and high amplitude PPG signals. This insertion can only be carried out by a trained anaesthetist, as untrained staff can accidentally insert the probe in the trachea or the lungs. The proximity of the probe to the lungs may induce heavy ventilator artefact into the acquired PPG signals.

Fibre-optic reflectance sensor -Another exciting advancement in pulse oximeter sensor technology is the fibre-optic reflectance sensor, used to measure PPGs directly from the surface of the organs such as the brain, small bowel, large bowel, liver and stomach. Hickey *et al.* developed the fibre optic sensor suitable for intra-operative monitoring of splanchnic perfusion [174, 249]. This sensor has made it possible for early detection of inadequate tissue oxygenation, reducing the risk of hypoperfusion, severe ischaemia and multiple organ failure. The performance of the fibre optic sensor was evaluated by Hickey *et al.*, in 20 patients undergoing laparotomy. The results obtained from their study demonstrated that good quality PPG signals can be obtained from the surface of the small bowel, large bowel, liver and stomach. Also, the SpO_2values estimated from the sensor showed good agreement with an optically identical peripheral sensor [250, 251]. The similar sensor was also developed by Phillips *et al.*, for monitoring the oxygen saturation of blood within the tissue of the cerebral cortex. The sensor was developed for use in patients recovering from traumatic head injury or stroke. Phillips *et al.* has demonstrated that good quality PPG signals could be obtained from human brain tissue using their fibre optic sensor by conducting a study on six patients undergoing neurosurgery [110, 252].

Although this sensor works well, it has a few limitations. The use of the sensor requires it to be held on top of the measurement site, hence making continuous monitoring of oxygen saturation during surgery very difficult. The sensor can not detect postoperative complications such as shock and internal haemorrhage as the design of the sensor prevents it from being used postoperatively. Nonetheless, the results acquired by Hickey *et al.*, show that fibre optic pulse oximetry is the way forward in monitoring splanchnic perfusion.

Table 5.1: Summary of the recent advancements in pulse oximetry and their limitations

Advancements	**Description**	**Limitation**
PPG waveform analysis	With further analysis of the PPG signal in time and frequency domains, parameters such as PI, PVI, PRV, PTT and respiration rate can be obtained. These variables if measured can enhance the clinical outcome of patients in critical care	Just as with SpO_2 measurements, PI, PVI, PRV, PTT, and respiration measurements are subjected to measurement sites and cannot be estimated in conditions of compromised peripheral perfusion.
Multiwavelength pulse oximetry	Multi-wavelength pulse oximeters were developed to avoid pulse oximeter failing from the presence of dysfunctional haemoglobins. Masimo introduced Pulse CO-Oximeter which uses eight wavelengths of light to measure lethal haemoglobin species such as COHb and MetHb	The SpO_2 measurements made by Pulse CO-Oximeters do not take advantage of the light absorbances from 8- wavelengths instead sticks to the conventional red and infrared wavelengths. Hence, the estimated SpO_2 values are still subjected to inaccuracies under the presence of significant levels of COHb or MetHb
Signal processing algorithms	Various Signal processing algorithms such as the Masimo's SET were introduced in modern pulse oximeters to detect PPG signals in the presence of motion. These algorithms have resulted in pulse oximeters with better capability to estimate SpO_2, compared to the conventional oximeters.	Although these new signal processing algorithms have reduced false alarms and improved PPG signal detection, they have failed to estimate SpO_2 accurately in patients experiencing 'low perfusion states'. Also, the degree of failure during low perfusion varies across different manufacturers
Novel reflectance sensors technology	In order to avoid pulse oximeter failure in low perfusion states, novel reflection based sensors were developed to measure PPGs and SpO_2s from alternative measurement sites such as the oesophagus, larynx, liver, bowel, brain, forehead, and anterior fontanelle. These new sensors had shown to estimate SpO_2 accurately in conditions when the finger pulse oximeters failed	These new sensors suffer from few functional difficulties such as attachment problems, venous pulsations, motion artefacts and require considerable expertise to use them. Some of these sensors are invasive, hence limiting their usage to patients undergoing surgery and under anaesthesia.

5.4 Summary of the advancements and proposed research

Pulse oximeters, since their invention, have been under constant development in both hardware and software aspects. These developments have made the device into a clinical tool with a potential to provide far greater clinical information than just oxygen saturation. However, there are still unsolved problems that limit their performance. A summary of these advancements in the technology and their limitations are provided in Table 5.1.

Significant improvements were made in utilising the PPG signal from a pulse oximeter. The PPG signal is now used to estimate parameters such as perfusion index, pleth variability index, respiration rate and pulse rate variability. These parameters provide vital information that can enhance the clinical outcome of the patients in critical care. However, as with SpO_2 measurements, all these parameters are subjected to the ability of the pulse oximeter to detect an undistorted peripheral signal. Hence in conditions of compromised peripheral perfusion or heavy motion, none of these parameters can be estimated. To avoid this limitation, manufacturers have developed many algorithms that can better detect the PPG signal, in conditions of motion and low perfusion. Pulse oximeters equipped with these algorithms have proven to perform better than the conventional pulse oximeters. However, they have failed to estimate SpO_2 in patients experiencing 'low perfusion states', although the degree of failure varied across different manufacturers.

Few researchers have taken an alternate route to counter this issue, as opposed to working on peripheral sites which are usually affected by low perfusion states, they have developed reflectance sensors to detect PPG signals from more centrally perfused areas of the body. These new sensors had shown promising results in detecting PPG signals and estimating SpO_2 accurately in conditions when the finger pulse oximeters failed. These novel sensors have also made it possible to monitor perfusion of vital organs in the body. However, some of these sensors experience functional difficulties such as attachment problems, venous pulsations, motion artefacts and require considerable expertise to use them. Other sensors which are semi-invasive can only be used in patients undergoing surgery and under anaesthesia.

Hence, there is a clear need for a non-invasive PPG sensor system which can detect PPGs reliably and estimate SpO_2 accurately from an area where perfusion is not easily compromised. To address this issue, we propose the ear canal as an alternative location for oxygen saturation monitoring on the hypothesis that this central site will have much-reduced influence from low perfusion states and, as a result, a better quality PPG signal during critical conditions. The ear canal as a measurement location offers many physiological and mechanical advantages over other peripheral and central sites. A complete review on the choice of the ear canal as a measurement site is provided in Chapter 6, some of the key advantages are highlighted here

- The ear canal provides stable temperature close to the core temperature of the body and is less influenced by the sympathetic nervous system during low perfusion states.
- This sensor location is non-invasive and provides factor of comfort and invisibility of the sensor as it can be concealed by the ear and hair
- As proven by hearing aids and headsets, the ear canal provides a natural anchoring point for the sensor, thus avoiding the need for adhesives or bands
- Furthermore, ear canal offers fewer motion artefacts, as the head is less affected by motion than the other extremities

To validate this hypothesis, a micro-optic reflectance ear canal sensor was developed along with the instrumentation and software required for acquisition of PPG signals and computation of variables from the PPG signals. An optically identical finger sensor was also developed to allow for comparison between the peripheral and central circulations. Detailed description of the developed technology is provided in Chapter 7 and Chapter 8

5.5 Summary

Although pulse oximeters give reliable readings of blood oxygen saturation, there are significant limitations on the accuracy and the availability of pulse oximetry data in some circumstances. These limitations include motion artefact, low perfusion, electromagnetic interference, venous pulsations, etc. In the past two decades, researchers and manufacturers have constantly improved the pulse oximetry technology to overcome these limitations. The improvements to the technology were in four main streams, namely the analysis of the PPG waveform, multi-wavelength PPG signal analysis, signal processing algorithms and novel reflectance sensors. These developments to the device have made it into a clinical tool with a potential to provide far greater clinical information than just oxygen saturation. However, there is still room for further improvement and optimisation of the technique. Particularly in tackling the problems associated with pulse oximeters in low perfusion states. Hence, the ear canal is proposed as an alternative measurement site for measuring PPG signals in conditions of compromised peripheral blood supply. A detailed description of the choice of the ear canal as a measurement site and previous work carried out is discussed in the next chapters.

— I'm not enthusiastic about the forehead, I don't have high hopes for this sensor site. Researchers and manufacturers need to explore other probe sites on the head.

Steven J. Barker, during 2004 annual meeting of the Society for technology in anaesthesia

6

The ear canal as a location for oxygen saturation monitoring

Since their invention in 1974, pulse oximeters have undergone many technological changes. The device has become a quasi-standard, if not standard, monitoring device in hospital critical care units and surgical theatres. The oximetry measurements provided by the instrument are often referred to as the "fifth vital sign".

However, as with any technology, the device possesses a few limitations. Despite many efforts over the years to curb these limitations, the device is still reported to fail in a few conditions. One of the major situations, where pulse oximeters fail to yield an accurate SpO_2 reading, is in conditions of compromised peripheral perfusion. Failure in such circumstances is related to the utilisation of the sensor in locations where perfusion is easily compromised (i.e. finger, toe, earlobe). In order to overcome this limitation, the ear canal has been proposed as an alternative monitoring site on the basis that this central site would not experience effects of compromised perfusion.

This chapter describes the basic anatomy and blood circulation of the human ear canal. The hypothesis and the justification of choosing the ear canal as the alternative measurement site are provided in this chapter. Also, previous attempts made to develop an ear canal PPG/SpO_2 sensor are discussed in this chapter.

6.1 Anatomy of Ear

The human ear is divided into three main regions: (1) the external ear, which funnels the sound through the external auditory canal, to the tympanic membrane; (2) the middle ear, which conveys sound vibrations from the eardrum to the oval window and converts the sound vibrations to liquid form; and (3) the internal ear, which translates the fluid vibrations into electrical signals that are sent to the brain for interpretation (Figure 6.1) [253, 254].

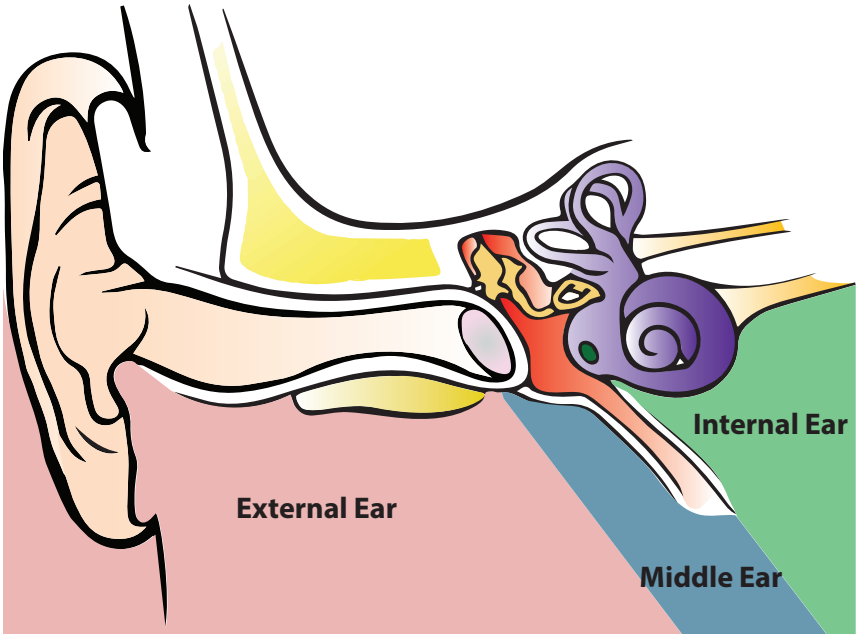

FIGURE 6.1: Frontal section through the right side of the skull showing the three principal regions of the ear, the external, middle and internal ear (illustration inspired from [255]).

6.1.1 The external ear

The external ear consists of the auricle, external auditory canal and tympanic membrane. The auricle is the cartilaginous part of the external ear on the outside of the head (Figure 6.2(a)). It is shaped like the flared end of a trumpet and is also referred to as *Pinna*. The auricle, which extends from the skull with an approximate angle of 30 degrees, is attached to the head by way of three extrinsic muscles, the superior, anterior, and posterior auricular muscle. Major cartilages of the auricle are the helix, antihelix, tragus, and antitragus. The depression in the centre is the concha and the ear lobe is called lobule [256].

External auditory canal (*external auditory meatus, external acoustic meatus*) is a curved tube about 25 mm in length and 8 mm in diameter. The opening of the ear canal is oval,

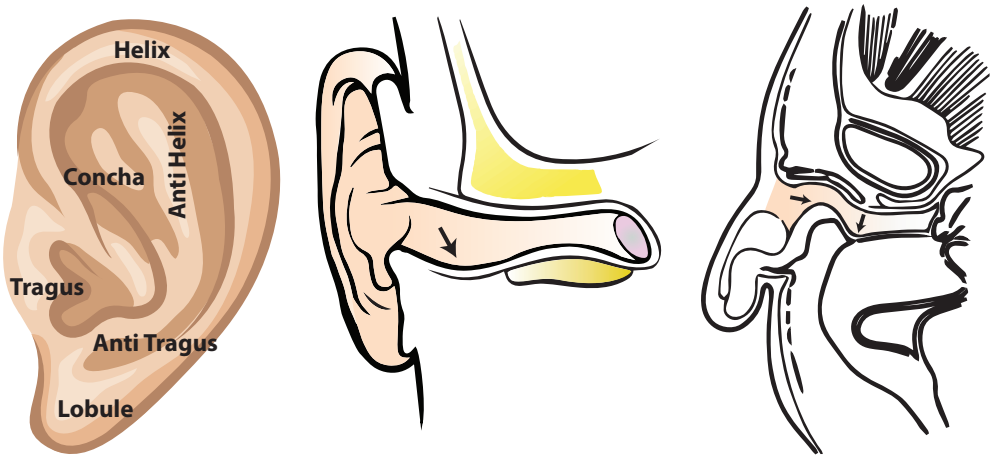

(a) Auricle (b) Ear canal frontal view (c) Ear canal transverse view

FIGURE 6.2: Shows (a) the auricle: cartilaginous part of the external ear, (b) the frontal view of ear canal showing the osseo-cartilaginous junction and (c) the transverse view of the ear canal showing the two less pronounced bends

averaging 9 mm in height and 7 mm in width [257, 258]. The outer part of the canal consists of a soft cartilaginous body and a 0.5 - 1.0 mm thick skin with glands and hair follicles. The outer part forms one-third to one-half of total canal length. The rest of the canal is a more sensitive skin lining a bony canal. The skin here is approximately 0.2 mm thick. When seen from the front, as in Figure 6.2(b), there is a curvy bend in the junction between the cartilage and bone sections. This junction is termed the osteocartilaginous junction [259]. When seen from above, as in Figure 6.2(c) there are two less pronounced bends. The first of which is in the lateral part of the canal near the canal entrance. The second is near the junction of the cartilage and the bony parts. The ear canal also narrows down towards the second bend. The tympanic membrane is a thin pearl-gray membrane with an average thickness of 0.074 mm and separates the external ear from the middle ear [258]. Sound waves reaching the tympanic membrane cause it to vibrate.

6.1.2 The middle ear

The middle ear is the air-filled cavity of the ear; it extends from the tympanic membrane to a bony wall containing two small openings called the oval window and the round window. Three small bones are found between the tympanic membrane and the oval window, collectively called the ossicles. These bones called the *malleus* (hammer), *incus* (anvil) and *stapes* (stirrup) are the smallest bones in the human body (Figure 6.3) [260]. The sound vibrations from the tympanic membrane push the malleus, which then begins to vibrate in sync with the sound. When the malleus vibrates against the incus, it also begins to vibrate and transfers the vibration to the last ossicle, the stapes. The plate at the end

of the stapes lies on top of the oval window of the cochlea and the vibration of the plate creates pressure waves into the fluid-filled cavity of the cochlea in the inner ear. There is a tube connecting the tympanic cavity in the middle ear with the nasal cavity called the *eustachian tube*. This tube permits equalisation of air pressure. The eustachian tube is usually closed, but it can open to keep the pressure difference between the two cavities at minimum [257].

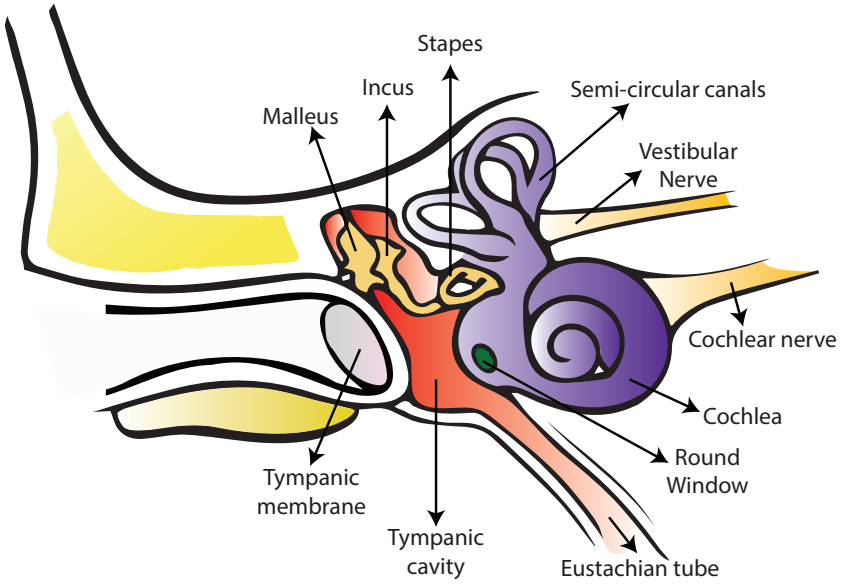

FIGURE 6.3: Diagram of the middle and inner ear showing parts for hearing and equilibrium.

6.1.3 The inner ear

The inner ear is a fluid-filled chamber with various passages and cavities. The inner ear can be divided into three regions; the semi-circular canals, the vestibule and cochlea (Figure 6.3). The semi-circular canals and the vestibule provide information regarding rotational and gravitational equilibrium. The cochlea is a fluid-filled coiled structure consisting of three canals called the vestibular canal, the cochlear canal, and the tympanic canal [254]. The cochlea is lined with about 18,000 microscopic hair cells, on top of which are hair-like structures called stereocilia, and it transforms fluid motion into electric energy. These electrical impulses are passed to the auditory cortex of the cerebral cortex, for interpretation.

6.1.4 Blood supply to ear

To monitor the blood oxygen saturations from the ear, it is important to understand how oxygenated blood is supplied to the ear and deoxygenated blood is drained from the ear.

As mentioned in Chapter 2, oxygenated blood from the left ventricle of the heart enters the aorta during systemic circulation. The aorta branches into many arteries, which carry blood to various body parts. The arch of aorta gives out two main arteries that supply blood to the head and the neck; the right and left common carotid arteries. The common carotid arteries branch in the neck to form the external and internal carotid arteries. The internal carotid arteries supply blood to the brain. The external carotid arteries supply blood to face, ears and other external parts of the head. The ear, in particular, gets a rich blood supply blood supply from two main branches of the external carotid artery, namely the posterior auricular artery and the superficial temporal artery (Figure 6.4) [261]. Additional supply to the deeper parts of the ear comes from branches of the maxillary and occipital arteries.

The auricular branches of the superficial temporal artery distribute blood to the lobule, anterior portion of the auricle, and to the external auditory canal. The posterior auricular artery supply blood to the posterior portion of the auricle [262]. The ear canal is partially provided by the same vessels as the auricle, but the deeper portion, including the external surface of the tympanic membrane, is supplied by the deep auricular artery, a branch of the internal maxillary artery [256]. Venous drainage is primarily through the posterior auricular vein. The superficial temporal vein and the maxillary vein also return blood from the middle and inner parts of the ear. All three veins drain blood into the external jugular vein, which returns blood to the heart via superior vena cava.

FIGURE 6.4: Branches of common carotid artery which supply blood to human ear [33].

6.2 Ear canal as a location for oxygen saturation monitoring

Blood oxygen monitoring using peripheral pulse oximetry is susceptible to inaccuracies in conditions of compromised peripheral perfusion and motion. Such a situation usually occurs in patients experiencing hypothermia caused due to decreased heat production (hypopituitarism, hypothyroidism), increased heat loss (vasodilation, erythrodermas, burns), impaired thermoregulation, drug administration (such as anaesthetic agents, clonidine, neuroleptics), and dehydration. Motion artefact from shivering and the lack of detectable peripheral pulse due to peripheral vasoconstriction causes the pulse oximeter to fail.

In order to address this issue, the ear canal has been proposed as a new monitoring site for measuring blood oxygen saturation. The rationale behind the proposal is that the ear canal being closer to the trunk will have a much-reduced influence from low perfusion states and, as a result, a better quality signal during critical conditions. For instance, in conditions of severe hypothermia or multiple organ failures due to cardiogenic shock, the circulatory system reacts by shutting down blood supply firstly to the periphery followed by kidneys and mesenteric vascular bed. This is so that blood can be shunted to essential organs such as the heart and the brain, at the expense of other non-essential organs. Since blood supply to the ear is by the same arteries which supply blood to the brain (Carotid arteries), it should be possible for oxygen saturation to be measured from the ear canal in such cases. Additionally, the ear canal offers many advantages over other peripheral and central sites, which are listed below.

FIGURE 6.5: Thermogram of the ear of an adult male showing variations in temperature. The temperature runs from red (warmest) through yellow, green, cyan and blue to mauve (coldest) [263].

Physiological advantages of the ear canal

- The walls of the ear canal and the tympanic region follow the body's core temperature with high fidelity as they share the blood supply with the "hypothalamus" - the body's thermostat, making it a uniquely desirable site for SpO_2 monitoring (Figure 6.5).
- The ear canal is an alternate monitoring site with easy access during surgery, resuscitation, in patients with finger deformities, or when digit access or other peripheral sites are not accessible. It also allows for hands-free monitoring.
- The ear canal as a location provides a factor of comfort and invisibility of the sensor, as it can be concealed by the ear and hair, thus widening the possibility of its use in day to day activities.
- The changes in beat-to-beat rhythm due to respiration are more pronounced in the ear canal than other sites such as finger due to the relatively short distance from the heart. This makes it possible for accurate determination of respiration rate extracted from the ear canal PPG signals.
- The influence of sympathetic and parasympathetic nerve activity on cerebral blood flow is reported to be peculiarly little even in conditions of haemorrhagic hypotension. Although this remains controversial, if true, it would enable uninterrupted monitoring of SpO_2 from the ear canal at all times.

Advantages of ear canal over other sensor locations

- This central site could offer fast desaturation response time and high sensitivity which is invaluable in patients at risk of hypoventilation and hypoxaemia. The routinely used finger clip pulse oximeter has the slowest response time of up to two minutes in healthy subjects.
- Compared to some of the other central sites discussed in Chapter 5, this sensor location is non-invasive and does not require any training or expertise to place the sensor.
- As with reflectance forehead sensor, the ear canal does not suffer from attachment problems, as the shape and structure of the ear canal provide a natural anchoring point for the sensor, thus avoiding the need for adhesives.
- As shown in Figure 6.5, the ear canal offers better perfusion than the ear lobe. i.e. improved signal quality in the ear canal than the ear lobe.

- The ear canal probe would not suffer from the effects of EMI (from the visible region), as the hollow, tube-shaped cylindrical structure of the ear canal prevents any excessive ambient light energy from saturating or flooding the photodiode.
- The commercial applications of the device are also numerous and are associated with patient monitoring during surgical procedures, diagnostic procedures, alternative care, etc. A unique niche market for the ear canal sensor is in patients suffering from Chronic Obstructive Pulmonary Disease (COPD) and sleep apnoea. The sensor can also be used for vital sign monitoring from emergency operators such as fire-fighters, military combatants, law enforcement officers or paramedics operating in harsh and hazardous environments.

Based on a similar hypothesis, a team of biomedical engineers from Philips Chair for Medical Information Technology (MedIT) and the CiS Research Institute for Micro Sensors and Photovoltaics GmbH (Erfurt, Germany) have previously developed a wearable in-ear measuring system (IN-MONIT) for 24/7 monitoring of vital parameters in cardiovascular patients [264]. The IN-MONIT sensor system consisted of a micro-optic reflection sensor (MORES® technology, CiS Research Institute for Micro Sensors and Photovoltaics GmbH) and a body box containing the signal processing unit. The MORES® sensor consists of two LEDs with peak emission wavelengths at 760 nm and 900 nm and a photodiode placed 2 mm away from the LEDs. This in-ear sensor was designed to acquire PPG signals from the back of the targus *(small pointed eminence of the ear canal- Figure 11.11)* [265].

Their initial investigation was focused on estimating heart rate from the red and infrared PPG signals acquired from the targus of the healthy volunteers [266]. The results demonstrated that accurate determination of heart rate is possible. The developed sensor was then calibrated using a hypoxic study in 10 healthy volunteers [267]. The accuracy level of the global calibration curve acquired from this study was, however, reported to be unacceptable for use in SpO_2 measurements. More recently, Venema *et al.* investigated the feasibility of measuring heart rate and SpO_2 in 29 adult patients undergoing various surgeries [268]. They compared their in-ear SpO_2 measurements with simultaneous SaO_2 measurements from a blood gas analyser, and SpO_2 measurements from two reflectance commercial pulse oximeters. The estimated SpO_2 values were reported to be inaccurate with standard deviation (STD) in most cases exceeding -3 $\pm$ 7 %, which is well beyond the requirements for medical pulse oximeters.

The red PPG signals acquired from the IN-MONIT system were also reported to be noisy. Venema *et al.* has attributed the low SNR of the red PPG signals to the small separation distance between the emitter and the photodiode (2 mm). The other possible source of error in their design could be from the use of red LED with peak emission at 760 nm. As the selected wavelength is close to the isobestic point, the difference in absorption between

the Hb and HbO_2 at this wavelength will be smaller (Figure 4.4). Hence, the absorption measured at this wavelength would not be proportional to the concentration of Hb, leading to inaccurate SpO_2 readings. So far, none of the studies by Venema *et al.* have presented any investigations into the morphology or the quality of PPG signals that can be acquired from the targus or from any other site from the ear.

To overcome the drawbacks of Venema's design, and the difficulties associated with attempts to measure SpO_2 in conditions of poor peripheral circulation, the investigation of PPG signals from the surfaces of the external auditory canal is suggested. This novel location - the ear canal - could offer better quality PPG signals than the targus, eventually allowing for reliable monitoring of SpO_2.

To validate the hypothesis that perfusion in the ear canal might be preferentially preserved, an earphone shaped ear canal probe has been developed and is described in detail in the next chapter. Along with the reflectance ear canal probe, an optically identical finger probe, instrumentation unit (Chapter 8) and the software required for data acquisition and storage (Chapter 9) was also implemented. The developed technology was then used to

- investigate the quality and morphology of PPG signals obtainable from different surfaces of the ear canal (i.e. top, bottom, left and right sides of the ear canal).
- investigate the suitability of the ear canal for monitoring PPG signals and arterial oxygen saturation in conditions of induced local hypothermia using a cold pressor test (healthy volunteer study, n= 15).
- investigate the differences in the quality of PPG signals, pulse amplitude and SpO_2 measured from the ear canal, finger, toe, and the earlobe sensors during induced hypothermia by whole body cold exposure (healthy volunteer study, n= 15).
- study the differences in the degree of sympathetic nerve activity over cerebral and peripheral blood circulations utilising low-frequency analysis.

6.3 Summary

The external auditory canal has been proposed as a new measurement site for PPG and SpO_2 monitoring in conditions of poor peripheral perfusion. The ear canal is a curved tube approximately 25 mm in length and 7 mm in diameter. It has a rich blood supply from the branches of the external carotid artery. The ear canal is a suitable choice for SpO_2 monitoring as it offers many physiological and technological advantages over other central sites. To validate this hypothesis, a miniaturised ear canal probe has been developed and is described in detail in the next chapter.

— The robustness of the PPG signal in this location is no great surprise given that the ear canal has long been recognised as an environment maintained at a stable temperature close to the core temperature of the body.

Steve Perring, IPEM SCOPE, 2014

7

Design and development of the reflectance ear canal PPG probe

To overcome the limitations of commercial pulse oximeters (Chapter 6), in cases of poor peripheral perfusion, it is proposed that the ear canal could be used as an alternative measurement site to monitor photoplethysmograph (PPG) signals and measure arterial oxygen saturation (SpO_2). For this purpose, two identical ear canal PPG probes with different dimensions were initially developed. These sensors were used to investigate the quality of PPG signals from different surfaces and depths of the ear canal. Based on the results of the preliminary investigation and feedback from a participant survey, the probe underwent evolutionary design optimisations. This chapter describes in-detail the various stages in the design and fabrication of the reflectance ear canal PPG probe.

The chapter also describes the design and development of two conventional PPG probes which are used to acquire PPGs from the finger or the toe. These sensors were developed to facilitate comparisons between the ear canal (central site) and the finger (peripheral site). All sensors were designed to be optically and electrically identical. All sensors were constructed to be reusable, to eliminate any sensor dependent variables that may influence the data during clinical investigations. To avoid any infections, all the probes were manufactured with medical grade materials, which can be sanitised with standard sanitization fluids/wipes. Finally, the performance evaluation tests carried out in the laboratory at all stages of the probes' design are described in this chapter.

7.1 Reflectance ear canal photoplethysmography (RECAP) probe I

Two identical ear canal PPG probes with different dimensions were initially developed for the measurement of photoplethysmograms from various depths and different surfaces across the circumference of the ear canal. The probes comprised of two surface mounted LEDs and a surface mounted photodetector. As transmission mode measurements are not possible from the tissue lining the ear canal, the ear canal probe was designed to operate in reflection mode. In this configuration, both the LEDs emitted light into the tissue lining of the ear canal and the photodetector detected the backscattered radiation and produced an output proportional to the detected radiation level. The detected signals were preconditioned and preprocessed by a PPG instrumentation unit. The probe was connected to the instrumentation unit using a multi-core cable, interfaced through a DE9 connector. The preprocessed signals from the instrumentation unit were digitised by a National Instruments data acquisition card *(NI PCIe-6321)* and were displayed and stored on a computer running LabVIEW *(National instruments corporation, Texas, USA)*. These stages are explained in detail in Chapters 8 and 9.

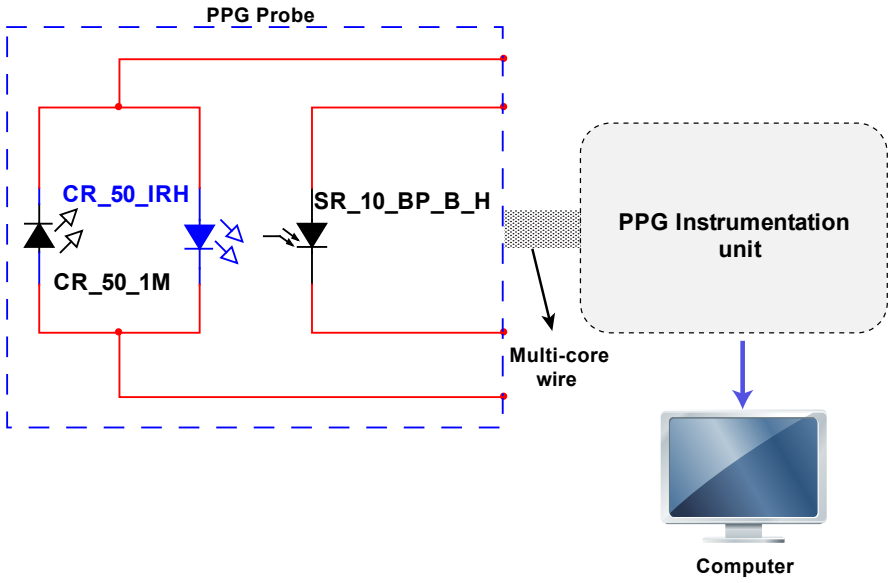

FIGURE 7.1: Block diagram of the ear canal PPG probe connected to the PPG processing system.

7.1.1 Choice of optical components

The red and infrared emitters used in the design of the probes are surface mount ceramic chip type LEDs, with peak emission wavelength at 658 nm and 870 nm respectively *(CR 50-1M and CR 50 IRH, Excelitas technologies, USA)*. The reason for the choice of these

wavelengths is that the absorption spectra of oxyhaemoglobin and deoxyhaemoglobin at these wavelengths is relatively flat and there is a large difference in the absorption characteristics. The physical dimensions of both the LEDs are 3.2 $mm \times 1.27\ mm \times 1.2\ mm$. The photodetector used is a flattop photodiode with an active area of 0.65 mm^2 and peak sensitivity at 900 nm *(SR 10 BP-BH, Excelitas technologies, USA)*. The physical dimensions of the photodiode are 3.2 $mm \times 1.6\ mm \times 1.2\ mm$. The optical, electrical and packaging specifications of the LEDs and the photodiode are shown in Table 7.1 and Table 7.2 respectively.

Note that the peak emission wavelength of the infrared LED (870 nm) differs from the wavelength commonly used in pulse oximetry (940 nm). This, however, is not an issue since the absorption spectra of oxyhaemoglobin and deoxyhaemoglobin in the region of 820 nm to 940 nm are relatively flat (see Figure 4.4).

TABLE 7.1: Optical, electrical and packaging specifications of the red and infrared emitters

Optical and electrical characteristics	**CR 50-1M**	**CR 50-IRH**
Peak emission wavelength (λ)	658 nm	870 nm
Radiation power or luminous intensity at 20 mA	50 mcd	4.5 mW
Power dissipation (PD)	130 mW	130 mW
Forward voltage (Vr) at 20 mA	1.8 V	1.35 V
Minimum reverse voltage	5 V	8 V
Reverse leakage current	100 μA	100 μA
Peak forward current at 10 μs	600 mA	800 mA
Light emitting angle	180°	160°
Size	1206 (imperial)	1206 (imperial)
Packaging details:	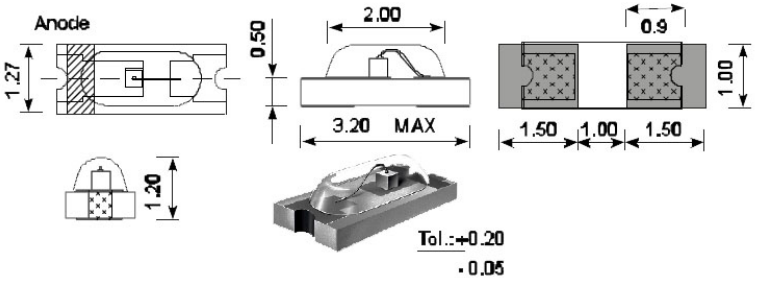	

TABLE 7.2: Optical, electrical and packaging specifications of the photodiode

Optical and electrical characteristics	**SR 10 BP-BH**
Peak wavelength sensitivity (λ_{max})	900 nm
Radiation sensitive area	0.65 mm^2
Junction capacitance	10 pF
Open circuit voltage	400 mV
Reverse breakdown voltage	170 V
Reverse dark current	10 nA
Size	1206 (imperial)
Packaging details:	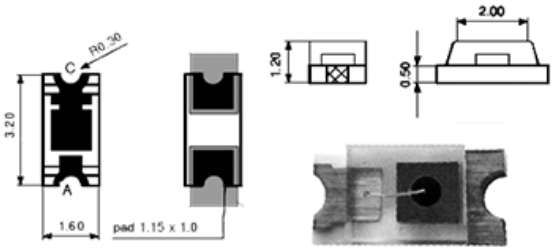

7.1.2 Geometry of the probe

The physical dimensions and the shape of the ear canal probes were determined by the anatomical characteristics of the auditory canal. In adults, the external auditory canal is approximately 25 mm in length and 8 mm in diameter. The opening of the ear canal is oval, averaging 9 mm in height and 7 mm in width [259]. The outer auditory canal is skin lined soft cartilage connected to a hard bony inner auditory canal. There is a slight angulation between the outer and inner parts (see Figure 6.2(b)). Therefore, the physical dimensions of the probe should be small enough to fit comfortably inside the external auditory canal, while being big enough to firmly hold itself against the walls of the ear canal. The length of the probe should also be slightly smaller than the outer auditory canal so that the angulation between the cartilaginous outer canal and bony inner canal can be avoided. Hence, the dimensions of the ear canal probe should ideally be between 10 mm - 15 mm in length and 6 mm - 8 mm in diameter.

7.1.3 Fabrication of RECAP probe I

With the optical components and the dimensions specified, it was decided that two round nosed cylindrical (bullet shaped) probes will initially be developed. The probes were intended to assess a suitable length and a surface across the circumference of the ear canal

at which good quality PPG signals can be acquired. The probes were designed to fit 10 mm and 15 mm inside the ear canal (measured from the targus as the reference point). These prototype probes were designed to be cylindrical so that they can be rotated in the ear canal to acquire PPG signals from various surfaces. Hence avoiding the need for the development of multiple PPG probes. The developed probes consisted of two main modules; a miniaturised optoelectronic sensor, and a specially designed sensor case. Note that both the probes are identical in design and only differ from each other in dimensions.

7.1.3.1 Miniaturised optoelectronic sensor

The miniaturised optical sensor is a small Printed Circuit Board (PCB) consisting of a red and an infrared LED and a photodiode. As with any reflectance probe, the emitters and the photodiode were placed next to each other and were separated by a center-to-center distance of 5 mm. The source-detector separation was chosen to be 5 mm, as experimental studies have shown that a separation of 4 to 5 mm provides the best sensitivity in terms of detecting adequately large pulsatile PPG signals [117]. The LEDs in both the probes were connected anti-parallel to each other as shown in Figure 7.1 and were switched on and off alternatively by a constant current produced from the PPG instrumentation unit. The dimensions of the optical sensors developed were 15 mm × 5.5 mm × 0.3 mm and 10 mm × 5 mm × 0.3 mm respectively. The 3D models and the mechanical drawings of one of the two optoelectronic sensors are shown in Figure 7.2.

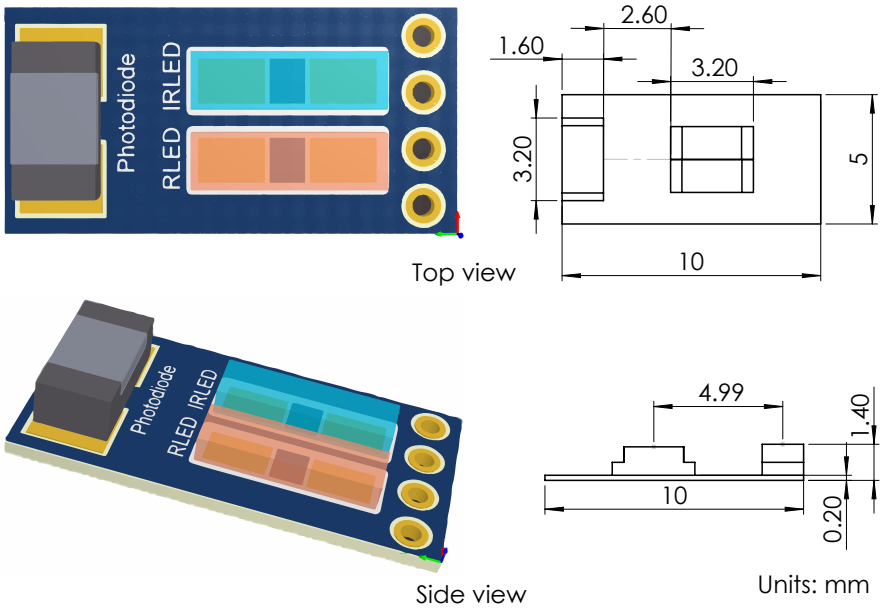

FIGURE 7.2: The 3D model and mechanical drawing of the optoelectronic reflectance sensor used in the smaller version (10 mm) of the RECAP probe I.

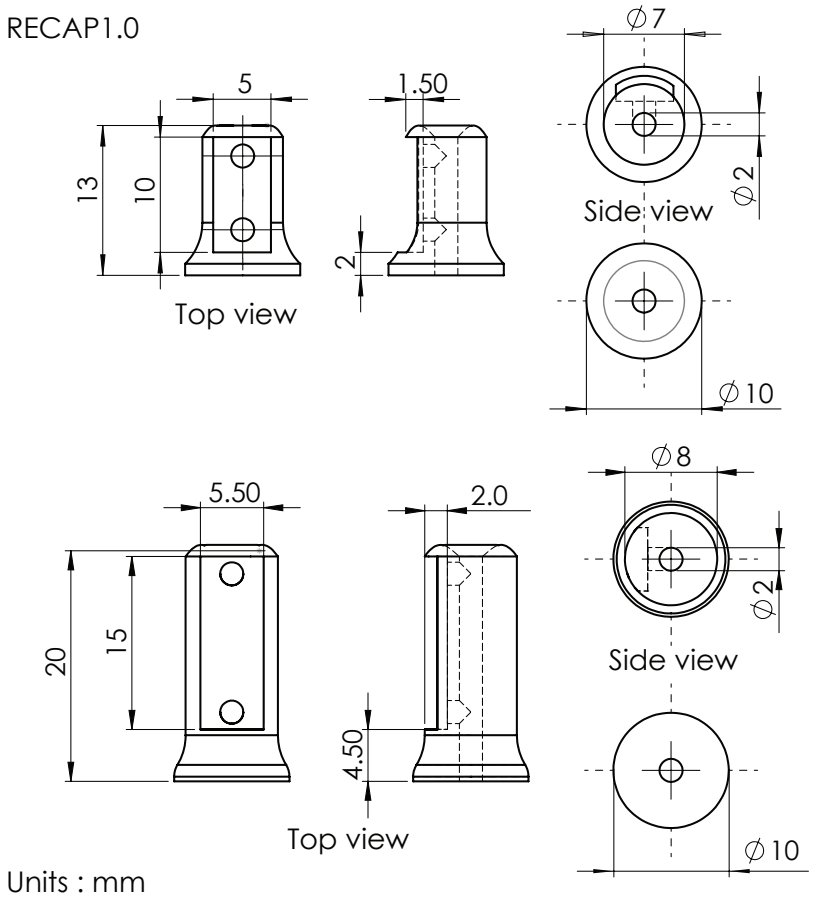

FIGURE 7.3: The mechanical drawings of the both the probe cases.

The sensors were first virtually designed using Altium designer *(Altium Limited, Sydney, Australia)*, an electronic design automation software package. Once the design was ready, the PCBs were manufactured by the process of photolithography. In this process, the completed designs were first printed on a LaserStar PCB printing paper using a laser printer to produce PCB artwork. The artwork was then aligned on top of a photo-resist coated copper-clad board and was exposed to UV light. Once sufficiently exposed, the copper boards were rinsed in photoresist developer and were then dipped in a bubble tank containing ferric chloride solution maintained at 40°C to etch the tracks. The sensors were then cut to the designed length and were tip plated using tin sulphate solution to stop the tracks from oxidation. The width of the etched copper tracks was 0.4 mm. All optical components were then soldered to the respective copper pads of the PCBs, using a reflow soldering oven maintained at low temperatures (180°C to 220°C).

7.1.3.2 Sensor case

The sensor case which holds the miniaturised optical sensor was designed to fit comfortably inside the ear canal. The cases were designed using Solid Works 2012 *(Dassault Systemes*

SolidWorks Corp., Velizy, France) and were manufactured using 3D printing technology. Solid Works is a 3D CAD draughting software which utilises a parametric feature-based approach to creating models and assemblies. As specified previously, both sensor cases were designed to be bullet shaped with varying dimensions. The mechanical drawings of the sensor cases are shown in Figure 7.3. The total length of the probes was 20 mm and 13 mm respectively while the diameter of the probes is 8 mm and 7 mm respectively. The sensor casing consisted of a small rectangular aperture to accommodate the optical sensor. The dimensions of the rectangular slots were the same as the optoelectronic sensor (i.e., 15 mm $\times$ 5.5 mm $\times$ 0.3 mm and 10 mm $\times$ 5 mm $\times$ 0.3 mm). The cases were designed to fit approximately 15 mm and 10 mm inside the ear canal.

Both the sensor cases were designed with a 2 mm hollow bore extending from one side of the probe to another and two small holes perpendicular to the bore. These apertures were used to run a four core ultra-flexible cable which provided electrical contact between the optical components and the PPG processing system. To stop the probe from being inserted too deep into the ear canal, the diameter of the probes distal end was increased by a few millimetres. The front end of the probe was designed to be dome-shaped to provide a smooth and comfortable feeling while placing the probe in the ear canal.

Once the 3D models were ready, the files required for 3D printing the models such as STereoLithography (STL) files and print path files (G–code) were generated. Using the generated files, the sensor cases were then 3D printed. The 3D printer used to manufacture the designed sensors was the Objet24 Desktop 3D Printer *(Stratasys Ltd., Minnesota, USA)*. The material used to 3D print the sensor cases was Polymerized Objet VeroWhitePlus–RGD835 *(Stratasys Ltd., Minnesota, USA)*. VeroWhitePlus–RGD835 is a rigid opaque white material used for rapid prototyping of highly accurate and complex medical device models. The sensor cases were printed with a Z resolution (layer thickness) of 30 μm.

Once both the optoelectronic sensors and the sensor cases were manufactured, a four core screened cable (external $\oslash$: 3.5 mm) was drawn through the mechanical casing of the ear canal sensor and was soldered onto the PCB using the vertical interconnecting access (vias) holes. Once the wires were soldered, the PCB was fixed firmly into the specially designed PCB slot in the sensor casing. The other end of the screened cable was soldered to a male DE9 connector, which provides communication between the probe and the PPG processing system. In order to avoid direct contact between the optical components and the skin lining the ear canal, the whole aperture holding the PCB was sealed using medical graded clear epoxy resin *(DYMAX 141-M, Dymax Corporation, Torrington, CT)*. The other end of the multicore cable was soldered to a male DE9 connector. Figure 7.4 displays 3D models and photographs of the RECAP I probe.

FIGURE 7.4: 3D models and photographs of one of the first prototype RECAP probes.

7.2 Preliminary evaluation of RECAP probes I

The following evaluation tests were carried out in the laboratory to validate the functionality of the prototype ear canal probes. The probes were tested with the help of the PPG processing system and the software described in Chapter 8 and 9.

7.2.1 Acquisition of PPG signals from different depths of the ear canal

Following Institutional Senate Research Ethics approval, a brief study was carried out in 7 healthy volunteers, with the following objectives

- to investigate the likelihood of measuring good quality PPG signals from the external auditory canal
- to determine an optimal length within the ear canal at which PPG signals with high amplitude can be recorded
- to check with the help of a participant survey the compatibility and factor of comfort the developed prototype probes offer, and to enquire about the possible modifications in the probe's shape and structure to make it more comfortable.

7.2.1.1 Method

During the study, each volunteer was made to sit comfortably in a chair, and the ear canal probes were placed inside the left and right ear canals of the volunteer. One of the probes was placed 15 mm into the ear canal (left) and the other probe was inserted 10 mm into the (right) ear canal (measured from the targus as a reference point). Prior to the study, both the probes were cleaned thoroughly using disinfectant alcohol wipes to avoid cross-contamination. Once the sensors were in place, the red and infrared PPG signals were acquired from the volunteer for approximately 3 min. The prototype PPG processing system comprised of two constant current sources, which drove the red and infrared LEDs alternatively at 40 mA. The output of the processing system was then digitised and acquired by the NI USB-6212 and a virtual instrument (VI) designed in LabVIEW.

As a next step in the study, all volunteers were asked to wear both the probes for an additional 15 min, at the end of which, they were asked to fill in a participant survey. In this survey the volunteer was asked to answer a few questions concerning the comfort level of the probes. They have been invited to rate the comfort level of the probes on a scale of 0 (unbearable) to 10 (very comfortable). Volunteers were also requested to give input on any aspects of the probe design which would make the probe more appealing for everyday use.

7.2.1.2 Results

The raw PPG signals recorded from both 10 mm and 15 mm inside the ear canals of the volunteers were extracted for analysis in MATLAB *(The MathWorks Inc., Massachusetts, USA)*. The AC components of the PPG signals were derived by filtering the raw PPG signals using an equiripple band-pass filter with cut-off frequencies at 0.5 Hz and 12 Hz respectively. The DC component was extracted using a low-pass filter with a cut-off frequency of 20 Hz.

The red and infrared AC PPG signals detected from the auditory canal of the volunteers were generally of good quality with large amplitudes and high signal to noise ratio. Figure 7.5 depicts the typical red and infrared AC PPG traces acquired from variable depths (10 mm and 15 mm) of the ear canal in a random volunteer. As expected, the variability in PPG signal amplitude due to respiration was pronounced in both the AC and DC PPG signals acquired from the ear canal. The DC PPG signals acquired from 10 and 15 mm inside the ear canal of a volunteer, during normal breathing are shown in Figure 7.6.

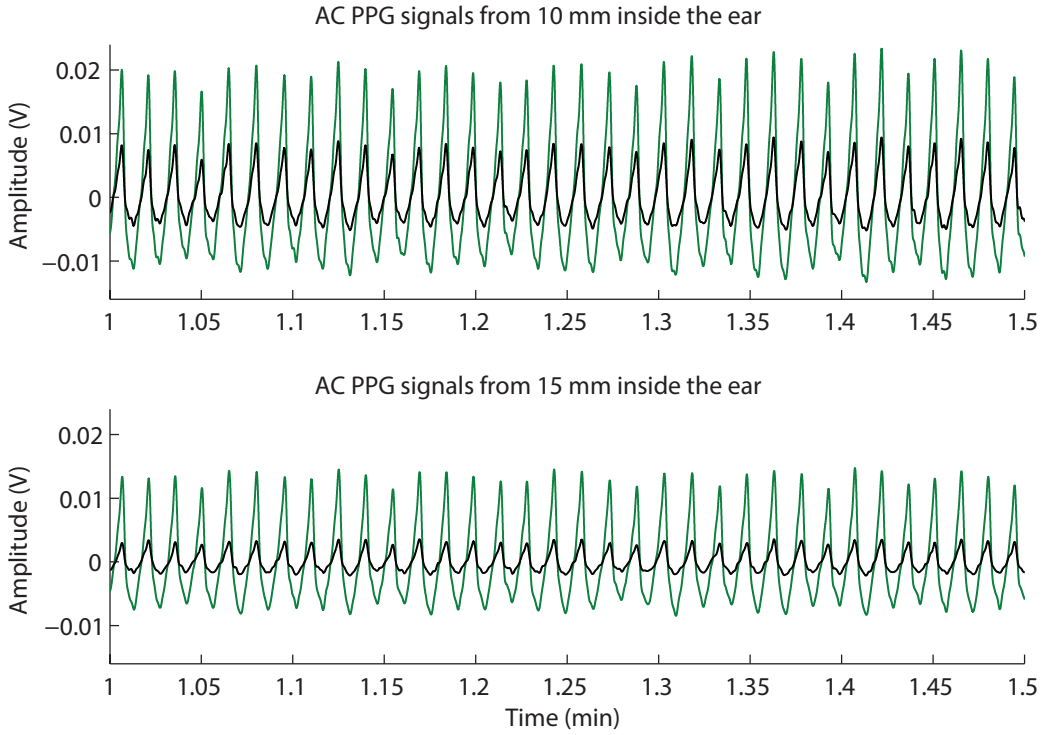

FIGURE 7.5: Typical red (black trace) and infrared (green trace) AC PPG traces acquired from variable depths (10 mm and 15 mm) of the ear canals in a random volunteer.

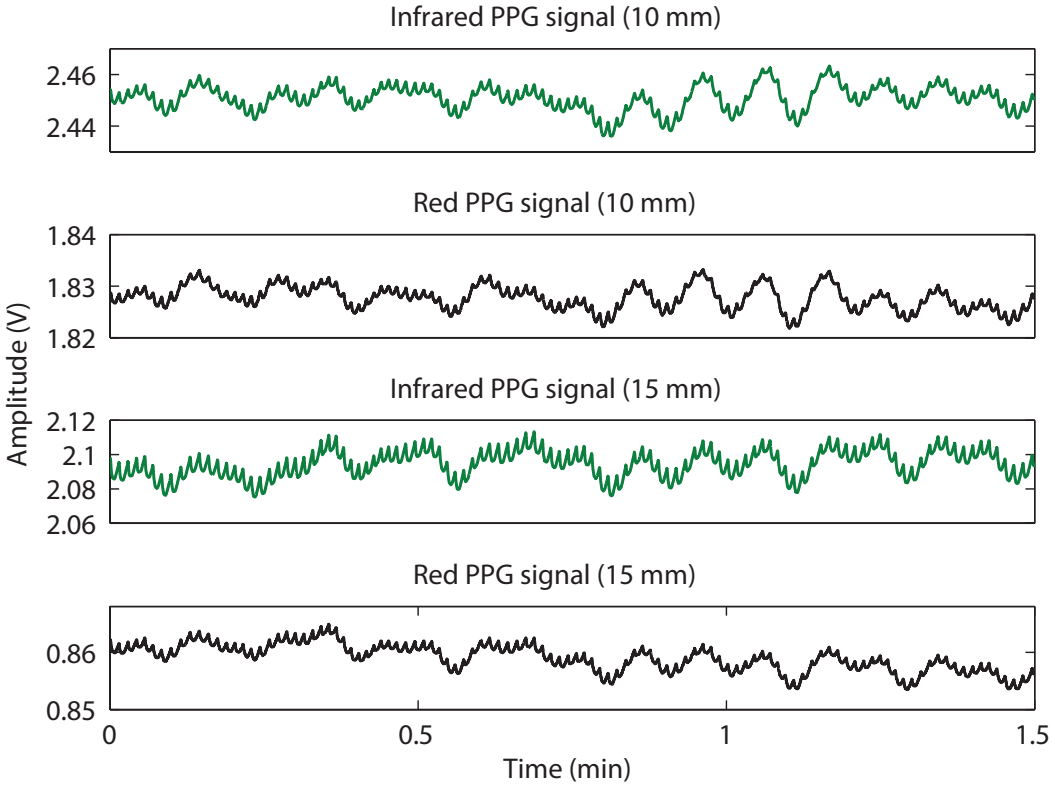

FIGURE 7.6: The DC PPG signals acquired from 10 and 15 mm inside the ear canal of a randomly selected volunteer.

Although PPG traces were detected at both depths inside the ear canal, there were clear differences in the amplitude of the PPG signals acquired in both locations. To quantitatively assess the differences between the amplitude of PPG signals obtained from the outer ear canal and the inner ear canal, the mean normalised pulse amplitude (NPA) of the red and infrared PPG signals was computed and compared. NPA, also known as normalised pulse volume (NPV), is usually expressed as ΔI_a/I, where ΔI_a is the intensity of pulsatile component superimposed on the transmitted light I (i.e., AC component of PPG signal divided by the DC component).

The NPA was measured instead of conventional pulse amplitude (PA) as NPA reflects ΔV_a (the pulsatile component of the arterial blood volume) in a more exact manner than PA. Also, the magnitude of both the pulsatile (AC) and the non-pulsatile (DC) components usually differs from one site to another, hence to draw a true comparison, all the signals were normalised.

Table 7.3 shows the mean NPA and the standard deviation (±SD) of red and infrared PPG signals acquired from the outer (10 mm) and inner (15 mm) ear canals of 7 healthy volunteers. The data is graphically displayed with the use of a bar plot in Figure 7.7. The red and infrared PPG signals acquired from the outer ear canal of the volunteers were smaller in amplitude when compared to those acquired from the inner ear canal. However, the red PPG signals recorded deeper inside the auditory canal (15 mm) were slightly noisy and sensitive to artefacts caused due to heavy breathing and jaw movements. This is expected as the Eustachian tube conducts respiratory and jaw movements to the middle ear and deeper regions of the outer ear.

To check for any statistical significance between the mean amplitude of PPG signals measured from the outer and the inner ear canal, a paired t-test was performed on the data.

TABLE 7.3: Shows the mean NPA of red and infrared PPG signals acquired from the outer and inner ear canals of 7 healthy volunteers

Volunteer	Outer ear canal		Inner ear canal	
	IRED NPA ± SD ($10^{-}3$)	RED NPA ± SD ($10^{-}3$)	IRED NPA ± SD ($10^{-}3$)	RED NPA ± SD ($10^{-}3$)
1	41.8 ± 12.7	21.2 ± 6.3	31 ± 9.3	15.2 ± 4.6
2	20.5 ± 6.5	6.7 ± 2	40.7 ± 12.4	10.1 ± 2.8
3	18.9 ± 5.8	6.6 ± 2	15.3 ± 4.6	7.1 ± 2
4	11.9 ± 3.6	5.3 ± 1.6	21.5 ± 6.5	6.9 ± 2
5	18.7 ± 6	10.5 ± 3.3	47.2 ± 15.1	20.9 ± 6.6
6	18.2 ± 5.8	10.2 ± 3.2	45.3 ± 14.4	18.8 ± 5.8
7	29.9 ± 9.4	10.5 ± 3.3	42.6 ± 13.6	16 ± 4.7

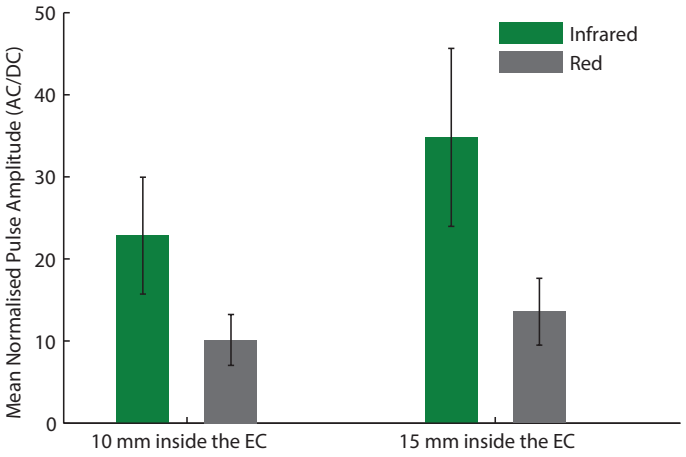

FIGURE 7.7: Mean of the means (n=7), ±SD of normalised infrared and red PPG signals acquired from 10 mm and 15 mm deeper inside the ear canal.

The normality was tested using the KolmogorovSmirnov test. All statistical tests were carried out using SigmaPlot-12.0 *(Systat software Inc., Chicago, USA)*. It was found that all the data were normally distributed, and there was no statistical significance (infrared: P= 0.07, red: P= 0.26) between the amplitude of PPG signals acquired from the outer and the inner ear canals. From these observations, it is safe to say that the outer ear canal is possibly the best location for PPG signal monitoring, especially since the PPG signals acquired in this area are not noisy and free from respiratory artefacts. However before making any decision on the sensor location, the participant survey was also considered. In this survey the participants were asked to answer seven questions in the survey, which were designed to aid the further development and optimisation of the technology.

Table 7.4 shows the participants' responses and comments to the questions asked in the participation survey. Some of the participants in the study have expressed discomfort with the larger size of the ear canal sensor (15 mm) placed in the left ear canal. Most volunteers were comfortable wearing the slightly smaller version of the prototype (10 mm) even for long periods of time. Some of the volunteers have, however, reported that both the sensors were slightly tight inside the ear. A couple of the volunteers have also reported that the probes were slightly warm when worn for more than 15 min. Overall, none of the volunteers found the probes to be completely uncomfortable. Based on these comments and responses from the survey, and the results obtained from the preliminary investigation, it is evident that the outer auditory canal would be the optimal site for monitoring PPG signals and arterial oxygen saturation.

TABLE 7.4: Summarises the responses of the volunteers to the participation survey

Questions	**Volunteers**						
	1	2	3	4	5	6	7
On a scale of 1-10, how comfortable is the probe in your left ear	8	6	7	7.5	7	6	5.5
On a scale of 1-10, how comfortable is the probe in your right ear	9.5	8	9	10	10	9	9
How does the probe feel when worn in the ear? Please number all that apply (1.Tickling, 2. Tight 3. Prickle 4. Warm)	1	✗	4	✗	✗	2, 4	2
Was it uncomfortable to wear the probe for any of the previously stated reasons? (Yes/No)	No	No	No	No	No	No	No
Would you wear the device on a routine basis? (Yes/ Maybe/ No/ Dont know)	Yes	Maybe	Maybe	Yes	Yes	Maybe	No
How long would you be willing to wear the probe over a 12 h interval? (> 1 h, > 3 h, > 6 h, > 8 h, < 8 h)	> 3 h	> 6 h	> 3 h	> 3 h	> 6 h	> 3 h	> 3 h
Please provide any specific comment regarding the probe	Comment–1: Can the probe be designed to look like a discreet hearing aid. That might increase the sensor's acceptability						

✗ – No answer

7.2.2 PPG signal acquisition from various surfaces of the ear canal

Similar to the earlier experiment, a short study was conducted in 7 healthy volunteers (following Institutional Senate Research Ethics approval) to determine the surface (anterior, ventral, posterior and dorsal) along the circumference of the ear canal from which the acquired PPGs will be of the best possible quality (Figure 7.8). It is essential that the PPG signals acquired from the ear canal are of good quality with large amplitudes, since the quality of the signals acquired has a direct impact on the SpO_2 estimated. Different surfaces across the circumference of the outer ear canal (10 mm inside the ear canal) were explored during this experiment. Investigations were focused only on the outer region since the earlier study has shown the outer ear canal to be the optimal site for monitoring PPGs.

7.2.2.1 Methods

Four different surfaces across the circumference of the outer ear canal were investigated during this study. The experiments were carried out in the research laboratory under room temperatures between $22 \pm 2°C$. During the experiment, each volunteer was first made to

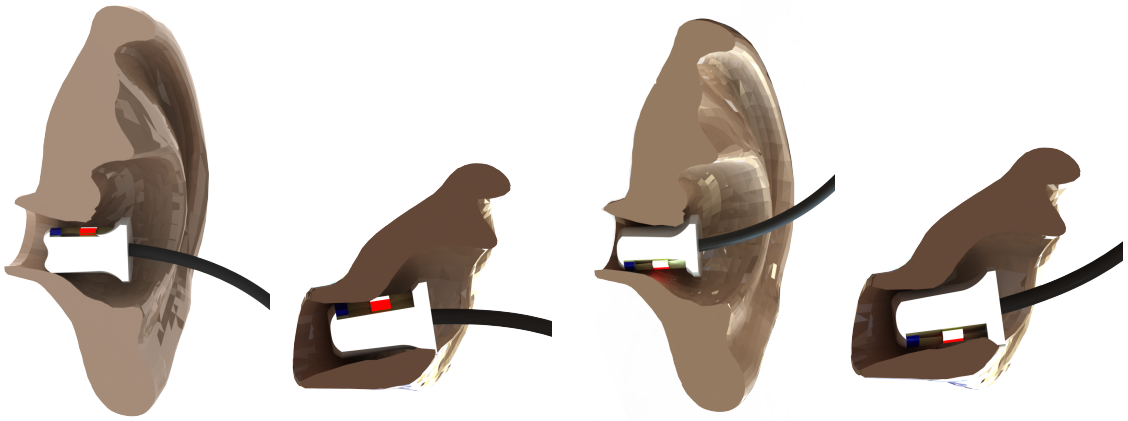

(a) Anterior (b) Ventral (c) Posterior (d) Dorsal

FIGURE 7.8: 3D models showing the frontal (a and c) and transverse views (b and d) of the RECAP probe inside the ear canal. PPG signals were recorded from (a) anterior, (b) ventral, (c) posterior and (d) dorsal surfaces of the ear canal.

sit comfortably on a chair, after which the ear canal probe was inserted 10 mm inside the right ear canal. To provide a reference measurement to the PPG signals being acquired from the ear canal, data was also acquired from a commercial finger pulse oximeter probe connected to the processing system. The probe used was an LNCS DCI-Masimo reusable finger probe *(Masimo corp., CA, USA)*. The raw PPG signals from both the ear canal and the finger were stored on a desktop computer for offline analysis.

Once the setup was ready, PPG signals were recorded from the ear canal for a duration of 2 min with the optical components in the probe facing the top (anterior) surface of the ear canal. At the end of the 2 min recording, the probe was rotated by 90° - clockwise inside the ear canal, and the recording was continued for another 2 min. The same procedure was repeated another couple of times. This was to acquire PPG signals from all four surfaces (anterior, ventral, posterior and dorsal) of the ear canal as shown in Figure 7.8. During this process, PPG signals were continuously acquired from the finger clip sensor attached to the right index finger.

7.2.2.2 Results

The raw PPG signals acquired from the ear canal and the finger were analysed in Matlab. The AC and the DC components of the red and infrared PPG signals were extracted by filtering the raw PPG signals using band-pass (f_c = 0.4 Hz *and* 12 Hz) and low-pass filters (f_C = 20 Hz). Figure 7.9 shows the AC PPG signals acquired from the posterior surface of the ear canal and the simultaneously acquired finger PPGs for 10 sec. The first observation that can be made from Figure 7.9 is the differences in the morphology of PPG signals acquired from the ear canal and the finger. The dicrotic notch is clearly visible in

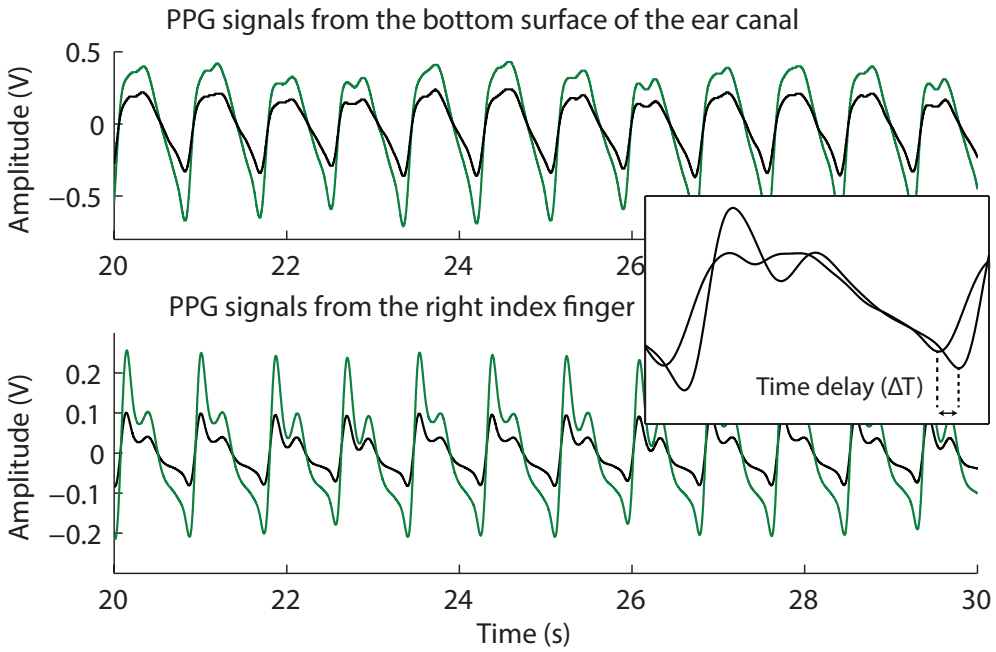

FIGURE 7.9: The AC red (black trace) and infrared (green trace) PPG signals acquired from the posterior surface of the ear canal and simultaneously acquired finger PPGs for a period of 10 sec.

the diastolic phase of the finger PPG signals, whereas in the ear canal PPGs, it seems to be almost merged with the systolic peak of the PPG signal. Secondly, there is an expected time delay between the ear canal and the finger PPG signals. These changes in the morphology of the PPG signals are thought to be due to variations in vascular compliance and peripheral resistance of various arteries. An in-detailed investigation looking at these changes is presented in Chapter 10.

The mean NPA (AC/DC) of red and infrared PPG signals (acquired from all four surfaces of the ear canal) was measured, to quantitatively determine a surface from which PPGs with high amplitude and quality can be acquired. Figure 7.10 shows the red and infrared PPG signals acquired from all four surfaces of the ear canal in a randomly selected volunteer. As can be seen from Figure 7.10, the PPG signals acquired from all locations were of good quality and were more than adequate for SpO_2 measurements. However, the amplitude of the PPG signals acquired across all four locations differed.

Table 7.5 summarises the mean NPA (± SD) of red and infrared PPG signals acquired from all four surfaces of the ear canal in 7 healthy volunteers. Figure 7.11 presents the mean PPG amplitudes from all 7 volunteers along with the mean of the mean NPA of the red and infrared AC PPG signals measured at the index finger. From the graph, it can be observed that the mean NPA measured from the ear canal varied across all four locations while the mean NPA of the simultaneously acquired PPG signals from the index finger stayed relatively constant. This suggests that the changes noticed in the NPA of PPG

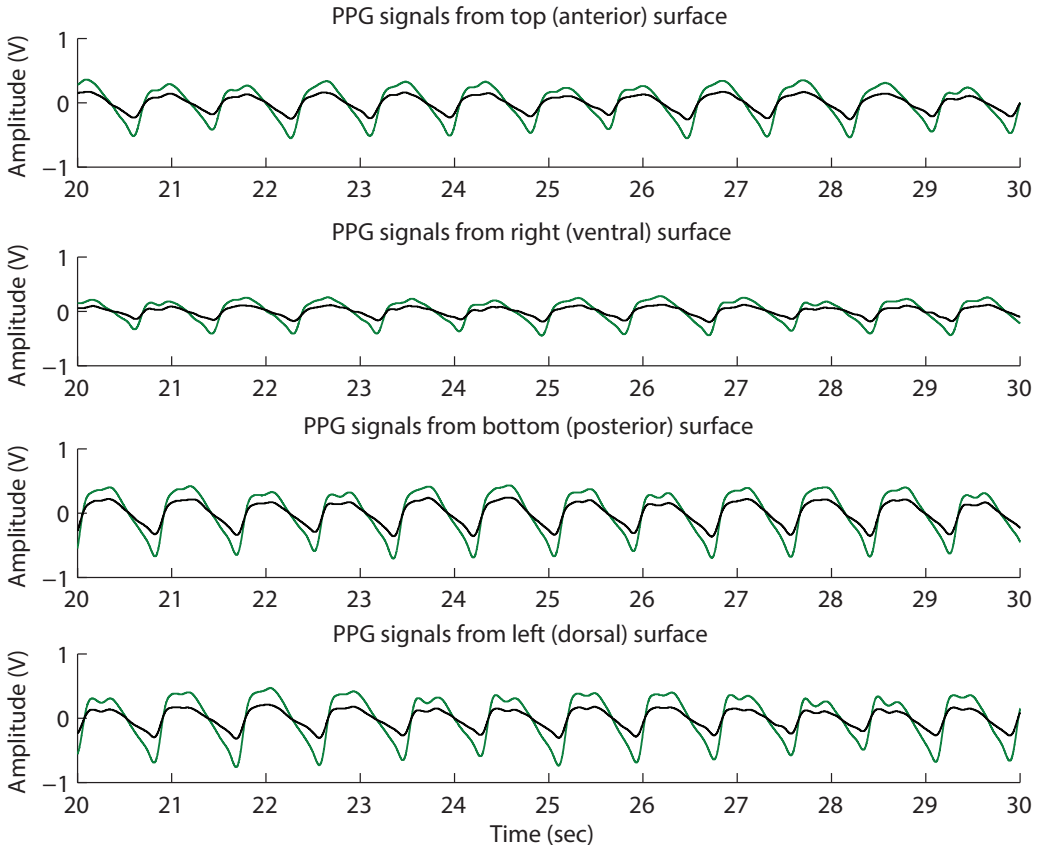

FIGURE 7.10: The red (black trace) and infrared (green trace) PPG signals acquired from anterior, ventral, posterior and dorsal surfaces of the ear canal.

TABLE 7.5: The mean NPA ($\pm$ *SD*) of red (R) and infrared (IR) PPG signals acquired from anterior, ventral, posterior and dorsal surfaces of the ear canal.

Surface	PPG signals	Volunteers						
		1	2	3	4	5	6	7
Anterior (Top)	IR $\pm$ SD (mV)	21 $\pm$ 6	39 $\pm$ 12	5 $\pm$ 2	10 $\pm$ 3	10 $\pm$ 3	18 $\pm$ 6	8 $\pm$ 3
	R $\pm$ SD (mV)	9 $\pm$ 3	19 $\pm$ 6	2 $\pm$ 1	4 $\pm$ 1	4 $\pm$ 1	9 $\pm$ 3	2 $\pm$ 1
Ventral (Right)	IR $\pm$ SD (mV)	41 $\pm$ 13	29 $\pm$ 9	8 $\pm$ 2	5 $\pm$ 2	12 $\pm$ 4	26 $\pm$ 8	27 $\pm$ 9
	R $\pm$ SD (mV)	21 $\pm$ 7	11 $\pm$ 3	3 $\pm$ 1	3 $\pm$ 1	3 $\pm$ 1	13 $\pm$ 4	14 $\pm$ 5
Posterior (Bottom)	IR $\pm$ SD (mV)	28 $\pm$ 9	49 $\pm$ 16	19 $\pm$ 6	35 $\pm$ 11	40 $\pm$ 4	30 $\pm$ 10	50 $\pm$ 16
	R $\pm$ SD (mV)	9 $\pm$ 3	24 $\pm$ 8	7 $\pm$ 2	16 $\pm$ 5	17 $\pm$ 1	13 $\pm$ 4	12 $\pm$ 3
Dorsal (Left)	IR $\pm$ SD (mV)	32 $\pm$ 10	49 $\pm$ 16	24 $\pm$ 8	34 $\pm$ 11	12 $\pm$ 13	37 $\pm$ 12	29 $\pm$ 9
	R $\pm$ SD (mV)	11 $\pm$ 3	23 $\pm$ 7	10 $\pm$ 3	17 $\pm$ 5	5 $\pm$ 5	15 $\pm$ 5	5 $\pm$ 2

signals acquired from different surfaces of the ear canal are purely due to the difference in tissue vasculature of the respective surfaces, rather than from any external changes such as temperature, etc. From Figure 7.11, the amplitude of PPG signals acquired from the finger are almost ten times the size of the ear canal PPGs. This was however expected,

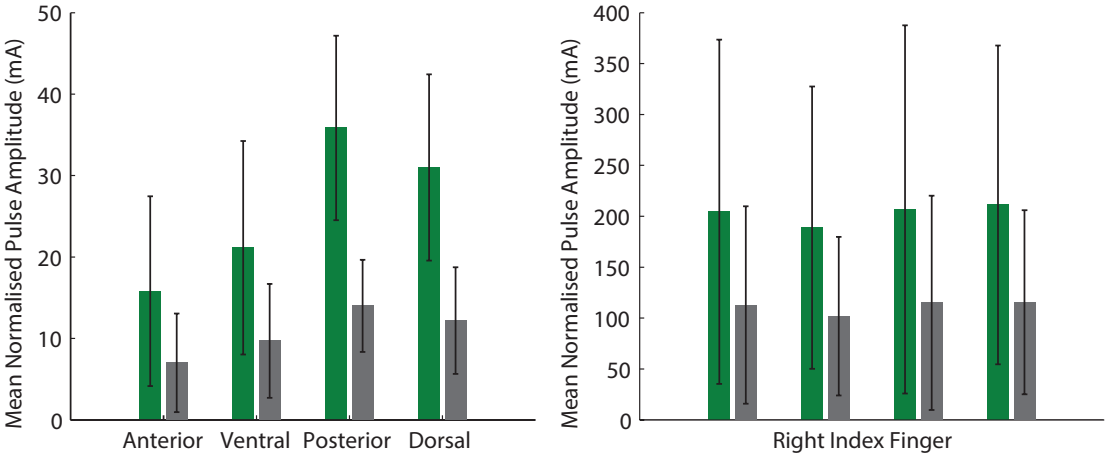

FIGURE 7.11: Mean of the means (n=7), ±SD of normalised infrared and red PPG signals acquired from all four surfaces of the ear canal and the index finger.

since there is less tissue lining the ear canal (approx: 1-2 mm) than the finger (approx: 10-15 mm), and, therefore, lower light absorption in the ear canal than the finger.

To check for any statistical significance among the amplitudes of the PPG signals acquired from anterior, ventral, posterior and dorsal surfaces of the ear canal, a paired t-test was performed on the data. Before performing a paired t-test, the normality of the data was tested using the Kolmogorov–Smirnov test. All the data were normally distributed. A significant difference was found between the amplitude of PPG signals acquired from the anterior and posterior surfaces of the ear canal (P value: Red – 0.008, Infrared – 0.006). No significant differences were found when other surfaces were compared. From these observations, it can be said that the posterior (bottom) surface of the ear canal will be the best surface for monitoring good quality PPG signals and, therefore, SpO_2.

7.2.3 Summary of the preliminary investigations

The prototype probes developed to monitor PPG signals from the ear canal performed very well during the preliminary investigations. It is evident from the results that the posterior surface of the outer ear canal is the most optimal site for monitoring good quality PPG signals. However, the preliminary tests and the participant survey have also highlighted a few constraints in the probes design, which are discussed as follows:

- As mentioned earlier, most volunteers have reported one of the probes (L:13 mm, ⊘:7 mm) to be more comfortable than the other. However, some of the volunteers have expressed a tight feeling inside the ear with both the probes. Hence careful considerations were taken in refining the probes dimensions.
- Although the operating current used to drive the LEDs was relatively low (40 mA), a couple of the volunteers have reported the sensor to be slightly warm inside the

ear canal. Hence, there is a need to test the probability of direct thermal damage to the skin lining the ear canal.

- Although the cylindrical shape of the sensor offers universal fit (i.e., would fit in both left and right ear canals in most of the population), the probe needs to be redesigned to make it more appealing for the user, as suggested by one of the volunteers in Table 7.4 (comment-1).
- The material used to manufacture is very rigid and is non-biocompatible. Hence, new biocompatible materials need to be explored.

The further development of the probe was therefore focused on eliminating these elements.

7.3 RECAP probe II

Building upon the previously developed prototype, a new ear canal PPG probe was designed and fabricated. The probe underwent evolutionary design modifications to overcome the above-mentioned limitations. The 2nd prototype probe was designed to look like an earphone and was made from a more flexible material.

7.3.1 Optical components and their characteristics

The red and infrared emitters and the photodiode used in the 2nd prototype are the same as the ones used in the 1st prototype. The optical and electrical characteristics and packaging details of these components are shown in Table 7.1 and 7.2. However, before using these components in the next prototype, it was important to determine the amount of thermal radiation emitted by the LEDs, especially since a couple of the volunteers have reported that the sensor felt slightly warm after long periods of usage. Thermal safety tests at various drive currents are usually carried out to test the effect of thermal stress on surrounding tissue. *In vitro* and *in vivo* thermal safety tests using these optical components were previously carried out by Kyriacou *et al.* in [108]. During the *in vitro* and *in vivo* tests, they found the temperature of their probe to raise by 3°C and 0.7°C respectively. To reiterate these results and to test the thermal emission of the RECAP probe, an *in vitro* investigation was carried out.

The investigation was carried out in a room maintained at 25 ± 0.5°C. Measurements were made of the changes in temperature at the surface of the RECAP–I PPG probe and of the changes in room temperature using two type–K (chromel–alumel) thermocouples *(Omega Engineering Limited, Manchester, UK)*. The first thermocouple was attached to the outer surface of the RECAP probe directly on top of the LEDs with kepton tape. The second

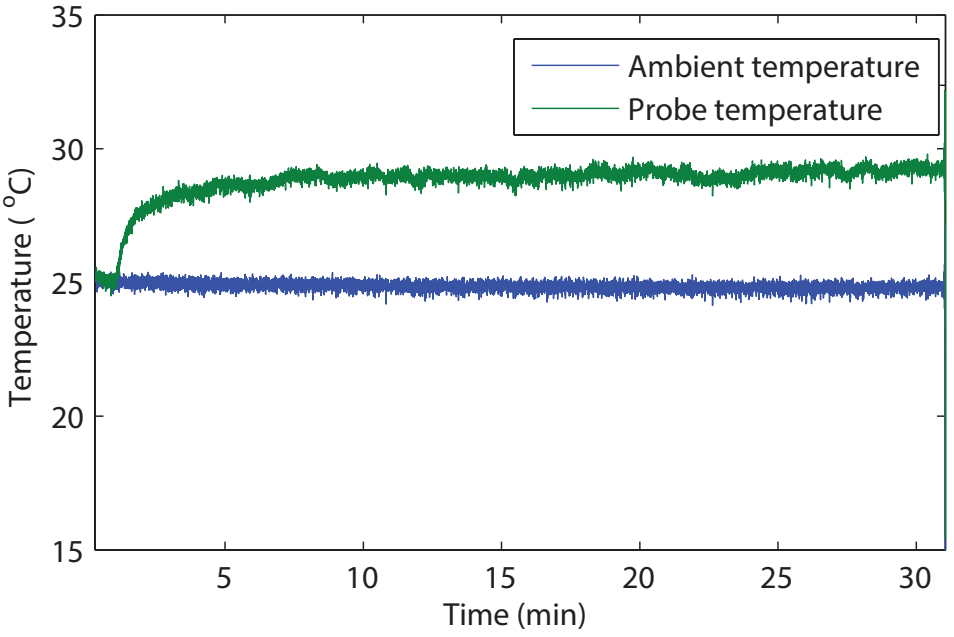

FIGURE 7.12: Measurement of the changes in thermal emission by the LEDs in the RECAP probe and the simultaneously recorded ambient temperature.

thermocouple was attached to the measurement unit and was exposed to the surrounding air. Two thermocouple amplifiers (AD595CQ, Analog Devices, MA, USA) were used to produce linear voltage outputs with sensitivity of 10 mV/°C. The AD595CQ is a complete instrumentation amplifier and thermocouple cold junction compensator on a monolithic chip. The output of the thermocouple amplifiers was recorded into a text file using NI USB-6212 DAQ card and a virtual instrument (VI) designed in LabVIEW (Chapter 9). The measurements started with a one minute off-time (LEDs off) recording followed by a 30 minute on-time recording. Both the LEDs were driven at 20 mA of current during the on-time recording. Figure 7.12 shows the changes in the temperature of the RECAP–I probe and the simultaneously acquired measure of room temperature.

As it can be seen from Figure 7.12, the temperature of the probe has raised with time in the first 5 minutes of the study and has then remained relatively constant. While the ambient temperature has remained constant throughout the study. This shows that the rise in temperature of the probe is purely due to the thermal emission of the LEDs. The maximum rise in temperature of the probe during the study was 3.2°C. The maximum temperature of the probe was 28.7°C. Based on these results, it is safe to assume that there is a negligible risk of tissue damage from thermal heating, as the temperature of the skin surrounding the ear canal (34 and 35°C) is much greater than the maximum probe temperature. The warm feeling reported by the volunteers could be associated with the insulation factor provided by the probes. Also, none of the volunteers has reported the temperature change to be uncomfortable. Therefore, same optical components were used.

7.3.2 Fabrication of RECAP probe II

A new dual-wavelength reflectance PPG sensor was designed and fabricated to acquire PPG signals from the bottom surface of the outer ear canal. Similar to the earlier design, the probe consisted of a miniaturised optoelectronic sensor and a sensor casing.

7.3.2.1 Miniaturised optoelectronic sensor

The optoelectronic sensor itself was a small PCB consisting of a red and an infrared LED and a photodetector. The emitters and the detector were placed 4 mm apart from each other. The separation distance between the optical components was reduced by a millimetre when compared to the previous design. It is hoped that the change in separation distance will not have an impact on the quality of the PPG signals or the estimated SpO_2 since previous studies have shown that a separation between 4 mm and 5 mm results in PPG signals with similar SNR [117]. The dimensions of the PCB were also reduced to 9 mm × 5 mm × 0.2 mm. The mechanical drawings of the optoelectronic sensor are shown in Figure 7.13.

Similar to the optoelectronic sensor described in Section 7.1.3.1, the PCB was first virtually designed using Altium designer *(Altium Limited, Sydney, Australia)*, and was then manufactured by the process of photolithography. The width of the copper track used

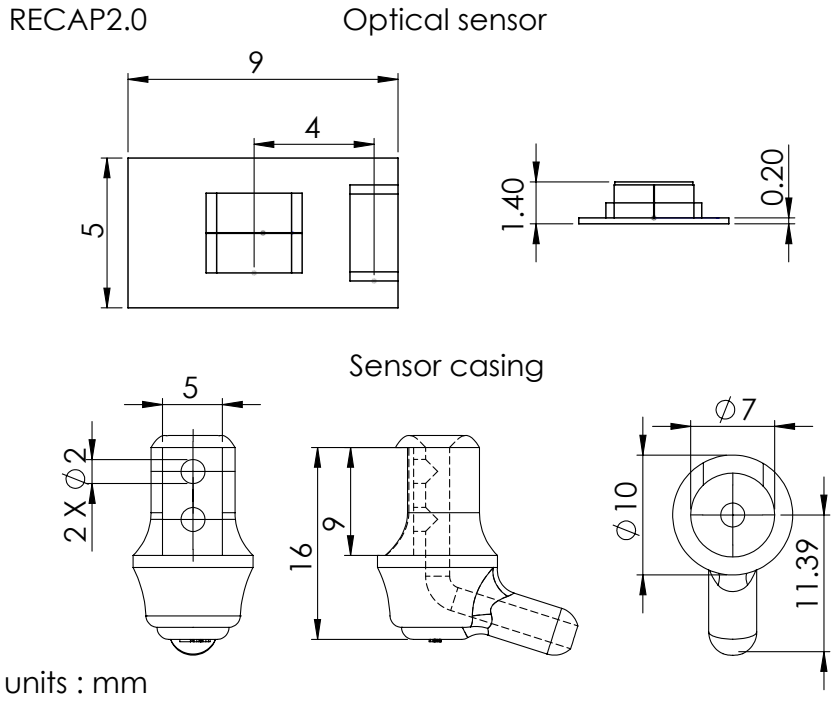

FIGURE 7.13: The mechanical drawings of the optoelectronic sensor and the earphone shaped sensor casing.

in this design was 0.4 mm. All optical components were then soldered to the respective copper pads of the PCBs, using a reflow soldering oven maintained at 200°C.

7.3.2.2 Sensor case

The sensor case which holds the optoelectronic sensor was designed to look like an earphone. The sensor was designed to fit approximately 9 mm inside the ear canal. The external diameter of the part of the casing which is inserted into the auditory canal is 7 mm. The mechanical drawings of the sensor casing are shown in Figure 7.13. The sensor case consists of a small rectangular extruded cut in which the micro-optic sensor is sealed. The dimensions of the rectangular slot are the same as the optoelectronic sensor. The casing also contains an inverted 'L' shaped hollow cavity extending from one side of the probe to the other and two small holes perpendicular to the cavity with a diameter of 2 mm. These apertures are used to run a four core cable, which provides electrical contact between the optical components and the PPG processing system. The cable used in this design was a four core ultra flexible cable with an external diameter of 2.1 mm. A lightweight miniaturised cable was used as opposed to the previously used four core screened wire (⌀ 3.5 mm), this is to avoid the added weight of the wire from dragging the

FIGURE 7.14: 3D models and photographs of the RECAP probe II.

sensor out from the ear canal. The diameter of the sensor at the distal end was increased by 3 mm to prevent the probe from accidently being inserted too deep into the ear canal.

The case was designed using Solid Works 2012 *(Dassault Systemes SolidWorks Corp., Velizy, France)*, and was 3D printed using the FORMIGA P-110 SLS 3D printer *(EOS - Electro-Optical Systems, Munich, Germany)*. The material used to manufacture the case is different from the one used in the previous design, this is to make the probe biocompatible. The material used was Feinpolyamid PA-2200 (Nylon) *(EOS - Electro-Optical Systems, Munich, Germany)*. The PA-2200 is a strong, flexible and biocompatible material *(EN ISO 10993-1 & USP/level VI/121° C)*. Figure 7.14 shows the 3D models and the photographs of the RECAP probe prototype 2.

7.3.3 Functionality test of RECAP probe II and further development

The functionality of the 2nd prototype was tested in the laboratory. The RECAP probe was connected to the PPG processing system, and PPG signals were acquired from 3 healthy volunteers. All three volunteers have reported the probe to be very comfortable inside the ear canal. The PPG signals acquired from the ear canal of the volunteers were again of good quality and high amplitude. Figure 7.15 shows the typical red and infrared PPG traces acquired from one of the volunteers using the 2nd prototype probe. The peak-to-peak amplitude of a typical IR AC PPG signal was approximately between 200 mV - 400 mV.

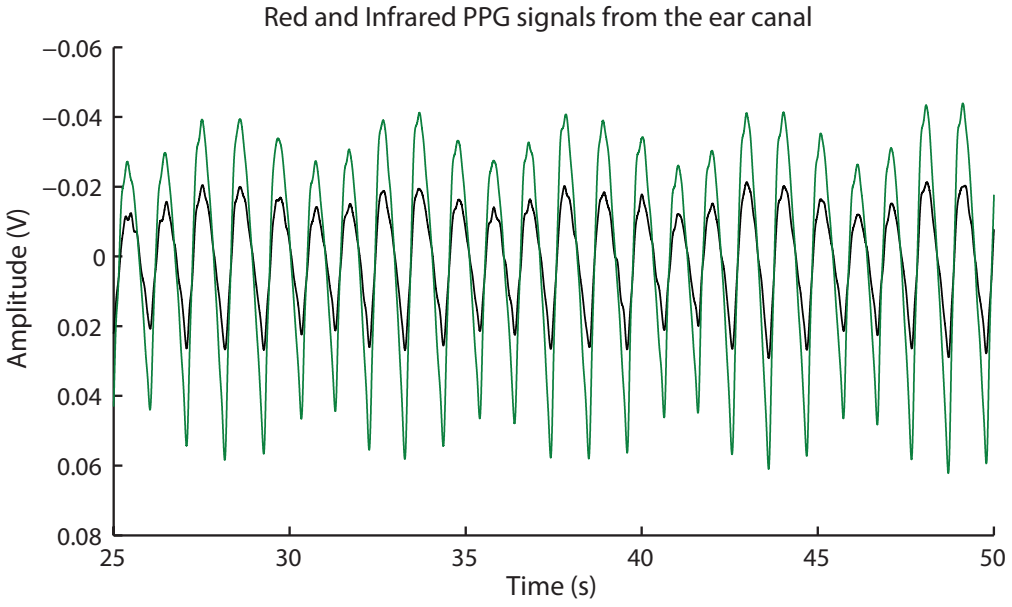

FIGURE 7.15: The AC red (black trace) and infrared (green trace) PPG signals acquired from the ear canal using the RECAP probe II.

Although the sensor performed very well at rest, during motion the probe was susceptible to motion artefacts. The smaller dimensions of the 2nd prototype also meant that the probe was loosely fitted in the ear canal for someone with large ears. This caused the probe to fall out of the ear, whenever there was heavy motion.

To avoid this limitation, the probe needs to be fixed to the ear in a more effective and comfortable manner. Hence, it was first decided that an earhook (that can anchor on top of the helix) will be incorporated into prototype probe as shown in Figure 7.16. However, this will restrict the probes' usage to either left or the right ear, and might not fit all ear sizes. Hence, it was decided that replaceable ear hooks (commonly used in blue-tooth headsets) will be used to anchor the probe to the ear. This will enable the probe to be used either in the left or the right ear. The hook can also be interchanged to fit all ear sizes. Hence, ear hooks of three different sizes were used. For added support and comfort it was decided that replaceable silicon ear fins will also be used. The silicone ear fins fit inside the concha of the ear and hold the probe in place during motion. The ear fins used were the DelTex StayHear ear buds *(DelTex®, UK)*, which are available in three different sizes. To accommodate both the earhook and the silicon ear fin, the earphone shaped probe was further modified as shown in Figure 7.16.

FIGURE 7.16: A flowchart of 3D models and photographs illustrating the incremental design and development of the RECAP PPG probe.

7.4 Reflectance finger PPG probes

Two reflectance finger PPG probes, optically and electrically identical to the RECAP probe, were also designed and manufactured. The probes were designed to acquire PPG signals from the finger or the toe. The probes were intended to facilitate comparison between the PPG signals acquired from the ear canal with that acquired from the periphery. By comparing the PPG signals acquired from both sites, especially in conditions of poor peripheral perfusion, it will help in supporting the hypothesis.

7.4.1 Optical components and their characteristics

The finger PPG probes consisted of red and infrared surface mount LEDs and a surface-mount photodiode. The emitters and the detector are the same as the ones used in the fabrication of the RECAP probe. The optical, electrical and packaging details of the optical components are provided in Table 7.1 and 7.2.

7.4.2 Fabrication of the reflectance finger PPG probes

The mechanical design of the finger PPG probes is similar to the most commercial pulse oximetry probes. The probes consist of a small PCB with all the optical components arranged next to each other. The dimensions of the PCB are 13 mm × 20 mm × 0.6 mm. On the PCB, the emitters are arranged perpendicularly 4 mm away from the detector. The 3D models of the components and the PCB itself were first designed virtually in Altium Designer. Based on the artwork generated from Altium, the tracks were etched onto a copper clad board through the process of photolithography. Once the PCB was manufactured, the optical components were soldered to the respective pads using reflow

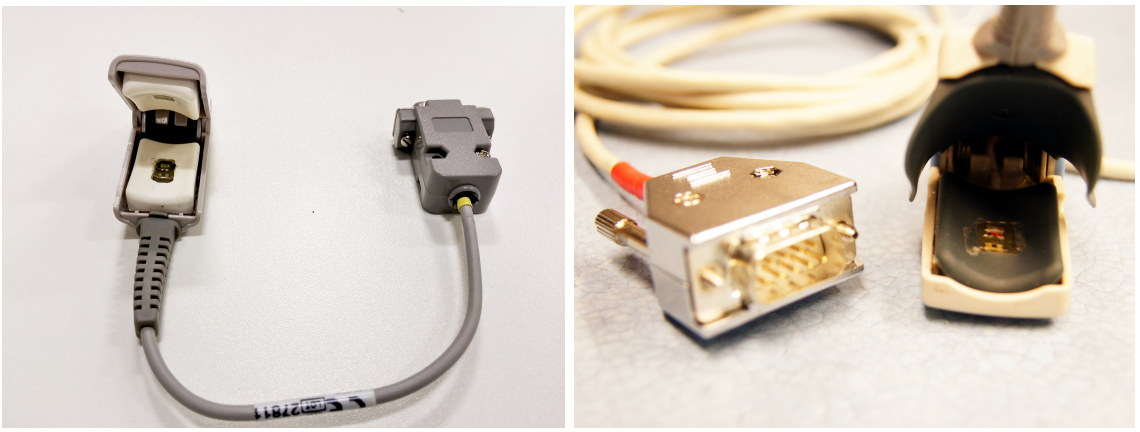

FIGURE 7.17: Close up photographs of the reflectance finger PPG probes.

soldering oven maintained at 200°C. A four-core screened cable was used to provide electrical contact between the optical components and the PPG processing unit. A DE9 male connector provided the interface between the probe and processing system.

Two damaged commercial finger clip type pulse oximeter probes were used to accommodate the PCBs containing the optical components. The optical components and cable of the commercial finger probe were removed and only the finger clip was used. To avoid direct contact with the optical components and the skin the PCBs have been entirely sealed using clear epoxy resin *(DYMAX 141-M, Dymax Corporation, Torrington, CT)*. Figure 7.17 shows the close-up photographs of the reflectance finger PPG probes.

7.4.3 Performance evaluation of the reflectance finger PPG probes

The performance of the finger probes was tested in the laboratory using the prototype PPG processing system. The developed probes were tested in two healthy volunteers. During the test, the finger clips were attached to the right and left index finger of the volunteer. The probes were then connected to the PPG processing system to acquire raw PPG signals. The PPG processing system consisted of the circuitry required to drive the LEDs, acquired the PPG signals and preconditioned the signals. The drive current used to power the LEDs was 40 mA. The raw PPG signals acquired from the PPG processing system were then digitised using an NI DAQ card *(NI USB-6212, National instruments*

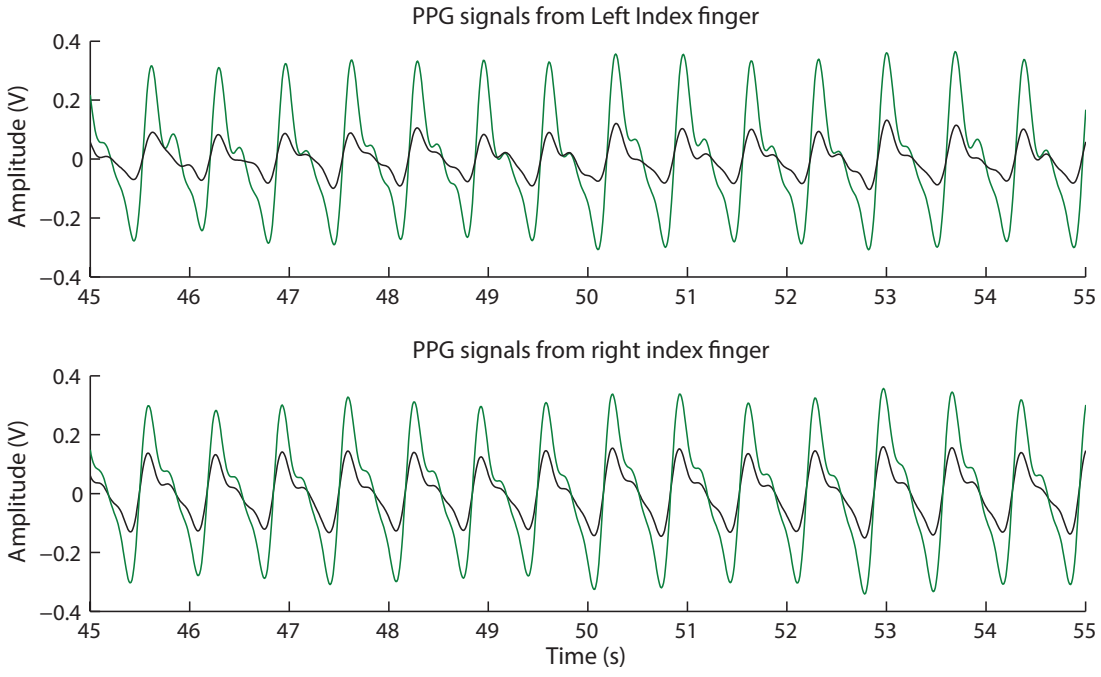

FIGURE 7.18: The AC red (black trace) and infrared (green trace) PPG signals acquired from the ear canal using the 2nd probe.

corporation, Austin, Texas). The digitised PPG signals were displayed and stored on the computer with the help of a LabVIEW VI.

The PPG signals acquired during the preliminary testing were of good quality with large amplitude and high signal-to-noise ratio. Figure 7.18 shows the typical red and infrared AC PPG traces acquired from the left and right index fingers of a volunteer using the reflectance finger PPG probes.

7.5 Summary

To investigate the hypothesis that the ear canal is better perfused than extremities such as the finger in cases of compromised peripheral perfusion, an ear canal PPG probe based on reflection photoplethysmography was developed. Two cylindrical bullet shaped PPG sensors with different dimensions were first developed to investigate the quality of PPG signals acquirable from different depths and surfaces of the ear canal. The developed sensors were optically and electrically identical and consisted of a micro-optic sensor and sensor casing. The micro-optic sensor is a small PCB consisting of two emitters and a photo-detector. The sensor's case was manufactured using a 3D printer.

Preliminary investigations were carried out in 7 healthy volunteers to determine (1) an optimal probe length at which PPG signals of good quality and high amplitude can be acquired, (2) and a surface along the circumference of the ear canal from which the acquired PPGs will be of the best possible quality. A participant survey was also conducted to enquire if the probes required any further modifications in its shape and structure to make it more comfortable. The results of the investigations showed that PPGs with high amplitude and quality can be acquired from the posterior surface of the outer auditory canal. The results and the participant survey also suggest that the ear canal sensor with smaller dimensions (length: 13 mm, diameter: 7 mm) to be optimal in monitoring PPG signals from the ear canal.

Building upon the first prototype, a new earphone shaped ear canal PPG probe was designed and fabricated. This probe underwent further modifications to make it more comfortable to use and to reduce motion artefact. Two identical finger PPG probes were also developed to facilitate comparison between the PPG signals obtained from the central and peripheral locations. Both the finger probes are optically identical to the ear canal probe. The signals obtained from the finger PPG probes during preliminary evaluation were of good quality. The following chapter describes the PPG instrumentation system, developed to drive the optical components, detect both the ear canal and the finger PPG probes, as well as enabling measurements of PPG signals from both sites.

— Complexity that works is built up out of modules that work perfectly, layered one over the other

Kevin Kelly, The Healthcare Forum Journal, vol. 38, no. 1, Feb 1995

8

Design and development of ZenPPG – A modular PPG processing system

Together with the ear canal PPG probes and the finger PPG probes described in Chapter 7, a PPG processing system was designed and developed. The system consists of three main channels – two dual wavelength PPG channels and an ECG channel. The system was designed to drive the optical components, detect and sample the red and infrared PPG signals from both locations, and precondition the acquired PPG signals.

The electronic circuitry required to perform these tasks was split into individual modules which are connected together by a double sided *system bus*. Through this modular approach, various functions in the system were kept independent of each other, allowing for incremental improvements during subsequent development. The main modules in the system are: *the system bus, PPG modules* (current supplies, probe connector board and transimpedance amplifiers) and the *power supply conditioning module*. The system was named 'ZenPPG'. This chapter describes the theory of operation, high-level and low-level design architecture and the implementation of the system. A complete review of the systems circuit optimisation and measured performance is also provided in this chapter.

8.1 Design brief and specifications

The successful validation of the developed sensors requires the use of multiple PPG systems which work in sync with one another, so that a true comparison can be made between the ear canal and the periphery. Most commercially available systems only produce amplitude modulated, phase modulated and post processed signals. This post processing often results in suppression of PPG signal features, and loss of valuable clinical information. It is also meticulous to simultaneously acquire data from two or more pulse oximeters along with data from other physiological systems such as electrocardiogram (ECG) amplifier, temperature sensor, respiration monitor etc. The phase differences between multiple measurement systems can also be a major concern while analysing the acquired data, as the acquired signals will be out of phase with one another. Hence, it was decided that a portable, multi-channel, multi wavelength, multi parametric PPG system with the added capability to record other physiological signals such as ECG signals or respiration signals will be designed and developed.

The design of the system was based on previous instrumentation developed by the Research Centre for Biomedical Engineering (RCBE), at City University London. The system was designed to satisfy the following requirements:

- The design of the system should be modular and allow for incremental improvements, so that further improvement of any single module should 'not' affect the performance or the architecture of other modules
- The system should be portable in size, and contain a minimum of two PPG channels, with each channel capable of generating PPG signals with at least two wavelengths
- The system should accommodate an ECG amplifier with standard 3-lead or 5-lead connector, so that the ECG signal can be used as a timing reference for the PPG signals
- The system should operate with both custom built PPG probes and standard commercial pulse oximeter probes
- The system should output 'raw' PPG (AC and DC) and ECG signals with no amplitude or phase modulations
- The system should be easy to use and run on both batteries and power supplies
- To keep the system cost effective, all the mechanical and electrical components used in the system should be standard components.

Taking these requirements into consideration, the 'ZenPPG' was constructed. The current version of the system accommodates two dual-wavelength PPG channels along with an ECG amplifier, and an airflow pressure sensor to measure respiration. The name 'ZenPPG' introduced in this project, will be used further in this work to refer to the developed PPG signal monitoring system prototype.

8.2 Top-level design architecture

The block diagram shown in Figure 8.1 gives the top level architecture of the 'ZenPPG'. The electrical and design characteristics of both the PPG channels in the system are identical. This is to ensure that the ear canal PPG signals and peripheral PPG signals can be qualitatively and quantitatively compared. As both PPG channels are identical, their design here is described collectively. Before describing the circuit level design and implementation of the system, a generic overview of the systems operation is provided here.

The red and infrared emitters in each channel are driven by a constant emitter driver which consists of three parts: a reference control voltage circuit, a multiplexer and a modified Howland current source. The reference voltage circuit generates the constant

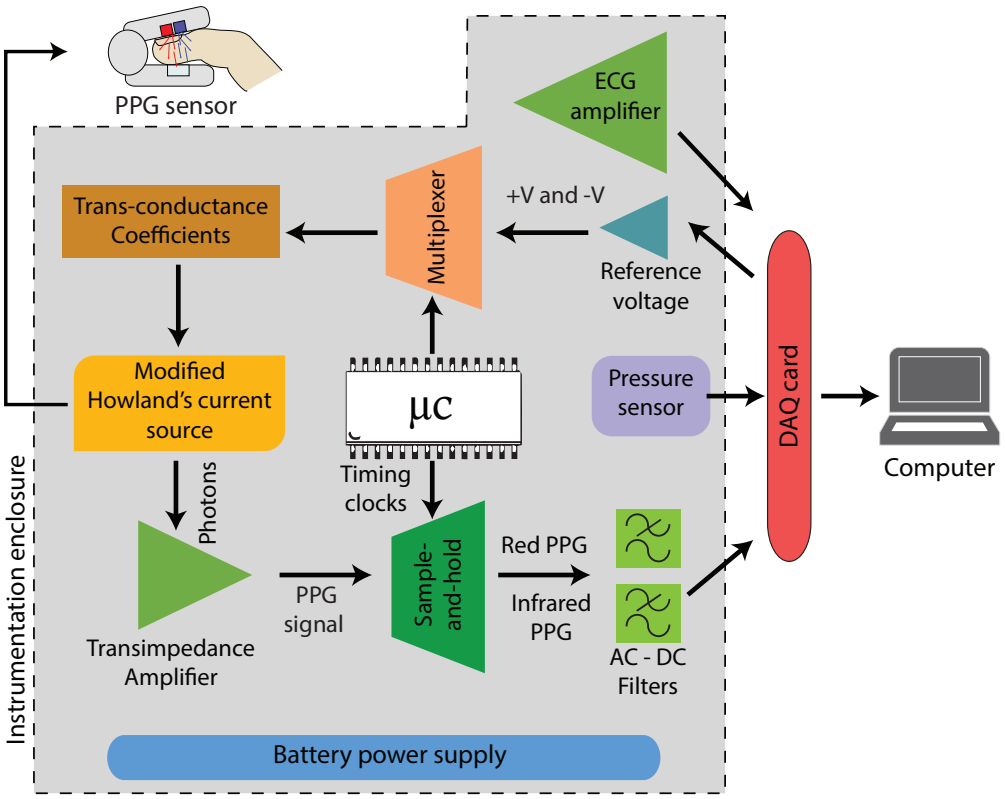

FIGURE 8.1: Top-level architecture of ZenPPG.

voltage required to drive the LEDs. This voltage can be altered by the user on-demand using the controls on the back panel of the system, and digitally using the computer user interface. Hence, providing independent control over LED currents on both channels. The multiplexer is to generate a timed switching signal used to turn on the red and infrared LEDs alternatively. The LEDs are switched on alternatively in order to allow for independent sampling of red and infrared light by the photodetector. A modified Howland's current source is then used to convert the switching voltage signal into the current that is used to turn the LEDs in the probe 'on' and 'off'.

The reflected or transmitted light photons from the vascular tissue are then detected by the photodetector, which generates a current proportional to the incident light power. This current is then converted into a mixed voltage signal consisting of both red and infrared components by the TransImpedance Amplifier (TIA). A Sample-and-Hold Amplifier (SHA) separates the TIA output into red and infrared PPG signals. A programmable microcontroller is used to control the LED switching and demultiplexing of the signals. The red and infrared PPG signals are then lowpass filtered to remove the high frequency switching noise. The AC component of the PPG signals was extracted by highpass filtering the raw PPG signals. The system also hosts an ECG amplifier to detect the QRS complex of the ECG signal and an airflow pressure sensor that can be used to measure respiration rate. The raw AC and DC PPG signals, the ECG signal and the respiration signal are digitised by a National Instruments data acquisition (DAQ) card *(National Instrument Corporation, Austin, Texas)* and are displayed and stored on the laptop computer. Software to handle data acquisition and online signal processing is covered in Chapter 9.

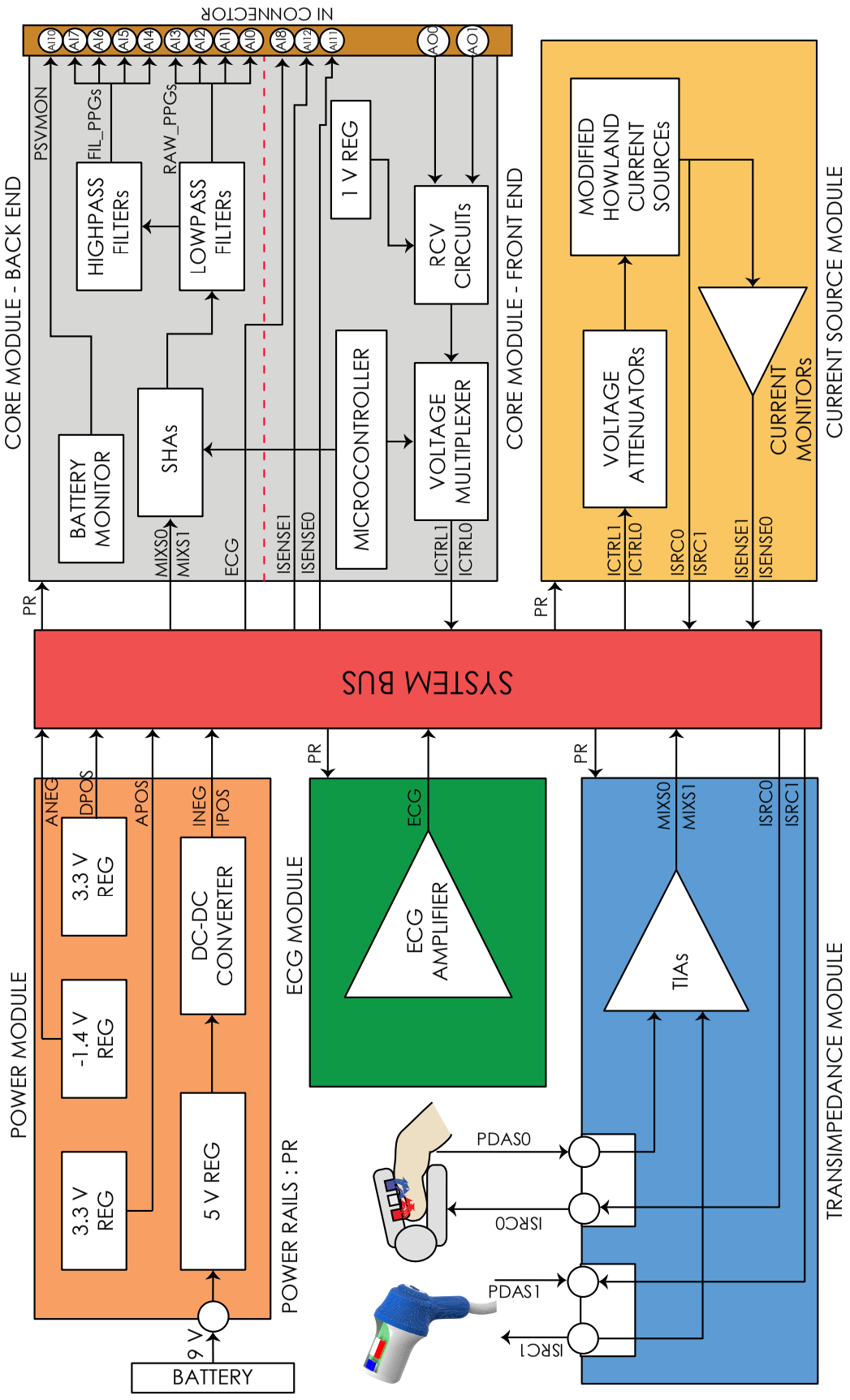

FIGURE 8.2: Detailed block diagram showing the architecture of ZenPPG

8.3 Circuit-level design architecture

The circuitry of the entire system was split into five individual modules which were interconnected by a double sided system bus. Each individual module has a specific function in acquiring and processing various signals. The PPG modules are the TransImpedance Amplifier (TIA) module, the Current Source (CS) module, and the Core module. The other two modules are the power supply conditioning module and the vital sign monitoring module. The core module is the "heart" of the PPG processing system. The circuitry within the core board can be divided into two parts, the front-end and the back-end. The front-end consists of the circuitry required for emitter driver control, and the back-end consists of demultiplexers and filters, as shown in Figure 8.2. For ease of understanding, both parts are detailed separately. The vital sign monitoring module consists of an ECG amplifier and a pressure sensor. A detailed block diagram showing the architecture of the ZenPPG is shown in Figure 8.2. The theoretical description of the circuits in each module are described below. The schematic diagrams of all the modules are given in Appendix A.

8.3.1 System bus

To make the system modular and re-usable, a system bus was designed, which interconnects all other modules together. The system bus consists of six (three on each side) receptacle 50 way surface mount connectors (SAMTEC, Indiana, USA). It is designed in such a way that every single pin in any connector corresponds to the same pin in all the connectors. Since all the 50 pins on every connector are the same, it provides a medium of interaction between various modules. All the PPG modules, ECG modules and the power supply conditioning board are furnished with gold plated, through-hole, right angle 50 way headers that connect to the bus. Each pin in the system bus is assigned to a particular net, hence making it the only module in the system that is inflexible or unalterable. Table 8.1 shows the pin-out of the system bus in ZenPPG.

8.3.2 Power supply conditioning module

The ZenPPG system runs on two standard 9 V PP3 batteries encased within the portable system case or on the 5 V supply from a mini USB. The batteries used were rechargeable NiMH batteries with a capacity of 280 mAh *(Extreme power, UK)*. These have been set in a parallel configuration to give a total of 580 mAh charge capacity. The power supply conditioning module consists of the circuitry required to regulate the main battery power supply into multiple DC power rails. This is to reduce power consumption, provide operational stability and improve system efficiency.

TABLE 8.1: Pin-out of the system bus in ZenPPG

Description	Net	Pin	Pin	Net	Description
Not Connected	NC	1	26	MAN0	Monitoring Photodiode Anode 0
Not Connected	NC	2	27	MKA0	Monitoring Photodiode Cathode 0
Not Connected	NC	3	28	PSENSE0	LED Optical Power Sense 0
Not Connected	NC	4	29	ICTRL0	LED Current Source Control Voltage 0
Not Connected	NC	5	30	ISRC0	LED Current Source (Drains to IGND) 0
Not Connected	NC	6	31	ISENSE0	LED Current Sense 0
SPI / Micro-wire Serial Interface	MOSI0 / TWD0	7	32	ICTRL1	LED Current Source Control Voltage 1
SPI Serial Interface	MISO0	8	33	ISRC1	LED Current Source (Drains to IGND) 1
SPI / Micro-wire Serial Interface	SCK0 / TWCK0	9	34	ISENSE1	LED Current Sense 1
Gain Control 0	GC0	10	35	SEL0	LED selection 0
Gain Control 1	GC1	11	36	SEL1	LED selection 1
Not Connected	NC	12	37	NC	Not Connected
Not Connected	NC	13	38	NC	Not Connected
Not Connected	NC	14	39	NC	Not Connected
Not Connected	NC	15	40	NC	Not Connected
Not Connected	NC	16	41	NC	Not Connected
Not Connected	NC	17	42	MIX0	Transimpedance Output 0
Temperature	TEMP	18	43	IPOS	Current Source Power Positive = +5 V
Respiration	RESP	19	44	IGND	Current Source Ground
ECG Lead 1	ECG	20	45	INEG	Current Source Power Negative = -5 V
Transimpedance Output 1	MIX1	21	46	APOS	Analogue Power Positive = +3.3 V
Not Connected	NC	22	47	AGND	Analogue Power Ground
Power Cable (USB connector)	CBLV	23	48	ANEG	Analogue Power Supply Negative = -1.4 V
Power Supply (from power switch)	PSV	24	49	DPOS	Digital Power Supply Positive = +3.3 V
Power Supply Ground	PSGND	25	50	DGND	Digital Power Supply Ground

The 9 V battery power supply (BATV) from the batteries is first regulated down to 5 V using a positive voltage regulator *(MC78M05CDTG, ON Semiconductor, Arizona, USA)*. This is to keep both the battery and USB power supply at the same voltage. Also, since all the microchips used in the system are based on CMOS technology, the system does not require high power. When powered with USB, this microchip is switched off. Switching between USB and battery supply is through a two pin mini jumper. Figure 8.3(a) shows the configuration of the circuit.

The 5 V supply from the regulator (RBATV) or the USB (CBLV) is passed through an isolated point-of-load DC-DC converter *(IA0505D, XP power, singapore)* that regulates the 5 V input to +5 *(IPOS)* and -5 *(INEG)* volts, and a common ground (IGND). These ±5 V supplies are used to power the current source module, the multiplexers in the Core module and the ECG module. INEG, IPOS, and IGND are also further regulated to power the rest of the system. The isolation barrier in the DC-DC converter separates the input (CBLV or RBATV) and the output power supplies (INEG, IPOS and IGND). Hence protecting the system, sensors and the user (patient) from any malfunction. The high frequency transformer in IA0505D withstands up to 10,000 V. Figure 8.3(b) shows the configuration of the circuit.

All other analogue microchips in the system run on +3.3 V (APOS) and -1.4 V (ANEG) supplies. These power rails are generated using IPOS and INEG. The +3.3 V supply is generated using a linear low drop-out voltage regulator *(MCP1703T, Microchip Technology, Arizona, USA)*, while the -1.4 V supply is generated using a low drop-out negative micro-power regulator *(LT1964ES5, Linear Technology, California, USA)*. The circuit configuration of APOS, ANEG and AGND are shown in Figure 8.3 (c) and (d).

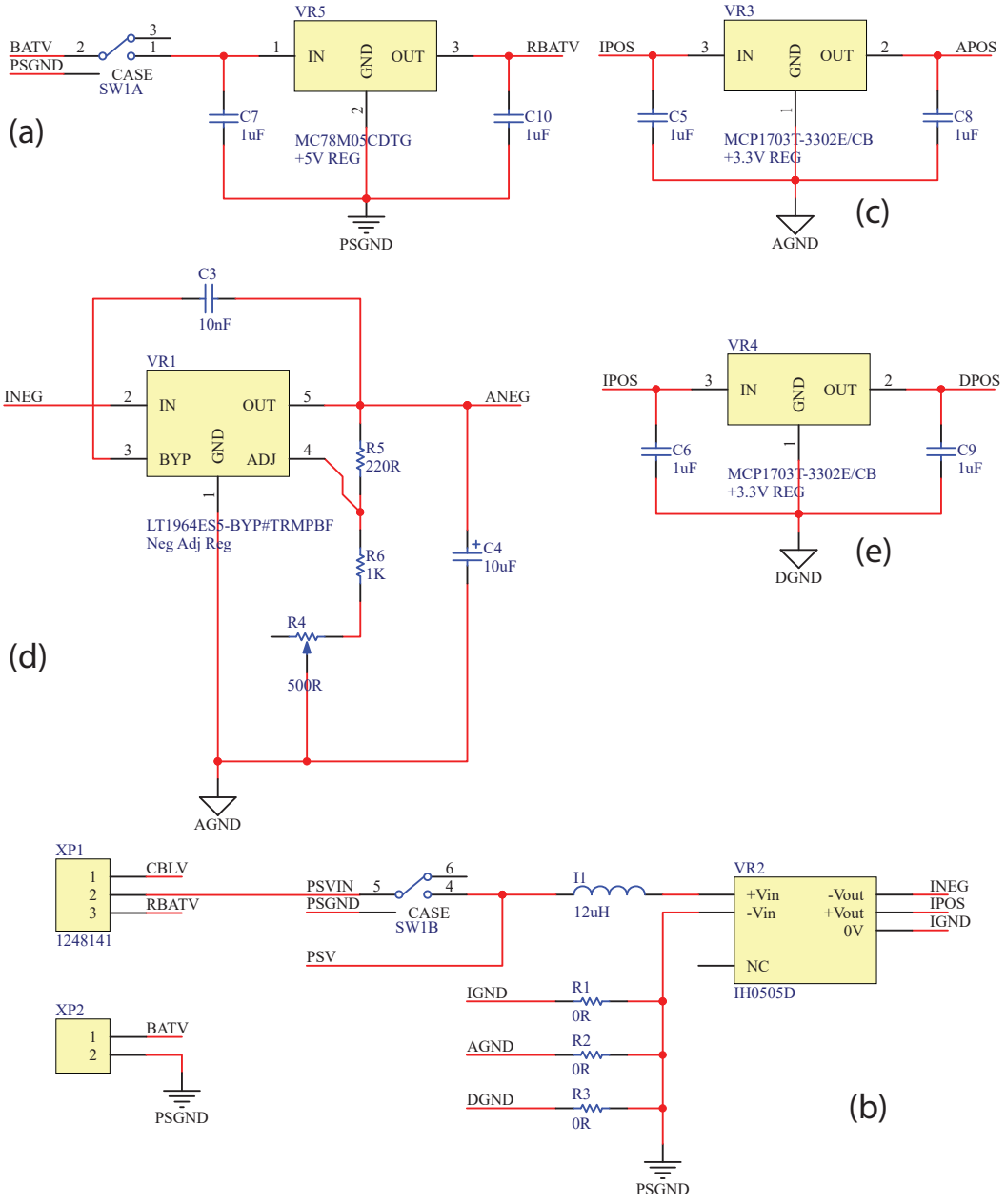

FIGURE 8.3: The circuits used to generate various supply rails in power board: (a) the 5 V regulator to regulate the 9 V battery supply to 5 V, (B) The DC-DC converter to convert the 5V supply to ± 5 V (IPOS, INEG) (c) The 3.3 V regulator generate APOS– positive supply to analogue microchips, (d) the -1.4 V regulator to generate ANEG– negative supply to analogue microchips and (e) a 3.3 V regulator to generate DPOS– supply to digital microchips.

A separate +3.3 V supply is generated using a linear low drop-out voltage regulator *(MCP1703T, Microchip Technology, Arizona, USA)*, and is used to power digital microchips such as the micro-controller. Digital circuitry usually draws large currents from its supply during switching and are very noisy. On the other hand analogue circuitry is quite vulnerable to noise on both supply rails and grounds. Thus, to prevent digital noise from corrupting analogue performance, separate power rails and ground returns were implemented in the system. The circuit configuration of DPOS and DGND are shown in Figure 8.3 (e).

8.3.3 Core module - Front end

As mentioned earlier, the red and infrared emitters on each channel are driven by an emitter driver circuit consisting of three main parts: a reference control voltage circuit, a current multiplexing circuit and a modified Howland current source. The front end of the core board hosts both the reference control voltage circuit and the multiplexing circuit. These circuits were designed by keeping two main specifications in mind:

- Each LED has to be able to switch on and off at a frequency of at least 100 Hz, as it is sufficient to sample the PPG signal
- Each LED 'on time' should be sufficient to obtain an undistorted light intensity sample.

8.3.3.1 Reference control voltage circuit

The purpose of the reference control voltage (RCV) circuit is to provide independent control over LED currents on both channels. Each LED in both PPG channels is controlled

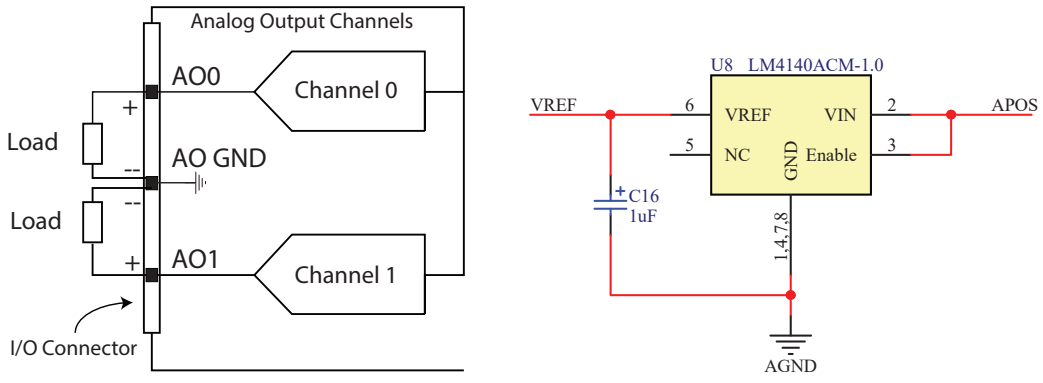

(a) DAQ card output configuration

(b) Voltage regulator output configuration

FIGURE 8.4: Circuit configuration used to generate reference voltage source in Channel-1 and Channel-2.

by an individual RCV circuit. The design of all four RCV circuits is similar, and consists of two parts – a reference voltage source and a voltage attenuator. The reference voltage (V_{Ref}) on channel-1 is generated by a 16-bit NI DAQ card *(National Instrument Corporation, Austin, Texas)*. V_{Ref} on channel-2 is by a constant on-board 1 V regulator. This configuration allows for digital control of LEDs on channel-1 and analogue control of LEDs using trimmers on the other. Digital control of LEDs on both channels is not possible in this design, as the number of analog output channels on the DAQ card are limited. Figure 8.4 shows the configuration of the reference voltage source circuit used in Channel-1 and Channel-2.

On channel-1, the DAQ card's analogue output ports AO0 and AO1 were used to generate V_{Ref}. The DAQ card has an analogue output voltage range of ± 10 V, with a 16-bit resolution. Hence each port can drive the LED current source with voltages between -10 to 10 V and a resolution of $20\ V/2^{16} = 305\ \mu V$. In the current setup, AO0 was configured to generate voltage between -5 and 0 V. Port AO1 was configured to generate voltage between 0 and 5 V. On channel-2, V_{Ref} was generated using a low noise drop-out 1 V regulator *(LM4140ACM, Texas Instruments, Texas, USA)*.

The output ranges of AO0 and AO1 were then attenuated down to -1 – 0 V (ICNEG0) and 0 – 1 V (ICPOS0) using the voltage attenuator circuit. The attenuator circuit is a simple voltage divider with an op-amp buffer, which divides the input voltage by 5, as shown in Figure 8.5(a). Similarly, the 1 V output from the voltage regulator in channel-2 was attenuated to ± 1 V using the attenuator circuits shown in Figure 8.5(b). The variable resistors R20 and R27 (Figure 8.5(b)) can be used to adjust the positive and negative

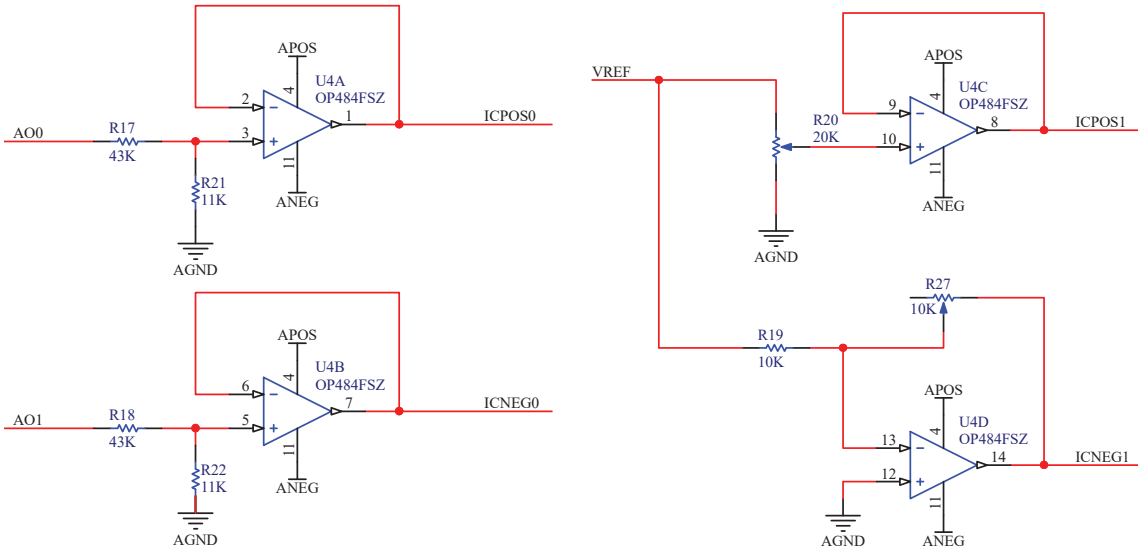

(a) Voltage attenuators for channel-1

(b) Voltage attenuators for channel-2

FIGURE 8.5: The four voltage attenuator circuits used to control LED currents in both channels of the system

voltage between -1 to 0 V and 0V to 1 V. The positive and negative voltage generated by RCV circuits in channel-1 are referred to as ICPOS0 and ICNEG0, while in channel-2 they are referred to as ICPOS0 and ICNEG1. The op-amp used in the attenuator design is the OP484FSZ quad op-amp *(Analog Instruments, Massachusetts, USA)*.

8.3.3.2 Voltage multiplexing circuit

The positive and the negative voltages from the RCV circuits of each channel are time multiplexed using the multiplexing circuit. This is to switch the red and infrared LEDs alternatively. The positive voltage switched the infrared LED 'on', while the negative voltage switched the red LED 'on'. Hence, this allowed independent sampling of red and infrared light by the photodetector.

The voltage multiplexer circuit consists of a double pole 4–throw (DP4T) analogue multiplexer *(MC14052BD, ON Semiconductor, Arizona, USA)* that connects to a timing generator as shown in Figure 8.6(a). The multiplexer produces a continuous switching signal by selecting one of its four inputs (X0 to X3 and Y0 to Y3) on each channel, and making the selected inputs appear on the respective output (X and Y). The data select lines (A,B and INHIBIT) determine which input is passed on to the output. The truth table in Figure 8.6(b), shows how the inputs of the multiplexer relate to its outputs. For instance, if A, B and INHIBIT are at a logic level low (i.e, 0), then the outputs X and Y receive X0 and Y0. Similarly, if A was at logical high, B and INHIBIT were at logical low, then X and Y would receive X1 and Y1.

In the current design, this multiplexer was configured as shown in Figure 8.7(a). The RCV circuit outputs ICPOS0 and ICNEG0 were connected to the multiplexer inputs X0 and X1, while ICPOS1 and ICNEG1 were connected to Y0 and Y1. The other two inputs on

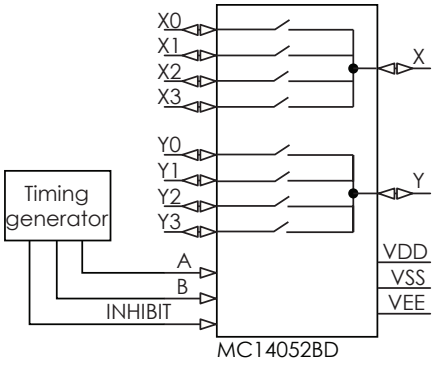

(a)

Truth table

Control inputs			Output	
INHIBIT	A	B		
0	0	0	X0	Y0
0	1	0	X1	Y1
0	0	1	X2	Y2
0	1	1	X3	Y3

(b)

FIGURE 8.6: The (a) functional diagram of the multiplexer and the (b) truth table of the multiplexer.

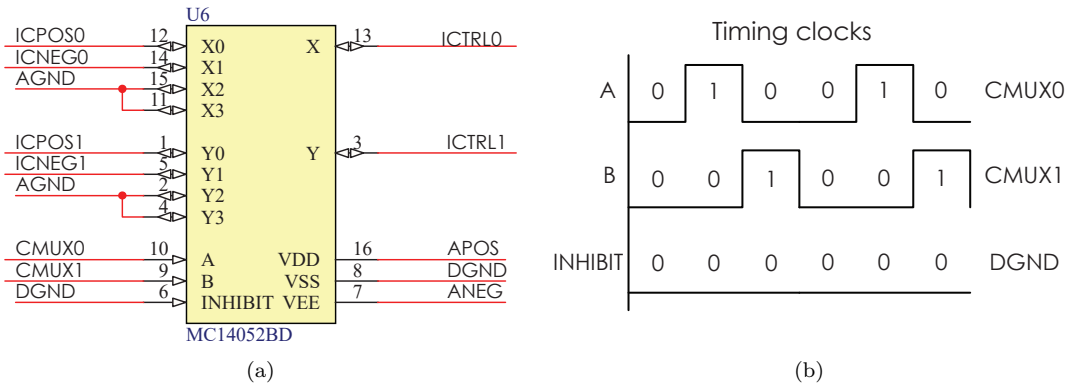

FIGURE 8.7: (a) The configuration of the multiplexer circuit used in the ZenPPG and (b) the clocks used to control the multiplexer.

each channel of the multiplexer (X2, X3 and Y2, Y3) were connected to AGND. The data select lines A and B of the multiplexer were connected to the timing generator, which is an 8–bit Atmel ATtiny 2313–20SU micro-controller unit (MCU) *(Atmel corp, CA, USA)*. Two timed clocks (CMUX0 and CMUX1) at a frequency of 800 Hz were generated from the port-D of the MCU. Figure 8.7(b) shows the timing clocks CMUX0 and CMUX1 used to control the multiplexer. The INHIBIT of the multiplexer was always set to logical low by connecting it to DGND.

This configuration has yielded two outputs (ICTRL0, ICTRL1) which fluctuated between positive and negative voltage. When timing clocks CMUX0 and CMUX1 were at logical low, then the outputs were positive (ICPOS0 and ICPOS1), which switched the infrared LEDs 'on'. When CMUX0 was at logical high and CMUX1 was at logical low, then the outputs were negative (ICNEG0 and ICNEG1), which switched the red LEDs 'on'. Finally, when CMUX0 was at logical low and CMUX1 was at logical high, the output was AGND, which switched both the LEDs 'off', as shown in Figure 8.8. The duty cycle time (t) of

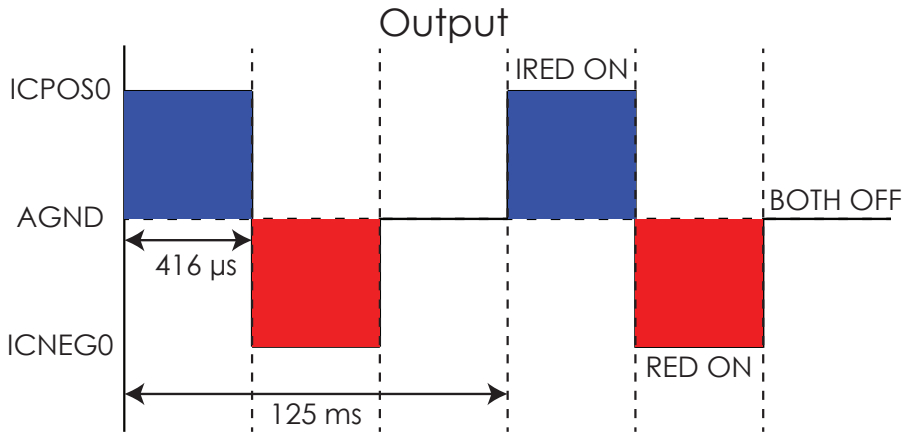

FIGURE 8.8: One of the outputs (ICTRL0) of the dual- 4 channel multiplexer. The infrared LED is first switched on for 416 μs, followed by the red LED, and then an off period, where both LEDs are off.

each LED was

$$t = \frac{1}{f} \times d;\ where\ d = \frac{Time\ the\ signal\ is\ active}{Total\ period\ of\ the\ signal} \times 100\ \%\ = 416\ \mu s \tag{8.1}$$

Each emitter was hence switched 'on' every 125 ms for a duration of 416 μs. The multiplexer outputs – ICTRL0 and ICTRL1 are passed through the system bus into the current source module, where the voltage is converted into current required to power the LEDs.

8.3.4 Current source module

The current source module consists of two identical current driver circuits that are used to drive the LEDs on both the channels. The module also consists of two current monitoring circuits, which are used to continuously monitor the red and infrared LED currents. As both current driver circuits are identical, their design is described collectively.

8.3.4.1 Current driver circuit

The current driver circuit used in this system is a modified Howland current source. The basic configuration of this classic circuit is shown in Figure 8.9. A detailed explanation of the circuit and its variants is given in [269]. The primary advantages of the Howland current source over other current sources are its simplicity and the ability to produce high output impedance. This ground referenced current source is controlled by the positive reference voltage, hence avoiding the 'floating common point' issues usually experienced

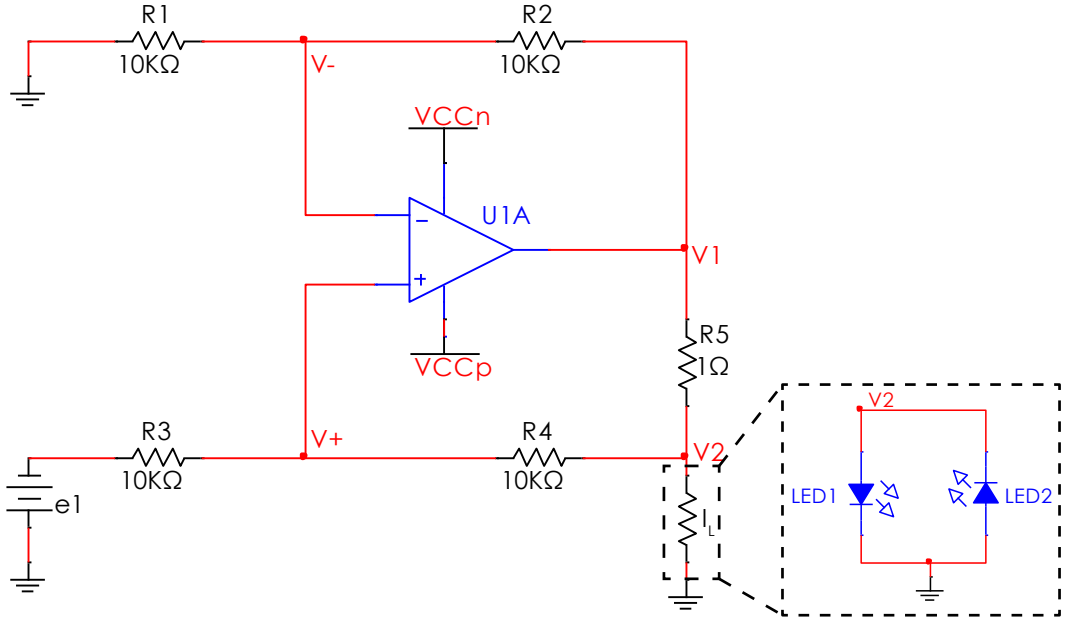

FIGURE 8.9: Circuit diagram showing a linear modified Howland current source with a tranconductance gain of 1.

by other current sources such as the H-bridge or transistor based switching current sources. However, when using the Howland current source, the resistors R_1, R_3 and R_2, R_4 must be precisely matched for good linearity. Also the ratio R_1/R_2 must be stable, to keep good current accuracy. Under ideal op-amp characteristics ($V_- = V_+$), the current across the load resister (I_L) is given by Equation 8.2, when $R_2/R_1 = R_4/R_3$.

$$I_L = e1 \times \frac{R_4}{R_3} \times \frac{1}{R_5} \tag{8.2}$$

Hence, by precisely selecting resistors R_1, R_2, R_3, and R_4 to the same value, and choosing the load resistor (R_5) to be 1 Ω, as shown in Figure 8.9, a linear current source with a transconductance gain of 1 can be achieved. With this current source, a linear current proportional to the input voltage – e1 can be supplied to the load. However, if the load (I_L) has large impedance, then the circuit can sometimes present significant current error. Since the current load in this application is an LED, which has a fairly small impedance in active stage, particularly in comparison with R_4, LED current accuracy is not a concern. Therefore, by replacing the load with the red and infrared LEDs as shown in Figure 8.9, and making e1 a bidirectional switching voltage, LEDs can be turned on intermittently.

However, in the current setup, if e1 was replaced by the bidirectional voltage from the multiplexer (ICTRL0 or ICTRL1), then the maximum current produced by the current source will be 1 A, at a maximum reference voltage of 1 V. Such large current can burn the LEDs in the probe. Therefore, the output of the multiplexer needs to be brought down by at least 10 fold, so that the maximum reference voltage of the multiplexed signal will be 100 mV and the maximum current through the LEDs will be 100 mA. This can either be achieved by adjusting the resistors R_1 and R_5 on the current source, or by passing the outputs of the multiplexer (ICTRL0, ICTRL1) through a voltage divider circuit which divides the input by 10. As altering the resistors would lead to instability in output

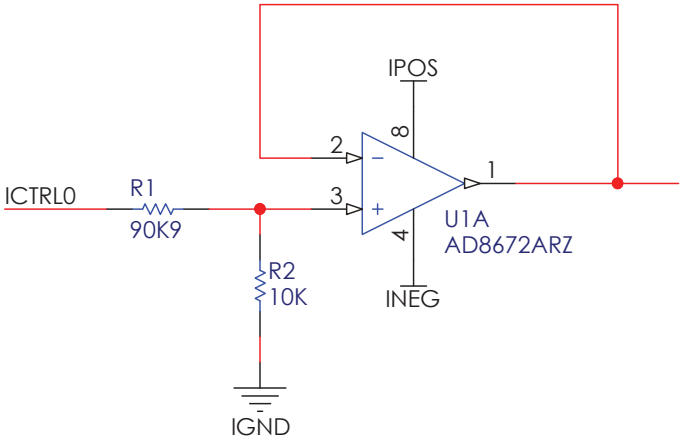

FIGURE 8.10: The voltage attenuator circuit which divides the input voltage by 10.

currents, voltage dividers with op-amp buffers were used. The circuit diagram of the voltage divider with an op-amp buffer used to divide ICTRL0 is shown in Figure 8.10.

This modified Howland current source with the voltage divider input worked very well during laboratory testing, however possessed two key limitations:

- As there are no current limiters in the circuit, in the event of a malfunction, large currents can pass through the LEDs, causing damage to the developed sensors.
- An ordinary fast op-amp cannot deliver sufficient current to drive power LEDs and available power op-amps do not have good static and dynamic characteristics.

To overcome these limitations, a fast power push–pull (NPN–PNP) transistor switch (PMD3001D, NXP Semiconductors, Eindhoven, Netherlands) was added between the op-amp output and the LEDs, as shown in Figure 8.11. In this circuit, when the current source driving voltage is positive, the NPN transistor is active and switches one emitter on and, when the driving voltage is negative, the PNP transistor is active, switching the other emitter on. The maximum current supplied to the LEDs is limited to 100 mA by resistors R_6 and R_7. When the input reference voltage is between ± 100 mV, the transistor is in open state, and the current across the LED will be proportional to the set reference voltage. In the event of a malfunction, if the driving reference voltage was fortuitously increased to a value higher than ± 100 mV, then the transistor is in a saturated state,

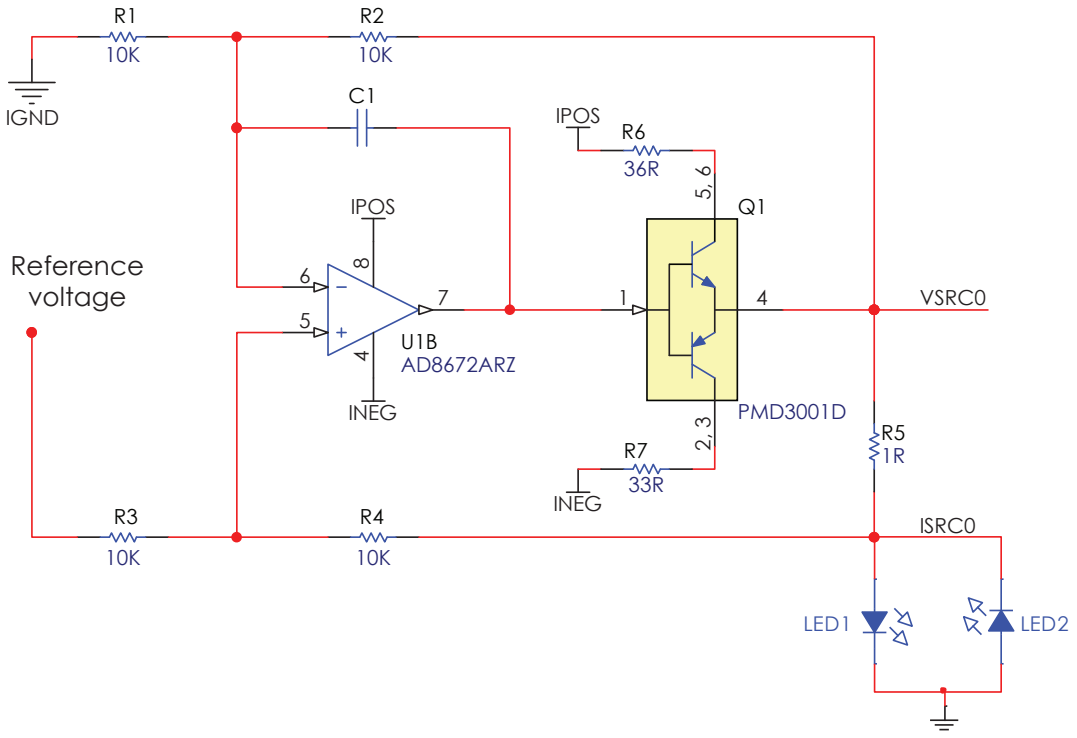

FIGURE 8.11: Ground referenced Howland current source with fast power NPN-PNP transistor switch used to protect the LEDs.

allowing for current to flow from the collector to the emitter, which is limited to 100 mV. The value of the current limiting resistor can be calculated using:

$$R = \frac{V_{CC} - V_{CEsat} - V_f}{I_{max}} \tag{8.3}$$

where V_{CC} is the supply voltage (IPOS or INEG), V_{CEsat} is the collector–emitter saturation voltage, V_f is the voltage drop across the LED (forward voltage), and I_{max} is the maximum limiting current. The V_{CEsat} of the NPN–PNP transistor used is 30 mV and -40 mV respectively. The forward voltage of infrared and red LEDs used in the PPG probes are 1.35 and 1.8 V respectively (see Table 7.1). The positive and negative power supplies are +5 and -5 V. Hence, the value of the limiting resistors will be 36.2 Ω and 31.6 Ω. As resistors with these values are not commercially available, standard resistors (36 Ω and 33 Ω) close to these values were used.

Before using these components (transistor, resistor and Op-amp), the static and dynamic performance of the circuit shown in Figure 8.11 was tested through Simulation Program

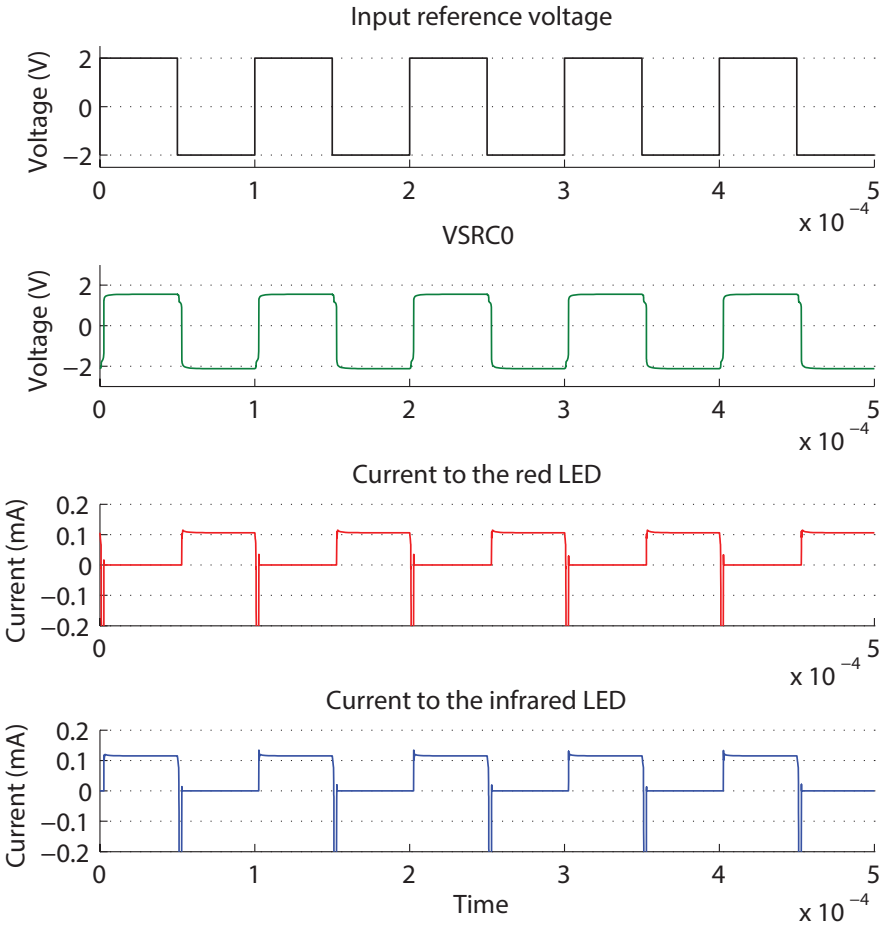

FIGURE 8.12: SPICE simulation results showing the performance of the modified Howland current source. Black trace shows the input reference voltage, green traces shows the output of the transistor, red and blue traces show the current across the red and infrared emitters.

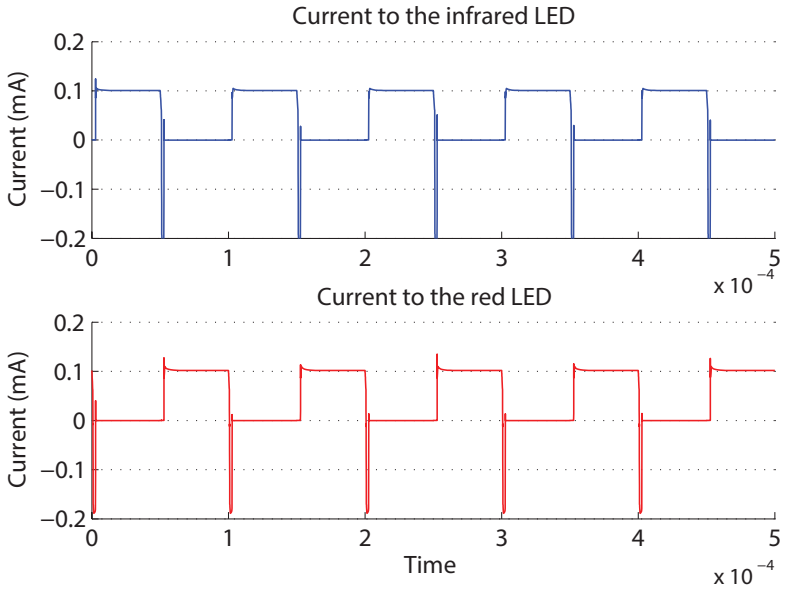

FIGURE 8.13: Simulation results showing the performance of the optimised current limiting circuit. The current limiting resistors in the ciruit were changed to 43 Ω and 36 Ω.

with Integrated Circuit Emphasis (SPICE) modelling. SPICE simulations were carried out using Altium designer *(Altium Limited, Sydney, Australia)*. During SPICE simulations, the input reference voltage was set to ±2 V, which is well beyond the systems designed input range (± 100 mV). This is to check the performance of the current limiting circuit in the event of a malfunction. The results of the SPICE simulations are shown in Figure 8.12. Although the designed circuits performed well, the maximum current supplied to the infrared LEDs was slightly higher than the set value (100 mA). Hence, to further optimise the circuit's performance, the current limiting resistors were changed to 43 Ω (R_6) and 36 Ω (R_7). Figure 8.13 shows the current across the red and infrared LEDs, when the current limiting resistors were changed to 43 Ω and 36 Ω.

The final version of the circuit used in the design of current source module is shown in

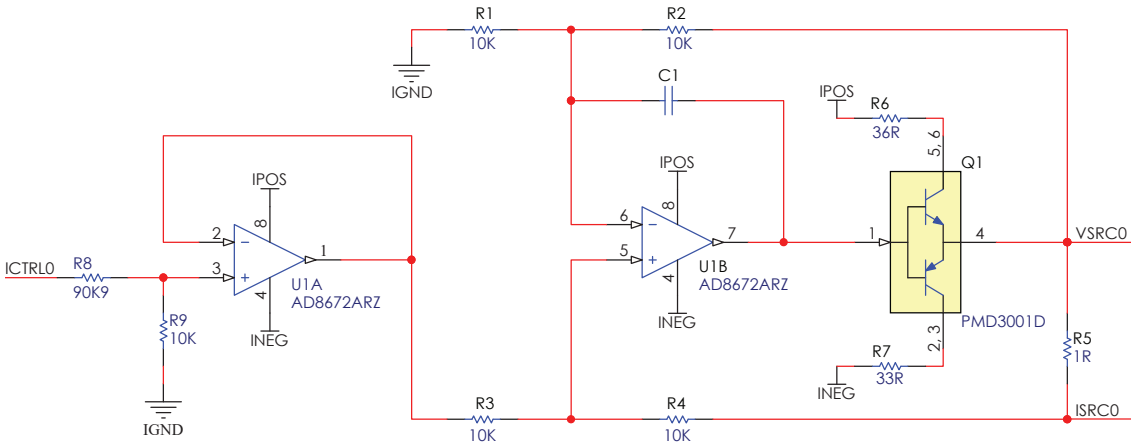

FIGURE 8.14: Circuit diagram of the current source used in the ZenPPG system.

Figure 8.14. In summary, the alternating input voltage from the multiplexer (ICTRL0 or ICTRL1) is passed through the voltage divider, which divides the input voltage by 10, and then the current source converts this voltage into current used to power the LEDs. The current outputs of both the CS circuits – ISRC0 and ISCR1 are passed through the system bus and the TIA module into the PPG probe, where the LEDs are switched on alternatively.

8.3.4.2 Current monitoring circuit

LED current monitoring is one of the distinctive features of the ZEN PPG system. The current across the LEDs in each probe is continuously monitored by an instrumentation amplifier. This is attained by inputting voltage across the load resistor (VSRC0) and the current after the load resistor (ISRC0) as differential inputs to the instrumentation amplifier. The voltage sensed by the instrumentation amplifier (ISENSE0 or ISENSE1) gives the indication of the amount of current across the LEDs. The sensed voltage signal is however amplified linearly by the instrumentation amplifier to get a measurable output that can be sampled by the DAQ card. The signal amplification depends on the gain resistor, which was set to 5.6 kΩ (gain =10). The circuit configuration of the current sensing circuit is shown in Figure 8.15. The output of both the current monitoring circuits (ISENSE0 and ISENSE1) is passed through the system bus into the core module, where the NI DAQ card samples the signals.

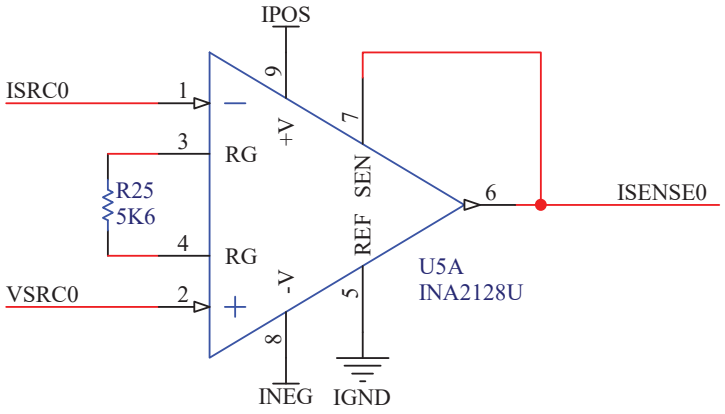

FIGURE 8.15: Configuration of the current monitoring circuit. The differential inputs of the instrumentation amplifier are used to monitor the current across the load resistor.

8.3.5 TransImpedance Amplifier (TIA) module

The TIA module consists of two identical transimpedance amplifiers, that convert the light photons detected by the photodetector into a mixed voltage signal. This voltage

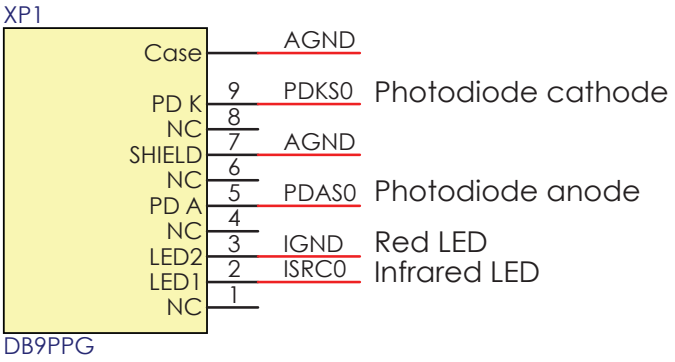

FIGURE 8.16: Pin-out diagram of the DB9 connector.

signal contains photometric information from both red and infrared wavelengths. The strength of the signal from the amplifier depends on the intensity of light detected by the photodiode and the TIA gain resistor. The module also hosts two female DB9 connectors for interfacing with the PPG probes. The connectors and the pin-out of the connector (Shown in Figure 8.16) used is similar to commercial pulse oximeter probes. Hence, giving the flexibility to use most commercial PPG probes without any additional requirements.

The TIA is a simple op-amp circuit with a gain resistor in the negative feedback configuration connected to a photodiode as shown in 8.17(a). In applications such as PPG, where the required gain is in the order of few hundred kΩ to a few MΩ, this simple circuit can display surprisingly complex AC behaviour. This behaviour complicates the determination of circuit bandwidth, requires additional phase compensation and makes the noise response frequency dependent. If attention is not paid during circuit design and layout, the digitizing at the end of the signal path would be unable to discern signal from noise. Hence, characteristics such as the TIA topology, stability, bandwidth and phase compensation were studied while designing the TIA, and are described below.

8.3.5.1 Choice of TIA circuit configuration

In optical applications such as PPG, the TIA can particularly be affected by circuit design topology, as often the detected signals are complex and small. The two most commonly used TIA design topologies in optical monitoring are zero biased (Figure 8.17(a)) and reverse biased (Figure 8.17(b)) configurations. In reverse bias configuration, a positive voltage is applied at the cathode of the photodiode. This causes an increase in the width of the depletion region of the photodiode and lowers the junction capacitance, hence improving the high frequency performance. However, the design trade-off for this increase in speed is an increase in dark current (DC error) and nonlinearities. In zero biased configuration, the cathode of the photodiode is grounded (at 0V). The zero bias produces a very

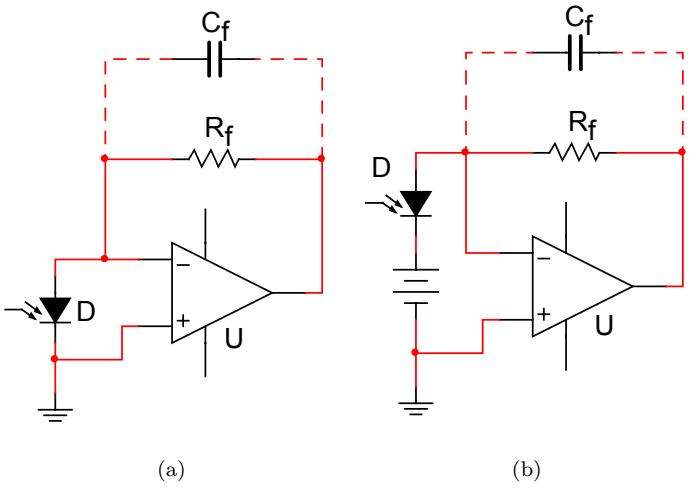

FIGURE 8.17: Transimpedance amplifier as a photodiode front-end (a) without reverse bias voltage, (b) with a reverse bias voltage.

little DC error and very little noise. In addition, the photodiode response is more linear than can be achieved with reverse biasing. Its parasitic capacitance, however, is higher.

In the current system, a zero biased TIA was used, with the expense of high parasitic capacitance. The reasons for this are as follows:

- The multiplexing frequency of the ZenPPG system is not high enough (only 800 Hz) to use the reverse bias circuits
- Linearity to light intensity in the current application is of paramount importance, as the estimation of SpO_2 relies on the detected PPGs.
- Also, since zero biased circuit produces low noise, the detection of small amplitude PPGs becomes easily possible.

The circuit diagram of the TIA used in the ZenPPG is shown in Figure 8.18. In this circuit, the operational amplifier maintains zero voltage across the photodiode due to the virtual ground. Current flows through the feedback resistor (R_2) and creates a voltage at the output that is proportional to the light intensity. The output is given by:

$$MIXS0\ (Output) = R_2 \times I_p \tag{8.4}$$

The outputs of both the TIA amplifiers MIXS0 and MIXS1 are passed through the system bus to the core board back end, where they are demultiplexed and preconditioned. The TIAs were built into metal screening cans to reduce their susceptibility to stray light.

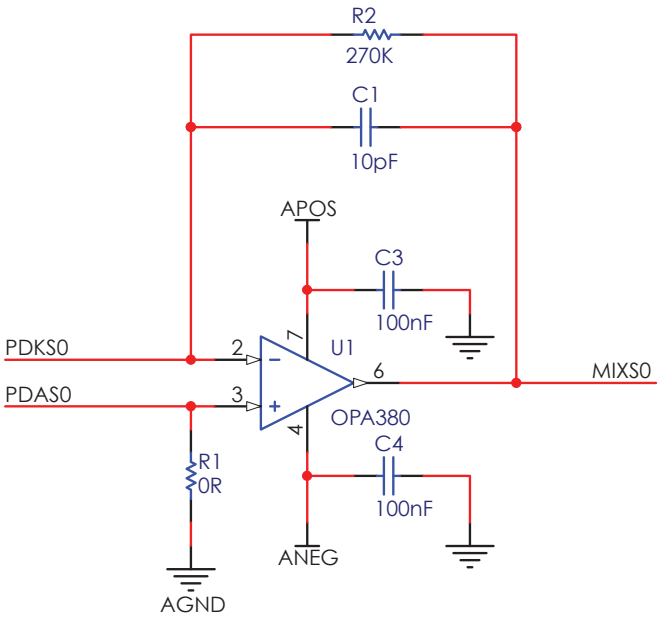

FIGURE 8.18: Circuit diagram of the TIA used in ZenPPG system

8.3.5.2 Bandwidth limiting

In TIA circuits, three separate response limits can potentially set the bandwidth of the TIA. These are the parasitic capacitance of the photodiode, the bandwidth of the op-amp, and the phase compensation capacitor [270]. In very high gain cases, the parasitic capacitance bypasses the feedback resistor; this effect generally sets the bandwidth. Lower-gain applications reduce the significance of the parasitic bypass, in which case the op-amp bandwidth and phase compensation set the TIA bandwidth [271]. In intermediate gain applications, such as in the current PPG system, the op-amp bandwidth, the phase compensation and the large parasitic capacitance of the photodiode sets the bandwidth. Hence while designing TIA for ZenPPG:

- Op-amps (OPA380, Texas Instruments, Texas, USA) with large bandwidth (90 MHz) and open loop gain (130 dB) were used
- Photodiodes with small surface area (0.65 mm^2) were used in the desin of ear canal and the finger probes, to reduce the parasitic capacitance
- A phase compensation capacitor in the order of few picofarads (pF) was used in the TIA circuit, to provide stability to the circuit.

The value of the capacitor required for optimal compensation was calculated using [270].

$$C_f = \sqrt{\frac{C_i}{2\pi.R_f.f_c}} = 0.3pF \tag{8.5}$$

where C_i is the total input capacitance (photodiode junction capacitance : 10 pF + op-amp input capacitance : 4.1 pF), R_f is feedback resistor value and f_c is a unity-gain crossover frequency of the op-amp (90 MHz). The 0.3pF capacitor (C_f) is not a standard capacitor, and since the bandwidth of the op-amp is fairly large, a larger capacitor can be used without causing a reduction in usable TIA bandwidth and without overcompensating the TIA response. Hence a 10 pF (C_f) capacitor was used. The -3 dB frequency and the open-loop gain bandwidth of the TIA circuit shown in Figure 8.18 is:

$$f_{-3dB} = \frac{1}{2\pi.R_f.C_f} = 58.9 \text{ kHz} \tag{8.6}$$

$$f_{GBW} > \frac{C_i + C_f}{2\pi.R_f.{C_f}^2} = 142 \text{ kHz} \tag{8.7}$$

Experiments showing the effects of C_f on the TIA's performance is detailed in Section 8.5.2.

8.3.6 Core module – Back end

The back end of the core module consists of three main circuits

- a micro-controller to generate timing signals that control the multiplexer and the SHA
- a SHA circuit to separate the mixed signals from the TIAs into red and infrared PPG signals
- Low pass and high pass filters to precondition the acquired signals.

8.3.6.1 Micro–Controller unit (MCU)

An Atmel ATtiny 2313A-20SU *(Atmel corp, CA, USA)* micro-controller was used as a master clock and timing generator. The ATtiny 2313A-20SU is an 8-bit MCU with 18-programmable I/O lines and a maximum operating frequency of 20 MHz. As mentioned earlier in Section 8.3.3.2, the port-D of the MCU was used to generate two clocks: CMUX0 and CMUX1, for multiplexing the LEDs. Port B of the MCU was programmed to output another three clocks: MUX0, MUX1, and SMP_INH0. These clocks were used for synchronizing the SHA that separated the mixed PPG signals into red and infrared PPGs. The clocks from port-B were in synch with the clocks from port-D, as mistiming would lead to inappropriate sampling of red and infrared signals. Figure 8.7(b) and 8.19(b) show the clocks generated by port-D and port-B of the MCU. The MCU was programmed using the Atmel STK500 MCU programmer. A 'C' program (Appendix A) written in Win-AVR studio *(Atmel Corp, CA, USA)* was flash-programmed onto the MCU through the Serial

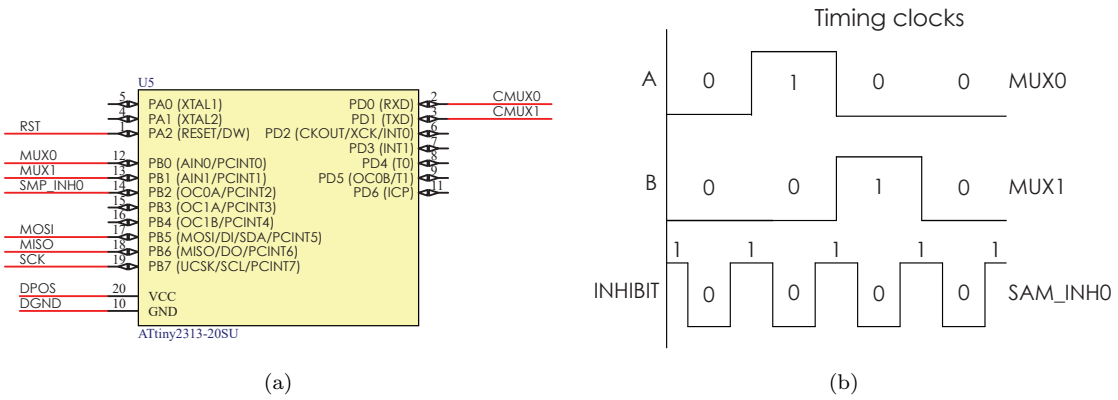

(a) (b)

FIGURE 8.19: (a) The pin-out of the ATtiny 2313A-20SU and (b) the clocks generated form Port–B of the micro-controller.

In-System Programming (ISP) header on the core module. The pin-out diagram of the ATtiny 2313A-20SU MCU is shown in Figure 8.19(a).

8.3.6.2 Time multiplexing for PPG signal sampling

As mentioned earlier, the photons detected by the photodetector in a PPG probe are continuously recorded as a voltage signal using the TIA. Direct sampling and digitisation of this signal is possible when the photodiode sees just one light source. In which case the signal can simply be sampled at the Nyquist rate.

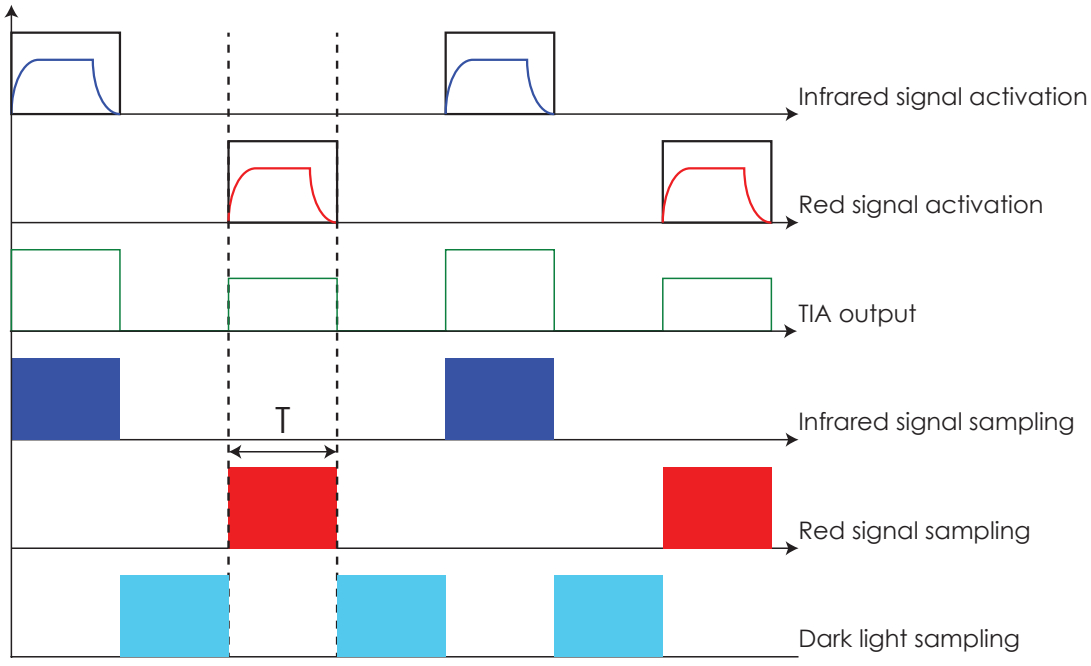

FIGURE 8.20: PPG signal sampling at two different wavelengths using time windowing

However, when there are two or more light sources, the photodetector cannot distinguish between parts of the light power received from different light sources. To overcome this limitation time windowing is used. An example of a two channel time windowing sequence usually used in pulse oximeters is shown in Figure 8.20. Although the time diagram might seem very straight forward, in practice the signal is not as clean as it is in Figure 8.20. Numerous high frequency distortions are mixed together with the useful PPG signal. When a light source such as an LED is switched from an 'off' to 'on' state and vice versa, there is a slight delay between the transitions, usually referred to as the transient response of a diode. During these transition states, the intensity of the light detected does not represent the true light level. Therefore, by sampling the PPG signals during the entire LED activation period as in Figure 8.20, the switching noise is also sampled.

To overcome this problem, a new schema was implemented in the 'ZenPPG'. In this new approach, a slight time delay was introduced between the switching of the emitters and the triggering of the demultiplexer sampling circuit. In this way, the photodetector output is sampled from the middle of the 'plateau' region of the signal as shown in Figure 8.21. This ensures that the detection circuit has enough time to settle before sampling. Thus producing an output signal that is more representative of the true light level. However, this schema requires the light source activation time window to be sufficiently long so that a proper sample can be acquired. Long light source activation windows mean low multiplexing rate and reduced number of optical channels. But since the output is only

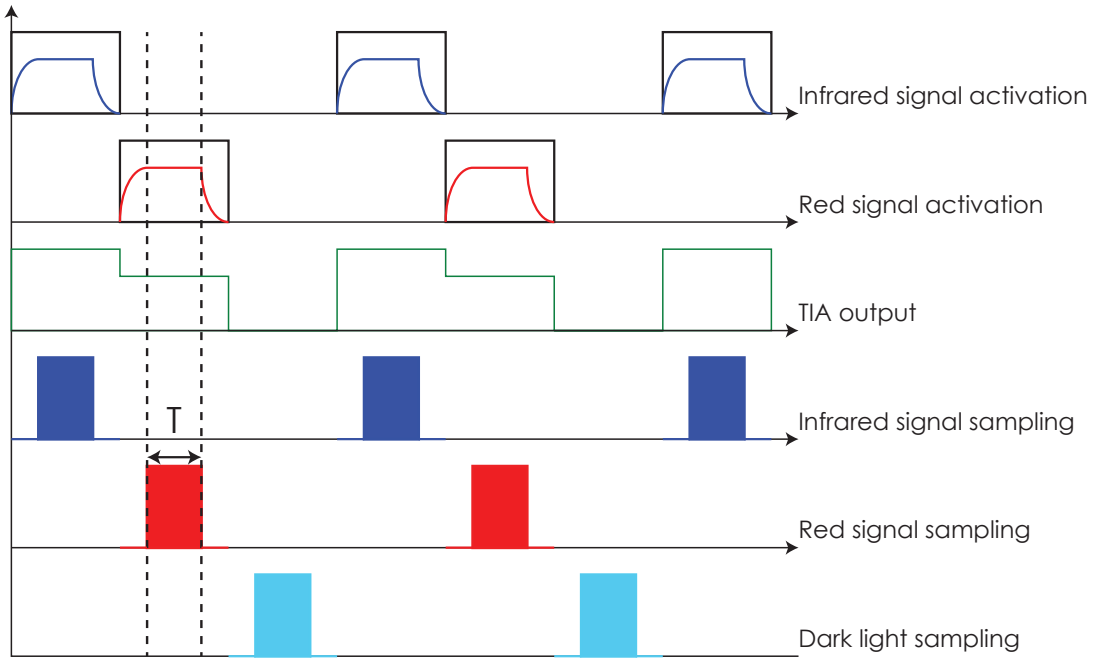

FIGURE 8.21: Time windowing solution for avoiding switching noise, by sampling at the plateau of the LED on time.

sampled in the middle of the plateau region, there is no need to sample dark light after activation of each LED. Instead, dark light can be sampled once both the LEDs are activated. Thereby improving the sampling time and multiplexing rate. In the current system the LEDs were multiplexed at 800 Hz.

8.3.6.3 Sample-and-Hold Amplifier (SHA)

The mixed voltage signal from the TIA was split into red and infrared PPG signals, using a sample and hold amplifier (SHA) circuit, which adopted the time windowing schema shown in Figure 8.21. The SHA circuit consisted of a switch (demultiplexer), an energy storage device (capacitor), and an output buffer, as shown in Figure 8.22.

The demultiplexer is a switch which connects its input to one of its many outputs lines depending on the commands from data select lines. The demultiplexer used is a double pole 4–throw (DP4T) analogue demultiplexer *(MC14052BD, ON Semiconductor, Arizona, USA)*. The clocks used to control the demultiplexer and its truth table are shown in Figure 8.6(b) and 8.19(b). The TIA outputs MIXS0 and MIXS1 were connected to the demultiplexer inputs X and Y as shown in Figure 8.22. In this circuit, when the control clocks MUX0, MUX1 and SAM_INH0 are at logical low, the output is on X0 and Y0. Similarly, when the MUX0 is at logical high, and MUX1 and SAM_INH0 are at logical low, the output is on X1 and Y1. Hence splitting the mixed voltage signal into infrared (X0 and Y0) and red (X1 and Y1) components.

However, when the PPG signal is split into red and infrared components, it is necessary to 'hold' the sampled voltage until the next clock pulse triggers a new acquisition. Hence a storage device i.e. the capacitor, is used to hold the sampled voltage. In the sample mode, the voltage on the hold capacitor follows the specific input voltage (i.e. red or infrared). In the hold mode, the demultiplexer switch is open, and the capacitor retains the voltage present before it was disconnected from the demultiplexer. The output buffer offers a high

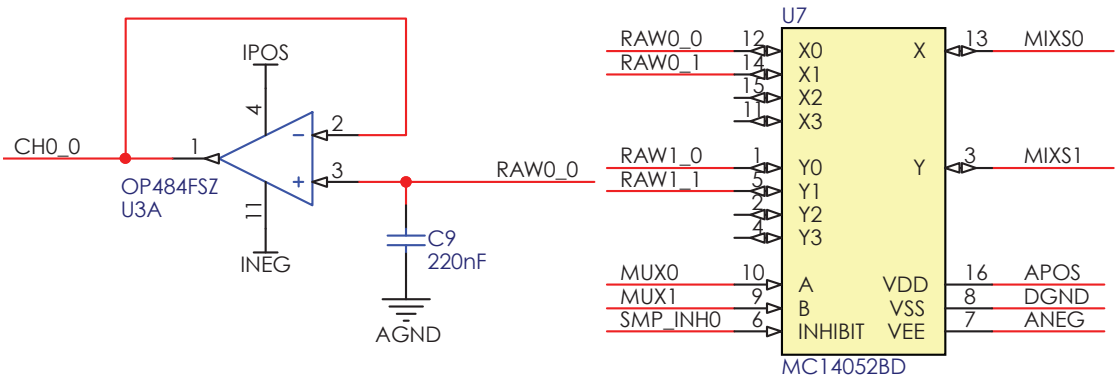

FIGURE 8.22: The circuit diagram of the SHA consisting of a switch (demultiplexer), an energy storage device (the capacitor), and the op-amp buffer.

impedance to the hold capacitor to keep the held voltage from discharging prematurely [272].

The performance of this circuit is mostly dependent on the switching frequency and the chosen capacitor value. If the value of the capacitor is too large then there is a corresponding increase in acquisition time and a reduction in bandwidth and slew rate. On the other hand, if the capacitor value is too small then the capacitor discharges quickly resulting in chopping effects and 'saw' shaped modulations. The frequency of switching also needs to be sufficiently large as low switching speeds result in the circuit being open for extended times, during which the capacitor can retain some of its charge. A 220 nF capacitor was used in the current system to provide optimal performance. Experiments showing the effect of hold capacitor on the acquired PPG signals is shown in Section 8.5.3.

The other parameters on which the SHA performance is based on are the passive output of the demultiplexer and the input impedance of the op-amp. Hence, careful consideration was taken when choosing the op-amp and the demultiplexer. Four SHA circuits were built to acquire red and infrared PPGs from both channels. In the current version, the dark light was not sampled.

8.3.6.4 Analogue filters

The outputs of the sample-and-hold amplifiers were fed through individual anti-aliasing filters with a cut-off frequency of 80 Hz. This is to stop the high-frequency switching noise or any pickup from the stray signals such as power lines from corrupting the PPG signals. The filter was designed with the help of specialised filter design software known as Filter Wiz PRO v3.0. This software automatically computes filter parameters and resistor-capacitor values, using predefined filter frequency response as its input. The designed circuit is a fairly simple passive RC filter stage providing a low-frequency path to the input of an op-amp buffer, as shown in Figure 8.23. The filtered PPG signals are passed

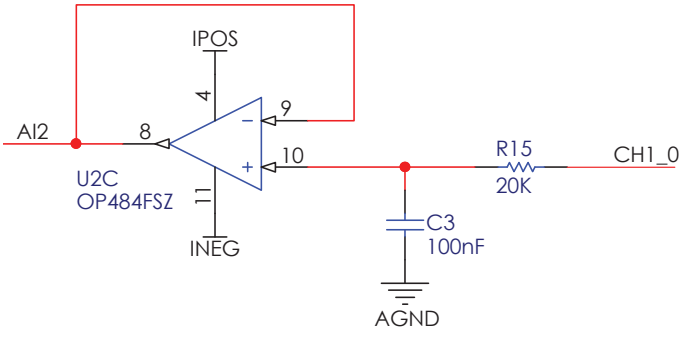

FIGURE 8.23: Anti-aliasing filter with a cut-off frequency of 80 Hz to reduce the bandwidth of the PPG signals.

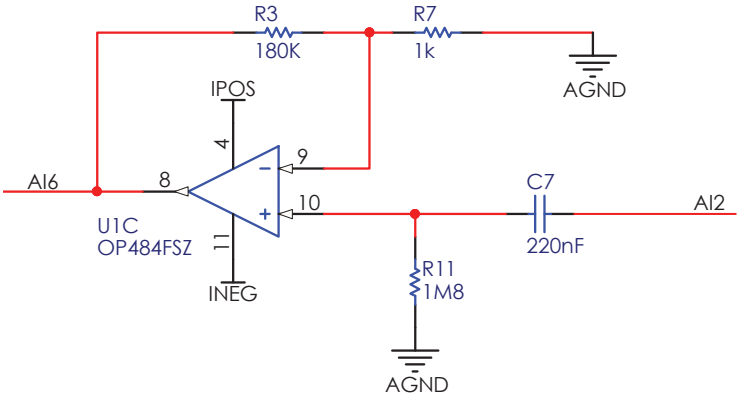

FIGURE 8.24: Highpass filter with a cut-off frequency of 0.4 Hz used to remove the DC component from raw PPG signals.

onto the NI DAQ card for digitisation and further analysis from the onboard 68-pin NI connector.

The lowpass filtered signals contain both AC and DC components, which can be separated digitally using digital filters. However, to increase the AC resolution, the lowpass filtered PPG signals were also passed through a high pass filter with a gain of 180. This ensured that the DC components were removed from the PPG signal and the AC signal was amplified nearly to the full range of the DAQ card. The filter designed is a passive RC high pass stage connected to a non-inverting gain amplifier as shown in Figure 8.24.

The back-end of the core module also consists of a battery monitoring circuit, which is a simple voltage divider that divides the 5 V main supply to 1 V. This 1 V signal is continuously sampled by the DAQ card, and displayed on the PC, hence giving the user an indication of the battery's state of charge.

8.3.7 Vital sign monitoring module

The vital sign monitoring module consists of an ECG channel and a respiratory channel. The module is designed such that it can easily be modified to accommodate other vital sign sensors such as temperature sensors, etc. Although the system consists of a pressure transducer (40PC001B, Honeywell, New Jersey, USA) to measure respiration rate, the sensor was not used in any of the experiments described in this thesis. Hence, it is not in the scope of the thesis to explain its design and performance.

A Lead I ECG amplifier was developed for monitoring the R waves of the QRS complex of the ECG signal, which were used as a timing reference for the PPG signals. The ECG signals were acquired by placing one electrode on the right arm or right side of the chest (red lead), and another placed on the left arm or the left side of the chest. A third electrode placed on the left leg or left hip was used as a reference. The differences between

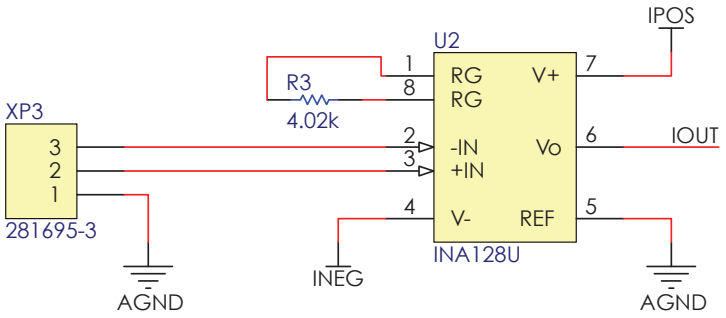

FIGURE 8.25: Circuit diagram of the instrumentation amplifier used in ZenPPG system.

these biopotentials were amplified using an instrumentation amplifier. The ECG signal acquired from the amplifier was band-pass filtered before being digitised and displayed on the PC. The electrodes were connected to the instrumentation in the system through a standard 6-pin AAMI connector. The instrumentation amplifier circuit in Figure 8.25 was constructed using INA128 *(Texas Instruments, Texas, USA)*, a general purpose instrumentation amplifier providing high common-mode rejection ratio (120 dB) and a very high input impedance ($10^{10}\Omega$). The gain of the instrumentation amplifier can be set with an external resistor, R_G, to up to 10,000, and is given by:

$$Gain(A) = 1 + \frac{50\ k\Omega}{R_G} \tag{8.8}$$

The value of R_G used in the circuit was 4 KΩ, providing a gain of 14 from the instrumentation amplifier.

Measurement of the ECG signal is, however, challenging due to the presence of the large DC offset and various interference signals. These interference signals include the 50 Hz interference from the power supplies, motion artifacts due to patient movement, and radio frequency interferences. Therefore, the signal from the instrumentation amplifier was filtered to remove these distortions using a band-pass filter.

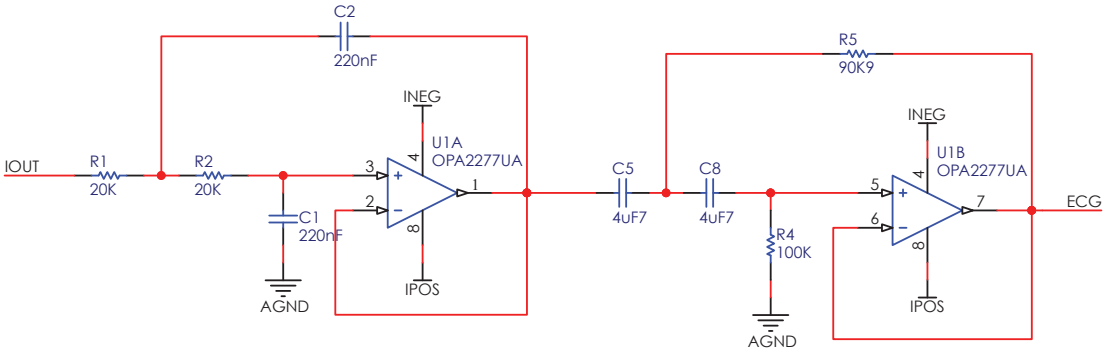

FIGURE 8.26: The second order Sallen-Key bandpass filter for limiting the bandwidth of the acquired ECG signal.

The band-pass filter used consists of a second-order Sallen-Key high-pass filter, to remove the DC component in the ECG signal, and a second-order Sallen-Key low pass filter which attenuated high frequencies. The lower and upper cut-off frequencies of the band-pass filter are 0.37 Hz and 36 Hz respectively. The band-pass filter is of unity gain with both resistors and capacitors of the same value, giving it a quality factor (Q) of 0.51. Figure 8.26 shows the band-pass filters used in the circuit.

8.4 Mechanical design and implementation

As mentioned earlier, a modular design approach was implemented in the mechanical design of the ZenPPG system, whereby the entire system was split into sub-systems which acted independently and were connected together through a bus interface. In addition to re-usability, this approach provides efficient troubleshooting, since bugs can be traced to specific system modules.

The ZenPPG system was designed with the aid of 3D CAD modelling software solutions. The inclusion of 3D modelling and electronic design automation in the design process has made it easier to recognise potential design flaws, better visualise how the modules interface with each other in the system and in reducing the number of revisions during manufacturing.

8.4.1 Enclosure

All six modules in the system along with a dual 9 V PP3 battery case were designed to fit inside a portable unit measuring 160 × 103 × 56.13 mm. The portable enclosure was made from clear anodized aluminium *(1455N1602, Hammond Manufacturing, Ontario, Canada)*. The rugged aluminium body consists of a slide removable belly plate and extruded internal slots that are used to mount the PCBs horizontally. The enclosure consists of two replaceable metal endplates which were milled in the laboratory to accommodate the connectors. An anodized aluminium body was used so that it can be connected to the ground plane, providing better shielding, reducing EMI and minimize electrical shock hazard.

The front panel of the system incorporated two standard DE9 connectors, an AAMI ECG connector, and a panel mounted female lure. These connectors are used to connect the PPG probes, the ECG cable and the breathing mask. The rear panel consists of an on/off switch to control the system, an LED indicator, a 68-pin serial bus connector for interfacing with National Instruments data acquisition card, and inlets to access the trimmers which

can be used to control the LED currents. The rear panel also hosts the mini USB connector and the battery case which are used for powering the system.

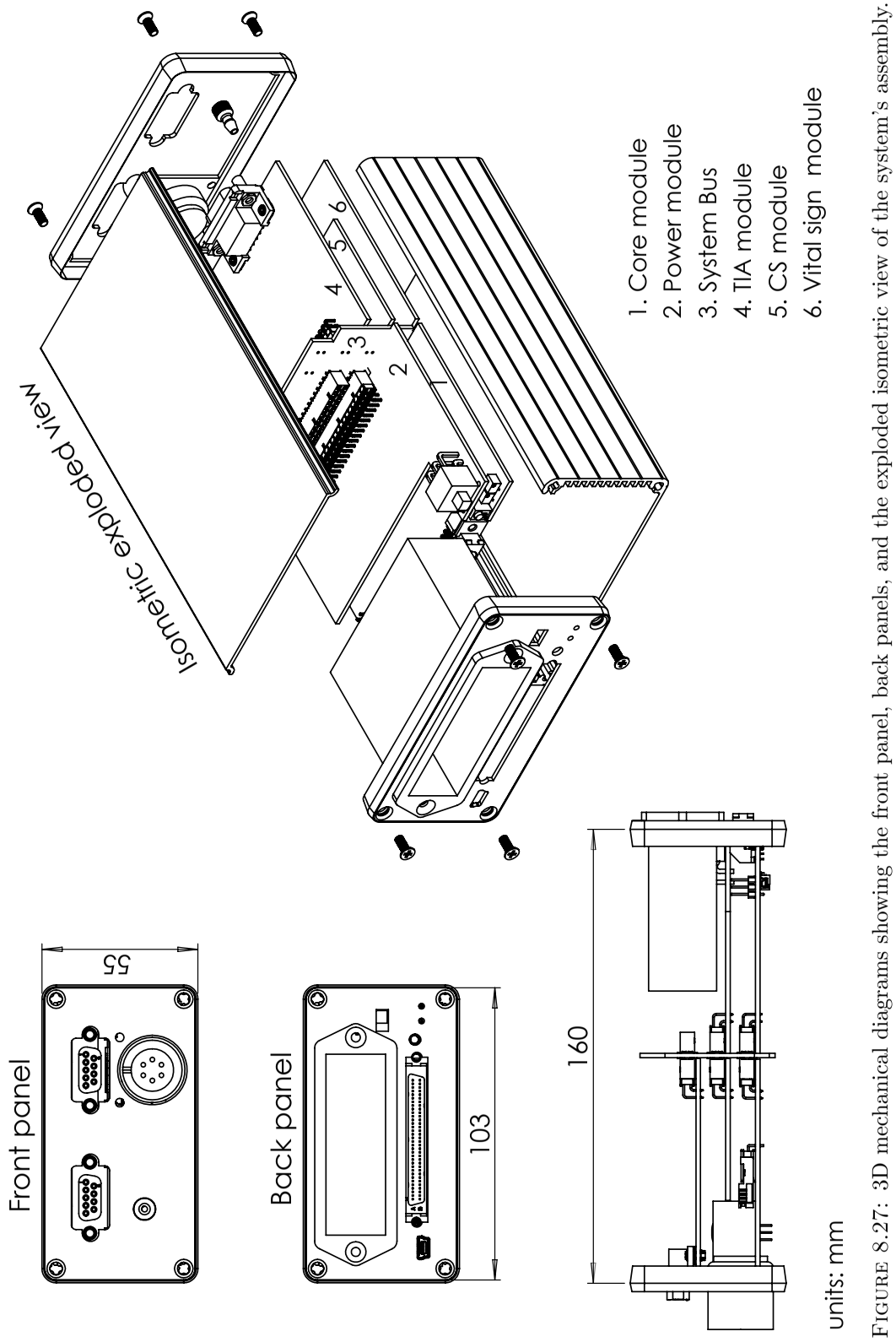

FIGURE 8.27: 3D mechanical diagrams showing the front panel, back panels, and the exploded isometric view of the system's assembly.

The 3D mechanical diagrams of the front and back panels, and the exploded isometric views of the system's assembly are shown in Figure 8.27. The CAD software used in the systems' design was Solid Works 2012 *(Dassault Systemes SolidWorks Corp., Velizy, France)*. The front and back panels were manufactured by using the Bungard Computer Controlled Drilling machine - CCD2 (Bungard Elektronik, Windeck, Germany).

8.4.2 PCBs

All the modules used in the processing system were designed using an electronic design automation software package known as Altium Designer *(Altium Limited, Sydney, Australia)* and were manufactured using a Computer Numeric Control machine (CNC). The dimensions of all the modules were $100 \times 78.95 \times 1.6$ mm, except for the current source module and the system bus. The dimensions of the CS module and system bus are $100 \times 50 \times 1.6$ mm and $95 \times 47.6 \times 1.6$ mm respectively. Each and every module in the system is equipped with gold plated through-hole right angle 50-way header with connects to the system bus.

Schematic symbols and 3D footprints for all the components used in the system were first designed in Altium. Using these schematic symbols, the schematic circuit diagrams were implemented for each module. The completed schematics were then transferred onto double sided virtual PCBs for component placement and routing. The shape and dimensions of the PC boards were defined using the STEP files (3D models) imported from Solid Works. Design rules and constraints such as routing width, routing topology,

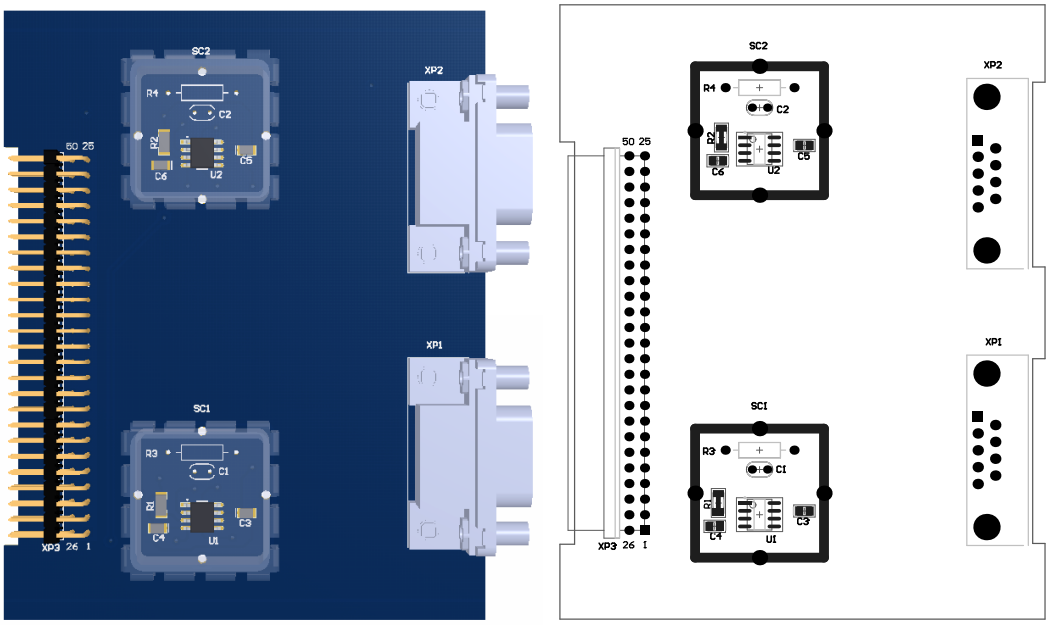

(a) (b)

FIGURE 8.28: The 3D model and the assembly drawing of TIA module.

component clearance, via to via difference, and the clearance between the pads were set for the virtual PCBs before routing. The maximum and minimum track width used in routing all the modules were 4 mm and 2 mm respectively. The 3D model and assembly diagram of one of the finalised virtual PCBs (TIA module) of the system is shown in Figure 8.28.

Once the design of all the PCBs were ready, Computer Aided Manufacturing (CAM) files such as Numerical Control (NC) drill files and Gerber files were generated for all the PCBs in the system. These files were then exported into a software package known as LPKF CircuitCAM *(Tracks Laser & Electronics Ltd, Berkshire, UK)* to create milling/routing and drilling data in the file format appropriate for the CNC machine (G-code). The Bungard CCD2 CNC was then used to manufacture PCBs. Double sided copper clad boards of 1.6 mm thickness were used to manufacture the PCBs. Along with the PCBs, soldering paste stencils used to transfer solder paste onto bare circuit boards were manufactured.

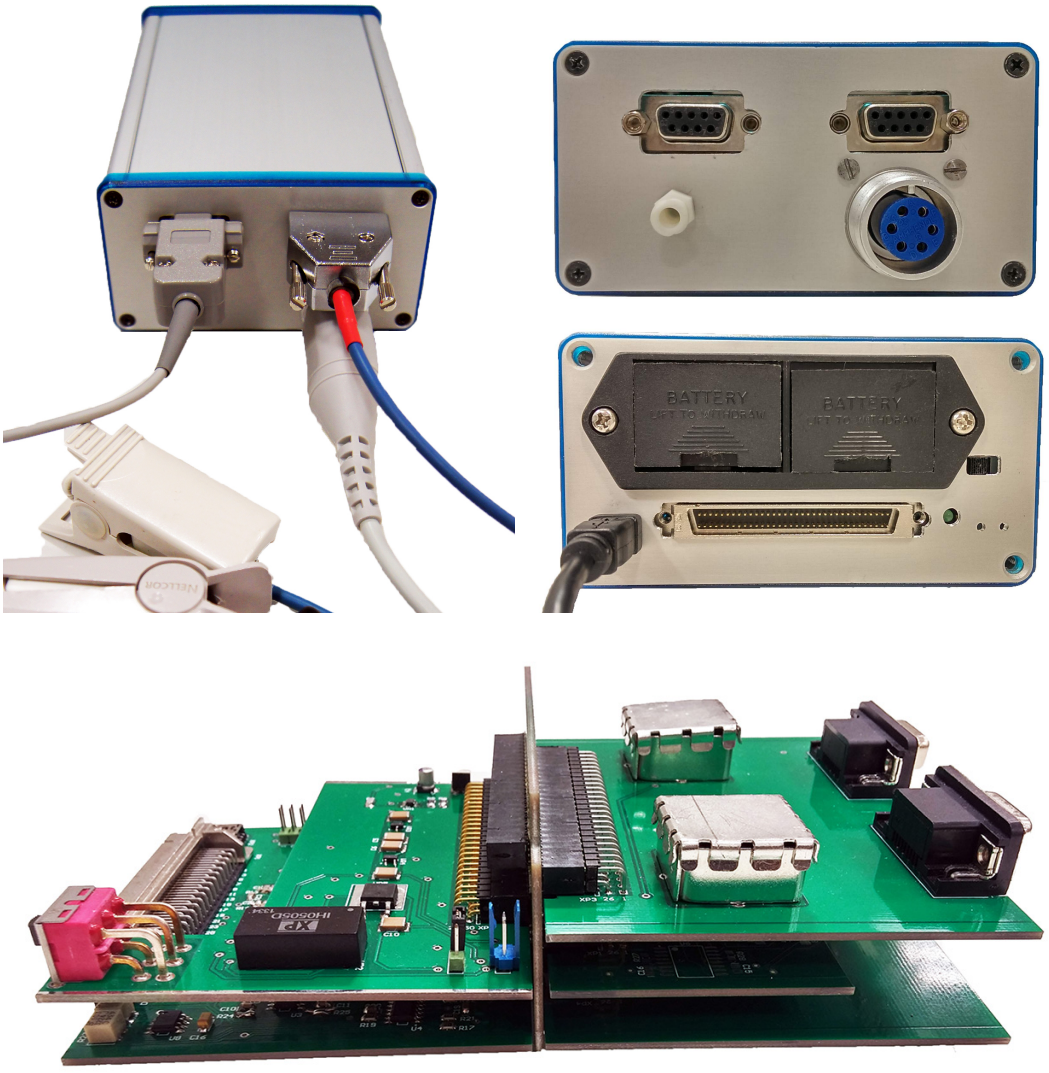

FIGURE 8.29: Photographs showing the front and back panel of the ZenPPG system along with the PCB assembly.

The PCBs were then tin plated using a tin sulphate solution to protect copper tracks from oxidising, hence preserving its solderability. The tin plated PCBs were then through hole plated to connect the top and bottom layers.

Using the soldering paste stencils and the assembly drawings, the surface mount components were placed on the respective pads and were soldered using a reflow soldering oven *(CIF-FT02, C.I.F, France)*, maintained at 200°C. Through hole components were hand soldered using a soldering iron. The photographs of the prototype ZenPPG system showing the front panel and the mechanical assembly of the PCBs is given in Figure 8.29.

8.5 Verification and measured performance

Following the design and fabrication of the ZenPPG system, the individual circuits within the system were tested thoroughly to verify the system's performance. The details of the testing conditions and the results obtained are described in this section.

8.5.1 Emitter driver circuit

The components within the emitter driver circuit, namely the RCV circuit, the multiplexer, the voltage attenuator, the modified Howland current source and the current monitoring circuit were tested together. Since the design of both the PPG channels is identical, they are described together. A 4-channel mixed signal oscilloscope and function generator (Agilent MSO-X 4024A, Agilent Technologies, CA, USA) was used to test the circuit's performance.

8.5.1.1 Test conditions

Two constant DC signals of amplitudes +1 V and -1 V were fed through the RCV circuits on channel 1 using the dual channel function generator. The output of the emitter driver circuit was then measured at points P_1 (RCV circuit output), P_2 (multiplexer output), P_3 (attenuator output) and P_4 (Current monitor output), as shown in Figure 8.30 using the oscilloscope. A two wavelength finger PPG probe (described in Chapter 7) was connected to the system during testing. The results displayed on the oscilloscope were stored on a

FIGURE 8.30: Functional diagram of the emitter driver circuit showing various measurement points– P_1, P_2, P_3, P_4.

USB stick in a comma-separated values (.CSV) file format. These text files were later plotted in MATLAB *(The MathWorks Inc., Massachusetts, USA).*

8.5.1.2 Results

The output of the emitter driver circuit measured at points P_1 P_2 P_3 and P_4 are displayed in Figure 8.31. The output measured at each point is accurate and is representative of the calculated voltage. At point P_1, the output of the circuit is $1/5^{th}$ of the input signal (± 1 V), as the RCV circuit divides the input by 5. At P_2, the ± 0.2 V are multiplexed to generate a switched signal fluctuating from 0.2 to -0.2 V by the multiplexer. The duty

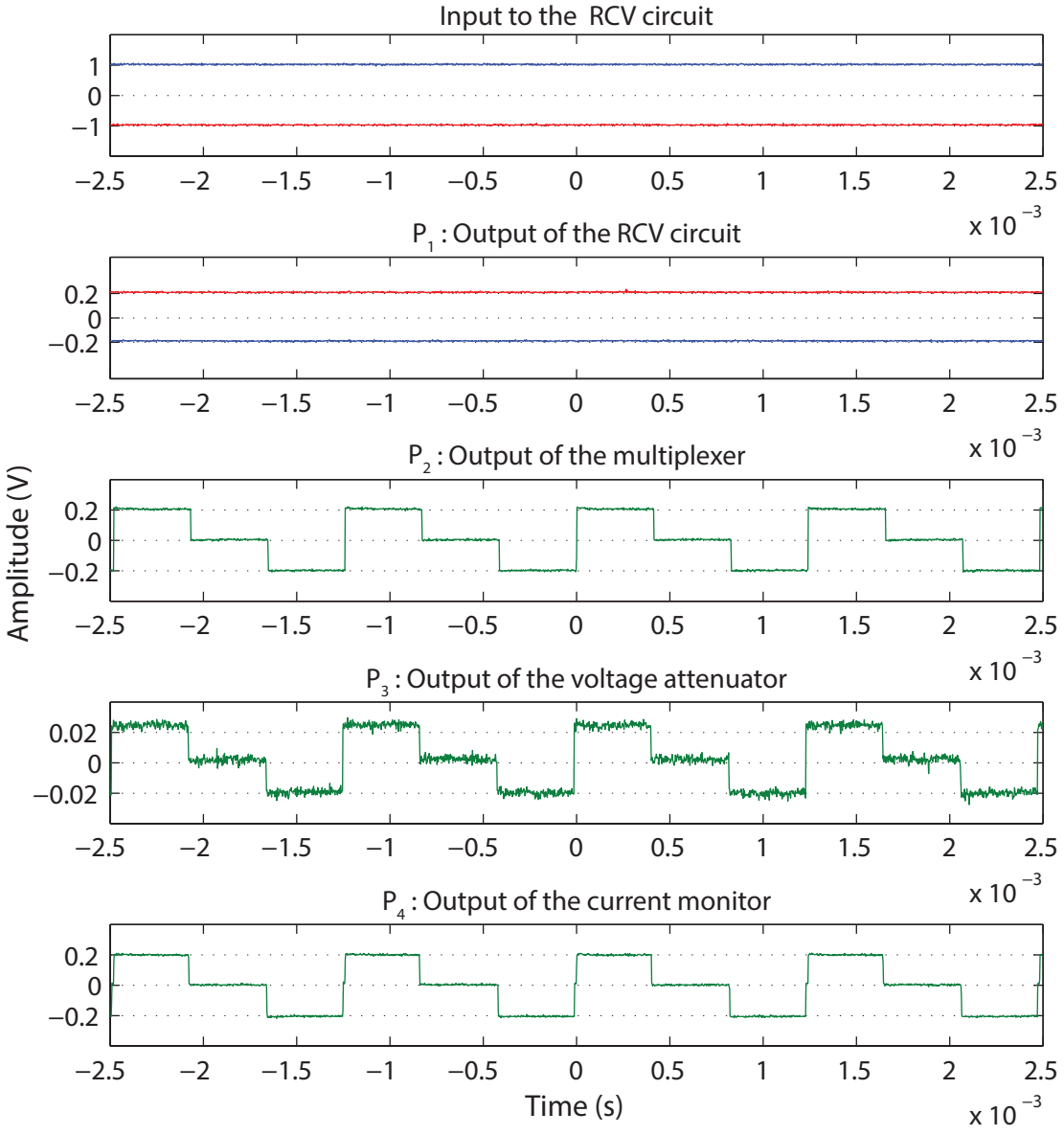

FIGURE 8.31: Output of the emitter driver circuit measured at various points in the circuit: P_1–RCV ciruit, P_2–multiplexer, P_3–voltage attenuator, P_4–current monitor.

cycle of the signal generated is 33%. The output of the voltage attenuator at P_3 is $^1/_{10}{}^{th}$ of the multiplexed signal. These ±20 mV are converted by the Howland current source into proportional current, i.e. ±20 mA. The current across the load resistor (20 mA) is sensed by the instrumentation amplifier and is amplified 10 times (0.2 V) to generate a signal that can be sampled by the DAQ card at P_4.

8.5.2 Trans-impedance amplifier (TIA)

As mentioned earlier in Section 8.3.5 the zero biased TIA circuit shown in Figure 8.18 can sometimes display complex AC behaviour, hence careful consideration is required in stabilising the amplifier. Three important parameters that determine the TIA's performance are the op-amp bandwidth (should be very high), the phase compensation capacitor (should be very small) and the photodiode junction capacitance (should be fairly small). However, the choice of the op-amp bandwidth and photodiode junction capacitance are sometimes limited either by the application or availability. Hence, C_f plays a key role in providing stability to the amplifier.

The calculated value of C_f for the circuit shown in Figure 8.18 is 0.3 pF, which is very small and is not available as a standard capacitor. The op-amp and the photodiode used in the design have high bandwidth (90 MHz) and small parasitic capacitance (10 pF), hence, in theory, a slightly larger capacitor can be used to stabilise the circuit without reducing the circuit's useful bandwidth. Moreover, due to non-linearities in the components, choosing compensation capacitance is most often by trial and error method. Another more rigorous method, which is considerably faster than the trial and error approach, is to use simulations to gain more insight about the loop behaviour over frequency. Hence, both the methods were employed while configuring C_f for TIA circuit.

8.5.2.1 Test conditions

Simulations– SPICE simulations were carried out to assess the loop stability of the TIA in NI Multisim 2013 *(National Instruments, Texas, USA)*. The closed loop I-to-V gain transfer function, open loop gain, Phase Margin (PM), and noise gain analysis were performed on the circuit by varying the feedback capacitor (C_f). The closed-loop AC transfer function was measured without the capacitor first and then with the capacitor at 0.3 pF, 5 pF, 10 pF, 47 pF and 100 pF, to determine the change in -3dB bandwidth. Similarly, the PM and the noise gain of the circuit was quantitatively determined at each capacitor value. The results were then compared to choose the optimal phase compensation capacitor.

Trial and error method– Transient analysis was carried out to measure the step response of the TIA with different phase compensation capacitors. In this method, the change in the

TIA output, to a change in the C_f value was recorded and compared using an oscilloscope. The output was first recorded with no C_f, and then with C_f at 5 pF, 10 pF, 47 pF and 100 pF. The gain resistor R_f was kept constant at 270 kΩ, throughout the experiment. The test was carried out with the finger PPG probe connected to the ZenPPG system. The output recorded by the oscilloscope was then plotted in MATLAB and compared. Based on the quantitative results from simulations and eye-balling the output of TIA during the trial and error method, C_f was chosen.

8.5.2.2 Results

Simulations – The simulated closed-loop I-to-V gain response of the TIA without the capacitor, and with the capacitor at 0.3 pF, 5 pF, 10 pF, 47 pF and 100 pF is shown in Figure 8.32. With no capacitor in the feedback loop of the TIA, the gain curve shows noise gain peaking of 8.5 dB just before the -3 dB frequency (2.8 MHz). This indicates that the circuit is unstable. With a 0.3 pF capacitor in the feedback loop, the gain peaking is mostly reduced, and the -3 dB frequency is shifted to 2 MHz. Similarly, with an increase in capacitance to 5 pF, 10 pF, 47 pF and 100 pF the bandwidth (-3 dB) is further reduced to 117 kHz, 59 kHz, 12.5 kHz and 5.9 kHz. Since the -3dB point at 47pF and 100pF is close to the sampling clock (SAM_INH0: 2.8 kHz) frequency, a capacitor ≥47 pF cannot be used. From these results, it is safe to assume that the optimal capacitance required for

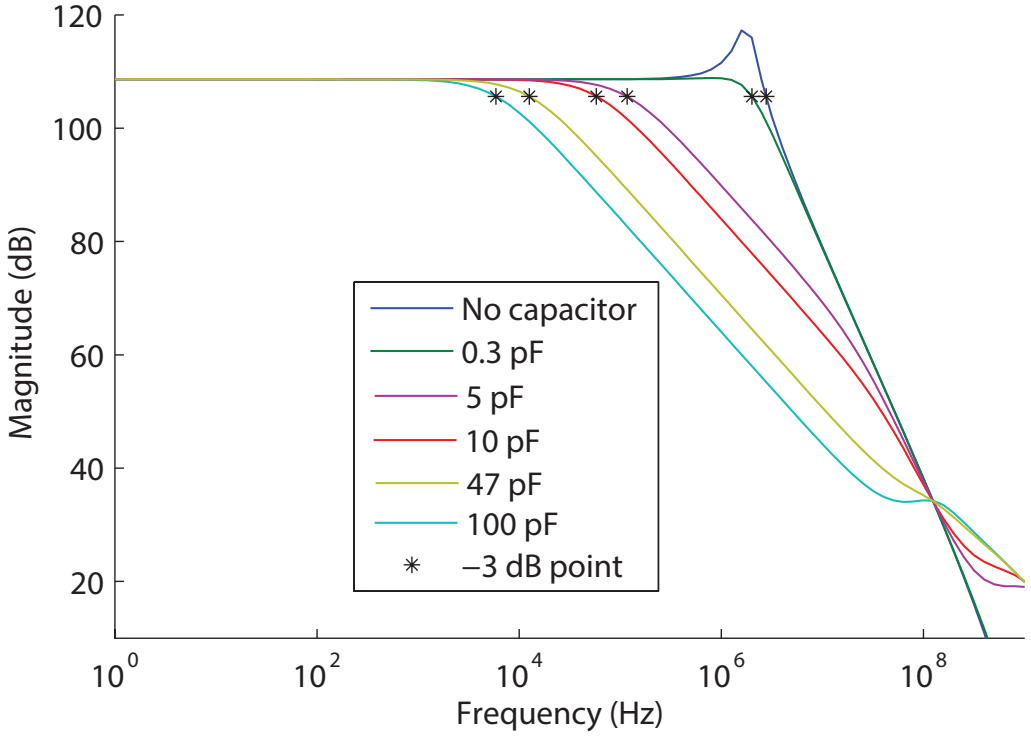

FIGURE 8.32: Closed-loop I-to-V gain response of the TIA without the capacitor, and with capacitor at 0.3 pF, 5 pF, 10 pF, 47 pF and 100 pF.

stabilizing the TIA is 5 pF or 10 pF, as they offer no gain peaking and reasonably large bandwidth.

However, before settling on a choice, the stability of the TIA was tested by finding the open-loop phase margin (PM) and the noise gain of the TIA circuit. PM is the phase angle of the open-loop gain transfer function when it crosses 0 dB. The value of PM should always be greater than 45° for good TIA stability. The PM of the circuit was first measured without C_f in the feedback loop and then with C_f at 0.3 pF, 5 pF, 10 pF, 47 pF and 100 pF. The simulated open-loop gain and phase response of the TIA without C_f, and with C_f (at 0.3 pF, 5 pF, 10 pF, 47 pF and 100 pF) is shown in Figure 8.33.

The low phase margin of 18.9° (Figure 8.33) with no capacitor in the feedback loop confirms the closed loop frequency response peaking which is evident in Figure 8.32. With the introduction of a 0.3 pF capacitor in the feedback loop, the PM of the circuit has increased to 62.5°, hence stabilising the circuit. Similarly, when the C_f was increased to 5 pF and 10 pF, the PM has increased to 86° and 84°. The PM is fairly flat in the capacitance range between 1 pF - 10 pF. With a further increase in capacitance to 47 pF or 100 pF, the phase angle has started to decrease, indicating overcompensation. The measured phase angle in these cases was 78° and 73°. In these situations the TIA will become unstable, again leading to ringing and noise in the acquired signal.

To further help find the optimal compensation capacitor value, and support the phase margin analysis, noise gain analysis was performed for various values of C_f. The noise gain of the TIA at various values of C_f was plotted along with the open-loop gain of the op-amp, and is shown in Figure 8.34. The optimal C_f value is the one which places a pole on the noise gain function at the frequency (f_i = 1.48 MHz) where it intercepts the op-amps (OPA380) open-loop gain. Here, $f_i = \sqrt{f_{zf}.f_c}$, $f_{zf} = 1/2\pi.R_f.(C_i+C_f)$ and f_c = op-amp gain bandwidth of 90MHz. From Figure 8.34, it is apparent that C_f= 0.3 pF is the optimal compensation capacitor.

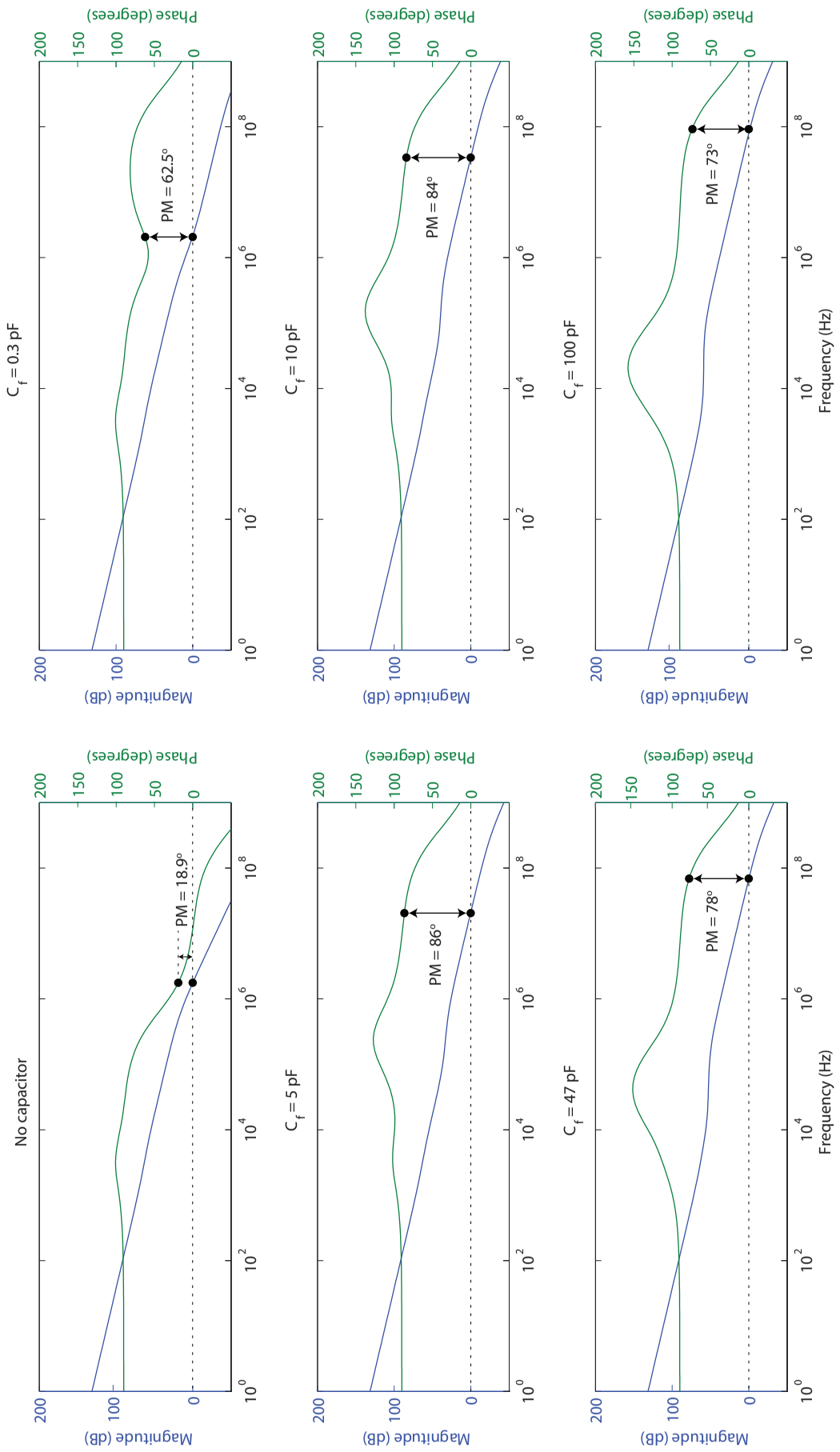

FIGURE 8.33: The simulated open-loop gain and phase response of the TIA without C_f, and with C_f at 0.3 pF, 5 pF, 10 pF, 47 pF and 100 pF. The phase margin should be $> 45°$ for good TIA stability.

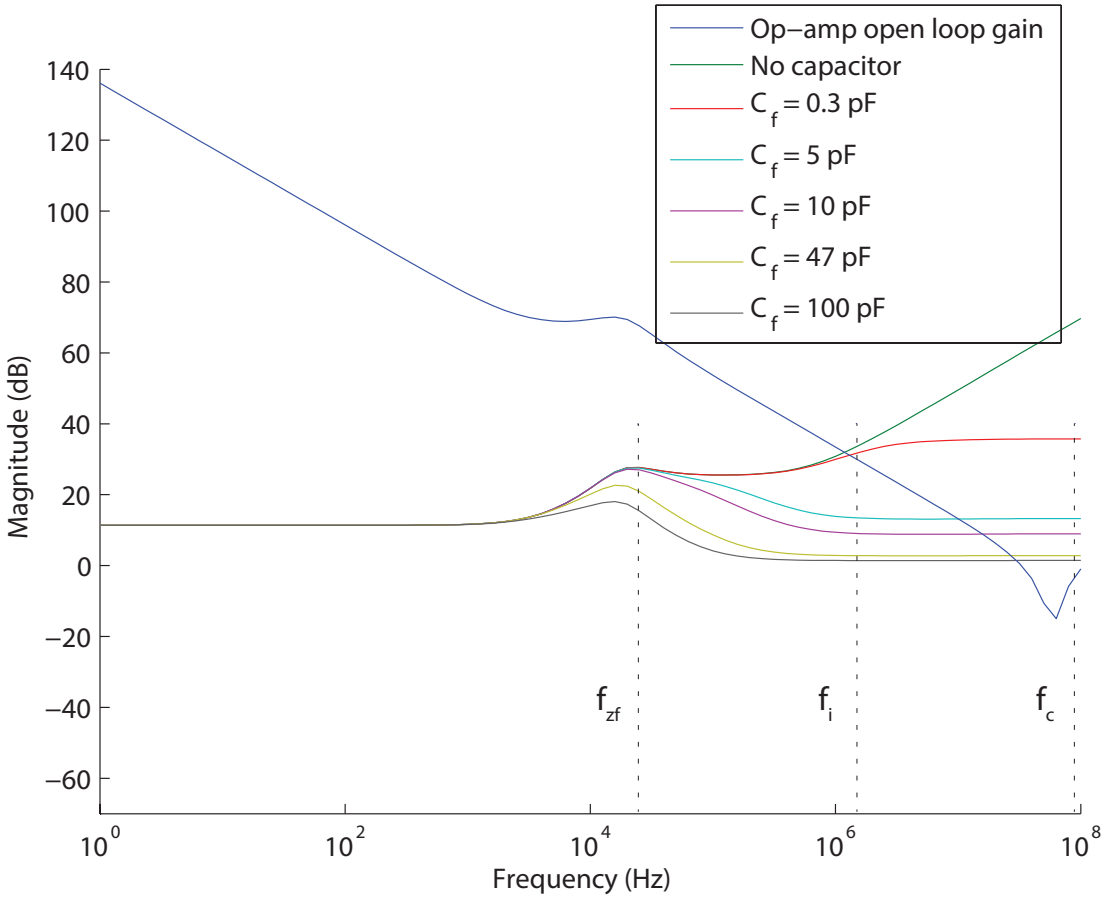

FIGURE 8.34: Noise gain of the TIA at different values of C_f plotted along with the open-loop gain of the op-amp. The optimal C_f is the one which places a pole on the noise gain function at the frequency where it intercepts the op-amps open-loop gain.

With an increase in C_f (5pF or 10 pF), the noise gain is further reduced and the open loop gain curve intersects the noise gain plot in the flat (stable) region. This leads to overcompensation, and a reduction in bandwidth but provides stability. With $C_f = 47$ pF or 100 pF the noise gain is close to 0 dB, which is below the stable gain of the OPA380 op-amp. Hence, these capacitors should not be used. The transimpedance circuit's output noise voltage was calculated for various capacitors using a Total Noise Calculator tool [273]. The total noise (V_T) and the signal-to-noise ratio (SNR) of the TIA circuit with a 0.3 pF capacitor were 669.66 μV and 61.65 dB. With a 5 pF capacitor in the loop, the V_T was 178.6 μV and S/N was 73.13 dB. Finally with a 10 pF capacitor, the V_T and S/N were 135.4 μV and 75.53 dB.

From the closed loop transient response, phase margin analysis and noise gain analysis, it is fair to say that a feedback capacitor of 10 pF provides good phase compensation and stability with large enough bandwidth (59 kHz). This can be verified by obtaining the closed-loop step response of the TIA with different values of C_f, as shown in Figure 8.35. The plot confirms that smaller C_f (0 pF or 0.3 pF) values could make the amplifier unstable

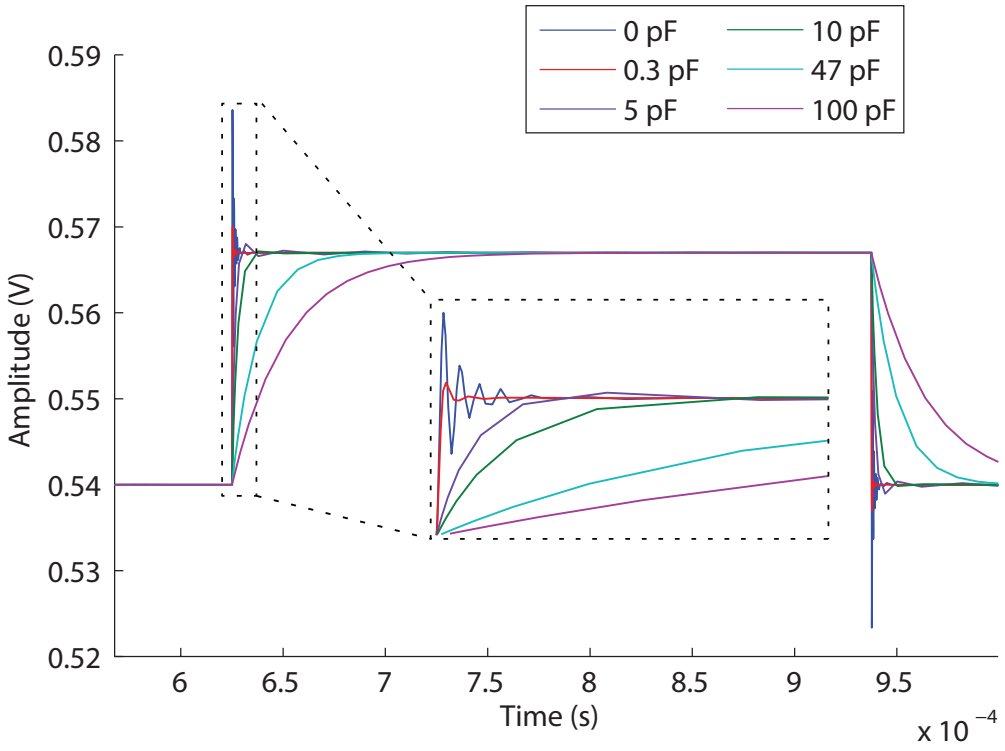

FIGURE 8.35: The closed-loop step response of the TIA with C_f = 0 pF, 0.3 pF, 5 pF, 10 pF, 47 pF, 100 pF

and produce long ringing noise, and larger C_f (47 pF, 100 pF) could have long settling times while optimum C_f (5 pF or 10 pF) results in a refined step response with no ringing.

Trial and error method – Having found the optimal capacitor value through simulations, experiments were carried out to check if the TIA performance matches the simulated results. The step response of the TIA was measured for various capacitor values, similar to the simulation in Figure 8.35. The changes in the output of the transimpedance amplifier due to variations in feedback capacitance are shown in Figure 8.36. Without a feedback capacitor in the TIA, large ringing and noise were observed. This reflects on the large gain peaking observed in AC transfer function (Figure 8.32). With a capacitor in the feedback loop of the TIA, the ringing noise and the overshoot started to decrease. Optimal performance with no overshoot, ringing or overcompensation was observed when the capacitor value was 10 pF. As the value of the capacitor was further increased to 47 pF and 100 pF, the leading and trailing edges of the signal became smoother (overcompensation). Since the signal is only sampled in the middle of the plateau region (as shown in the last sub-plot of Figure 8.36), this overcompensation at 47 pF or 100 pF might not be a major problem. However, as mentioned earlier, the bandwidth of the TIA decreases

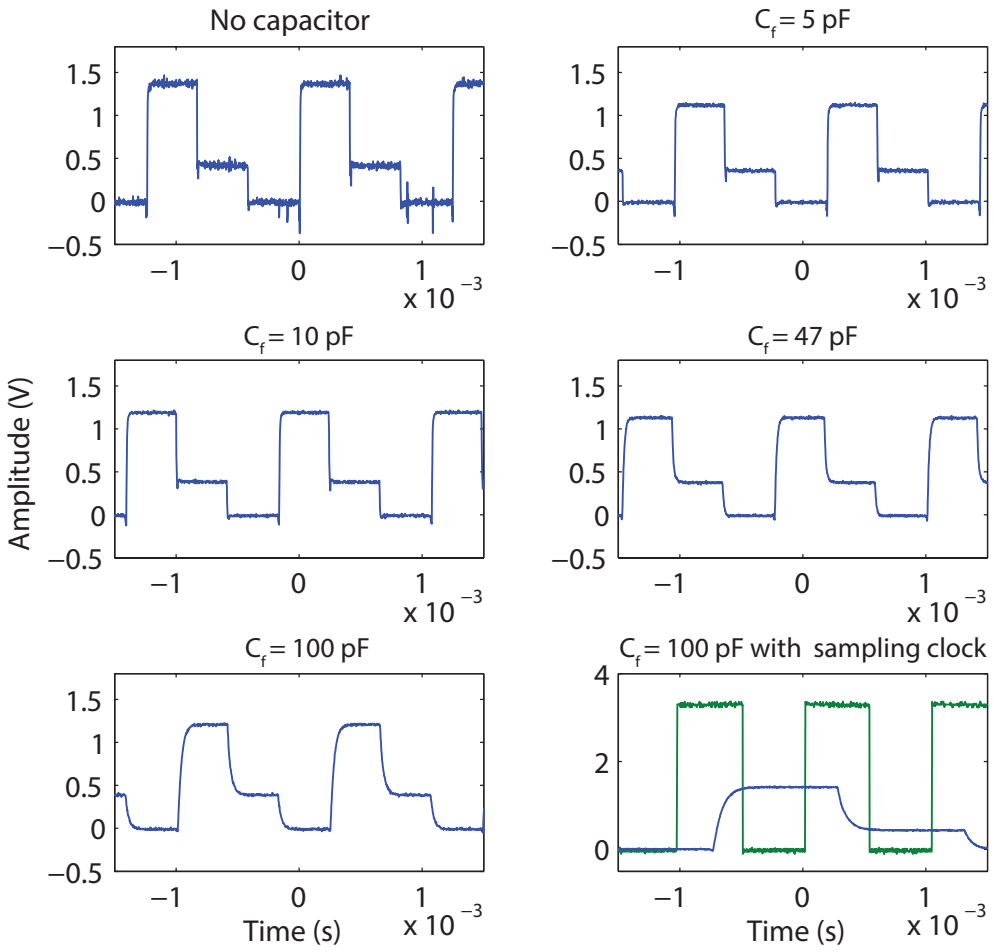

FIGURE 8.36: The changes in the output of the transimpedance amplifier due to variations in feedback capacitance

linearly with an increase in the feedback capacitance. Hence to have a reasonably large bandwidth and a stable TIA with no noise, a 10 pF capacitor was chosen.

8.5.3 Sample-and-hold amplifier

As mentioned in Section 8.3.6.3, the size of the hold capacitor in the SHA is critical for optimal performance of the amplifier. A low-value capacitor provides fast acquisition, but will increase errors due to hold step and droop (voltage difference in hold mode) caused by amplifier bias current. A very large hold capacitor, on the other hand, results in increased hold time and decreased bandwidth. Hence for good SHA performance, a large enough capacitor that is consistent with acquisition time and dynamic sampling error requirements is needed. To find the optimal hold capacitor for the SHA, experiments measuring the static and dynamic performance of the SHA were carried out with various values of hold capacitors.

8.5.3.1 Test conditions

Simulations– SPICE simulations were carried out in NI Multisim 2013 to find an optimal capacitor for the SHA shown in Figure 8.22. The performance characteristics such as hold mode droop, pedestal error, voltage offset, gain error and aperture delay time were measured for various hold capacitor values. The capacitor values used in the testing were 22 nF, 47 nF, 68 nF, 100 nF, 150 nF, 220 nF, 330 nF and 470 nF. The optimal capacitor was determined by comparing the errors and finding the best compromise between errors.

Experimental testing– following the simulations, the transient response and the signal-to-noise ratio of the SHA were measured to verify circuits performance. Similar to the simulations, the capacitor values used in the testing were 22 nF, 47 nF, 68 nF, 100 nF, 150 nF, 220 nF, 330 nF and 470 nF. A 1 Hz sine wave with an amplitude of 0.2 V and DC offset of 1 V was used as the input signal for testing the transient response of the SHA amplifier. The output was recorded using an oscilloscope.

The SNR of the SHA's output was also determined at each capacitor value. For this test, a pre-recorded PPG signal with a frequency of 0.84 Hz was used as the input to the SHA. The output of the SHA at each capacitor value was recorded with NI DAQ card. The off-line spectral analysis was performed in MATLAB on the acquired data, to extract the frequency content of the output signal in the 0-20 Hz range. The frequency spectrum acquired at each capacitor value was normalised to the component with the maximum power (i.e. cardiac component) to highlight the changes in the power of the noise component. Then by comparing the frequency spectrum of the input signal to the output signal, the noise component was located. The power of the noise component was then used to calculate the SNR.

8.5.3.2 Results

Simulations – Table 8.2 shows the dynamic and static characteristics of the SHA measured with different hold capacitors. The offset voltage is the voltage difference between the input and output when the input voltage is zero and the SHA is in sample mode. For good accuracy, the offset voltage must be lower than half of the least significant bit (LSB). LSB is given by

$$LSB = \frac{Full\ scale\ resolution\ (FSR)}{2^{n+1}} = \frac{10\ V}{2^{16+1}} = 76.29\ \mu V; \quad n\ is\ the\ no.\ of\ bits \tag{8.9}$$

The simulations reveal that the offset voltage in the sample mode is much smaller than $^1/_2$ LSB (38.14 μV) in all cases.

TABLE 8.2: Shows the dynamic and static characteristics of the SHA at different values of hold capacitance

Capacitor	SHA characteristic					
	Offset voltage	Gain error	Pedestal error	Effective aperture time	Hold mode droop	Acquisition time
22 nF	6.863 μV	2.591 μV	−38.6 μV	6.06 μs	−353.7 $^{\mu V}/_{ms}$	1.72 μs
47 nF	6.859 μV	0.406 μV	−16.5 μV	5.82 μs	−165.8 $^{\mu V}/_{ms}$	2.91 μs
68 nF	6.861 μV	−1.44 μV	−11.1 μV	5.64 μs	−114.6 $^{\mu V}/_{ms}$	4.27 μs
100 nF	6.861 μV	−3.758 μV	−7.5 μV	5.08 μs	−77.8 $^{\mu V}/_{ms}$	6.34 μs
150 nF	6.861 μV	−8.387 μV	−4.88 μV	3.36 μs	−51.8 $^{\mu V}/_{ms}$	8.81 μs
220 nF	6.861 μV	−1.066 μV	−3.23 μV	1.99 μs	−31.1 $^{\mu V}/_{ms}$	13.2 μs
330 nF	6.861 μV	−2.106 μV	−2.02 μV	1.37 μs	−20.7 $^{\mu V}/_{ms}$	18.8 μs
470 nF	6.861 μV	−4.052 μV	−1.52 μV	1.18 μs	−16.5 $^{\mu V}/_{ms}$	27.6 μs

The gain error is the deviation of the output voltage from the input voltage (excluding the offset voltage) when the SHA is in sample mode. For absolute accuracy, the gain error should be

$$\Delta A_V = \frac{V_{OUT} - V_{IN}}{V_{IN}} < \frac{1}{2^{16+1}} = 7.629\ \mu V \tag{8.10}$$

The results from simulations show the gain error of the SHA to increase with an increase in the hold capacitor value. The minimum (0.00001% of the FSR) and maximum (0.0004% of the FSR) gain error was seen with 47 nF and 470 nF capacitors.

The pedestal error, as shown in Figure 8.37, is the offset voltage that appears at the SHA output due to the sample-to-hold transition. Pedestal error must be less than $^1/_2$ LSB for good accuracy. The pedestal error measured with the 22 nF hold capacitor was 38.6 μV, which is marginally higher than $^1/_2$ LSB. Hence, a 22 nF capacitor is not suitable for good accuracy. In all other cases, the pedestal error was much smaller than $^1/_2$ LSB and has decreased with an increase in hold capacitance.

The effective aperture time (Figure 8.37) is the time delay between the generation of the hold command and the appearance of final held voltage that exists on the hold capacitor. For an ideal SHA, this delay should be as small as possible. The simulations show the effective aperture time to decrease with an increase in hold capacitance, suggesting a large capacitor to be ideal for good accuracy.

Hold mode droop is the rate at which the SHA output voltage changes in hold mode due to leakage from the hold capacitor. In applications such as PPG, where the sampled voltage must be held for long periods of time, the voltage drop should not be more than $^1/_2$ LSB during the hold time. The 22 nF, 47 nF, 68 nF, 100 nF and 150 nF capacitors produce

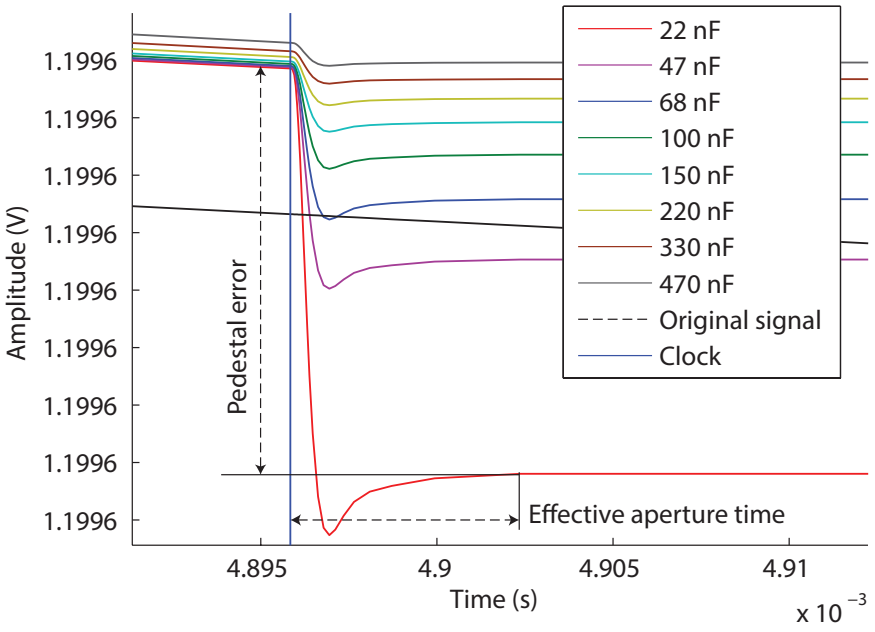

FIGURE 8.37: The sample-to-hold transition of the SHA with various hold capacitors. The offset voltage that appears in the SHA output during this transition is known as pedestal error.

a droop rate that is higher than $^1/_2$ LSB. Hence for optimal performance a capacitor $\geq$ 220 nF should be used.

The acquisition time is the maximum time required to acquire a new full-scale input signal to $^1/_2$ LSB accuracy, once a sample command has been given. The acquisition time should be significantly smaller than the sampling period for high accuracy. Simulations show the acquisition time to increase with an increase in hold capacitance. With a 470 nF capacitor, the acquisition time is approximately 10% of the sampling period, which is very large, hence smaller capacitors should be used.

In summary, hold capacitors $\leq$ 100 nF produced high pedestal error, large effective aperture delay and large hold mode droop. Hence, are not ideal for the current design. Similarly, a large capacitor such as 470 nF produced a high gain error, and large acquisition time, and thus, are also not ideal for the current design. The best compromise between all errors was found with hold-capacitor between 150 nF and 220 nF.

Experimental testing – Having found the optimal values through simulations, experiments were carried out to verify the simulated results. The transient response of the SHA was measured with various hold capacitors and is shown in Figure 8.38. The green trace in the graphs indicates the input signal while the blue trace shows the SHA output. Looking at the sub-plots, two observations can be made immediately. (1) In the sample mode, the gain error between the input and the output signals increases with an increase

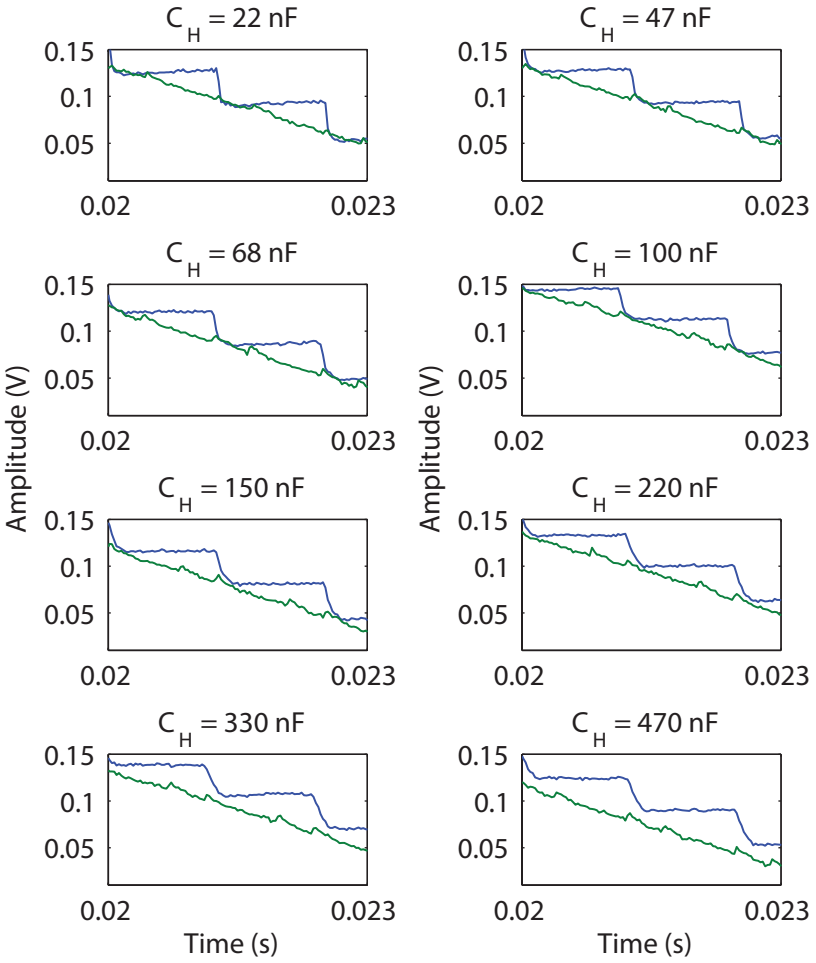

FIGURE 8.38: The output of the SHA with various feedback capacitors. The green trace in the graphs indicates the input signal, while the blue trace shows the SHA output.

in hold capacitor value. The gain error is visibly large at 330 nF and 470 nF. (2) The voltage droop in the hold mode decreases with an increase in the hold capacitor value. The hold mode voltage increased with time at 22 nF, 47 nF, 68 nF, and 100 nF, and is relatively flat with a capacitors $\geq$ 150 nF.

Similar to the simulations, the acquisition time in sample mode increased with an increase in the capacitor value. However, the response seems much worse in real time than the simulations. With a large capacitor such as 330 nF or 470 nF, the acquisition time appears to be maximum, i.e. equivalent to the sampling time. This usually occurs when the hold capacitor must charge to a full-scale voltage change. Therefore, capacitors $\geq$ 330 nF are not ideal for the current design.

Signal-to-Noise Ratio– A pre-recorded PPG signal shown in Figure 8.39 was used as the input signal for testing the SNR. The major component in the input signal is the cardiac component at 0.84 Hz. The output of the SHA was recorded with 22 nF, 47 nF, 68 nF, 100 nF, 150 nF, 220 nF, 330 nF and 470 nF capacitors using a data acquisition card. Figure 8.40 shows the output of the SHA measured with different hold capacitors.

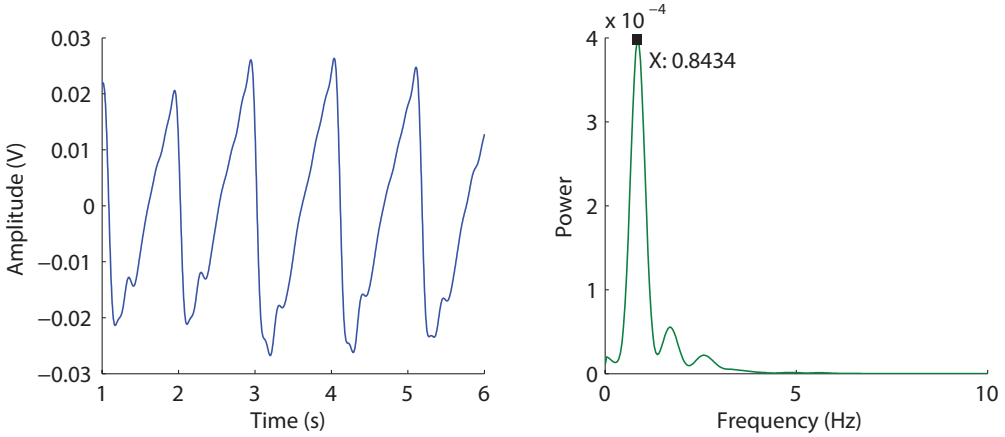

FIGURE 8.39: The pre-recorded input signal (in blue) and the frequency response (in green) of the input signal used to test the SHA.

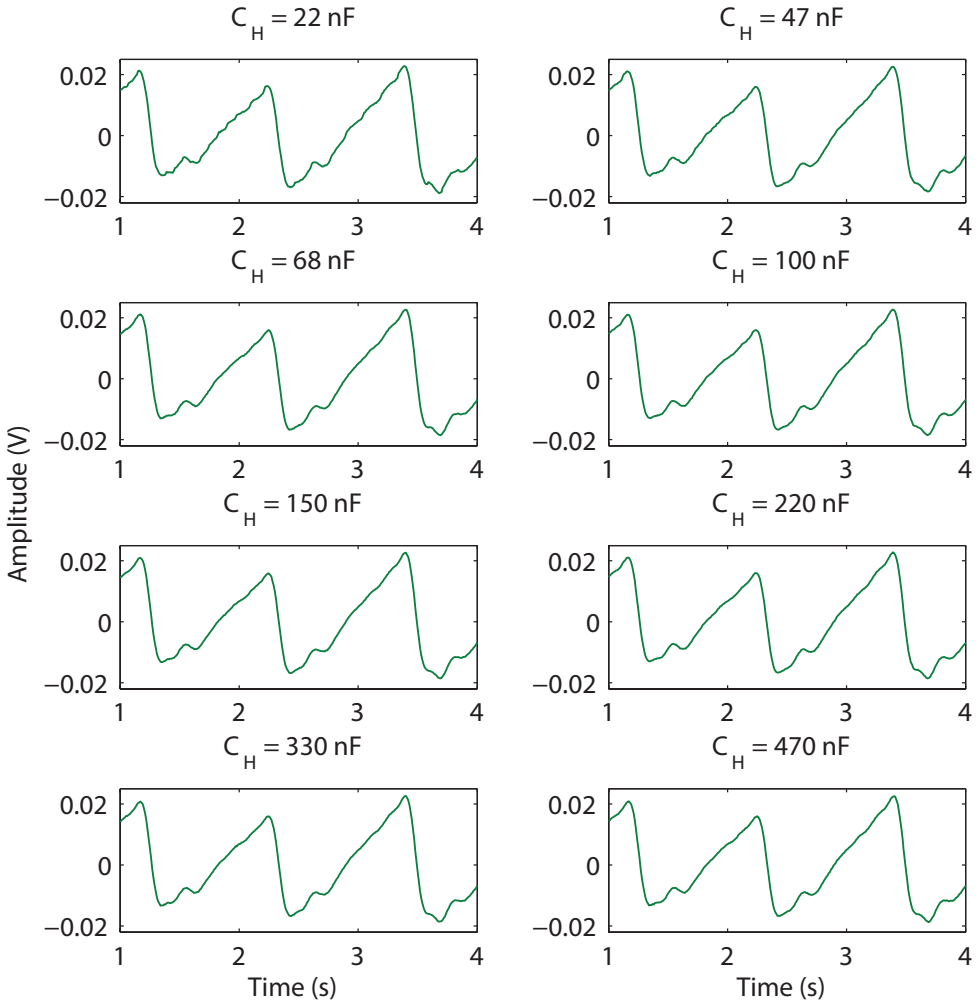

FIGURE 8.40: Depicts the output of the SHA measured with different hold capacitors. The noise in the signals reduces with an increase in hold capacitor value.

From the sub-plots, it is clear that the output signal gets smoother with an increase in the hold capacitor. Visibly large noise can be seen clearly in the output signals acquired with

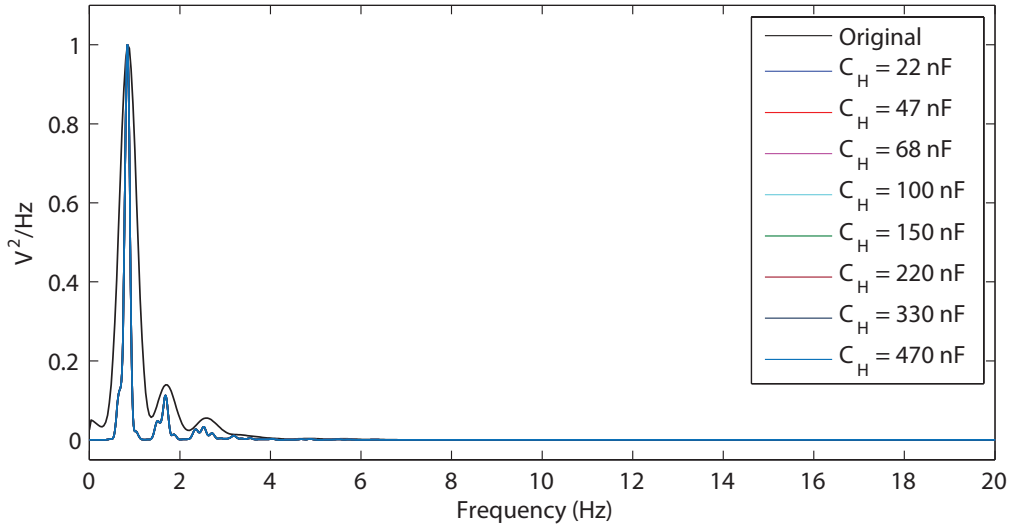

FIGURE 8.41: The frequency spectrum of the input signal and the SHA output when C_H is 22 nF, 47 nF, 68 nF, 100 nF, 150 nF, 150 nF, 220 nF, 330 nF and 470 nF.

22 nF and 47 nF capacitors. To find the frequency and the power of this noise component in the output signal, frequency domain analysis was performed.

The normalised frequency spectrum of the SHA output together with the normalised spectrum of the input signal is shown in Figure 8.41. Clear noise peaks were visible in the frequency spectrum of all the output signals acquired from the SHA between 10 Hz-18 Hz, as shown in Figure 8.42(a). However, apart from 22 nF and 47 nF capacitors, all other capacitors produce relatively similar noise level beyond 10 Hz. The signals from 22 nF and 47 nF capacitors produce large noise between 13 and 15 Hz. This verifies the noisy transient response is shown in Figure 8.40. Hence, these two capacitors are discarded from further analysis.

To further discriminate the noise components in the signals acquired from other capacitors, the 10 Hz noise component was closely examined. Figure 8.42(b) shows the relative changes in the power of the signals acquired at different capacitors (10 Hz). From this figure, it is evident that each hold capacitor produces a different level of noise. To compare them, the SNR was calculated by taking the ratio of the power of the noise component and the cardiac component. Table 8.3 shows the SNR (dB) of the SHA with various hold capacitors. The SNR of SHA is close to the original signal with 470 nF capacitor. However, there are no significant differences between the SNR produced by other capacitors.

From the simulations and the experimental observations, the best compromise between all errors was found with 150 nF and 220 nF capacitor. Hence, it was decided that a 220 nF capacitor will be used as the hold capacitor for the SHA.

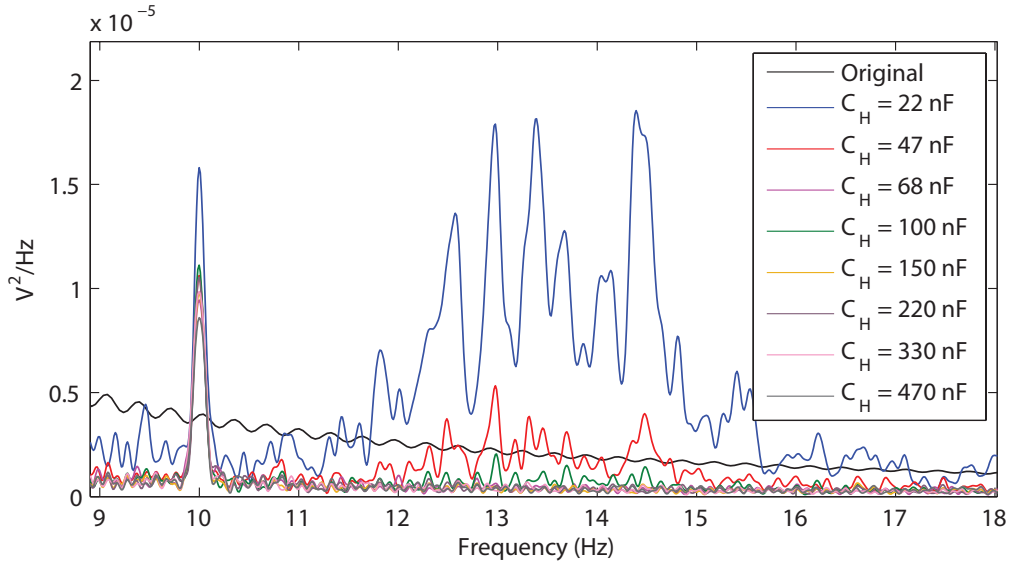

(a) The normalised frequency spectrum of the SHA output showing the noise components between 9 and 18 Hz

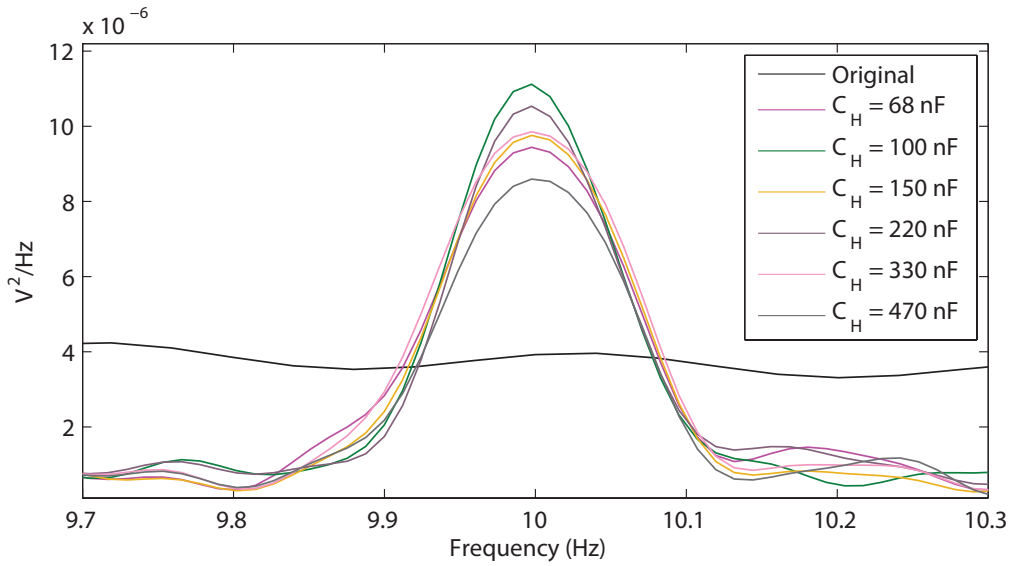

(b) The normalised frequency of SHA output showing the 10 Hz noise component.

FIGURE 8.42: The noise components in the SHA output acquired using different values of hold capacitors.

TABLE 8.3: Depicts the SNR of the Sample-and-hold amplifier with C_H at 68 nF, 100 nF, 150 nF, 220 nF, 330 nF and 470 nF.

Capacitors	68 nF	100 nF	150 nF	220 nF	330 nF	470 nF
Input signal			108 dB			
Output signal	100.4 dB	99.07 dB	100.21 dB	99.55 dB	100.12 dB	101.31 dB

8.5.4 Filters

The frequency response of the lowpass and highpass filters used in ZenPPG system, for filtering the PPG signals were tested through simulations. The simulated magnitude and phase response of the lowpass and the highpass filter is shown in Figure 8.43. The blue trace shows the magnitude of the filters in dB, and the green trace shows the phase response of the filters.

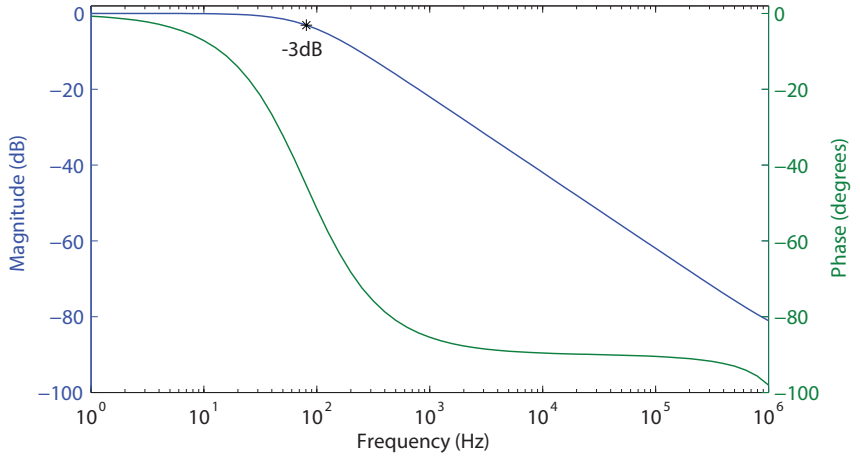

(a)

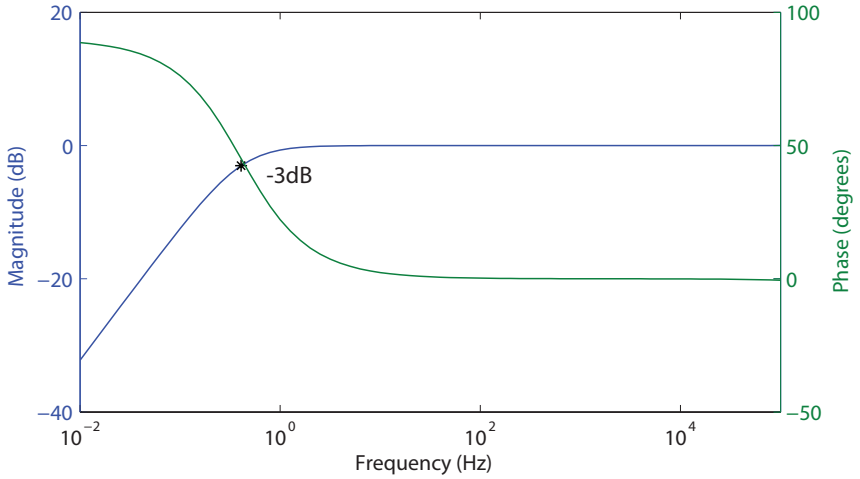

(b)

FIGURE 8.43: The magnitude and phase response of (a) the anti-aliasing filter and (b) the high pass filter

8.5.5 Signal-to-noise ratio of the ZenPPG system

The SNR of the PPG signals acquirable from the ZenPPG system was measured experimentally. A dual channel function generator was used as a PPG signal simulator (similar to a commercial SpO_2 simulator) and was connected to the ZenPPG system. The reflectance

finger PPG probe described in Chapter 7 was connected to the ZenPPG system during testing. The raw PPG signals from the ZenPPG system were digitised by the NI DAQ card and were stored on the laptop PC using LABVIEW. A simulator was used for SNR testing so that the output signal acquired can be compared to the reference input signal, and so that any external interferences can be avoided. Off-line analysis was performed on the acquired data to extract the frequency contents in 0 to 12Hz range.

The measured frequency spectrum of the input and output signals were normalised to the cardiac component to highlight the noise component. By comparing the input and the output frequency spectrum, the noise components were located. A noise peak with a power higher than the power of the input signal was found at 10 Hz (same noise peak seen during SHA testing). Figure 8.44 shows the frequency spectrum of the input and the output signals in 0-10 Hz range and a focused view of the noise components at 10 Hz. Since

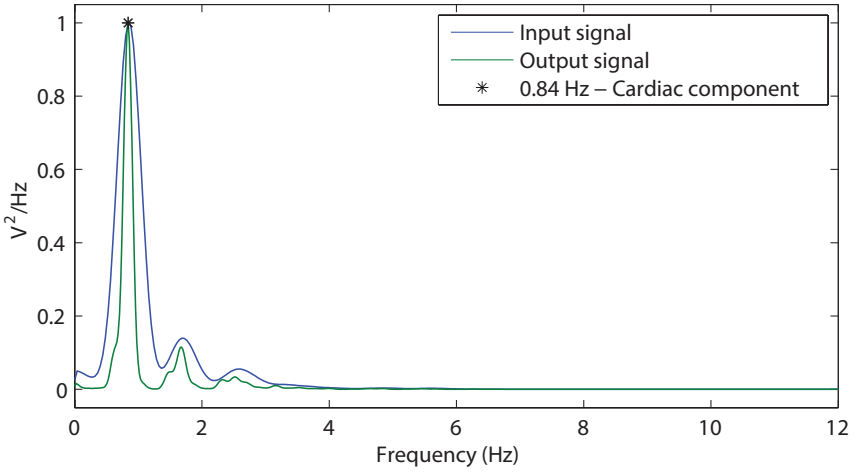

(a)

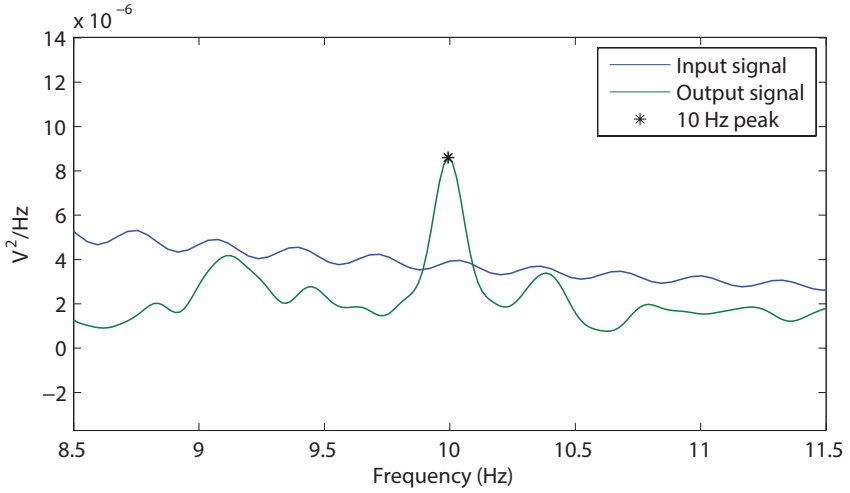

(b)

FIGURE 8.44: Frequency spectrum of the input and the output PPG signals showing (a) the cardiac and (b) the noise components. The 10 Hz noise peak is used to calculate SNR.

the frequency spectrum is normalised, the power of the noise peak at 10 Hz determines the SNR. Hence, the SNR of the raw PPG signals acquired from the PPG system is 101.31 dB.

8.5.6 ECG Amplifier

The performance of the ECG amplifier in the vital sign monitoring module was tested using an ECG simulator. During the experiment, the ECG simulator was connected to the respective leads of the ECG cable (RA, LA and LL), and then an ECG signal with a frequency of 1 Hz (60 BPM) and an amplitude of 0.1 mV was simulated. The output of the ECG amplifier from the ZenPPG system was then recorded using a DAQ card and was stored on laptop PC. Before testing the instrumentation amplifier in the ECG circuit, the frequency response of the bandpass filter used was tested. Figure 8.45 shows the ECG signal acquired from the ECG amplifier. The amplitude of the ECG signal is 14 times the amplitude of the input signal, which corresponds with the gain of the instrumentation amplifier.

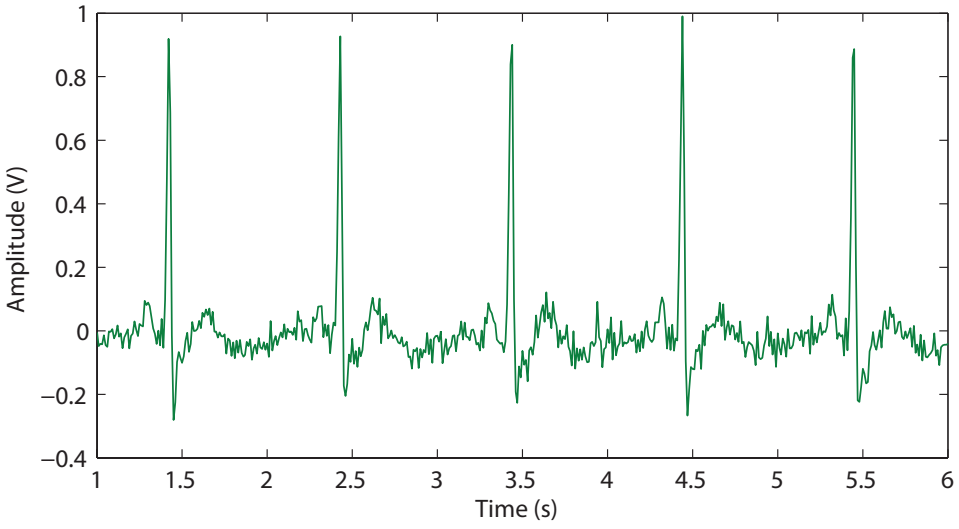

FIGURE 8.45: The ECG signal acquired form the ECG amplifier. The ECG leads were attached to a simulator configured to provide a simulated sinus rhythm of 60 beats per minute

8.5.7 Power consumption and Battery life

As mentioned earlier, the ZenPPG system works both on batteries and USB power supply. The power consumption of the system, when powered by either power supply, will be the same, and was measured using an ammeter. The current consumed by the ZenPPG system – I_{Zen}, was measured by connecting the ammeter in between (in series) the batteries and the ZenPPG system. During the measurement, both the ear canal and the finger PPG

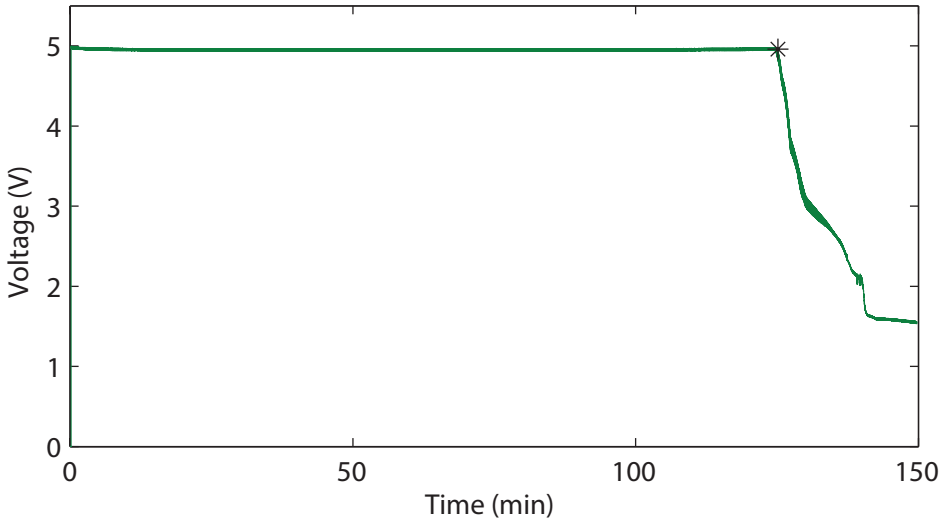

FIGURE 8.46: The changes in battery voltage with time. A steep drop in voltage is observed at 125^{th} min.

probes, and the ECG cable were connected to the system. The LEDs in each probe were driven by 40 mA of current.

The load current measured by the ammeter was 214 mA. Hence, the power consumption of the system $P_{Zen} = I_{Zen} \times V_{Zen}$ = 214 mA × 5V (Battery supply) = 1.07 W. From the measured load current, the battery life of the system can be calculated, and is given as

$$Battery\ life = \frac{Battery\ capacity}{Load\ Current} \times 0.70 \quad = \frac{560\ mA}{214\ mA} \times 0.7 = 109.8 min\ . \tag{8.11}$$

To verify the calculated result (battery time) experimentally, the changes in the battery voltage were recorded for two and half hours with the system being switched on and connected to all the sensors. The measurements were recorded using LABVIEW. Figure 8.46 shows the results obtained from the battery test. The battery voltage stayed relatively constant for the first 125 mins, after which there was a fast decline in the voltage. The system can, therefore, be used continuously for 2 hours when powered by batteries.

8.6 Summary

To drive the optical components of the reflectance ear canal and finger PPG probes and to pre-process the acquired PPG signals, a PPG instrumentation unit called 'ZenPPG' was developed and tested successfully.

A modular design approach was implemented in the system's design, whereby the electronic circuitry in the system was divided into multiple modules, which were connected together by a system bus. The developed system also hosted an ECG amplifier for detecting the

QRS wave of the ECG signal. The PPG modules of the system are the TransImpedance Amplifier (TIA) module, the Current Source (CS) module, and the Core module. The other two modules in the system are the power supply module and the vital sign monitoring module. The power module consists of the circuitry required to split the battery or USB supply into multiple power rails that supply the digital and analogue microchips. The CS module converts a constant voltage into current required to turn on the LEDs in the PPG probes. The TIA board converts the photocurrents detected by the photodiode in the PPG sensors into a voltage signal. The core module hosts the multiplexer, SHA, filters, and the microcontroller which controls the multiplexer and the SHA. The current of each LED is controlled digitally on channel-1, and on channel-2 using trimmers. The PPG signals from the ZenPPG system are digitised by an NI DAQ card, which connects to the system through a 68-pin connector.

Independent circuits within each module were tested and configured for optimal performance. The SNR of the PPG signals acquired from the system was 101.31 dB. Along with the AC and DC PPG signals, and the ECG signal the ZenPPG system measures the current on each LED and the battery level. However, the use of the software controlled emitter driver and absence of onboard DAC means that the PPG instrumentation system must be used in conjunction with the appropriate LabVIEW software and NI DAQ card. The following chapter details the implementation of the data acquisition system. This includes the analogue to digital conversion, VI for emitter driver control, Virtual Instrument (VI) for data acquisition and other algorithms for data logging and data analysis.

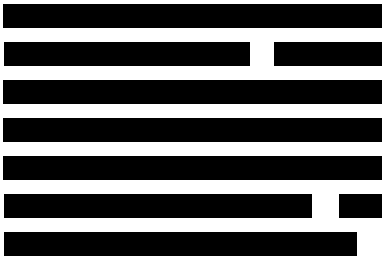

C. A. R. Hoare, The Emperor's
Old Clothes, 1981

9

Data acquisition and hardware control

A data acquisition system was developed which incorporated all the elements required for hardware control and acquisition of various signals from the PPG processing system (described in Chapter 8). The data acquisition system comprises a software program, or virtual instrument (VI), implemented in LabVIEW and a data acquisition card from National Instruments (National Instrument Corporation, Austin, Texas).

The two main functions of the developed VI are (1) digitization of signals from the PPG processing system (ZenPPG), and (2) controlling the emitter driver circuit. Other functions of the VI include recording and saving data, digital signal processing and estimation of SpO_2 and heart rate (HR). The data acquisition card used to acquire data was a NI USB-6212. The details of the digitisation stages together with the development of the VI for acquisition, processing, and analysis, as well as the performance evaluation tests, will be the subject of this chapter. Prior to this, a brief introduction to LabVIEW is also provided in this chapter.

9.1 Data Acquisition system

The data acquisition system was developed to sample, display, store and analyse photoplethysmograms from the ear canal and the finger. A generic block diagram illustrating

the main functions of the system is shown in Figure 9.1. Along with the PPG and ECG signals, the system was later modified to include the acquisition of signals from temperature sensors, Laser Doppler Flowmetry monitor and NIRS monitor (discussed further in Chapters 10 and 11).

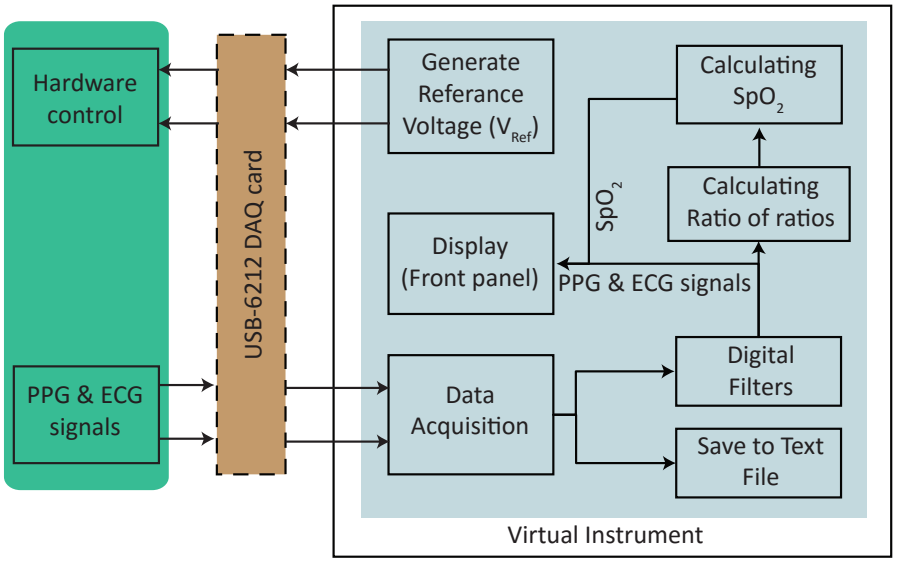

FIGURE 9.1: Block diagram of the data acquisition system illustrating the key features

9.1.1 Analogue-to-digital conversion

All 12 analogue signals from the PPG processing system (8 raw PPG signals, ECG signal, LED current sensing and battery monitor signals), were digitised by an analogue-to-digital converter (ADC) that was embedded in a data acquisition (DAQ) card. The card used was the National Instrument data acquisition card *(NI USB-6212 National Instrument Corporation, Austin, Texas)*.

The NI USB-6212 is a multifunction data acquisition (DAQ) device that provides plug-and-play connectivity via USB for acquiring, generating, and logging data in a variety of portable and desktop applications. The NI USB-6212 mass termination device features 16 analogue input channels and two output channels. The technical specifications of the DAQ card are provided in Table 9.1. The device supports differential and Non-Referenced Single-Ended (NRSE)/Referenced Single-Ended (RSE) signal input configurations. The USB-6212 mass termination device is connected to the PPG processing system via a 64-pin NI connector.

TABLE 9.1: Technical specifications of the USB-6212 DAQ card from National Instruments.

Specifications	**USB-6212 Mass termination DAQ card**
Number of input channels	16 single ended, 8 differential
Number of output channels	2
Number of Digital input and output channels	24
Maximum Input Sampling rate	400 kS/s single channel, 400 kS/s multichannel (aggregate)
Maximum Output Sampling rate	250 kS/s per channel
Analogue Input range	±10 V, ±5 V, ±1 V,±0.2 V
Analogue Output range	±10 V
Analogue input signal bandwidth (-3 dB)	1.5 MHz
ADC resolution	16 bits
CMRR (DC to 60Hz)	100 dB
Physical dimensions	19.3 × 9.4 × 3.1 cm
I/O connectors	one 68-pin SCSI
Bus interface	USB 2.0 Hi-speed

9.1.2 Introduction to LabVIEW

LabVIEW (Laboratory Virtual Instrument Engineering Workbench) is a system design platform and development environment from National Instruments *(National Instrument Corporation, Austin, Texas)*. Instead of using traditional text-based programming, as with C, C++, or Java, LabVIEW uses graphics to create programs in a pictorial form called a block diagram, eliminating a lot of the syntactical details [274]. This graphical programming in LabVIEW is called 'G'.

The functions in LabVIEW are connected in a hierarchical manner by wires which represent the flow of the data. Each function executes only after receiving the necessary data from the previous function. LabVIEW programs are called Virtual Instruments (VIs) as their appearance and operation imitate actual instruments. Any VI developed in LabVIEW consists of two main parts. (1) Front panel: the interactive user interface of a VI, so named because it simulates the front panel of a physical instrument. The front panel can contain knobs, push buttons, graphs, and many other controls and indicators. (2) Block diagram: the VI's executable source code, constructed in 'G'. The components of a block diagram are lower-level VIs, built-in functions, constants, and program execution control structures.

LabVIEW comes with another layer of software for easily communicating with the hardware (i.e. DAQ card), called the *NI–DAQmx Driver software*. It forms the middle layer

between the application software and the hardware. The driver software also prevents register-level programming hence providing easy access to the hardware functions.

9.1.3 Development of Virtual Instrument for emitter control

To digitally control the light intensity of the red and infrared emitters in the PPG probe, both analogue output ports available on the USB-6212 DAQ card were utilised. Digital control of LEDs on both channels of the PPG processing system was not possible, as the number of analogue output channels on the DAQ card were limited. Hence, channel 2 was driven by on-board circuitry. The two reference voltages (V_{Ref}) generated from the DAQ card were between -5 to 0 V and 0 to 5 V. The positive voltage powered one of the LEDs while the negative powered the other. As mentioned in the Chapter 8, the reference voltage generated by the DAQ card was then attenuated such that each volt supplied from the analogue output port produced 20 mA of current to drive the emitters. Figure 9.2 shows the source code of VI used to create the signal to control the intensity of the emitters.

The polymorphic function *"DAQmx Analogue Output (AO) Voltage"* was used to create virtual channels that will produce V_{Ref} on the analogue output terminals of the DAQ card. The channel on which the voltage is generated was specified using the physical channel (I/O) selection property, in this case, it was Dev1/ai0 and Dev1/ai1. The maximum and minimum voltage levels that can be generated were also specified on both the channels (ai0: 0 to -5V, ai1: 5 to 0V). Once the virtual channel was created, a *while loop* was used in conjunction with *DAQmx Write*, to continuously generate an output voltage on that channel. The *DAQmx Write* function writes samples to the task or virtual channel you specify. The value of the samples that *DAQmx Write* writes to the channel depends upon

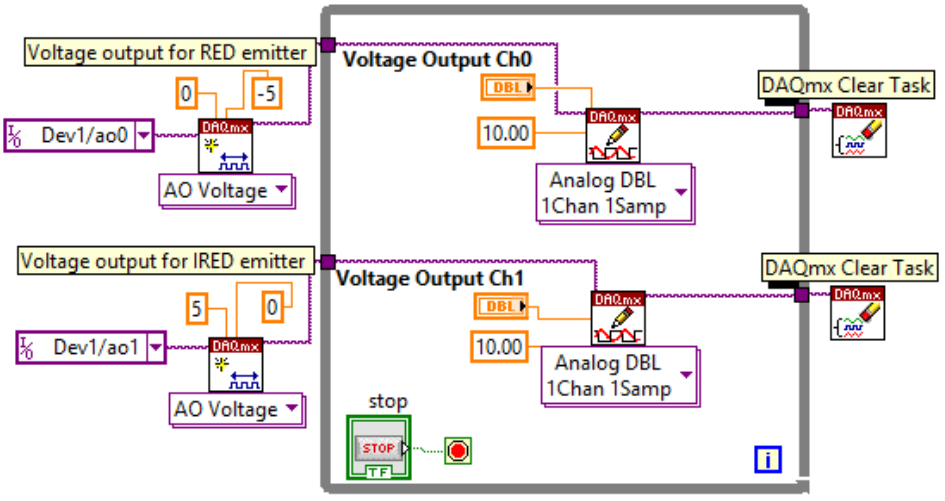

FIGURE 9.2: Section of the virtual instrument for emitter control, illustrating the generation of two analogue outputs, used to the control the LED currents on one of the channels

the desired V_{Ref} selected by the user on the front panel of the VI. Once the user hits the stop button, the task is cleared using the function *DAQmx Clear Task*. Before clearing, this VI aborts the task, if necessary, and releases any resources the task reserved.

9.1.4 Development of Virtual Instrument for data acquisition

The data acquisition part of the VI was designed to acquire 12 signals from the PPG processing system. They are as follows:

- the red and infrared AC PPG signals from both the channels (4 signals)
- the red and infrared DC PPG signals from both the channels (4 signals)
- the ECG signal
- the LED current sensing signals (I_{SENSE0} and I_{SENSE1})
- the power supply monitoring signal (PSV_{MON}).

The *DAQ Assistant* Express VI was used to acquire all the signals from the PPG processing system. The DAQ Assistant is a graphical, interactive guide that lets the user configure the DAQ card, the analogue inputs which needs to be sampled, the sampling frequency at which the signals needs to be sampled, and the mode of acquisition (i.e. differential, NRSE and RSE). *DAQ Assistant* also offers the capability to test the data being acquired. In the current setup, 12 analogue input channels from port ai0-ai8 and port ai10-ai12 were selected for sampling. All the input channels were configured in referenced single-ended mode. The sampling frequency was set to 1 kHz and the samples to read (buffer size) was set to 100. The maximum and minimum voltage range of the signals being acquired was set to 5V and -5 V respectively.

The Express VI was then placed inside a *for loop*, which was nested inside a *while loop*, for continuous data acquisition. The inclusion of the *for loop* is for the calculation of ratio of ratios (R_{OS}) and SpO_2 values, detailed in Section 9.1.6. The *for loop* executes its subdiagram n times, where n is the value wired to the count (N) terminal. In this case, it is set to twenty times. Therefore, for each iteration of the *while loop*, the *for loop* iterates twenty times. Hence, 2000 samples are acquired from each analogue input channel on each iteration of the while loop. The while loop continues to execute its subdiagram until execution is stopped by the user by pressing the stop button on the front panel.

The dynamic data output from the DAQ assistant was split into 12 separate signals using a split signals function. Each unit of the original signal contains the timing information (t0 and dt) of the waveform.

9.1.5 Algorithms for digital filters and display

Digital filters were implemented in the VI, to reduce the bandwidth of the acquired signals. This is so that any noise added to the signals during digitisation, such as quantisation noise can be removed from the signals. Also, the bandwidth of the analogue filters used in the PPG processing system was larger (80 Hz) than required (typical bandwidth of a PPG signal is 0.5 – 10 Hz), hence the acquired PPG signals needs to be filtered.

Three digital filters in varying configuration were hence used to filter the PPG and ECG signals from the PPG processing system. The *Filter Express VI* from the *Signal Analysis Express palette* was used to configure all three filters. The red and infrared raw AC PPG signals from the processing system were filtered using a bandpass filter with lower and upper cut-off frequencies at 0.5 Hz and 18 Hz. The DC red and infrared PPG signals were filtered using a lowpass filter with the cut-off frequency of 20 Hz. The ECG signal was filtered using a bandpass filter with lower and upper cut-off frequencies at 0.5 Hz and 40 Hz. All three filters were Finite Impulse Response (FIR) filters, with the filter coefficient set to 511 taps. FIR filters were used as FIR return a linear phase response. All three filters were designed with stop-band attenuation higher than 30 dB. Figure 9.3 shows the magnitude and phase response of all three filters. The filtered AC PPG signals from both the PPG channels and the ECG signal were displayed on the front panel of the VI during runtime using a single chart. This enabled the user to monitor the morphology and the amplitude of the acquired signals. The *Waveform chart* function in LabVIEW was used to display these signals. The DC value of the PPG signals was displayed on the front panel using the *Numerical Indicators*.

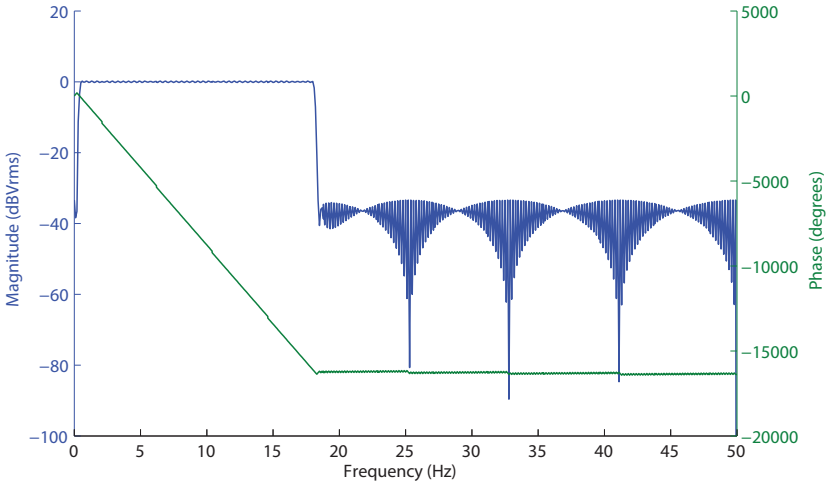

(a)

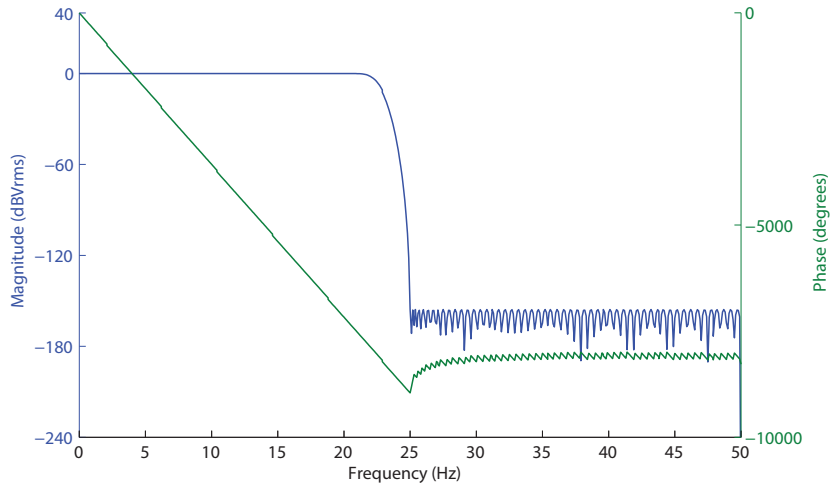

(b)

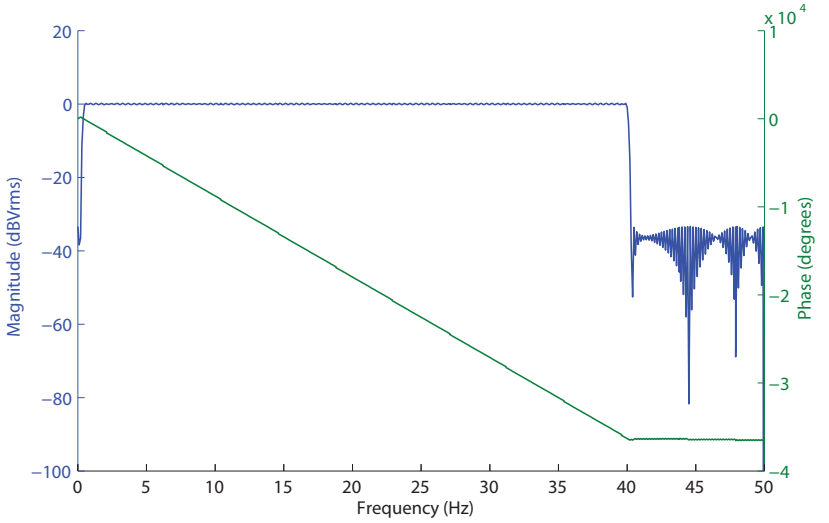

(c)

FIGURE 9.3: The magnitude and phase response of (a) the bandpass filter used to filter the AC PPG signals, (b) the lowpass filter used to filter the DC PPG signals, and (c) the bandpass filter used to filter the raw ECG signal.

9.1.6 Algorithms for calculating Ratio of ratios (R_{OS}), SpO_2 and heart rate

To provide an indication of the systems performance, blood oxygen saturation levels and heart rate were estimated. SpO_2 was estimated using the following linear equation.

$$SpO_2 = 110 \; - \; 25 \; (R_{OS}) \tag{9.1}$$

$$where \; R_{OS} = \frac{(AC/DC)_R}{(AC/DC)_{IR}} \tag{9.2}$$

As mentioned earlier, the *for loop* in this VI executes its subdiagram or functions within the loop 20 times. After every twenty iterations, arrays of data corresponding to each signal are collected by a collector and passed out of the loop. This process keeps repeating unless the user pushes the stop button.

Each iteration of the *for loop* acquires 100 samples at a sampling rate of 1 kHz. Therefore, after 20 iterations of the loop, 2000 samples are acquired, or, in other words, every 2 seconds 2000 samples are acquired. The *collector* Express VI then collects these input samples and returns the most recent data. Every 2 seconds the *collector* discards the oldest data and adds the newest data to the collected samples.

The PPG signals continuously collected every 2 sec are then used to estimate SpO_2. A sub–VI was implemented in LabVIEW for calculation of SpO_2, as shown in Figure 9.4. The sub–VI consisted of *Amplitude and level measurement* Express VI's which measured the mean peak-to-peak amplitude of AC PPGs and the mean value of the DC PPG signals. The AC and DC amplitudes of both the red and infrared signals were then divided to provide

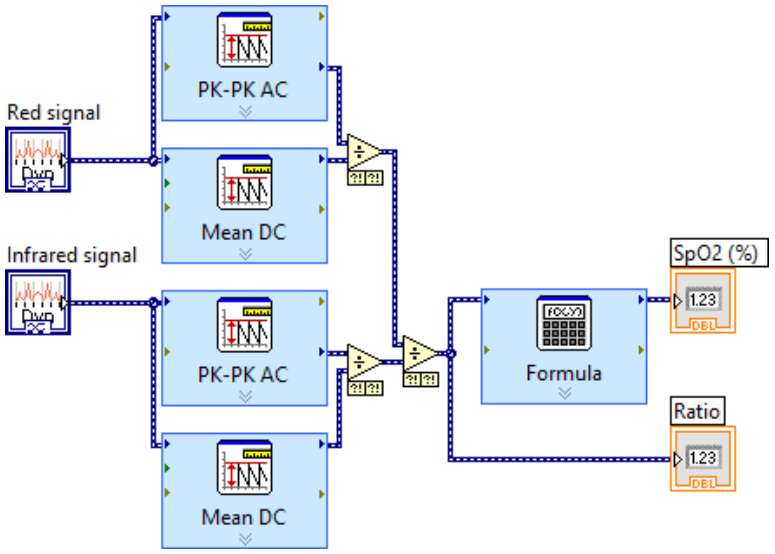

FIGURE 9.4: Section of the virtual instrument for ratio (R_{OS}) calculation and SpO_2 estimation.

R_{OS} using Equation 9.2. A *Formula* express VI was then used to invoke Equation 9.1. The input variable (x1) to the *Formula* Express VI is the R value, and the output of the VI is the estimated SpO_2 value. An identical method was applied for both the ear canal and the finger PPG signals to estimate SpO_2 from both the locations. The estimated SpO_2 and R_{OS} were displayed on the front panel using *Numerical indicators*.

The ECG signal acquired every 2 seconds was used to estimate HR. The acquired ECG signal was processed through the *Tone Measurement* Express VI, which finds the dominant frequency within the sampled data. The measured frequency is then used to measure HR instantaneously using

$$HR = 60 \times f_d; \text{ where } f_d \text{ is the dominant frequency} \tag{9.3}$$

The estimated heart rate was then averaged over every 20 samples to improve accuracy. Along with the physiological data, other electrical parameters acquired from the PPG processing system such as the power supply status and the LED current levels were also displayed on the front panel.

9.1.7 Algorithm for data storage

All the analogue data acquired from the PPG processing system using the *DAQ Assistant* VI was saved to a text file for offline analysis. Only raw data were saved to preserve as much information as possible.

Data was recorded using the *Write to Measurement File* Express VI. This DAQmx function lets the user configure how the data is saved. The VI was designed to save data to a file ('.LVM' file) continuously in an ASCII formatted spreadsheet. Each column in the text file corresponds to one of the digitised signals. Data is written in the tab delimited method with an accuracy of 5 decimal places. Figure 9.5 shows the block diagram of the algorithm for data storage.

The Express VI was configured in such a way that, when the VI was run, the user was prompted with a system dialogue to input the name and the location of the file. If a file with the same name already exists in that location, then the user was prompted to change the name. Although the user was encouraged to choose the file name when the VI was run, the data recording was not enabled until the user clicked the *Record* button on the front panel. The *Record* button also enabled elapsed time measurement, which is the amount of time that has elapsed since the recording was started. Since the Express VI was also placed inside the *for loop* which is embedded within the *while loop*, data acquisition and file writing occurred simultaneously. Writing to the file is continuous until the stop button is pressed by the user.

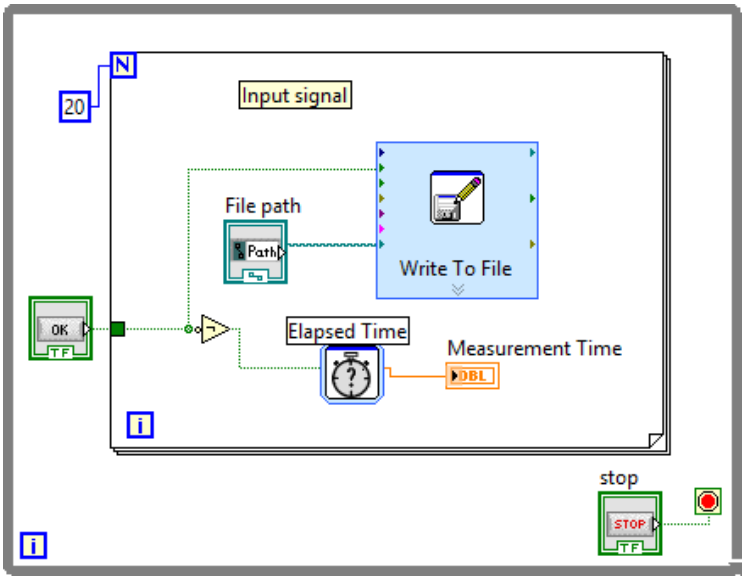

FIGURE 9.5: Section of the virtual instrument for saving all PPG and ECG data to a text file.

9.2 Evaluation of the data acquisition system

All the algorithms discussed so far in this chapter were incorporated into one single VI that could acquire, process, display and save various signals, as well as control the emitter drive currents (as shown in Figure 9.9). Functionality tests were carried out to check the performance of different elements in the VI.

Firstly, the reference drive voltage function in the VI was tested using an oscilloscope.

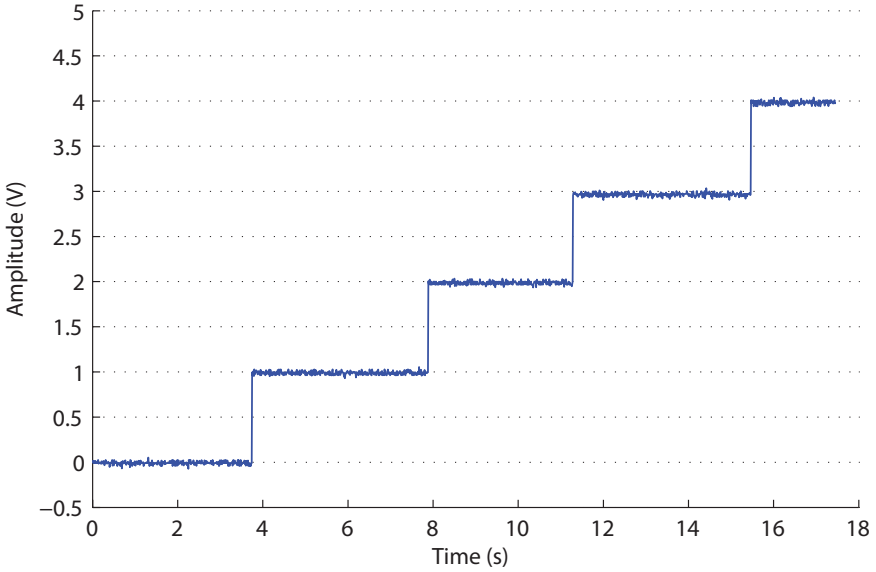

FIGURE 9.6: The accuracy and the sensitivity of the measured V_{Ref} to a value set on the front panel.

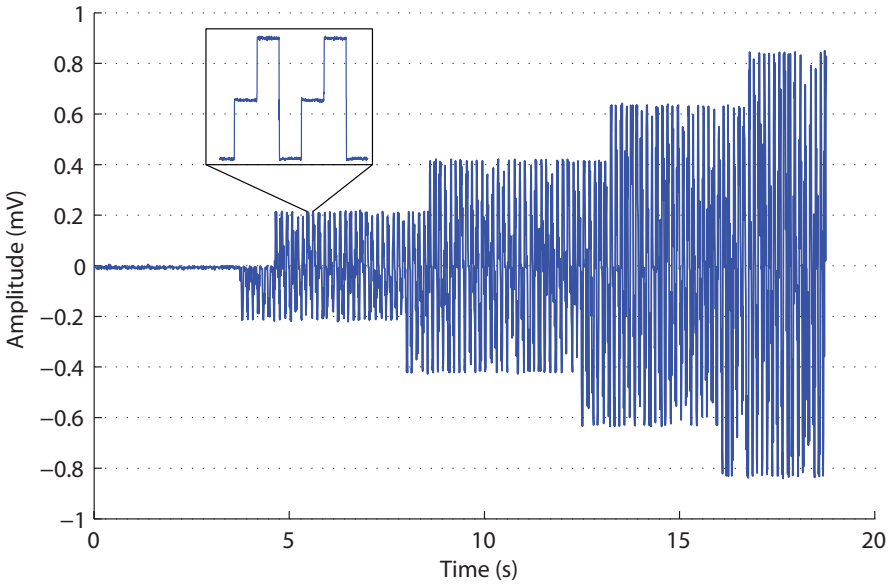

FIGURE 9.7: The accuracy and the sensitivity of measured I_{SENSE0} to the values set on the front panel.

Figure 9.6 shows the accuracy and the sensitivity of the measured V_{Ref} to the values set on the front panel. The V_{Ref} was changed from 0 V to 4 V, with 1 V increment every 2 seconds. Similarly, the accuracy of the current generated to a V_{Ref} set on the front panel was tested. Figure 9.7 shows the accuracy and the sensitivity of measured I_{SENSE0} to the values set on the front panel. Again, the V_{Ref} was varied from 0 V to 4 V, with 1 V increment every 2 seconds. From these results, it is evident that the V_{Ref} generated from the DAQ card is highly accurate and sensitive to the input value.

The functionality of the data acquisition part of the VI was tested by connecting the probes (Chapter 7) and the ECG leads to the PPG processing system (Chapter 8), and by acquiring raw signals from it using the DAQ card and the VI. The probes and the ECG cable were connected to a healthy volunteer during acquisition.

Figure 9.8 and shows the front panel of the virtual instrument during the acquisition of signals from a healthy volunteer. The front panel consists of two tabs namely the physiological parameters tab and the electrical parameters tab. The physiological parameters tab hosts the numerical indicators for displaying SpO_2, heart rate and mean DC values. It also hosts graphical indicators for displaying PPG signals, controls for setting the V_{Ref} and a control for choosing the file path. The signals, shown in Figure 9.8 are the red and infrared AC PPG signals acquired from the ear canal and the index finger of the volunteer. The graphical indicator also displays the ECG signal (green trace) acquired from the volunteer. The electrical parameters tab consists of indicators to display the ratio of ratios (R_{OS}), the battery level and the LED currents. The block diagram of the entire VI is shown in Figure 9.9.

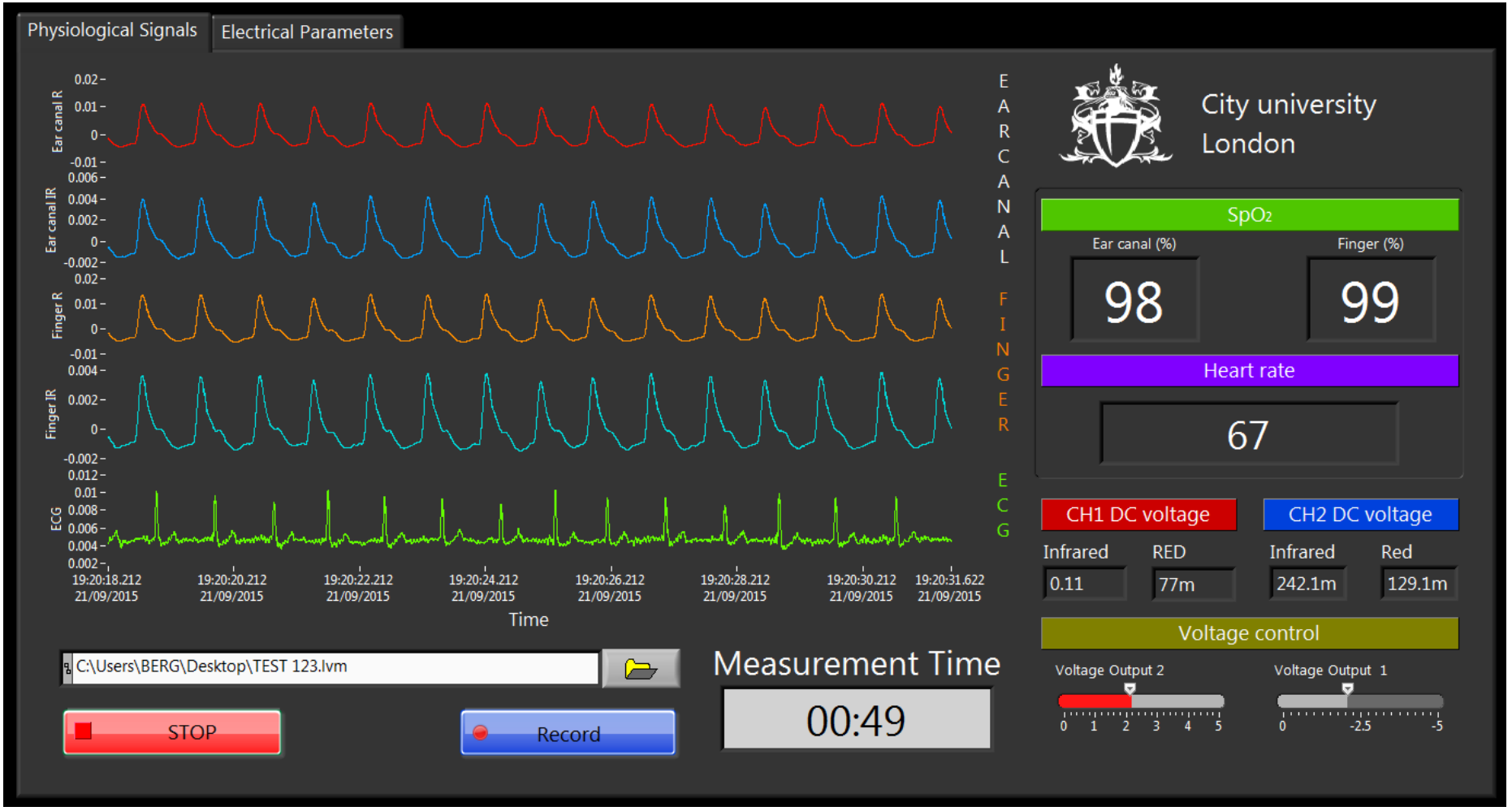

FIGURE 9.8: Front panel of the virtual instrument showing the continuous display of red (red) and infrared (blue) AC ear canal PPG signals, AC red (brown) and infrared (sky blue) finger PPGs and the ECG signal (green). The ear canal and the finger SpO_2 values are also displayed on the right of the VI.

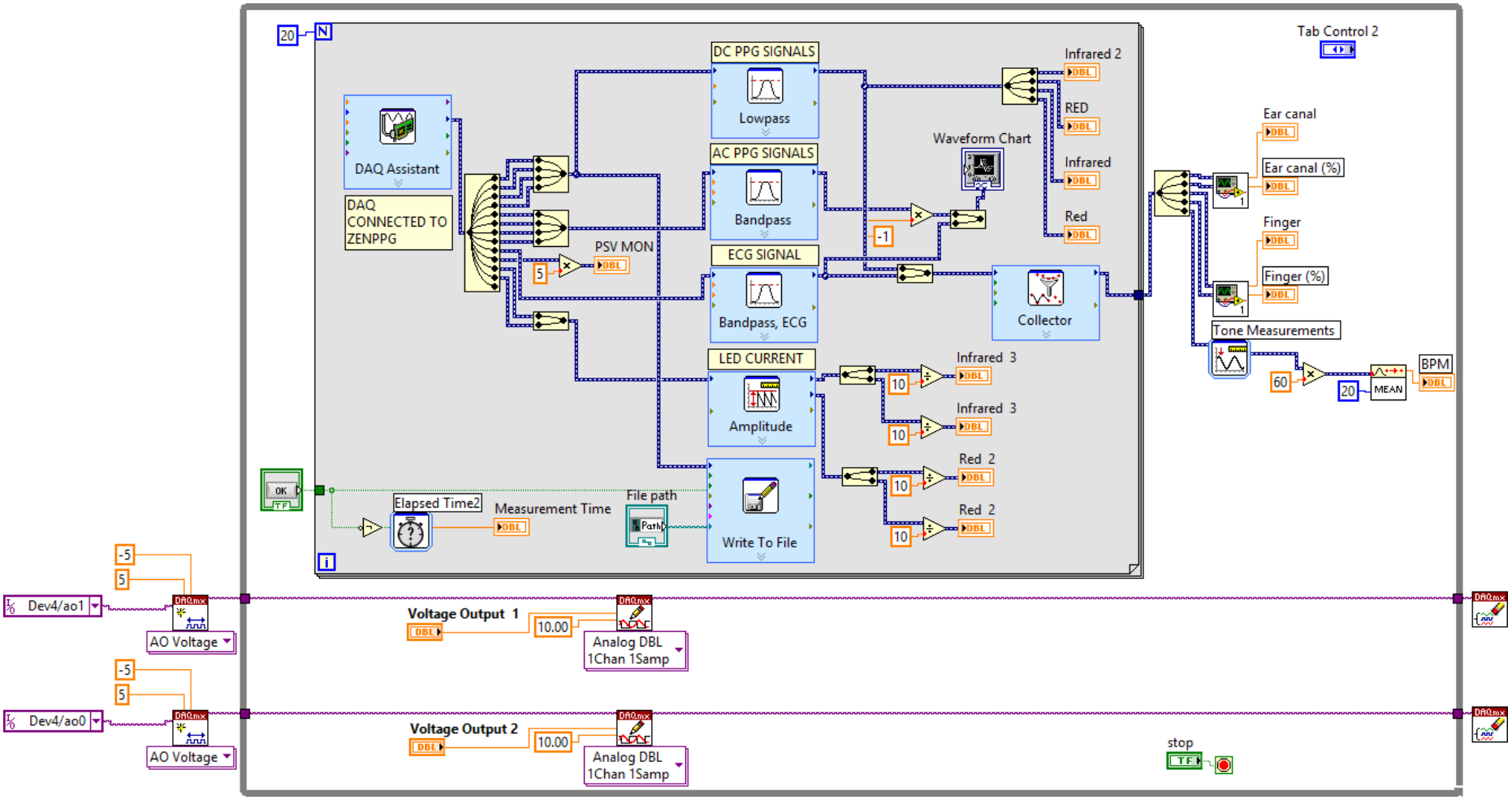

FIGURE 9.9: Block diagram of the virtual instrument showing the blocks used to generate analogue output voltages, acquire signals, store acquired data, and calculate SpO_2.

9.3 Summary

A data acquisition system with the capability to acquire, display and store various signals from the PPG processing system was successfully developed. The system incorporated a VI and a data acquisition card from National Instruments. The developed VI was designed to acquire 12 raw signals (8 – PPG signals, 1 – ECG signal, 2 – LED current sensing signals and 1 – battery level sensing signal) at a sampling frequency of 1 kHz. The V_{Ref} function in the VI was used to power the LEDs in one of the probes. This has reduced the power consumption and the circuitry in the PPG processing system. Algorithms required for the estimation of heart rate and SpO_2 were also implemented in the VI.

The developed VI was tested in the laboratory, and the results show fast and accurate acquisition of the data, clear display of the waveforms and optimal measurement of the required parameters. The system was planned to be used in conjunction with the developed hardware (PPG probes and the processing system) to investigate the hypothesis of this work.

— The sensitivity of the finger plethysmographic tracing to local vasoconstriction may significantly compromise its usefulness for monitoring systemic flow in many settings, and even as a measure of oxygen saturation in more extreme states.

Aymen A. Awad, Anesth Analg 2001; 92:14836

10

Investigation of photoplethysmograms and arterial oxygen saturation values in healthy volunteers during a cold pressor test

Over the last three decades, pulse oximeters have been used as a standard device for monitoring arterial oxygen saturation (SpO_2). However, SpO_2 measurements made from extremities such as the finger, earlobe and toes become susceptible to inaccuracies especially in conditions such as hypovolemia, hypothermia, and vasoconstriction. The failure of pulse oximeters in these circumstances is triggered by inadequate perfusion at the measurement site. To overcome this limitation, the external auditory canal is proposed as a potential measurement site for monitoring SpO_2. Being supplied by the core circulation, the auditory canal is expected to have a much-reduced influence from low perfusion states and, as a result, a better quality PPG signal during critical conditions which might compromise peripheral perfusion. Hence in an attempt to prove this hypothesis, a new reflectance ear canal PPG/pulse oximetry probe along with a PPG processing system was developed. Following the successful laboratory evaluation of the developed hardware, firmware and software, it was decided that the evaluation of the sensor should be conducted through measurements in healthy volunteers.

Subsequently, a study was carried out in 15 healthy volunteers undergoing artificially induced local hypothermia using a cold pressor test. The cold pressor test is a cardiovascular

test performed by immersing one of the hands into an ice water container, and changes in heart's response are measured. A cold pressor test (CPT) is used as it simulates the peripheral vasoconstrictive challenges commonly encountered in the clinical setting. During this study, the volunteers were asked to immerse their right hands into the ice-cold water, while PPG signals were monitored from the ear canal (EC) (central site), the left index finger (LIF) and the right index finger (RIF) (peripheral sites). Various methods of analysis such as the amplitude analysis of AC and DC PPG signals, estimation of SpO_2 and other methods to determine changes in cardiac function were performed on the acquired data. This chapter gives a brief outline of the main aims of the study, volunteer recruitment process and the measurement setup through which the PPG signals were acquired *in vivo*. The methodology of data analysis and the results obtained are then presented. Finally, the statistical analysis methods and the consequent results are presented.

10.1 Aims and objectives

- The primary aim of the study was to determine if good quality PPG signals could be obtained from the surface of the ear canal and to determine if there were any differences between PPG signals obtained from this central site with those obtained at the periphery.
- The study aimed to demonstrate the reliability of the PPG signals and SpO_2 estimated from the ear canal as opposed to the finger under conditions of local hypothermia or profound vasoconstriction.
- The study also aimed to examine the differences in cardiovascular reactivity to the induced stress stimuli and the neutralising autoregulatory response between the measurement sites by measuring changes in the beat-to-beat interval and Pulse Transit Time (PTT).

10.2 Methods and Materials

10.2.1 Measurement setup

The measurement setup was designed to simultaneously detect, sample, record and display PPG, ECG and temperature signals. The block diagram of the entire measurement system is shown in Figure 10.1. The technical details of every block in Figure 10.1 were described in the previous chapters. The PPG signals were recorded from the RECAP probe placed in the right ear canal and from the finger probes connected to the right and left index fingers of the volunteer. Two identical ZenPPG systems (PPG processing unit) were used

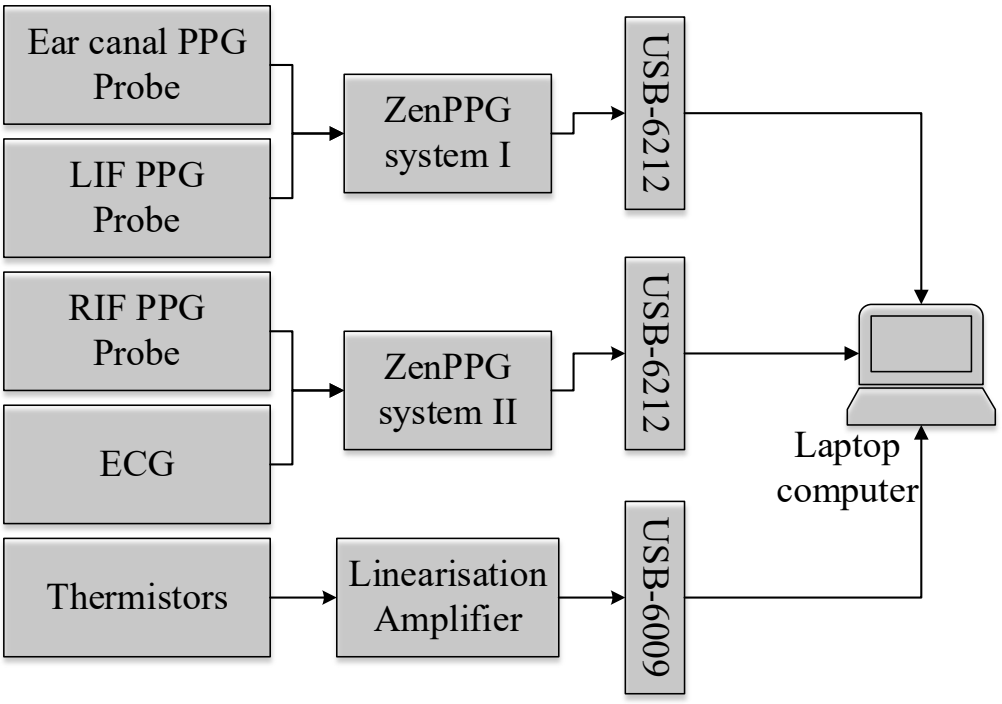

FIGURE 10.1: Block diagram showing the measurement setup of the experiment.

to acquire and pre-process the PPG signal from the probes, as each system only allowed for acquisition of signals from two probes.

The ECG signal was acquired through the Ag/AgCl electrode connected to the volunteer in Lead I configuration (chest lead). Skin temperature measurements were acquired from two thermistors attached to the left and the right hand of the volunteer. The PPG, ECG and temperature signals were acquired simultaneously using three different DAQ cards. The PPG and ECG signals were acquired using two USB-6212 mass termination DAQ cards while the temperature data was acquired using a USB 6009 DAQ card. The virtual instrument controlled acquisition of data from all three DAQ cards. The VI described in Chapter 9 was modified to include the acquisition and control of all three DAQ cards. The design, fabrication and evaluation of the PPG sensors and the ZenPPG processing system was presented in Chapter 7 and 8. Hence, only the development of the temperature sensing system is described here.

10.2.1.1 Temperature sensing system

Two thermistor based fast response temperature transducers were constructed to assess the temperature difference between left and right hands, during the experiment. The thermistor used was TP-TSD202A – a fast response thermistor from BIOPAC Systems, Inc (*CA, USA*). The response time and accuracy of the thermistors are 0.6 sec and 0.2°C respectively. The physical dimensions of the sensor are L – 5 mm and ⊘ – 1.7 mm.

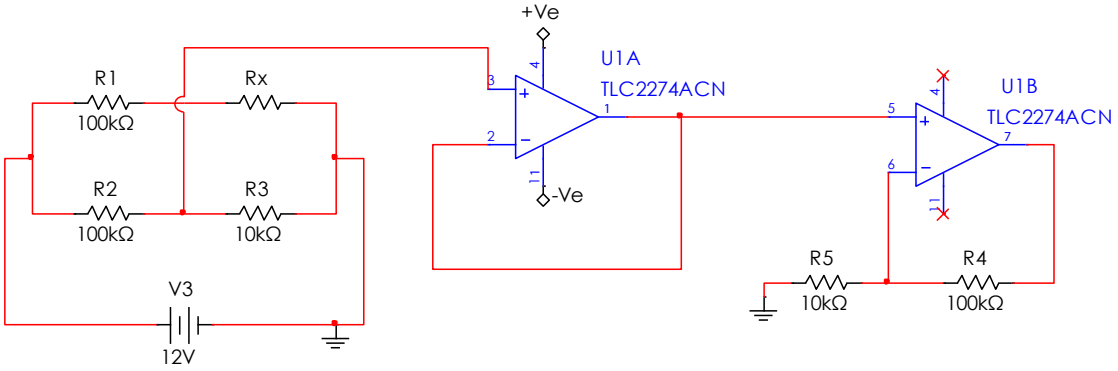

FIGURE 10.2: Circuit diagram of the thermistor linearization amplifier

Since the output of the thermistors was not linear, two identical thermistor linearisation amplifiers were built to produce a linear voltage output with a sensitivity of 20 mV/°C. The thermistor linearization circuit used is shown in Figure 10.2. The circuit consists of a Wheatstone bridge and a non-inverting amplifier. The thermistor was incorporated into the Wheatstone bridge which allowed the change in resistance of the thermistor to be converted into a voltage signal. To eliminate any loading effects, the Wheatstone bridge was connected to an op-amp buffer. The output voltage of the bridge is given as:

$$V_{out} = V_s \left(\frac{R_3}{R_1 + R_3} - \frac{R_x}{R_2 + R_x} \right) \tag{10.1}$$

Where R_x is the resistance of the thermistor, and V_s is the supply voltage. To obtain a measurable output that could be sampled by the DAQ card, the measured output of the linearization circuit was amplified by 11 times using the non-inverting amplifier.

As no calibration data was provided by the thermistor manufacturer, both the thermistors were calibrated in a controlled environmental chamber *(BINDER KMF 115, BINDER GmnH, Germany)*. During the calibration process, the temperature of the chamber was increased from 5 to 40°C, with 1°C increment every 10 minutes. A virtual instrument was used to record the change in voltage as a waveform into a text file in LABVIEW. Once the calibration procedure was complete, a linear fit polynomial equation was derived for both the thermistors. These equations (Equation 10.2) were later used to calculate skin temperature.

$$\begin{aligned} T_1 &= -52.23(x) + 50.01 \\ T_2 &= -49.06(x) + 47.36 \end{aligned} \tag{10.2}$$

'x' refers to the output voltage of the temperature circuit. The thermistor linearization circuits were assembled and hand soldered on a Veroboard and were powered by two 12 V batteries. The output of the temperature sensors was acquired and recorded by a USB 6009 DAQ card *(National Instruments Corporation, Texas, USA)*. The circuitry along

with the batteries and the DAQ card were housed inside an aluminium case (dimensions: 250 mm $\times$ 202.8 mm $\times$ 64 mm).

10.2.2 Subjects

With the approval of City University London Senate Research Ethics Committee, a cold pressor study was carried out on 15 healthy volunteers, seven male, eight female, aged between 18 – 36 (mean age $\pm$ SD: 26.2 $\pm$ 4.8 years), and with no history of cardiovascular disease. The experimental protocol was clearly explained to all the participants and written consent was obtained prior to the experiment. In the informed consent, all the volunteers were warned that they might experience a mild tingly feeling while the right hand is immersed in an ice bath and were to give a sign if they prefer to withdraw from the study at any point of time. The subjects were asked not to smoke or exercise for at least two hours before the experiment. All volunteers were rested for approximately 10 – 15 min before the start of the study. The volunteers were asked to keep their movement to a minimum during the study to avoid motion artefacts.

FIGURE 10.3: *In vivo* measurement of red and infrared ear canal and finger PPG signals from one of a volunteer during the cold pressor test.

10.2.3 Experimental protocol

The experiments were carried out at the Research Centre for Biomedical Engineering (RCBE) laboratory, City University London, under room temperatures between 22 ± 2°C. During the experiments, the subjects were made to sit on a comfortable chair, with both hands resting on soft cushions, arranged to a height equivalent to their heart position. Once the volunteer was comfortable in the position;

- The RECAP probe was placed 9 mm deep into the right ear canal
- Two in-house designed finger PPG probes were connected to the index fingers of the right and left hands
- The skin temperature sensors were attached to the dorsal surface of the right and left hand of the volunteer
- The red and yellow lead of the ECG cable were connected to the Ag-AgCl easitab ECG electrodes (SKINTACT, F-WA00) placed directly on the right and the left side of the chest, and the green (reference) lead connected to the electrode placed on left side of the hip.

Once all the sensors were in place, baseline readings were obtained from all the volunteer's for 2 minutes, before they were notified with a countdown (3 – 1) to start slowly immersing their right hand into the ice bath maintained at approximately 1°C. Thirty seconds into the ice bath, they were notified again to start slowly removing their right hand from the ice bath and place it back on the surface. The monitoring was continued until the volunteers hand rewarmed to a minimum temperature above 24°C.

10.2.4 Data analysis

The raw PPG, ECG and temperature data recorded during the study was extracted separately for offline analysis. Prior to any signal processing routines, all the acquired signals were resampled from the acquired sampling rate (1000 Hz) to 100 Hz. This was to eliminate the unwanted noise and to condition the acquired signals. This was implemented using the resample function in MATLAB (The MathWorks, USA). Figure 10.4 shows the raw infrared PPG signal acquired at 1000 Hz and the same signal re-sampled at 100 Hz.

The resampled signals were then filtered, and processed to calculate various parameters, described as follows:

PPG signal Amplitude analysis– The AC and DC components of the PPG signals acquired from all three sensors were first extracted using a band-pass (f_c = 0.5 Hz and 15 Hz) and

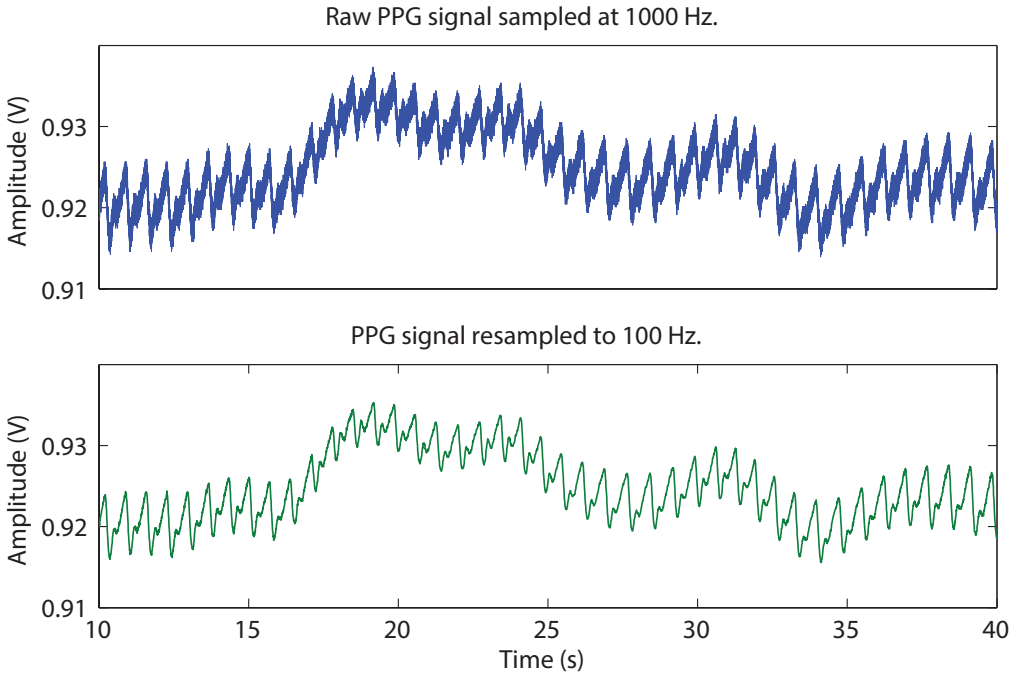

FIGURE 10.4: The raw ppg signal acquired at 1000 Hz and the resampled 100 Hz PPG signal.

a lowpass filter (f_c = 15 Hz) in LabChart–8.0 *(ADInstruments, Sydney, Australia)*. The filters used were linear-phase Finite Impulse Response (FIR) filters with a transition width of 20% and pass band ripple $< 0.5\%$ (the input amplitude). The effective length of the lowpass and bandpass FIR filters was 139 and 3980 respectively.

A peak detection algorithm was then used to detect the peaks and valleys of all the AC PPG signals. The peak-to-peak (pk-pk) amplitude was then calculated for the detected peaks. Figure 10.5 shows the infrared PPG signal acquired from the LIF and the calculated

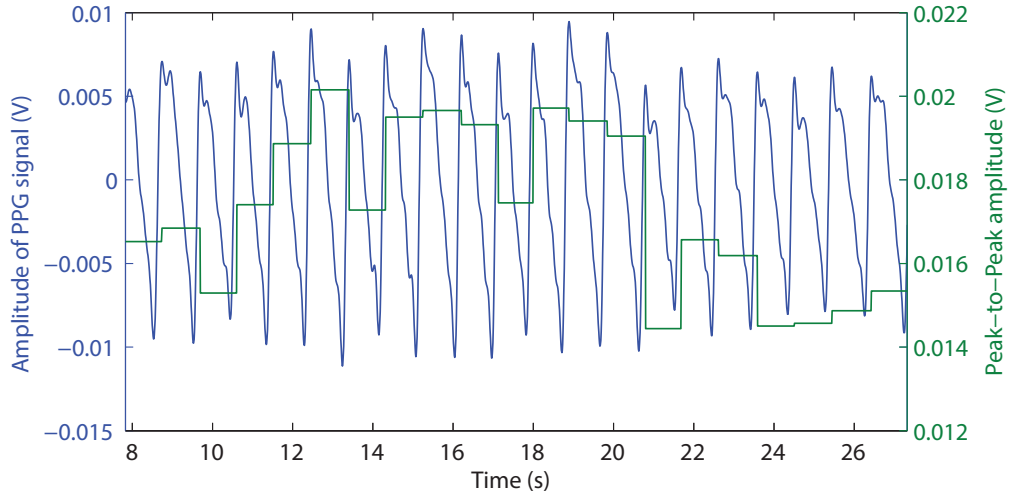

FIGURE 10.5: Infrared PPG signal acquired from the LIF and the estimated pk-pk amplitude of the signal as computed by the peak detection algorithm.

pk-pk amplitude of the signal by the algorithm used. The mean pk-pk amplitude of red and infrared AC PPG signals, acquired from all three locations was computed for all three stages of the experiment (before ice water immersion, during ice water immersion and after ice water immersion). The mean of the mean peak-to-peak amplitude across the entire study group for all three stages of the experiment was then calculated and compared. To check for any statistical significance between the amplitude of AC PPG signals between the ear canal and the periphery during all three stages of the experiment, non-parametric statistical tests were performed on the data. A P-value < 0.05 was considered to be statistically significant. Similarly, the mean DC amplitude of the red and infrared PPG signals was calculated and compared across all three probes and at three phases of the experiment.

SpO_2 analysis– In order to demonstrate the effect of compromised peripheral perfusion on the estimation of arterial oxygen saturation, SpO_2 values were calculated from the PPG signals acquired from all three probes, during all three phases of the experiment. SpO_2 was calculated in a three-seconds rolling window using equation Equation 10.3.

$$SpO_2 = 110 - 25 \times R_{OS};\ R_{OS} = \frac{\left(\frac{AC_R}{DC_R}\right)}{\left(\frac{AC_{IR}}{DC_{IR}}\right)} \tag{10.3}$$

Where R_{OS} is the Ratio of Ratios, AC_{IR} and AC_R are the peak-to-peak amplitudes of the infrared and red AC PPGs, and DC_{IR} and DC_R are the DC PPG components at respective wavelengths. The % drop in SpO_2 during ice water immersion (when compared to the baseline) was then calculated for each volunteer. The mean of the SpO_2 estimated from all three sensors was calculated for baseline, ice immersion period and the recovery period and was then compared.

Variations in cardiac function (HRV)– The ECG signals acquired from the volunteers were filtered using a linear phase bandpass FIR filter with cut-off frequencies at 0.5 Hz and 20 Hz. The R-wave peak of the ECG signal was detected using ECG peak-detection algorithm in LabChart-8.0. The detected R-wave peaks of the filtered ECG signal were then used to calculate the beat-to-beat interval (Figure 10.6), the beat-to-beat heart rate and the R-wave amplitude. The changes in the heart rate, R-to-R interval and r-wave amplitude were then plotted with the changes in skin temperature measurements. The mean changes in R–R interval, R-wave amplitude and heart rate during the CPT were calculated for each volunteer and compared.

Pulse Transit Time (PTT)– PTT measurements were made by calculating the time difference between the foot of the PPG signal and the R-wave peak of the ECG signal. The foot of the PPG signal was detected using the second derivative maximum method. This was to increase the accuracy and detection rate of the inflection points. The second derivative

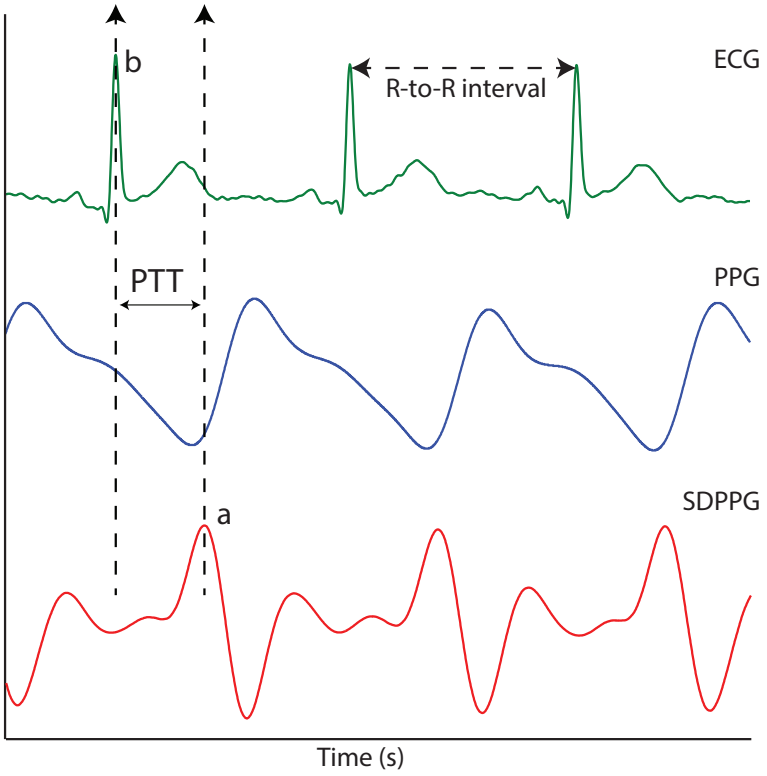

FIGURE 10.6: The ECG signal, the PPG signal and the second derivative photoplethysmogram (SDPPG). PTT is the time difference between points 'a' and 'b'.

of the infrared PPG signals was acquired using the SavitzkyGolay method with a window width of 31 points. The maximum of the second derivative PPG signal (SDPPG) represented the maximal acceleration point at the foot of PPG signal.

The time difference between the R-wave peak of the ECG signal and the maximum peak of the SDPPG was then used to calculate PTT as shown in Figure 10.6. Using the SDPPG signals from the EC, the LIF, and the RIF, mean PTT was calculated for all three stages of the experiment (before, during and after the ice immersion) for each volunteer. The mean PTT calculated from the EC, the LIF and the RIF were then compared during the CPT.

10.3 Results

Baseline raw PPGs– Good quality photoplethysmographic signals with high signal-to-noise ratio and large amplitude were obtained from the prototype ear canal and finger PPG probes. Figure 10.7 shows the baseline raw (AC + DC) infrared PPG traces obtained from the ear canal, the right index finger and the left index finger of a volunteer. Two key observations that can be made from Figure 10.7 are (1) the pronounced respiratory modulation in the ear canal PPG signals when compared to the left and right index finger

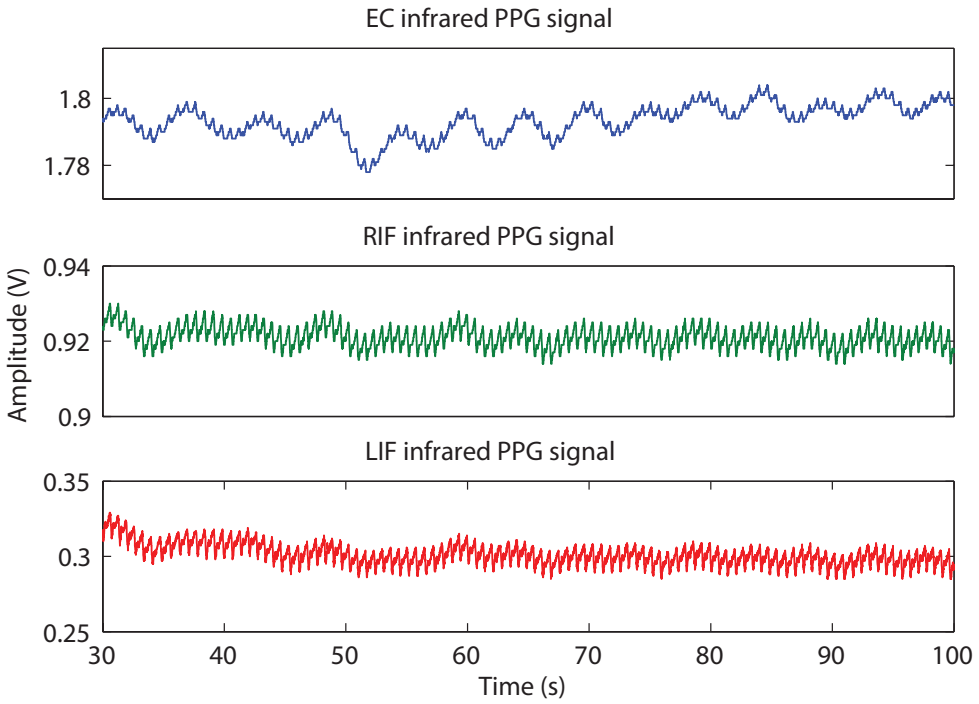

FIGURE 10.7: The raw baseline infrared PPG traces obtained from the ear canal, the right index finger and the left index finger of a volunteer

PPGs, and (2) the large DC amplitude and small AC amplitude of the ear canal PPG signals when compared to the PPG signals acquired from the periphery. The disparity in the amplitude of the PPG signals is expected as the tissue lining the ear canal (2-3 mm) is much smaller than the finger (10-15 mm). Hence, the light absorption by tissue and other non-pulsatile absorbers is much higher in the finger than that of the ear canal.

The respiratory modulation in the ear canal PPG signals was further investigated through spectral analysis. The power spectrum of the baseline raw infrared PPGs acquired from all three locations was derived. The power spectrum of the EC, RIF and LIF PPG signals were normalised with the power of the cardiac component to highlight the changes in the respiration related component. The power of the respiratory component (0.1 Hz to 0.5 Hz) between all three locations was then compared.

Figure 10.8 shows the frequency spectrum of the EC, the RIF, and the LIF PPG signals in 4 healthy volunteers. From the figure, it is evident that the power of the respiration related frequency component is much higher in the EC PPG signals than that of the periphery. Two factors are likely to contribute to these findings. First, the shorter distance of the EC from the heart compared to the finger, which meant less attenuation of the respiratory modulation. Second, the blood vessels in the head region are relatively less sensitive to sympathetically mediated vasoconstriction that may mask respiratory oscillations.

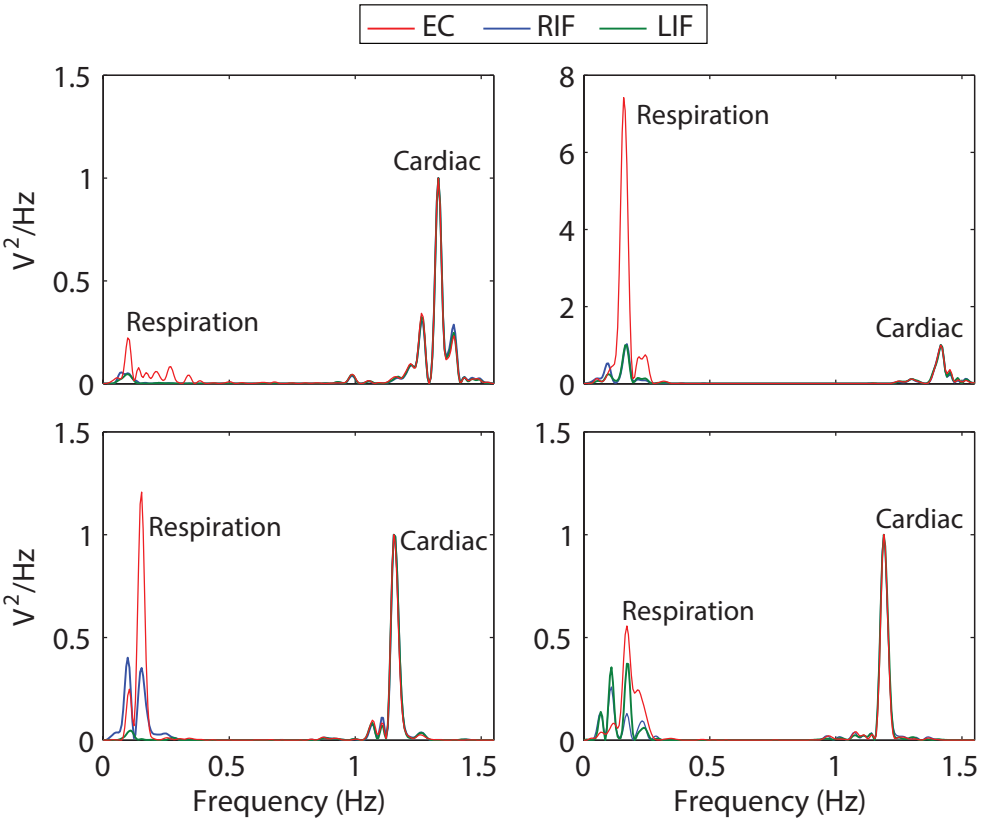

FIGURE 10.8: The power spectrum of the infrared DC PPG signals acquired from the EC, the RIF and the LIF in 4 healthy volunteers highlighting the respiratory and cardiac components. The power of the respiratory component in the EC PPG signals is significantly higher.

Baseline AC PPGs– A 8-second sample of the baseline red and infrared AC PPG signals acquired from the EC, the RIF and the LIF are shown in Figure 10.9. The morphology of the PPG signals obtained from the ear canal was somewhat different to the PPG signals acquired from the finger sensors in almost all the volunteers. However, all the signals correspond accurately with the cardiac cycle. In some volunteers, the morphology of the PPG signals resembled the aortic pressure waveform. The dicrotic notch is clearly visible in the diastolic phase of the finger PPG signals when compared to the ear canal PPG signals. These changes in the morphology of the PPG signals are thought to be due to the vascular resistance of large arteries that supply blood to the head and the brain (common carotid arteries). The higher vascular resistance of these arteries causes the dicrotic notch (reflected wave) to occur in the systolic phase instead of the diastolic phase of the PPG signal. A slight shift in phase between the finger and ear canal PPG signals is also apparent in Figure 10.9. This is expected, as the ear being closer to the heart than the finger, the time taken for arterial pulsations to travel from the heart to the ear canal is less than the time is taken for the pulsations to reach the finger.

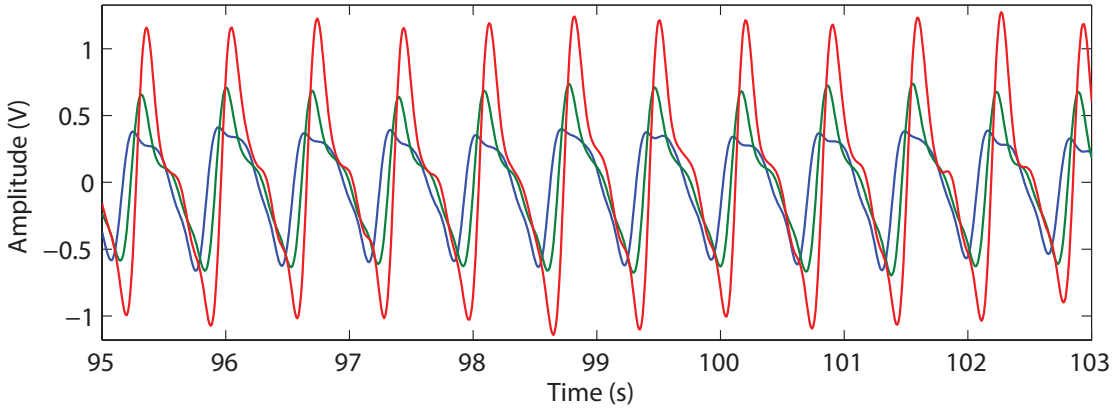

(a) Infrared AC PPG signals

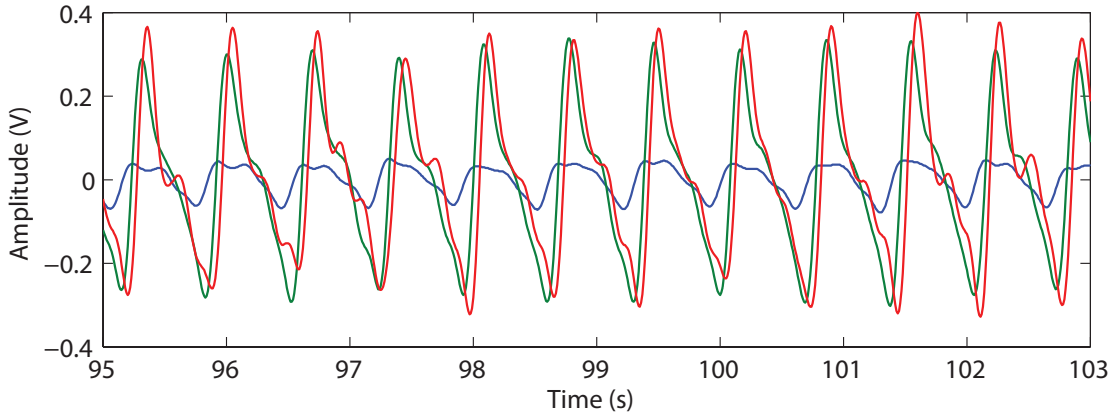

(b) Red AC PPG signals

FIGURE 10.9: The (a) infrared and (b) red AC PPG signals acquired from the EC (blue trace), the RIF (green trace) and the LIF (red trace) of a volunteer.

10.3.1 Variation in amplitude of the AC PPG signals

The infrared AC PPG signals acquired from the ear canal, the right index finger and the left index finger, and the simultaneously acquired temperature signals from both right and left index fingers of a randomly selected volunteer are shown in Figure 10.10. The y-axis on Figure 10.10(A) represents the amplitude of the AC PPG signals, whereas the y-axis on Figure 10.10(B) represents the temperature in degrees centigrade (°C) for 10 min. Three preliminary observations can be made from Figure 10.10 during the ice water immersion.

- the amplitude of the AC PPG signals acquired from the right index finger has decreased as soon as the right hand was immersed in the ice water. This is, however, expected since the ice water immersion causes a significant drop in skin temperature (from 33.5°C to 13.5°C), which leads to profound vasoconstriction in the right hand
- the amplitude of AC PPG signals acquired from the LIF has also reduced significantly, although the temperature of the left hand has remained relatively constant. In addition, the skin temperature of left hand has dropped by approximately one

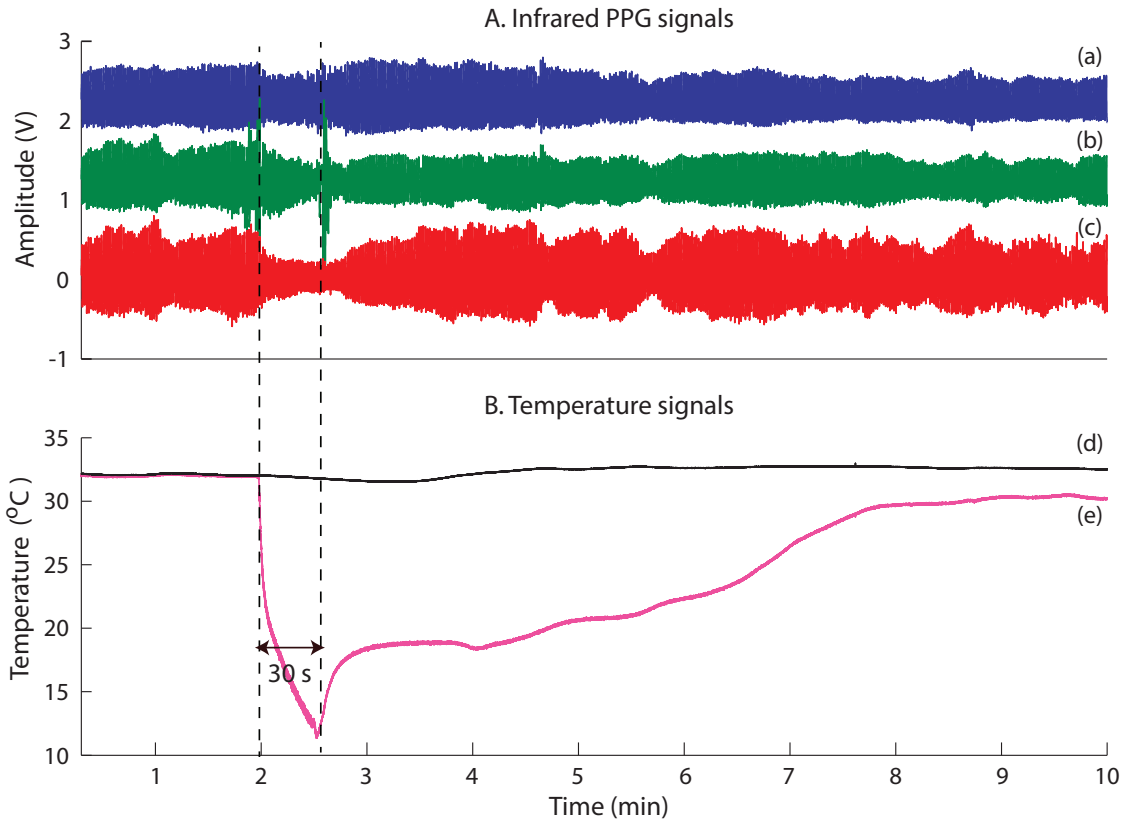

FIGURE 10.10: A. Infrared AC PPG signals recorded from (a) the ear canal, (b) the right index finger and (c) the left index finger of a volunteer. B. Simultaneously obtained temperature reading from (d) the left index finger and (e) the right index finger of the same volunteer for a period of 10 min.

degree at the end of the ice water immersion period (Figure 10.14(e)), which suggests that the significant reduction in blood supply in the left hand (reduction in amplitude of PPG) caused a drop in the left-hand skin temperature

- in contrast to the peripheral sites, the amplitude of the AC PPG signals from the ear canal have remained relatively constant. Although a small change in AC amplitude is noticeable.

Although there has been a significant drop in the amplitude of the AC PPG signals in both the left and the right index fingers, the cardiac component was still clearly visible in the PPG signals acquired from most of the volunteers. Hence, accurate estimation of SpO_2 is probable. However, few volunteers had a drop in the pulse amplitude sufficient to diminish the signal quality, whereby the PPG signals could not be distinguished from noise. Some volunteers have also reported discomfort and shivering towards the end of the ice water immersion, which resulted in some movement artefacts. One such case, where the quality of red PPG signals from RIF and LIF has deteriorated is shown in Figure 10.11. It is in these circumstances where the estimated SpO_2 is more likely to be inaccurate. However,

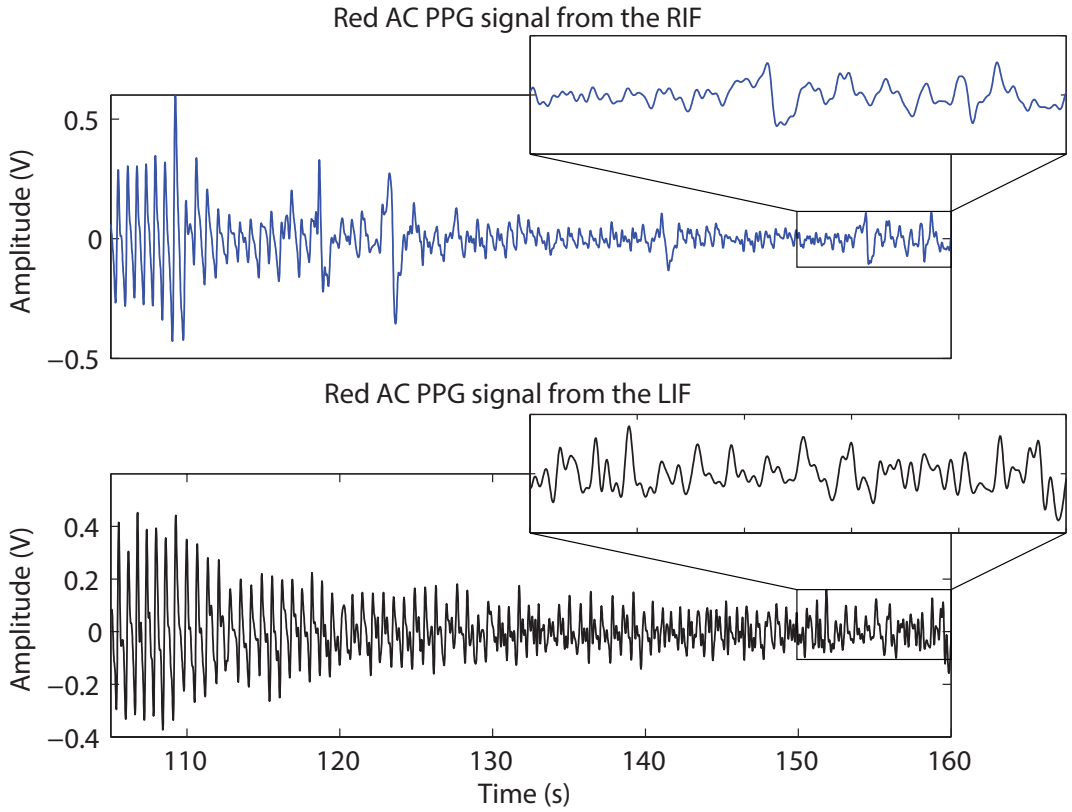

FIGURE 10.11: The quality of the red PPG signals from the right index finger and the left index finger have deteriorated towards the end of the cold pressor test in few volunteers.

in most volunteers the quality of the LIF PPG signals has remained consistent during the ice water immersion when compared to RIF.

After the ice water immersion, the amplitude of the RIF AC PPG signals has slowly started to increase with an increase in the temperature of the right hand. While, the amplitude of the LIF PPG signals has recovered back to the baseline value within the first few minutes of the recovery period. On the contrary, the amplitude of the ear canal PPG signals has stayed relatively constant throughout the experiment. These observations demonstrate the ability of the body to maintain relatively constant blood flow to the vicinity of the ear canal and more generally to the head despite changes in peripheral perfusion. Similar effects were seen in all the volunteers.

The mean of the mean amplitude and the standard error of the mean (±SEM) (across 15 volunteers) of AC red and infrared PPG signals acquired from the EC, the RIF and the LIF during baseline, ice water immersion and rewarming periods are shown in Table 10.1. The data is graphically displayed with the use of Box and Whiskers Plot in Figure 10.12. From the figure, the median value and interquartile range (amplitude of the red and infrared PPG signals) of the EC PPG signals have remained relatively constant throughout the experiment, while the LIF and the RIF median value has varied significantly.

TABLE 10.1: Mean (±SEM) of the mean AC red and infrared PPG signals acquired from the ear canal (EC), right index finger (RIF) and left index finger (LIF), during all three stages of the experiments.

	Before immersion			During immersion			After immersion		
	EC	RIF	LIF	EC	RIF	LIF	EC	RIF	LIF
Red									
Mean (mV)	109	321	424	121	151	222	104	159	521
SEM (±)	17	51	50	16	20	22	16	35	54
Infrared									
Mean (mV)	800	776	1715	790	324	912	797	391	1960
SEM (±)	99	110	216	79	54	97	83	88	215

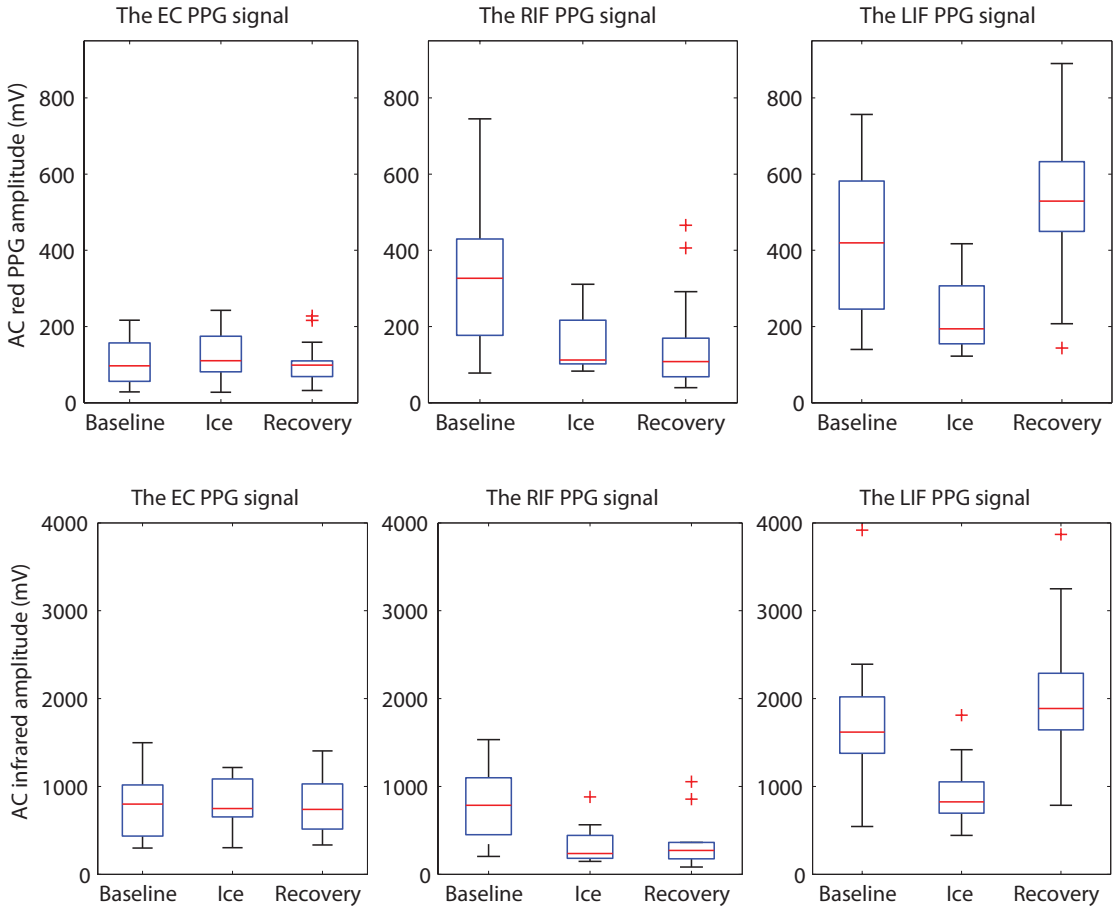

FIGURE 10.12: Box and whiskers plot demonstrating the change in mean amplitude of red and infrared PPG signals obtained from all three sensors during the cold pressor test.

During the ice water immersion, the mean amplitude of the red and infrared RIF PPG signals has dropped by 52.96% and 58.25%. While the LIF PPG signals have dropped by 47.64% (red) and 46.82% (infrared). In contrast, with the finger sensors, the mean

TABLE 10.2: The percentage change in amplitude of red and infrared PPG signals during ice water immersion in all the volunteers

% Drop	No. of volunteers					
	Red EC	Infrared EC	Red RIF	Infrared RIF	Red LIF	Infrared LIF
< 5%	10	9	1	1	1	0
5 % - 25 %	4	5	3	2	2	3
25 % - 45 %	1	1	2	2	2	5
45 % - 65 %	0	0	5	6	9	6
65 % - 85 %	0	0	4	4	1	1

amplitude of the red EC PPG signals have increased by 11.01% and the infrared EC PPG signals has decreased by 1.25%. To quantify this further, the % drop in the amplitude of red and infrared PPG signals during the ice water immersion in all the volunteers was calculated and is shown in Table 10.2. A substantial drop in amplitude <65% was seen in four healthy volunteers in the RIF, while, in the LIF the similar drop was seen in one volunteer.

Once the right hand was out of the ice water, the amplitude of the PPG signals has started to increase with temperature. However, the amplitude of RIF has never returned to the initial baseline value within the 10 min recovery period. The amplitude of the red and infrared PPG signals from RIF has only increased by 5.29% and 20.67% respectively during the recovery period, although the temperature of the right hand has increased to a minimum of 24°C. Compared to the RIF, the EC PPG signals have recovered back to the baseline value by the end of the measurement period. This is expected as the drop in the ear canal PPG signals was significantly low compared to the finger. The LIF PPG signals, on the other hand, have exceeded the baseline value by 22% (red) and 14.21% (infrared). When compared to the ice immersion period, the amplitude of RIF PPG signals has increased by 134.68% (red) and 114.91% (infrared) in the recovery period.

10.3.1.1 Temperature vs Amplitude

The mean temperature of the right and the left hand during baseline, ice water immersion and the recovery period are shown in Table 10.3. From the table, it is clear that the skin temperature measured from the right hand has dropped significantly in all the volunteers while the left-hand temperature stayed constant during ice water immersion. The effect of the significant drop in the temperature of the right hand on the amplitude of the PPG signals acquired from the bilateral index fingers was studied by comparing the mean temperature measurements with the mean amplitude of PPG signals.

TABLE 10.3: The mean of the mean temperature measured across 15 healthy volunteers in the right and left hand during all three phases of the experiment. The standard error of the mean (±SEM) is also depicted here.

Location	Baseline	Ice water immersion	Recovery
RIF	29.3 ± 0.907	8.1 ± 0.936	24.4 ± 1.420
LIF	29.7 ± 0.827	29.8 ± 0.790	29.6 ± 0.833

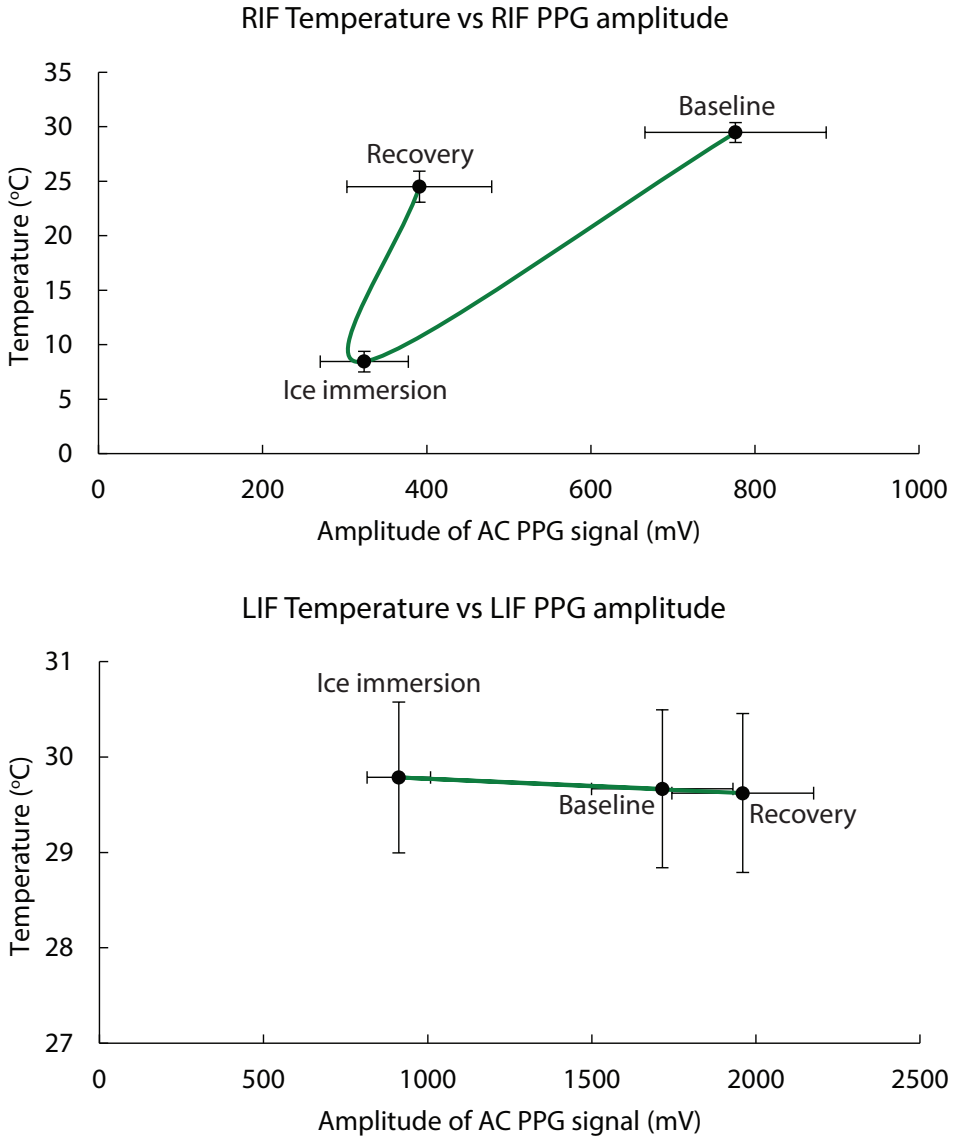

FIGURE 10.13: Effect of the right-hand immersion on the amplitude of the infrared PPG signals from right and left index fingers. The x-error bars represent the standard error of the mean amplitude (±SEM). The y-error bars represent the standard error fo the mean temperature.

The mean amplitude of the infrared PPG signals measured from the RIF and LIF during all three stages of the experiment are plotted against the skin temperature measurements

from the respective sites in Figure 10.13. In the RIF, the amplitude of the infrared PPG signal has decreased significantly with temperature during the ice water immersion. The average rate of change in amplitude of PPG signals from baseline to the end of the ice water immersion in the RIF was 21.52 mV/°C. The average rate of change in amplitude of PPG signals from the cold stimuli to the recovery period was 4.18 mV/°C. These results show that the PPG signal amplitude has not recovered with a rise in temperature at the same rate as they have declined during the ice water immersion. In contrast, with the RIF, the amplitude of infrared PPG signal from LIF has decreased significantly, although no detectable change in temperature was observed.

10.3.1.2 Statistical analysis

To check if there were any statistically significant differences between the amplitude of AC PPG signals measured during baseline, ice water immersion and the recovery period of the experiment, statistical analysis was performed on the measured data. All statistical analysis was performed using SigmaPlot 12.0 (Systat Software Inc., Chicago, USA). Prior to the statistical tests, the normality of the data was tested using the Kolmogorov-Smirnov test. It is important to determine if the measured data were normally distributed or not as the appropriate choice of statistical tests depends on it. Table 10.4 shows the results of the Kolmogorov-Smirnov normality test performed on the red and infrared AC PPG signals acquired from EC, RIF and LIF during baseline, ice water immersion and recovery periods of the experiment. The Kolmogorov-Smirnov distance (K-S Dist.) is the maximum cumulative distance between the histogram of the data and the Gaussian distribution curve of the data. The P-values represent the observations for normality using the Kolmogorov-Smirnov test. The data was considered normally distributed only if the computed P-value was greater than the set P-value (P=0.05). Not all the data were found to be normally distributed.

Hence, a non-parametric test was used to check if means of the measured AC PPG signals were significantly different from one another during different stages of the experiment. The test used was Kruskal-Wallis One Way Analysis of Variance on Ranks. The parametric equivalent of the Kruskal-Wallis test is the one-way analysis of variance (ANOVA). The Kruskal-Wallis test is a rank-based test that is commonly used to determine statistical significance between two or more groups. The test first ranks all the values from low to high, paying no attention to the group it belongs. The smallest number gets a rank of 1. The largest number gets a rank equal to the sample size. The discrepancies among the rank sums are combined to create a single value called the Kruskal-Wallis statistic (H-value). The test also produces a P-value, which is indicative of the difference between groups. A comparison between two groups of data was recognised as significantly different

TABLE 10.4: Results of the Kolmogorov-Smirnov normality test performed on the red and infrared AC PPG signals acquired from EC, RIF and LIF during baseline, ice water immersion and recovery periods of the experiment.

	Location	Wavelength	K-S Dist.	P-value	Result
Baseline	EC	Red	0.132	> 0.2	Passed
		Infrared	0.138	> 0.2	Passed
	RIF	Red	0.161	> 0.2	Passed
		Infrared	0.124	> 0.2	Passed
	LIF	Red	0.108	> 0.2	Passed
		Infrared	0.144	> 0.2	Passed
Ice water immersion	EC	Red	0.182	> 0.2	Passed
		Infrared	0.177	> 0.2	Passed
	RIF	Red	0.313	<0.001	Failed
		Infrared	0.247	=0.020	Failed
	LIF	Red	0.204	=0.116	Passed
		Infrared	0.141	>0.2	Passed
Recovery	EC	Red	0.251	=0.017	Failed
		Infrared	0.159	>0.2	Passed
	RIF	Red	0.257	=0.013	Failed
		Infrared	0.319	<0.001	Failed
	LIF	Red	0.152	>0.2	Passed
		Infrared	0.213	=0.083	Passed

if the computed P-value by Kruskal-Wallis test was < 0.05. A significant difference was found between the groups. To isolate the group or groups that differ from the others, all pairwise multiple comparison procedure (Student-Newman-Keuls Method) was used. The results of the statistical tests together with the corresponding P value are shown in Table 10.5.

From Table 10.5, it is easily observed that the effect of peripheral vasoconstriction on the amplitude of ear canal PPG signals is almost negligible. However, significant differences in the RIF PPG signals were found when the mean amplitude was compared from the baseline vs. ice water immersion period and recovery vs. baseline. While in the LIF, a significant difference was found when the mean amplitude was compared between the baseline and the ice water immersion period. This is expected as the amplitude of the PPG signals from the LIF has increased to a value equivalent to the baseline after the ice water immersion, while the amplitude of the PPGs in the RIF have not. These results demonstrate the robustness of the ear canal as the site for monitoring PPG signals.

TABLE 10.5: Results of One-Way Analysis of Variance Test between the mean amplitudes of each sensor during all three stages of the study along with corresponding the P-values. Statistically, significant differences in the mean amplitude of the PPG signals was found in the RIF and the LIF during ice water immersion.

Sensor	Wavelength	Comparison	Statistical significance	P-value
Ear canal	Red	Baseline vs Ice	No	=0.928
		Ice vs Recovery	No	
		Recovery vs Baseline	No	
	Infrared	Baseline vs Ice	No	=0.997
		Ice vs Recovery	No	
		Recovery vs Baseline	No	
Right index finger	Red	Baseline vs Ice	Yes	=0.019
		Ice vs Recovery	No	
		Recovery vs Baseline	Yes	
	Infrared	Baseline vs Ice	Yes	=0.007
		Ice vs Recovery	No	
		Recovery vs Baseline	Yes	
Left index finger	Red	Baseline vs Ice	Yes	<0.001
		Ice vs Recovery	Yes	
		Recovery vs Baseline	No	
	Infrared	Baseline vs Ice	Yes	<0.001
		Ice vs Recovery	Yes	
		Recovery vs Baseline	No	

10.3.2 Variations in amplitude of DC PPG signals

Figure 10.14 shows the variation in infrared DC PPG waveform acquired from the EC, the RIF and the LIF, along with simultaneously acquired temperature signals from the right and the left hand of a volunteer. It can be noticed that the amplitude of the ear canal DC PPG signal is larger than that of the right and the left index fingers during baseline. This is because the absorption of light by tissue and other non-pulsatile absorbers is much higher in the finger than the ear canal, which is a bony structure covered only with a few millimetres of tissue.

During the ice water immersion, the amplitude of the DC PPG signals in the RIF has increased with temperature. This is expected as the profound vasoconstriction resulting from the ice water immersion causes a significant reduction in the arterial and venous blood fractions in the measurement site. Hence, there will be a reduction in light absorption.

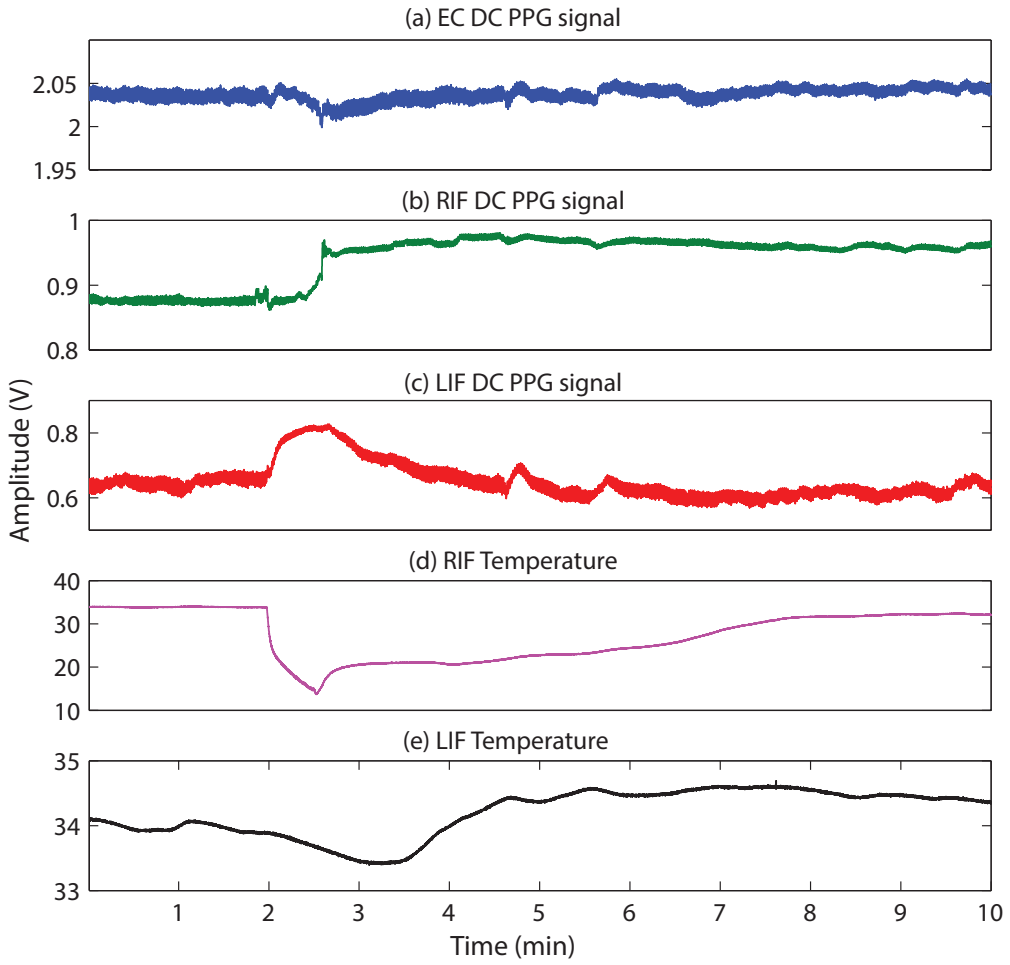

FIGURE 10.14: The infrared DC PPG signals recorded from (a) the ear canal (EC), (b) the right index finger (RIF) and (c) the left index finger (LIF) of a volunteer, along with the temperature reading from (d) the right index finger and (e) the left index finger.

Other contributing factors for this increase in DC amplitude include the constriction of muscles and the thickening of the dermis layer due to sympathetic response. Similar to the RIF, the LIF has shown an increase in the amplitude of the DC PPG signals, although there is no noticeable change in left-hand temperature. After the ice water immersion, the RIF DC PPG amplitude has either remained constant or has further increased in a few volunteers. In contrast, the LIF DC amplitude has reduced and returned to a value equivalent to the baseline. The ear canal DC PPG signal amplitude, on the other hand, has remained relatively constant throughout the experiment.

The changes in the mean DC red and infrared PPG signals acquired from the EC, the RIF and the LIF during all three stages of the experiments are plotted with the help of a Box and Whiskers plot in Figure 10.15.

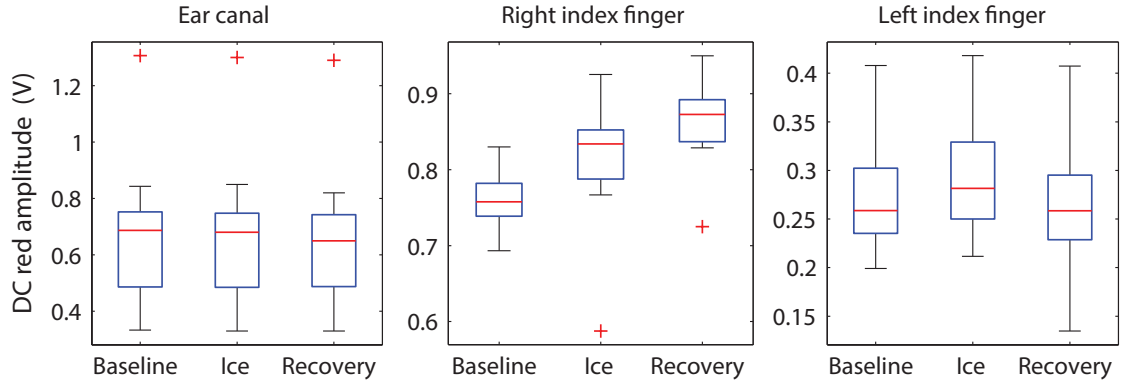

(a) Red DC amplitude

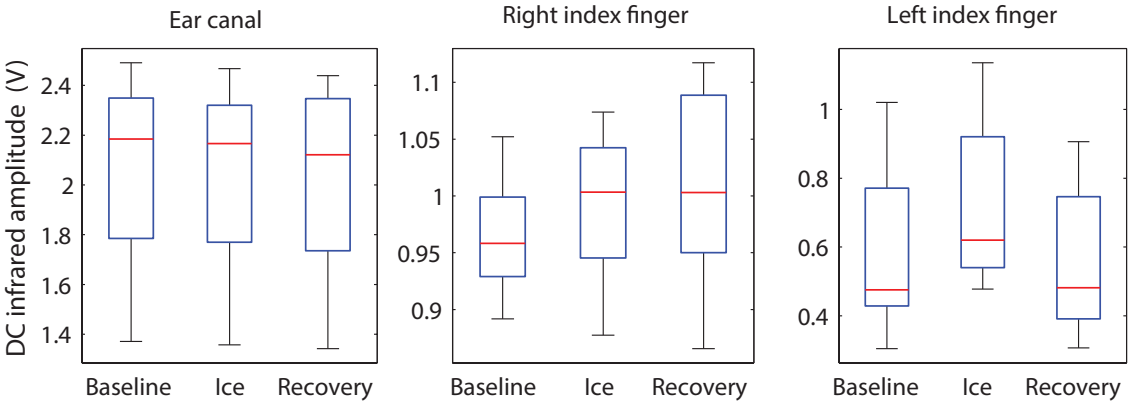

(b) Infrared DC amplitude

FIGURE 10.15: Box and whiskers plot demonstrating the change in mean amplitude of (a) red and (b) infrared DC PPG signals obtained from all three sensors before, during and after the cold pressor test.

10.3.3 Changes in arterial oxygen saturation values

Arterial oxygen saturation (SpO_2) values were calculated from the AC and DC fractions of the PPG signals acquired from the ear canal and the finger sensors for the entire duration of the study using Equation 10.3. To demonstrate the effect of compromised peripheral perfusion on the estimation of arterial oxygen saturation, a mean value of the estimated SpO_2 was calculated for the baseline, ice water immersion, and the recovery periods of each volunteer. The mean SpO_2 values calculated from the EC, the RIF and the LIF of all volunteers, during all three stages of the experiment are graphically displayed in Figure 10.16, with the help of a box plot. The mean range of SpO_2 values calculated from all three sensors during baseline was 102 – 97%, this is expected since all volunteers were healthy and well perfused. Hence, it can be said that there is a good agreement between all three sensors during baseline.

Table 10.6 shows the mean of the mean SpO_2 values calculated during all three stages of the experiment from all three sensors. Although SpO_2 is a global variable and would not change in healthy volunteers from one site to another, a decrease in the mean SpO_2 was

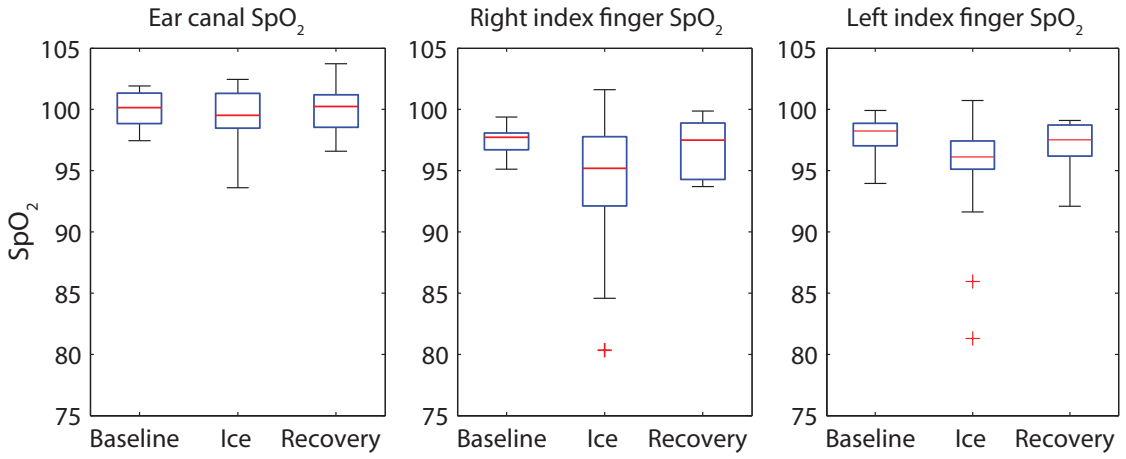

FIGURE 10.16: Demonstrates the change in mean SpO_2 estimated by the ear canal, the right index finger and the left index finger pulse oximeters during all three stages of the experiment.

TABLE 10.6: Mean SpO_2 values calculated from the EC, RIF and LIF PPG sensors during baseline, ice water immersion and recovery periods of the experiment.

Location	Baseline SpO_2 (%) ± SD	Ice water immersion SpO_2 (%) ± SD	Recovery SpO_2 (%) ± SD
Ear canal	100.2 ± 1.5	99.3 ± 2.3	100.2 ± 2.2
Right index finger	97.4 ± 1.2	94.0 ± 5.7	97.2 ± 2.1
Left index finger	97.8 ± 1.6	94.6 ± 5.1	96.7 ± 2.1

observed during ice water immersion in the right and left index fingers. In contrast with the finger sensors, the SpO_2 calculated from the ear canal remained relatively constant.

Although the mean SpO_2 values calculated from the right and left index finger have decreased during the ice water immersion, the sensors have truly only failed to estimate SpO_2 accurately in a few healthy volunteers. This is evident from the large standard deviation and the interquartile range of SpO_2 values (Figure 10.16) measured from RIF during the ice water immersion. In the rest of the volunteers, the estimated SpO_2s were accurate and close to the baseline reading. Hence to discriminate between cases where the finger sensor has failed to estimate SpO_2 with the others, the mean percentage drop in SpO_2 between baseline and ice water immersion was calculated. A drop in SpO_2 value greater than 5% during the ice water immersion was considered to be a failure.

The percentage drop in SpO_2 during ice water immersion in all the volunteers is given in Table 10.7. The right index finger pulse oximeter failed to estimate accurate SpO_2 in 5 healthy volunteers while the left index finger pulse oximeter failed to estimate SpO_2 in 4 healthy volunteers. Compared to the finger sensors, the ear canal pulse oximeter only failed in one volunteer. These results show that the SpO_2 measurements made from the

TABLE 10.7: Summary of pulse oximeters failure in 15 healthy volunteers.

SpO_2 (% drop)	No. of Volunteers		
	Ear canal	Right index finger	Left index finger
$< 1\%$	8	1	4
$1\% - 5\%$	6	9	7
$> 5\%$	1	5	4

periphery are to an extent dependent on the thermal state that, it really weakens the capacity of the pulse oximeter to provide accurate readings. While a central site such as the ear canal can increase the reliability of the pulse oximeter readings.

10.3.4 Variations in cardiac function

While demonstrating the dependence of pulse oximeters on the presence of a strong peripheral pulse to estimate SpO_2 accurately, the cardiovascular reactivity and the heart's function to induced stress stimuli were also studied. The sudden change in temperature due to the immersion of the right hand in ice triggers the activation of the sympathetic nervous system which reacts by changing the distensibility of blood vessels. Along with the initiation of vasoconstriction, the autonomic nervous system triggers the cardiac accelerator nerves which release norepinephrine. This interaction results in an increase in heart rate and the contractility of the heart to compensate for the sudden change in temperature (heat loss). These responses combine to an increase in blood pressure (BP).

These variations in the hearts function during the cold pressor test were captured by calculating the changes in heart rate, R-to-R interval and the R-wave amplitude from the QRS complex of the ECG signal acquired from each volunteer. The amplitude of the R-wave was measured as it corresponds to the voltage conducted with every contraction of ventricles. Figure 10.17 shows the changes in the beat-to-beat interval, heart rate, and peak-to-peak (R-wave) amplitude estimated from the ECG signal acquired from one of the volunteers. It can be observed from the figure that, as soon as the right hand is immersed in ice water, there is an increase in heart rate and the amplitude of the R-wave and the time between two consecutive R-peaks decreases. During the recovery period, as the hand rewarms, the heart rate and the amplitude of the QRS complex of the ECG signal dropped back to a value similar to the baseline. Similar effects were seen in all the volunteers.

Figure 10.18 shows the mean heart rate, R-R interval and the pk-pk amplitude calculated for all the volunteers during all three stages of the experiment. The heart rate has on an average increased by 8 ± 2 (SEM) BPM amongst the volunteers during ice water immersion. The R-R interval has on an average decreased by 73.4 ± 17.8 (SEM) milliseconds

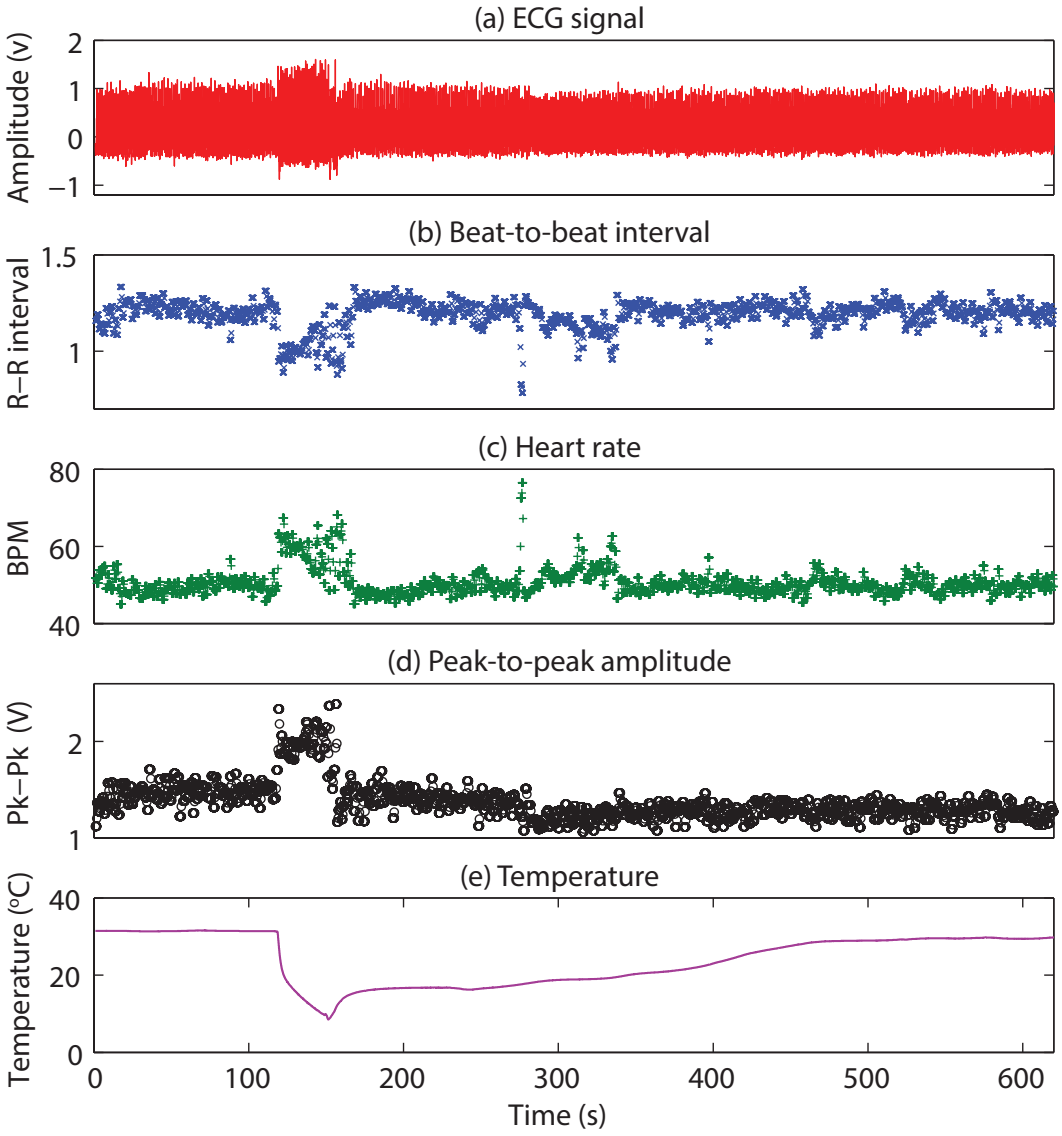

FIGURE 10.17: The changes in the (a) ECG signal, (b) R-R interval, (c) heart rate, (d) peak-to-peak amplitude (e) temperature of a volunteer during the CPT.

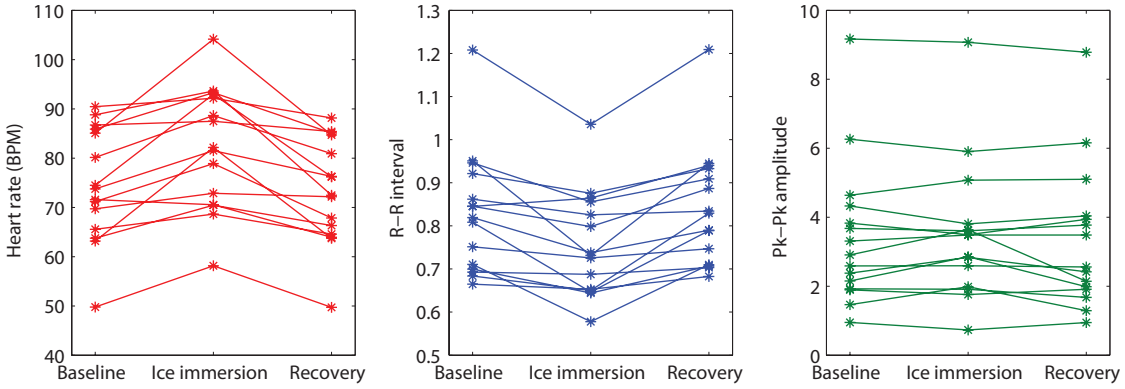

FIGURE 10.18: The mean heart rate, R-R interval and the pk-pk amplitude calculated for all the volunteers during baseline, ice water immersion and the recovery periods of the experiment.

during the ice water immersion amongst all the volunteers. The R-wave amplitude has on an average increased by 156 ± 110 mV (SEM) during this period.

10.3.5 Pulse Transit Time (PTT)

As mentioned earlier, the immersion of right hand in the ice water leads to an increase in heart rate and a decrease in the blood vessel diameter. These reactions combine to an increase in the velocity of the pulse propagating through arteries and the blood pressure. Conversely, after the ice water immersion, the dilation of blood vessels to rewarm the hand causes a decrease in pulse wave velocity (PWV) and blood pressure (BP). The velocity of a pulse propagating through the arteries is given as the pulse propagation distance divided by the pulse transit time. Therefore, the PTT is indirectly proportional to the PWV and the BP. Thus, by calculating the PTT from the PPG signals acquired from all three different locations, and monitoring the changes in the measured time during all three phases of the experiment, the extent of vasoconstriction and local change in PWV at each site can be indirectly measured. Similarly, the extent of vasodilation after the ice immersion can also be demonstrated.

Hence, PTT at each location was calculated using the ECG signal and the infrared PPG signals acquired from the respective areas. Three volunteers were exempted from the PTT analysis as the PPG signals acquired from these volunteers during ice water immersion were indistinguishable from noise. The mean PTT measured from the EC, the RIF and the LIF PPG signals during all three stages of the experiment are shown in Figure 10.19 using a box-plot. The mean of the mean PTT measurements made across all the volunteers is given in Table 10.8.

The mean baseline PTT measured from the EC is smaller than the PTT measured from the LIF and the RIF. This is expected since the ear is closer to the heart than the finger. The mean PTT measured from the EC, the RIF and the LIF has dropped during the ice water immersion. This indirectly indicates a general rise in PWV and BP in the body. However, the percentage drop in PTT varied across all three locations. The PTT in the

TABLE 10.8: Depicts the mean of the mean PTT measurements from the EC, the RIF and the LIF during baseline, ice immersion and recovery periods of the experiment.

Location	Pulse Transit Time (ms ± SD)		
	Baseline	Ice immersion	Recovery
Ear canal	135.8 ± 21.88	126.7 ± 21.56	142.7 ± 21.8
Right index finger	176.81 ± 22.7	159.98 ± 29.3	184.4 ± 24.2
Left index finger	206.9 ± 34.2	193.53 ± 35.8	257.69 ± 39.6

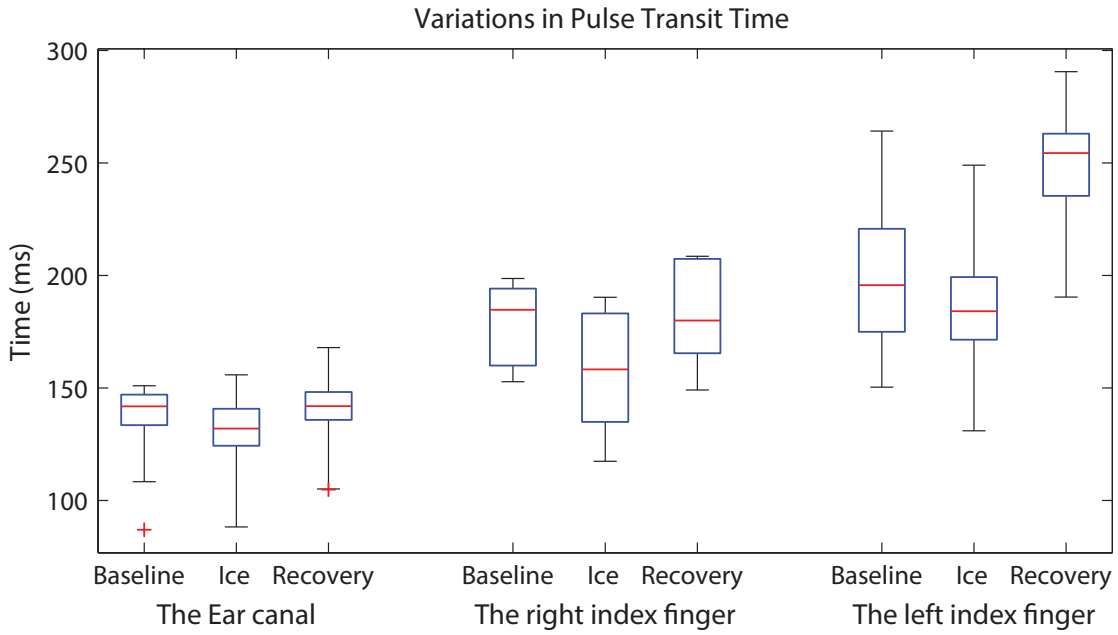

FIGURE 10.19: Box-plots showing the changes in PTT measured from the ear canal (EC), the right index finger (RIF) and the left index finger (LIF).

EC and the LIF has dropped by 3% and 7% while the RIF PTT has dropped significantly by 12%. These differences in the drop of PTT across the three locations indicates the disparity in the strengths of local vasoconstriction in the respective areas. During the recovery period, the mean PTT measured from the EC and the RIF has approximately returned to the baseline value, whereas the LIF PTT exceeded baseline values. This is due to the profound vasodilation resulted from the activation of the thermoregulatory mechanism. The percentage increase in mean PTT during the recovery period, when compared to baseline, was 4% in the EC, 2% in the RIF and 22% in the LIF. These observations demonstrate the ear canal is much more resistant to local changes in BP compared to the peripheral sites.

10.4 Summary

Following the laboratory testing of the novel RECAP probe, it was evaluated in 15 healthy volunteers undergoing a cold pressor test. The main aim of the study was to test the performance and reliability of the ear canal sensor in conditions of poor peripheral perfusion, as opposed to the traditional finger sensor. During the study, red and infrared PPG signals were acquired from the ear canal, the right index finger and the left index finger. Along with the PPG signals, skin temperature measurements were made from the dorsal surface of both left and right hands of the volunteer. The ECG signal was also recorded from all the volunteers. The study started with a 2 min baseline recording followed by a 30 sec right-hand immersion in ice cold water and a recovery period. The recording was stopped

when the right hand was rewarmed to a minimum temperature of 24°C. Data recorded during all these stages was analysed offline to extract various parameters such as pk-pk amplitude, SpO_2, heart rate, R-R interval, and PTT.

The PPG signals acquired from the volunteers show that measurable, good quality red and infrared PPG signals can be obtained from the human auditory canal. However, the ear canal PPG signals were found to be morphologically different to the finger PPG signals (Figure 10.9). PPG pulse features such as the dicrotic notch in the diastolic phase, arrive earlier in ear canal signals when compared to the finger PPG signals. The modulation of the raw PPG signals due to respiration was also more pronounced in the EC PPGs than the RIF and the LIF PPGs.

During the ice water immersion, the amplitude of the AC PPG signals acquired from the RIF decreased significantly with temperature. Similarly, the LIF AC PPG signals have also decreased significantly although no change was observed in skin temperature of the left hand. The EC AC PPG signals, on the contrary, remained relatively constant throughout the experiment. The infrared RIF PPG signals have decreased by 21.5 mV/°C during the ice water immersion. To check for any statistically significant differences between the amplitude of AC PPG signals measured during baseline, ice water immersion and the recovery periods of the experiment, one-way analysis of variance test was performed on the measured data. A statistically significant difference was found when the mean amplitude of the RIF and LIF (red and infrared) PPG signals from baseline were compared with ice water immersion. Statistically significant difference was also found when RIF PPG signals from baseline were compared with the recovery period, indicating that the amplitude of PPG signals from the right hand had not recovered back to baseline within the monitoring period. Meanwhile, no significant difference was found in the amplitude of the EC PPG signals among any of the three stages in the experiment.

The mean amplitude of the DC PPG signal in the RIF increased with a decrease in temperature of the right hand. A similar effect was observed in the LIF, although the temperature of the left hand remained constant. The increase in the DC amplitude is due to the reduced light absorption resulting from a significant reduction in arterial and venous blood fractions at the measurement site. The DC amplitude of the EC PPG signals, on the other hand, have remained relatively constant throughout the experiment. The AC and the DC fraction of the PPG signals acquired from all three locations were then used to calculate the SpO_2 for all three stages of the experiment. During baseline, the mean SpO_2 calculated from all three uncalibrated sensors was between 102 – 97%, this is expected since all volunteers were healthy and well perfused. During ice water immersion, a drop in the estimated SpO_2 was seen in the finger pulse oximeters. A drop in SpO_2 value greater than 5% was considered to be a failure. Therefore, the right index finger pulse oximeter had failed to estimate accurate SpO_2 in 5 healthy volunteers while the left index finger pulse

oximeter failed to estimate SpO_2 in 4 healthy volunteers. Compared to the finger sensors, the ear canal pulse oximeter only failed in one volunteer. These results demonstrate the dependence of the pulse oximeters on the thermal state of the measurement site. Hence, a central site such as the ear canal will increase the accuracy and reliability of the pulse oximeters.

The cardiovascular reactivity to an induced stress stimulus was also studied through this experiment. The variations in the heart's function were captured by calculating the changes in the heart rate, R–R interval, and the R-wave amplitude of the ECG signal during all three stages of the experiment. During the ice water immersion, the sudden change in temperature caused an increase in the heart rate and R-wave amplitude of the ECG signal in almost all the volunteers. Since the R-R interval is inversely proportional to the heart rate, the measured R–R interval decreased in all the volunteers. These results demonstrate the effect of the autonomic nervous system on the heart. The resistivity of the ear canal to local changes in BP or PWV was also demonstrated by measuring the PTT to all three locations during all three stages of the experiment. The mean PTT measured across all the volunteers during the ice immersion dropped by 3% in the EC, 7% in the LIF, and by 12% in the RIF. During the recovery period, the PTT increased back to baseline in the EC, while the RIF PTT increased by 2% and LIF PTT had increased by 22%. These results demonstrate the capability of the ear canal as a location for reliable monitoring of PPGs and SpO_2 in conditions of compromised peripheral perfusion.

— The skin vessels of the human hand constrict so effectively that the ratio of maximum-to-minimum blood flow can be 60 to 1, whereas the same ratio in the body shell is about 6 to 1

Thompson, Pulse oximetry, 1977

11

Investigation of ear canal pulse oximetry in conditions of artificially induced vasoconstriction

This chapter investigates in vivo the capability of the ear canal in producing high quality PPGs and reliable SpO_2 values in conditions of global hypothermia (whole body exposed to a cold environment). This investigation aims to create a more realistic environment compared with the more local hypothermia induced on the arm during the cold pressor test discussed in the previous chapter

In this chapter whole body cold exposure was used as it results in heat loss from all portions of the body and stimulates more natural responses a patient would experience in conditions leading up to hypothermia. Therefore, a study was carried out in 15 healthy volunteers who were exposed to room temperatures of 10°C. During this investigation, PPG signals were acquired from the ear canal and the finger using the custom built probes discussed in earlier chapters, and from the ear lobe using a commercial earlobe sensor. Comparisons were then made amongst all three sensors with respect to the amplitude of the PPG signals and SpO_2 values estimated. The degree of autonomic control over arteriolar vessels of the finger and the ear canal was also studied using the acquired PPG signals.

This chapter briefly describes the aims and objectives of the study followed by details of the procedure and methodology for the investigation. The various methods of data analysis are

then described in the chapter. Finally, the results obtained and their statistical significance is discussed.

11.1 Aims and objectives

- To validate the hypothesis that the ear canal remains sufficiently perfused in conditions leading to hypothermia, and good quality PPG signals can be obtained in those circumstances.
- To investigate the differences in SpO_2 measured from the finger and the ear canal in conditions of profound peripheral vasoconstriction.
- To illustrate the differences in the influence of sympathetic nerve activity on the peripheral and core circulation through low-frequency spectral analysis.

11.2 Methods and Materials

11.2.1 Measurement setup

The measurement setup described in Chapter 10 was adapted to acquire, display and store PPG, ECG, temperature, and NIRS signals in this investigation. The block diagram of the system is shown in Figure 11.1. The system consists of the following.

11.2.1.1 PPG and ECG monitor

PPG signals were acquired from three different locations during the course of this study. The custom built ear canal and finger PPG sensors were used to acquire red and infrared PPG signals from the ear canal and the finger. The configuration of these sensors and the materials used to manufacture these sensors are described in Chapter 7. Along with these sensors a commercial ear clip sensor *(LNCS TC-I, Reusable Tip-Clip Ear Sensor, Masimo corp., CA, USA)* was used to acquire PPG signals from the earlobe. The motivation of using a earlobe sensor was used to demonstrate that the ear canal is better perfused than the earlobe in conditions of whole body vasoconstriction. Raw red and infrared PPG signals from all three sensors were acquired using two PPG processing systems (described in Chapter 8). The acquisition system was also used to acquire the ECG signal, which acted as the timing reference for the acquired PPG signals.

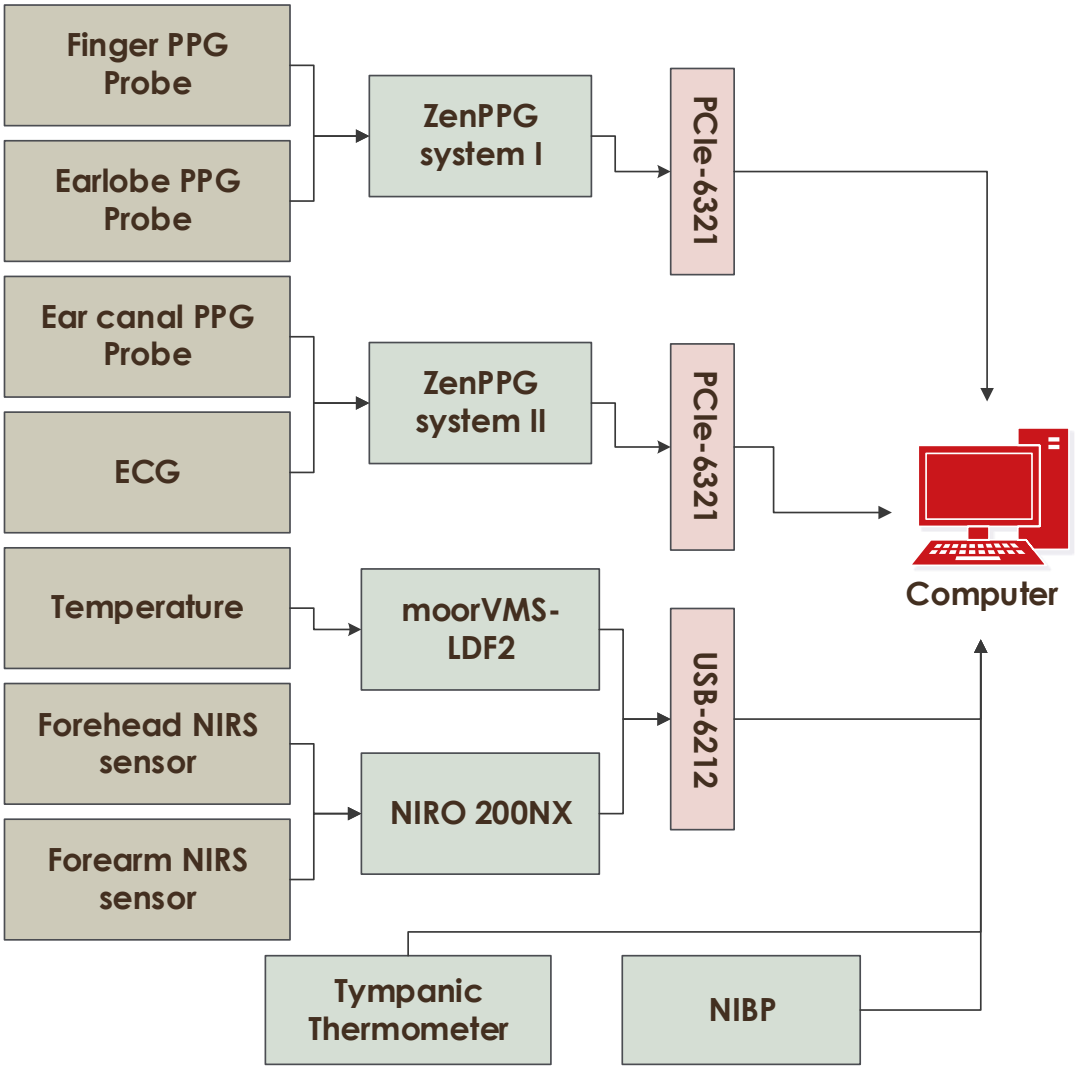

FIGURE 11.1: Block diagram showing the measurement setup used during the cold exposure test. PPG, ECG, temperature, NIRS and LDF signals were acquired using the setup.

11.2.1.2 NIRS and other monitors

A commercial NIRS monitor *(NIRO 200NX, Hamamatsu Photonics, Shizuoka, Japan)* was adopted to record changes in the Normalised Tissue Haemoglobin Index (nTHI) (which is a measure of changes in tissue blood volume) from both the peripheral and central sites. The NIRO 200NX adopted Spatially Resolved Spectroscopy and modified Beer-Lambert law to calculate changes in haemoglobin concentrations and blood volume. See Section 3.6 for more information on the principles and operation of NIRS. The NIRS sensors used to estimate these parameters consisted of 3 LEDs at specific emission wavelengths of 735, 810 and 850 nm, and two photodiodes with a small separation distance between each other. A separation distance of 4 cm between light emitters and detectors was used in this study to maximise the light penetration depth. nTHI was measured to study the effect of

cold stress on the blood volume in the measurement sites. nTHI was measured from the forearm (peripheral) and the forehead (central) of the volunteer.

A laser Doppler flowmeter *(moorVMS-LDF2, Moor Instruments, Devon, U.K.)* was used to measure peripheral skin temperature. Along with the NIRS and the LDF systems a commercial non-invasive blood pressure (NIBP) monitor was used to measure the systolic and diastolic blood pressure *(HEM-907, Omron Healthcare, Hoofddorp, The Netherlands)*. A tympanic thermometer *(ThermoScan-5 IRT4520, Braun GmbH, Frankfurt, Germany)* was used to measure the core temperature from the ear canal of the volunteer.

11.2.1.3 Data acquisition

The PPG signals from the ear canal, the finger and the earlobe were digitised and recorded along with the ECG signal using two PCIe-6321 NI DAQ cards (*(National Instrument Corporation, Austin, Texas)*). An NI USB-6212–bus powered USB DAQ card was used to record the nTHI signals from the NIRS and the skin temperature signal from the LDF. The simultaneous recording of signals and control of the systems was through a VI implemented in LabVIEW. The VI described in Chapter 9 was modified to include the acquisition and control of all three DAQ cards. All the signals were recorded at a sampling frequency of 1 kHz. The blood pressure reading and core temperatures were recorded manually in an Excel sheet during the study.

11.2.2 Subjects

With the approval of the Senate Research Ethics Committee of the City University London, fifteen healthy volunteers (6 – ♀ and 9 – ♂) aged between 19 and 45 (mean age ± SD – 28 ± 5 years) were recruited for this study. Based on the medical history and a general medical examination, subjects with cardiovascular, pulmonary, or metabolic diseases were excluded from the study. The general medical examination included a measure of heart rate, blood pressure and core body temperature. All the subjects were normotensive (mean BP ± SD – 116/70 ± 14/11), normothermic (mean core temp ± SD – 36.52 ± 0.33) and none was taking any medication. The subjects were informed of the details of the study and signed informed consent was sought from all the volunteers before the experiment. All the subjects were asked to refrain from ingesting beverages containing caffeine and alcohol and were asked not to exercise or smoke for at least two hours preceding the test. To maximise the effect of cold temperatures on the cardiovascular system, all the subjects were asked to wear just one layer of clothing during the experiment.

11.2.3 Measurement protocol

The trials were carried out in the Biomedical Engineering Research Laboratory, at City University London. Upon arrival, all the volunteers were seated in a room maintained at $24 \pm 1°C$ for a minimum of 10 min to ensure haemodynamic stabilisation. During the study, the subjects were made to sit in a comfortable chair, with both hands resting on armrests arranged to a height approximately equivalent to their heart's position. Once the volunteer was comfortable, heart rate (HR), blood pressure and core temperature were measured. If the volunteer was found to be normotensive and normothermic then, the study was continued.

The following sensors were then attached to the volunteer–

- The finger PPG probe was placed on the second digit of the left hand (Figure 11.2). The RECAP sensor was placed 9 mm inside the left ear canal, and the ear clip sensor was attached to the right earlobe of the volunteer
- The NIRS sensors were placed on the left forearm and the left side of the forehead. The sensors were kept in place using a double-sided clear medical adhesive tape
- The LDF sensor was placed just below the thumb on the dorsal surface of the left hand and it was attached to the skin by means of a ring-shaped double-sided adhesive
- The red, yellow and green leads of the ECG cable were connected to the Ag-AgCl easitab ECG electrodes (SKINTACT, F-WA00) placed directly on the chest (the right and the left side) and on the left hip.

Once all the sensors were in place, the investigation protocol (Figure 11.3) started with the acquisition of baseline measurements from the volunteer for at least two minutes. The volunteers were then moved to the adjacent temperature-controlled room maintained at

FIGURE 11.2: Photograph of the measurement set-up showing the forehead NIRS sensor and the ear canal PPG sensor on the left, and the finger PPG probe on the index finger, NIRS sensor on the forearm and LDF sensor on the back of the hand on the right.

FIGURE 11.3: Diagram showing the measurement protocol of the investigation.

10 ± 1°C for 10 minutes. After the cold exposure, the volunteers were moved back to normal room temperatures (24°C), where monitoring continued for another 10 minutes. PPG, ECG, NIRS and temperature data was continuously recorded during all three phases of the experiment. The core temperature was measured from the right ear of the volunteer once every minute for the entire duration of the study (22 minutes). Blood pressure was measured once at the start of the study, and then at the end of the cold exposure and the recovery period. The NIRS system was zero-set between each phase of the experiment to highlight just the changes in the measurements and avoid any motion artefacts from being recorded.

11.2.4 Data analysis

The raw PPG, ECG, NIRS and temperature data recorded during the study was extracted separately for offline analysis. Prior to any signal processing, the acquired signals were resampled from 1000 Hz to 100 Hz. This was to restrict the bandwidth of the signals and remove unwanted noise. This process is described in detail in Chapter 10.

Normalised Pulse Amplitude (NPA) – The red and infrared PPG signals acquired from all three locations were first divided into AC and DC components using bandpass and lowpass filters implemented in LabChart–8.0 *(ADInstruments, Sydney, Australia)*. The lower and upper cut-off frequencies of the bandpass filter (AC signal) were 0.5 Hz and 15 Hz respectively. The cut-off frequency of the lowpass filter (DC signal) was 15 Hz. Further details on the filters used are provided in Section 10.2.4. The AC component of the PPG signals was then divided by the DC component to normalise the PPG signals (Figure 11.4).

A peak detection algorithm was used to detect the peaks and valleys of all the normalised PPG signals. From the detected peaks, the normalised pulse amplitude (NPA) was calculated. The mean NPA estimated from the red and infrared PPG signals acquired from all three locations was then averaged for every two minutes of the study. NPA was estimated by the above procedure for all the subjects and was then averaged for the entire group. The mean NPA of all the subjects during the cold exposure (every 2 min) and the recovery (every 2 min) was analysed for their statistical significance compared to the baseline period. A non-parametric statistical test (ANOVA on ranks) was performed on the data.

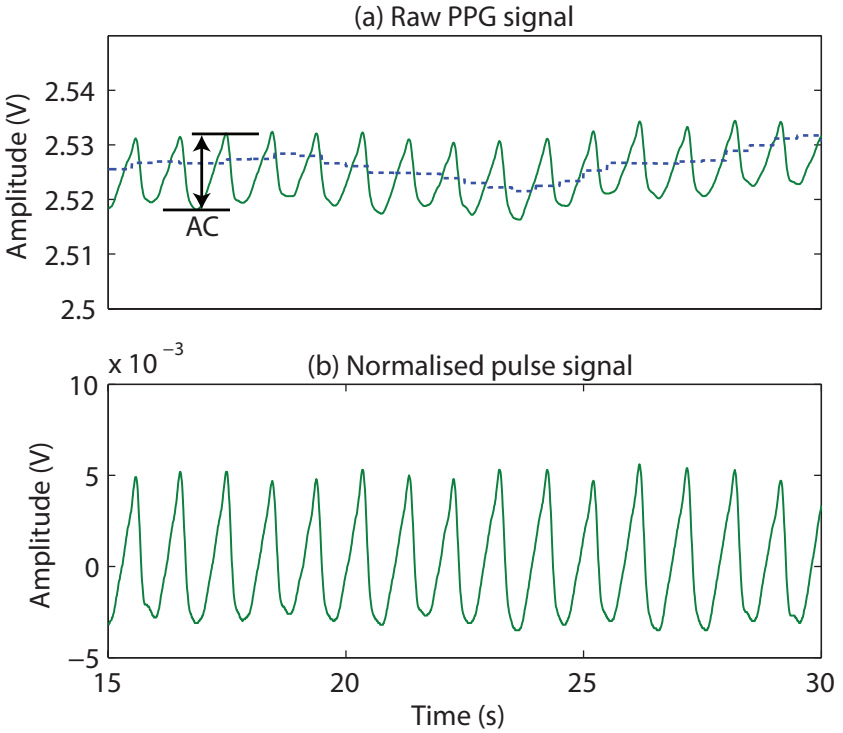

FIGURE 11.4: Shows (a) the raw PPG signal and (b) the normalised PPG signal. The blue trace in sub-plot 'a' shows the DC component. Normalised pulse signal is the ratio of AC and DC components of the PPG signal.

A P-value < 0.05 was considered to be statistically significant. Statistical analysis was performed using SigmaPlot-12.0 (SPSS Inc, Chicago, USA).

The NPA of the infrared PPG signals was then compared with the nTHI measured by the NIRS device since the nTHI and NPA both reflect changes in blood volume in the measurement areas. However, the comparisons were made keeping in mind the key difference between the two techniques. That is the light penetration depth, and hence, the information the variables provide. nTHI from NIRS is calculated from deeper layers of tissue and is a reflection of the arterial, venous and capillary blood volume. On the other hand, NPA of a PPG signal reflects just the changes in arterial blood volume. Hence, NIRS is probably superior to photoplethysmography in measuring changes in blood volume. Nonetheless, the changes in arterial blood volume during the cold exposure will reflect in both NPA and nTHI. Therefore, the trends can be compared. Hence, the nTHI measured from the forehead were compared with NPA from the ear canal and the nTHI from forearm was compared with the NPA from the finger.

SpO_2 analysis – The effect of cold exposure on the quality of the peripheral pulse and on the estimated SpO_2 by the pulse oximeter was demonstrated by calculating SpO_2 values from the acquired PPG signals. SpO_2 measurements were made from all three locations to highlight the superiority of the RECAP probe over other two probes. SpO_2 was calculated

in a three-seconds rolling window using the below equation.

$$SpO_2 = 110 - 25 \times R_{OS} \tag{11.1}$$

R_{OS} –the ratio of ratios is the ratio of the red and infrared NPA. The SpO_2 estimated from each volunteer was averaged for every two minutes of the study. The SpO_2 estimated from each volunteer during the first 2 min (i.e., baseline) was then compared with every 2 min (2–10) of the cold exposure and the recovery. Further, the change in SpO_2 as a response to the cold exposure was calculated, and the number of instances where the SpO_2 value has dropped below 90% was considered as a failure. The number of instances each sensor has failed during the cold exposure was then calculated and compared.

Sympathetic and parasympathetic activity– Exposure to cold temperatures commonly leads to a drop in the skin temperature due to heat loss. This effect triggers the activation of the sympathetic nervous system which causes a change in the arterial distensibility and cardiac function to counter the heat loss. However, the peripheral vasculature is known to more sensitive or is more affected by the sympathetic activation than the core vasculature. Hence, the degree of sympathetic control over blood vessels in the finger and the ear canal was studied through low-frequency spectral analysis of the PPG signals acquired from the respective areas. The infrared PPG signal acquired from the finger and the ear canal were imported and preprocessed for analysis in MATLAB *(The Math Works Inc., Massachusetts, USA)*. The acquired signals were bandpass filtered, with a linear-phase FIR filter. The lower and upper cut-off frequencies of the filter were 0.035 and 0.5 Hz respectively. The signals were filtered to eliminate all other components apart from the sympathetic and the parasympathetic components, which are known to be between 0.04 Hz and 0.4 Hz [275].

The filtered signals were then divided into three segments, each containing information from one stage of the study, i.e., the baseline, the cold exposure and the recovery. The power spectrum of all three segments was then obtained using the 'pwelch' function in Matlab. From the power spectrum, the power of the low-frequency components (LF) (between 0.04 – 0.15 Hz) and the high-frequency (HF) components (in the range 0.15 – 0.4 Hz) was computed. The power of LF components corresponds to both sympathetic and parasympathetic activity while the power of HF components corresponds to only parasympathetic activation. Hence, the ratio of LF to HF (LF/HF) components was calculated to quantify the changes in the sympathetic activity, as in [276]. The LF to HF ratio measured from the finger and the ear canal were then compared during all three stages of the experiment.

11.3 Results

Baseline – Good quality, easily recognisable PPG signals with large amplitudes were recorded from the finger, the ear canal and the earlobe in all the volunteers during baseline. Figure 11.5 depicts typical AC red and infrared PPG signals acquired from the finger, the ear canal, and the earlobe of a volunteer for a period of 15 seconds. The figure also depicts the ECG signal acquired from the volunteer during the same period. As can be seen from Figure 11.5, the PPG signals from all locations are synchronous with the R-wave peak of the ECG signal. The PPG signals acquired from the ear canal of the volunteer were smaller in magnitude than the finger and the earlobe probes. This is expected since the finger and earlobe contain more vascular tissue than the ear canal. As mentioned earlier in Chapter 10, the morphology of the PPG signals acquired from the ear canal were distinct from the finger and the earlobe PPG signals. A close-up of the PPG signals acquired from all three locations is presented in Figure 11.6. The earlobe PPG signal resembled the finger PPG signals in most volunteers, although earlobe is close to the ear canal. The

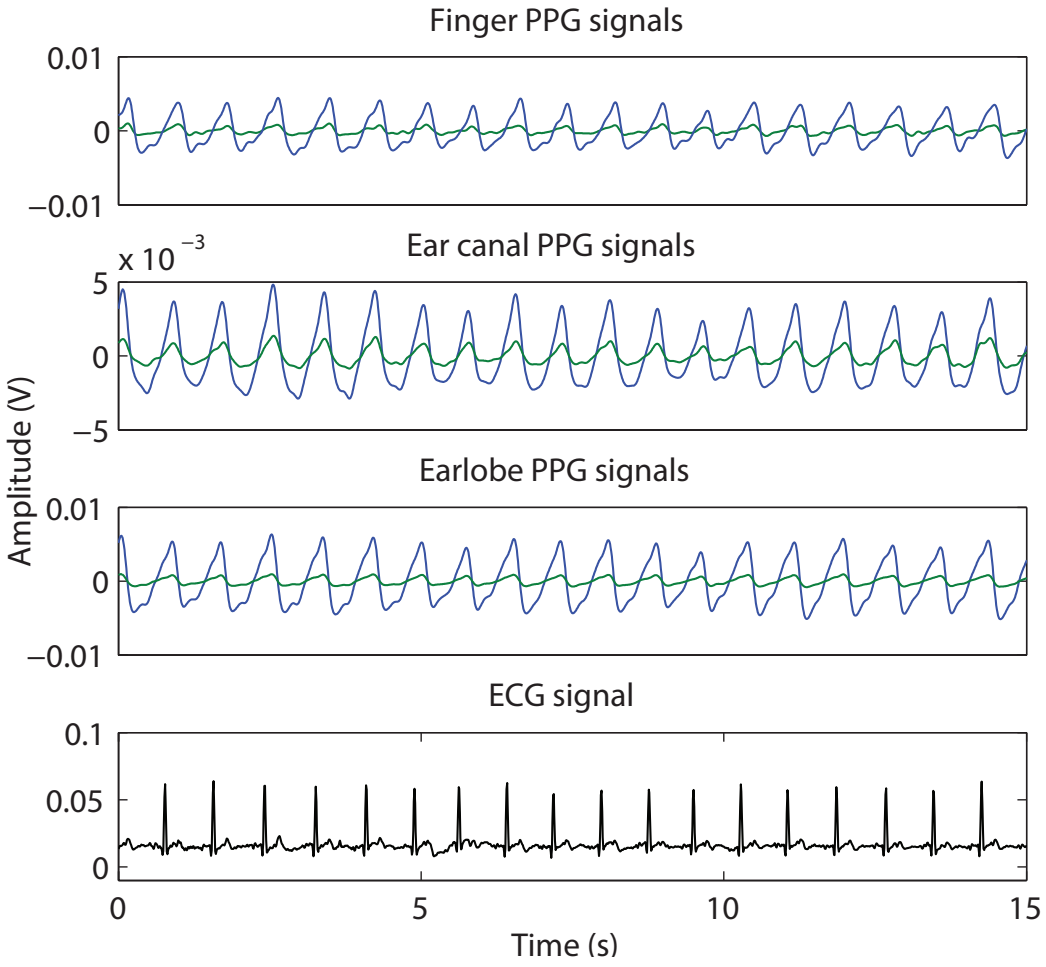

FIGURE 11.5: The red (green trace) and infrared (blue trace) PPG signals acquired from the finger, the ear canal and the earlobe, and the ECG signal acquired from one of the volunteers for a duration of 15 sec.

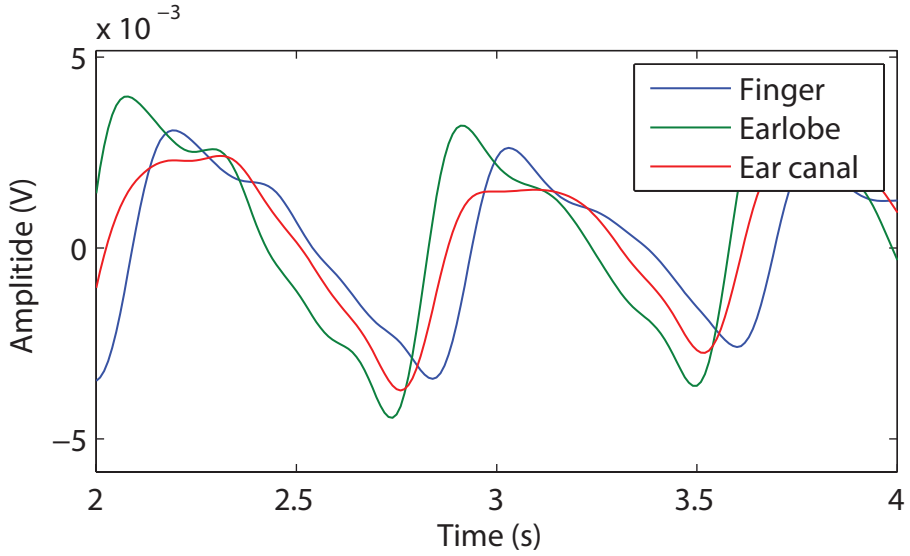

FIGURE 11.6: A close-up of the PPG signals acquired the finger, the ear canal and the ear lobe showing the differences in the morphology of the PPG signals.

mean (±SD) skin and core temperature of the volunteer during the baseline was 27.43 ± 0.02°C and 36.7 ± 0.1°C respectively. The blood pressure of the volunteer before the baseline recording was 110/60.

Cold exposure – Figure 11.7 shows the infrared PPG signals acquired from the finger, the earlobe and the ear canal along with the peripheral (skin) and the core temperature measured from one of the volunteers for the entire duration of the study (22 min). From the figure, the amplitude of the PPG signals acquired from the finger has reduced significantly with time during cold exposure. This is expected due to the profound vasoconstriction resulting from exposure to low temperatures. The skin temperature of the volunteer has dropped to 20.2°C by the end of the cold exposure. Similarly, the earlobe PPG signals have also reduced in amplitude during the cold exposure. However, the magnitude of reduction was much lower compared to the finger. On the other hand, the amplitude of the PPG signals from the ear canal has remained relatively constant throughout the cold exposure. The maximum drop in the core temperature of the volunteer during the cold stimulus was 0.9°C, which is below the ±1°C error of the digital tympanic thermometer. This conceivably explains the uncompromised blood flow to the ear canal and, therefore, the unwavering PPG signals obtained from the ear canal. The blood pressure of the volunteer has increased to 119/71 by the end of the cold exposure.

Recovery – The amplitude of the PPG signals acquired from all three locations has recovered with an increase in skin temperature over the recovery period. However, the amplitude of finger PPG signals did not return to the initial baseline value within the 10 min recovery period. The ear lobe PPG signals have recovered to the steady state baseline value in the first few minutes and remained unchanged. The ear canal PPG signals, on

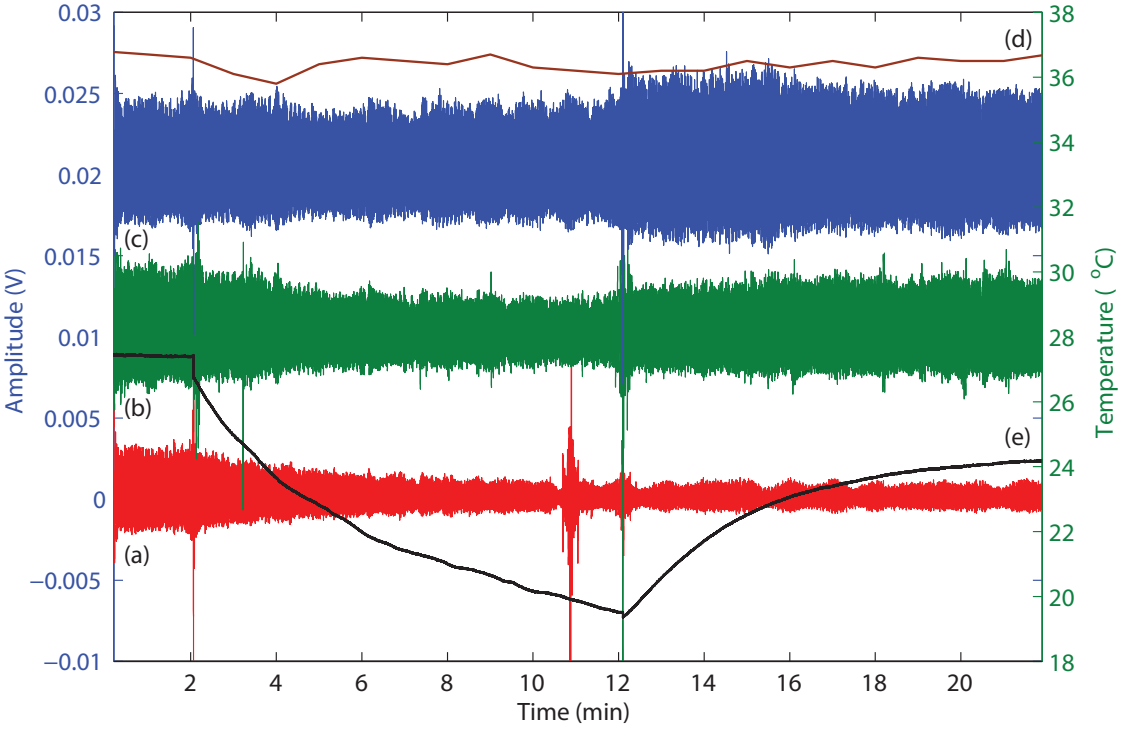

FIGURE 11.7: Infrared AC PPG signals acquired from (a) the finger, (b) the earlobe and (c) the ear canal of volunteer number 11 and the simultaneously acquired (d) core and (e) skin temperature signal for the entire duration of the study. The Y-axis on the left shows the amplitude of the PPG signals while the Y-axis on the right shows the temperature.

the contrary, have increased in amplitude as soon as the volunteer was removed from the air-conditioned room, and have remained relatively constant for the rest of the monitoring period. The skin and the core temperature of the volunteer by the end of the recovery period were 24.1°C and 36.8°C respectively. The blood pressure has recovered back to 111/60 by the end of the study. To analyse these changes further, and to take into account the changes in the DC portions of the PPG signals, NPA (AC/DC) of the PPG signals was measured.

11.3.1 Normalised Pulse Amplitude (NPA)

Figure 11.8 shows the NPA of the infrared PPG signals acquired from one of the randomly selected volunteers; the NPA measured here is averaged using a 5 sec rolling window. From the figure, it is evident that the NPA measured from the ear canal does not change during the cold exposure. While, the NPA from the finger and the earlobe have reduced significantly.

Similar to this volunteer, the NPA of the red and infrared PPG signals acquired from all three locations was measured and was averaged for every two minutes of the study in all the volunteers. The distribution of this data is graphically displayed here using the

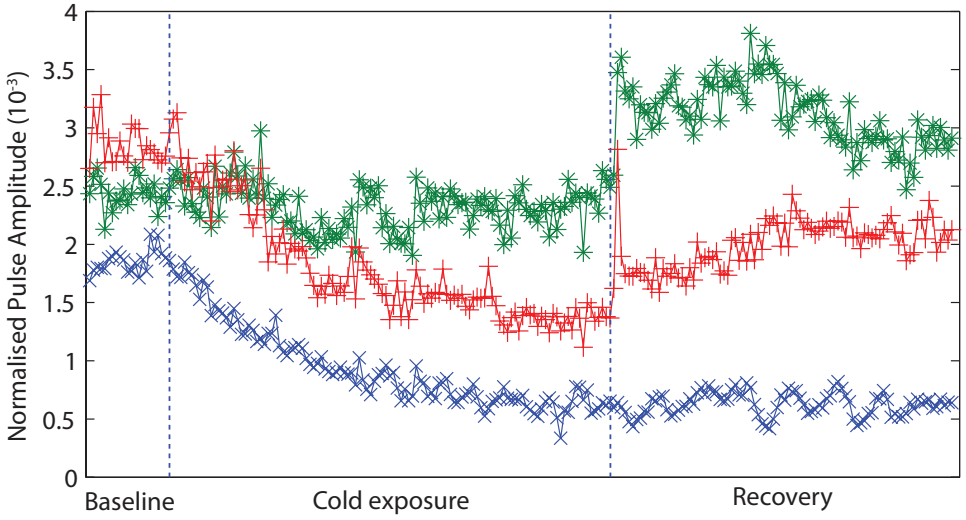

FIGURE 11.8: NPA of the infrared PPG signals acquired from the finger (blue trace), the earlobe (red trace) and the ear canal (green trace) of a randomly selected volunteer using a five-second rolling window.

Box and Whiskers plots in Figure 11.9, Figure 11.10, and Figure 11.11. The following observations can be made from these figures:

- The sudden exposure to cold temperatures during the experiment caused an instantaneous and significant drop in the mean NPA of red and infrared finger PPG signals in all volunteers. This is evident through the significant reduction in the interquartile range, the mean and the median at the 4^{th} minute in Figure 11.9 when compared to the first two minutes

- The NPA of the finger PPG signals had further reduced with time across the volunteer group at a steady rate till the end of the cold exposure. The mean percentage drop in the NPA of red and infrared finger PPG signals by the end of the cold exposure was 80.1% and 86.3% respectively. The magnitude of this change in the mean NPA of finger PPG signals demonstrates the sensitivity of the arterial vessels in the periphery to the vasoconstrictor stimuli. The mean skin temperature of the volunteers has dropped to 19.5 $\pm$ 0.49°C ($\pm$SEM) by the end of the cold exposure from 29.9 $\pm$ 0.42°C during baseline.

- During the recovery period, the NPA of the finger PPG signals slowly increased with time. However, the NPA did not rise to a value close to the baseline, although a steady state was achieved between the 20^{th} and 22^{nd} min. The percentage difference between the mean NPA measured by the end of the study to the baseline was 47.2% (red) and 54.5% (infrared)

- The NPA of red and infrared PPG signals from the earlobe reduced during the cold exposure. This is clearly visible in Figure 11.10, as the interquartile range, the

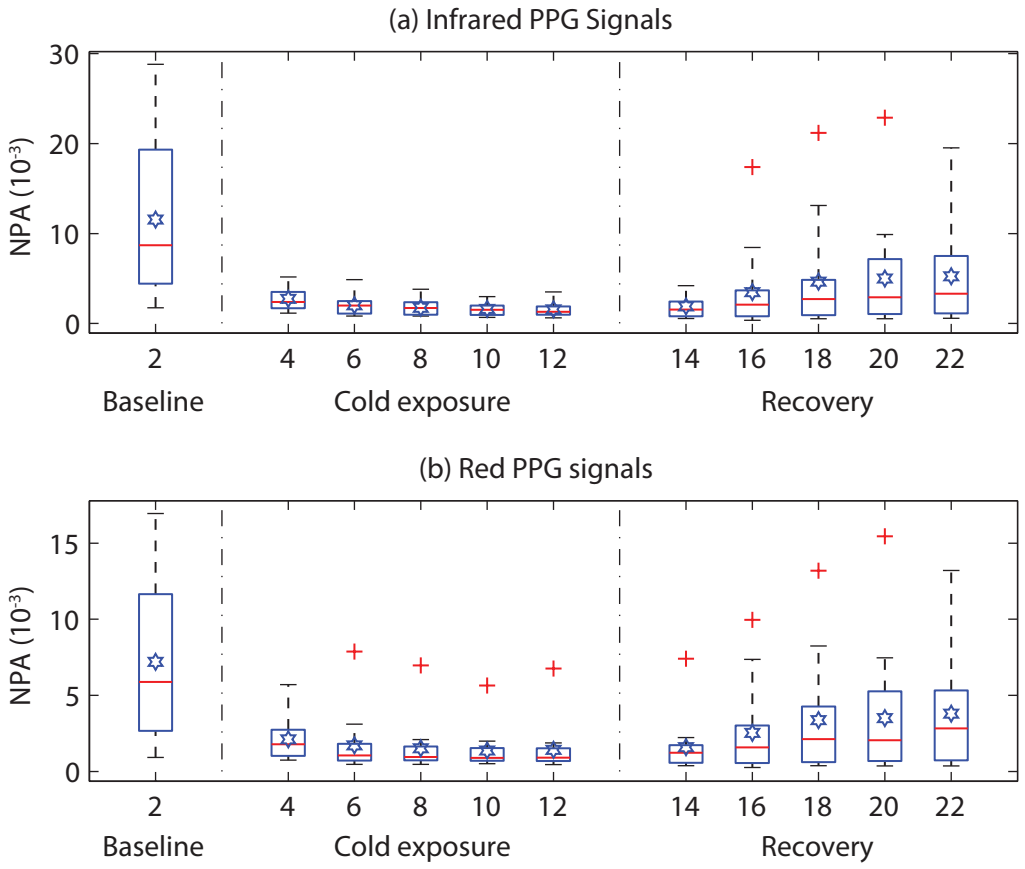

FIGURE 11.9: NPA of the (a) infrared and (b) red finger PPG signals acquired from 15 volunteers during all three stages of the experiment. Each box shows the mean NPA measured across a two minute period in all the volunteers. The red line in each box shows the median value of the data, the ☆ shows the mean, and + shows the outliers.

mean and the median have deviated down the y-axis with time. Nonetheless, the variability (i.e., the interquartile range) of the data has more or less remained the same during the cold exposure. The mean percentage drop in the NPA of earlobe PPG signals by the end of the cold exposure was 20% (red) and 26% (infrared). By the end of the study, the NPA of the red and infrared PPG signals from the earlobe has approximately returned to the baseline.

- In contrast with both the finger and the earlobe, the NPA measured from the ear canal did not change during the cold exposure. Again, this is clearly visible in Figure 11.11. The interquartile range, the mean and the median have all remained relatively constant throughout the experiment. The % drop in the mean NPA of red and infrared PPG signals from the ear canal during cold exposure was 0.2% and 13.7% respectively. The mean core temperature of the volunteers has remained unchanged (baseline: 36.6 ± 0.07°C, cold: 36.0 ± 0.11°C).

To quantify the changes in the mean NPA of the red and infrared PPG signals measured from all three locations for every two minutes of the study, statistical tests were carried

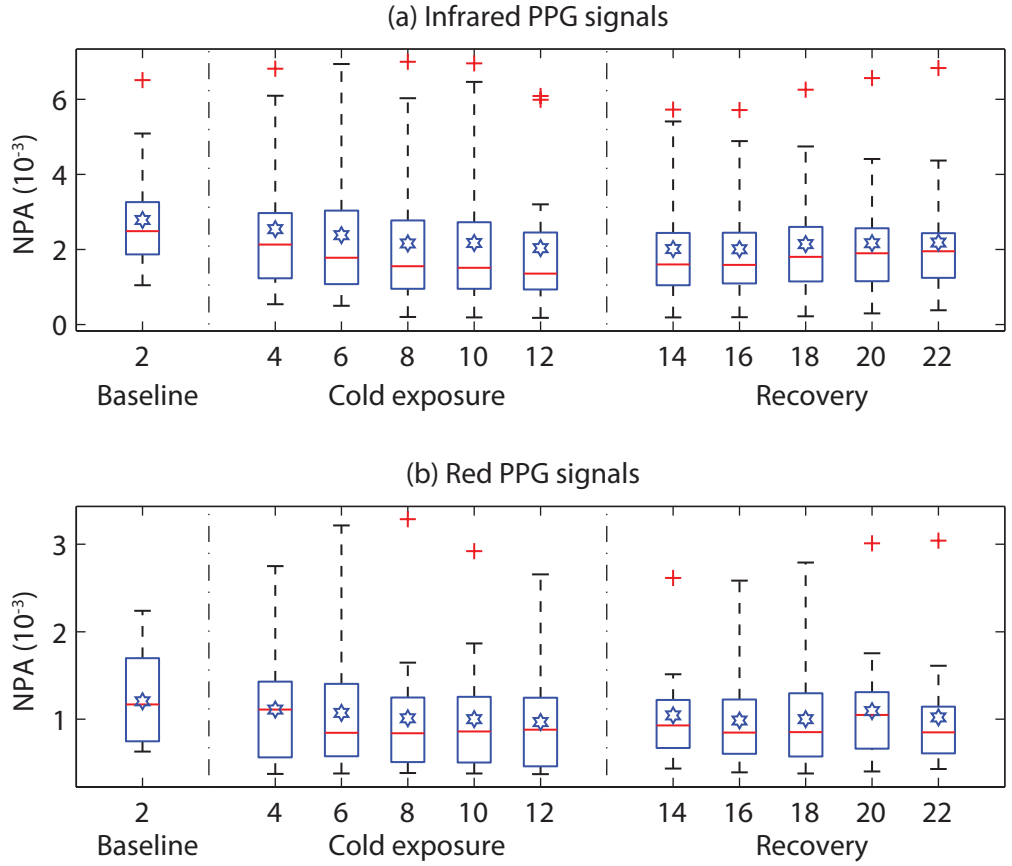

FIGURE 11.10: NPA of the (a) infrared and (b) red earlobe PPG signals acquired from 15 volunteers during all three stages of the experiment. Each box shows the mean NPA measured across a two minute period in all the volunteers. The red line in each box shows the median value of the data, the ✡ shows the mean, and + shows the outliers.

out. Before commencing statistical analysis, a normality test was performed on the data using the Kolmogorov-Smirnov test with Lilliefors' correction, as in Section 10.3.1.2. The P-value set in the test was 0.05. As not all the data was found to be normally distributed, it was decided that for further analysis a non-parametric test will be used. The test used was Kruskal-Wallis One Way Analysis of Variance on Ranks. A comparison between two groups of data was recognised as significantly different if the computed P-value by Kruskal-Wallis test was < 0.05.

As shown in Figure 11.12, the mean NPA of all the subjects during baseline (every 2 min) was compared with every 2 min mean of the cold exposure and the recovery periods for statistical significance (i.e., baseline vs 4 $\rightarrow$ 22 min, 10 comparisons per PPG signal). The summary of the results of the Kruskal-Wallis test is presented in Table 11.1. Statistically significant ($p < 0.05$) differences were found between all the groups when NPA of red and infrared finger PPG signals was compared during the study. This suggests that the NPA of red and infrared PPG signals has reduced significantly during the cold exposure and never recovered back to the baseline value in the monitoring period. The H-value of the red and infrared PPG signals were also large compared to the other locations. No

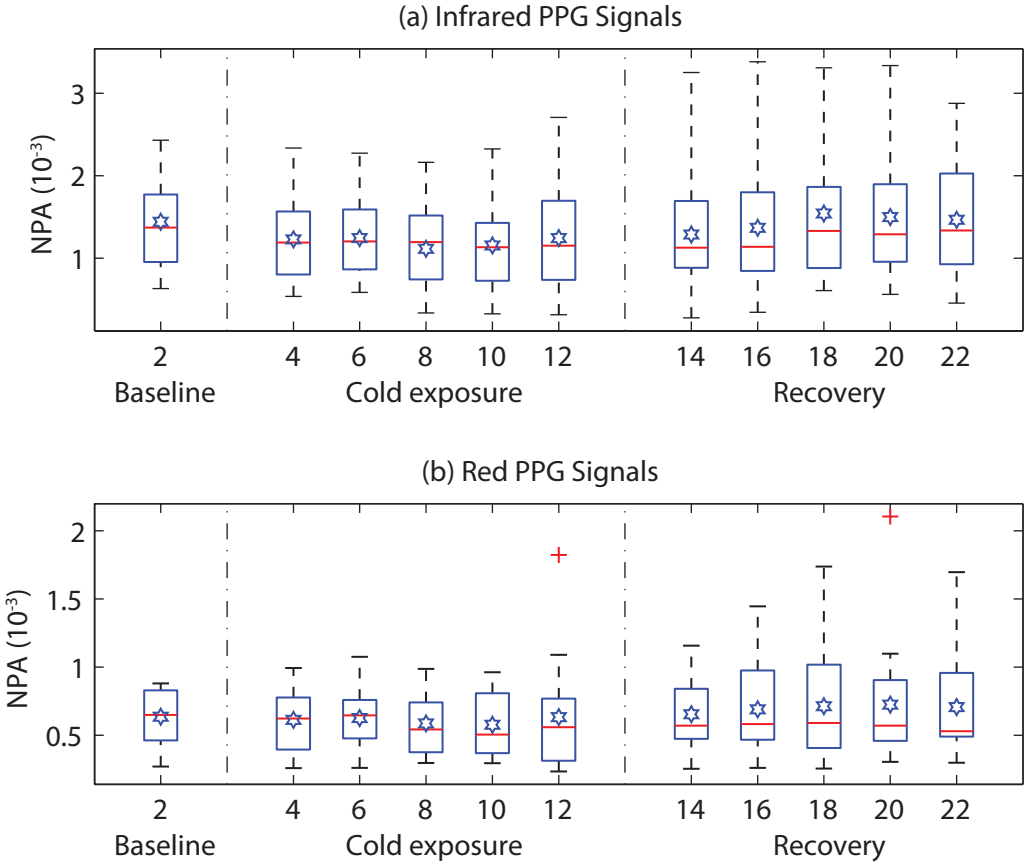

FIGURE 11.11: NPA of the (a) infrared and (b) red ear canal PPG signals acquired from 15 volunteers during all three stages of the experiment. Each box shows the mean NPA measured across a two minute period in all the volunteers. The red line in each box shows the median value of the data, the ☆ shows the mean, and + shows the outliers.

significant difference was found between any of the groups when the NPA of the red and infrared PPG signals from earlobe were compared. Similar to the earlobe, no significant difference was found between any of the groups in the ear canal. However, by comparing the P-values and the H-values, it could be said that the ear canal offers better quality PPG signals during the cold exposure than the earlobe.

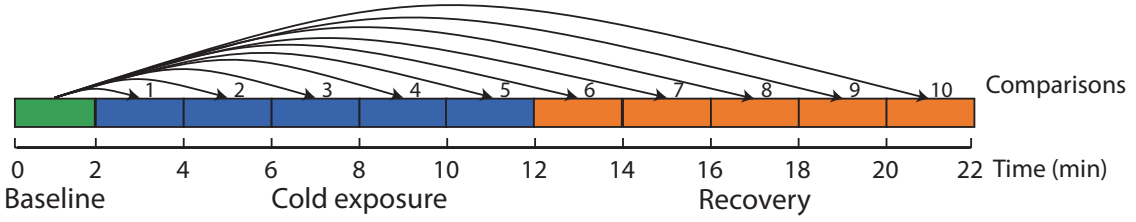

FIGURE 11.12: Statistical analysis was carried out to measure the significant difference between the mean NPA during baseline and every two minute mean of NPA during the cold exposure and recovery periods (10 comparisons).

TABLE 11.1: Summary of the statistical test results obtained from the Kruskal-Wallis test performed on the NPA of red and infrared PPG signals acquired from the finger, the ear canal and the earlobe of the volunteers. A P- value <0.05 indicates a statistically significant difference. The highest H-value corresponds to the largest discrepancy between rank sums.

Location	P-values		H-value		Statistical significance
	Red	Infrared	Red	Infrared	
Finger	$= 0.002$	< 0.001	28.05	35.67	Yes
Earlobe	$= 0.926$	$= 0.654$	4.37	7.74	No
Ear canal	$= 0.993$	$= 0.847$	2.38	5.61	No

11.3.2 NPA vs nTHI

The custom built finger and ear canal PPG sensors were so far used to measure changes in arterial blood volume from the respective areas during the cold exposure. In this analysis, the NPA changes measured from the finger and the ear canal sensors were compared with

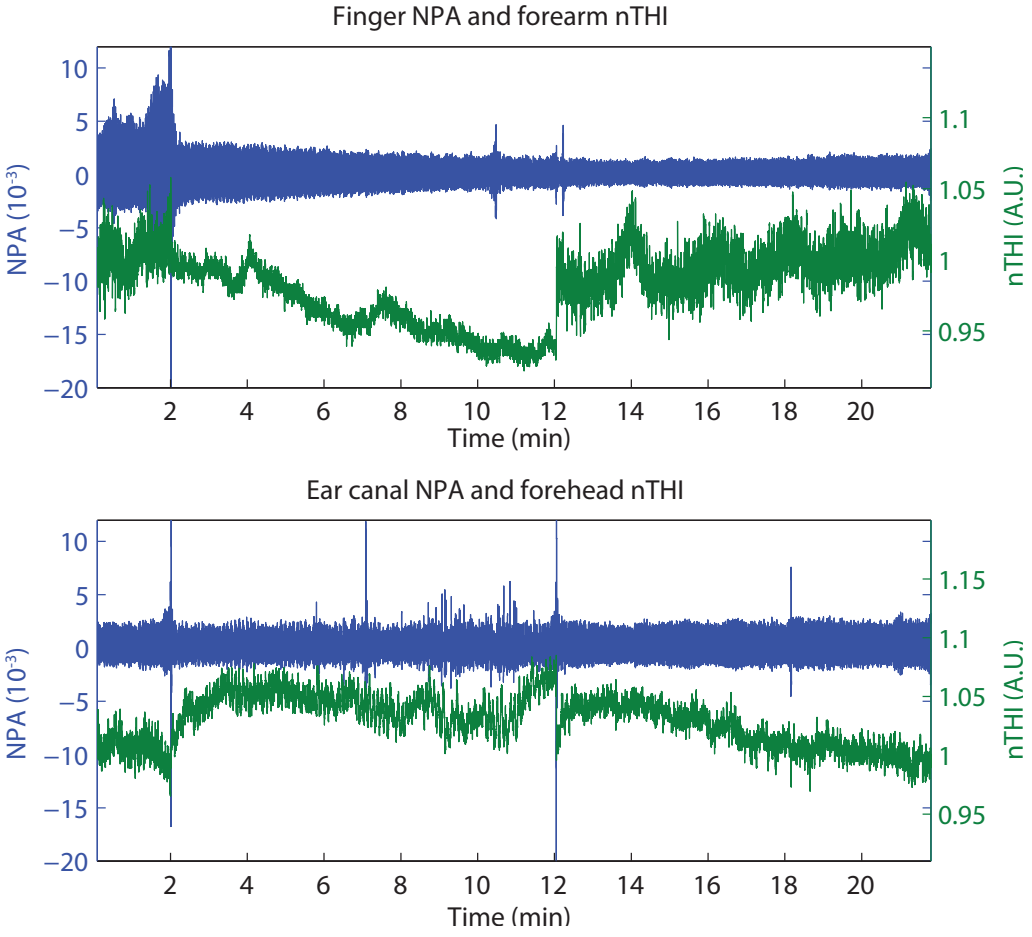

FIGURE 11.13: A comparison of (a) the finger NPA signal with the nTHI signal measured from the forearm, and (b) the ear canal NPA signal with the forehead nTHI signal.

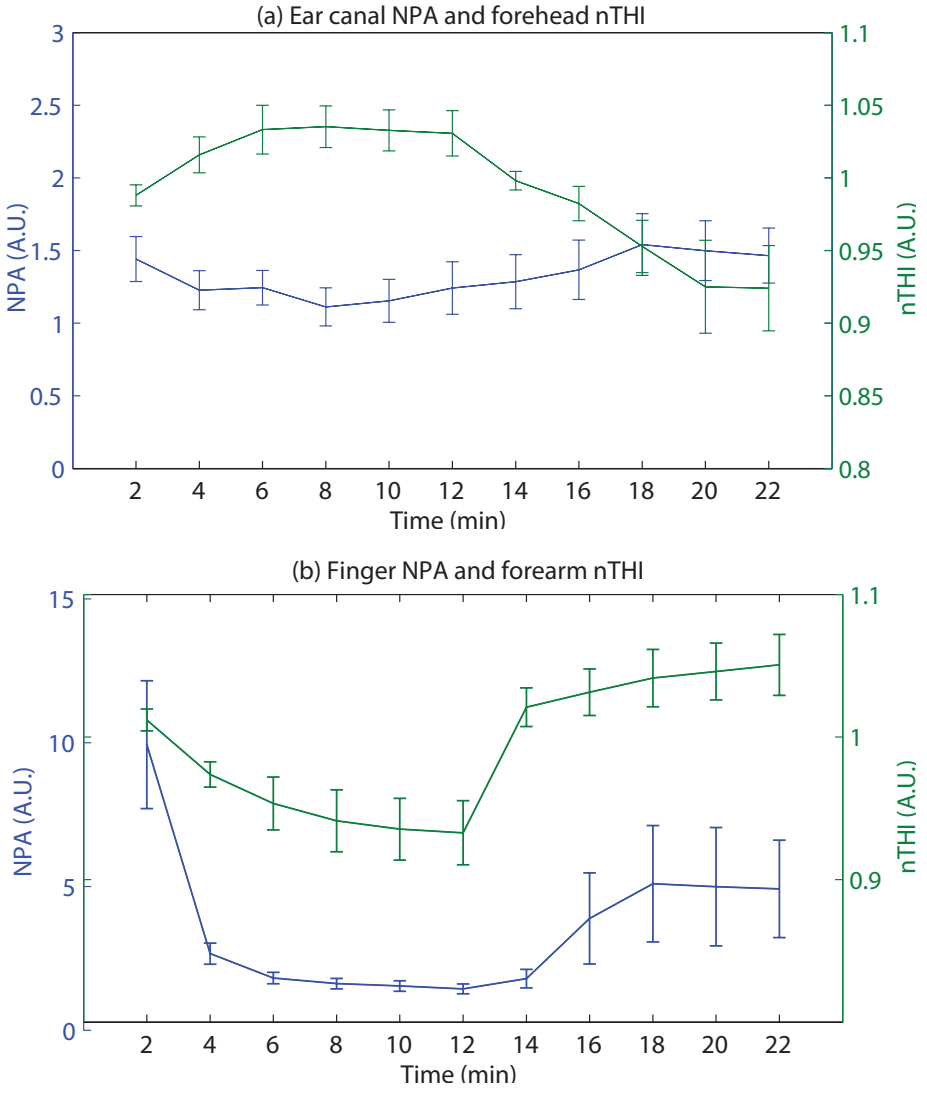

FIGURE 11.14: (a) A comparison of the mean nTHI measured from the forehead with the NPA measured from the ear canal. The y-error bars indicate the standard error of mean (±SEM). (b) A comparison of the mean nTHI measured from the forearm with the NPA measured from the finger.

the blood volume changes (nTHI) from a commercial NIRS system, to verify indirectly the results and to validate the performance of the developed sensors. Comparisons were made at both central and peripheral sites (i.e., the finger NPA vs. the forearm nTHI and the ear canal NPA vs. the forehead nTHI). It should be noted that the PPG and NIRS sensor locations are not exactly the same, and it is assumed that the finger and forearm reflect changes in peripheral blood volume, and the ear canal and the forehead reflect changes in central blood volume. NIRS sensors could not be used in the same locations as they require large separation distance between the emitters and the detector (4 cm).

Figure 11.13(a) shows the changes in normalised finger PPG signal, along with forearm nTHI acquired from a randomly selected volunteer for a duration of 22 min. From the figure, it is evident that as the NPA of the finger is reduced with time during the cold

exposure (between 2-12 min), the nTHI of the forearm has also reduced, indicating a decline in the blood volume, particularly the arterial blood volume. Figure 11.13(b) shows the changes in normalised ear canal PPG signal and the nTHI of the same volunteer measured from the ear canal and the forehead. From the plot, it is clear that the NPA of the ear canal PPG signal stays relatively constant during the cold exposure, indicating a constant blood flow to the area. The same could be said about the nTHI measured from the forehead, although a very small rise is observed during the start of the cold exposure. To verify if a similar response can be observed in all the volunteers, the mean nTHI was calculated for every 2 min of the study. The mean of the mean nTHI (±SEM) across the entire group was then compared with the mean of the mean NPA. The mean nTHI (±SEM) and the NPA (±SEM) measured across the volunteer group from the forehead and the ear canal are shown in Figure 11.14(a). The same parameters estimated from the finger and the forearm are shown in Figure 11.14(b).

From these figures, it is evident that the NPA and the nTHI measured from the finger and the forearm decrease rapidly during the cold exposure due to profound vasoconstriction. In contrast with the periphery, the NPA and nTHI measured from the ear canal and forehead remain relatively constant. However, minor differences can be observed between the NPA and nTHI in these regions. This is probably due to the anatomical differences between the forehead and the ear canal. The nTHI measured from the forehead is a direct indicator of changes in cerebral blood volume, whereas the NPA measured from the ear canal does not signify the same. Additionally, nTHI is an indicator of changes in total blood volume, while NPA is an indicator of changes only in arterial blood volume. Nonetheless, it is reasonable to say that the ear canal is recognisably defiant to profound vasoconstriction resulting from the cold exposure.

11.3.3 Arterial oxygen saturation (SpO_2)

To show the effect of the cold exposure on the acquired PPG signals and subsequently the effect on the SpO_2 estimated by the pulse oximeter, arterial oxygen saturation values were calculated from all three sensors for the entire duration of the study. SpO_2 was calculated using Equation 11.1 in a three-second rolling window, the R_{OS} in the equation is the ratio of the red and infrared NPA. Figure 11.15 shows the NPA of red and infrared ear canal PPG signals acquired from a volunteer and the SpO_2 estimated from the signals. The SpO_2 estimated from all three sensors in each volunteer was averaged for every two minutes of the study. The mean SpO_2 estimated from the first two minutes of the study (i.e. baseline) was then compared with the every two minute mean of the cold exposure and recovery periods.

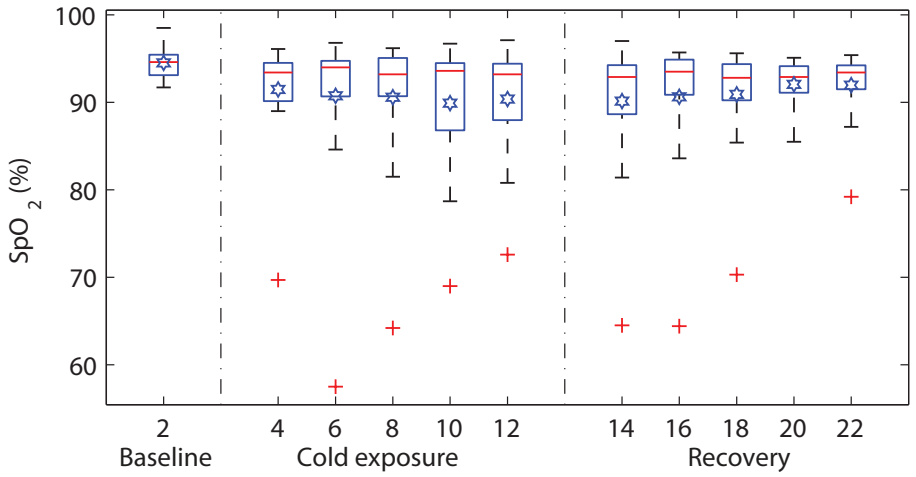

(a) Boxplot of the mean finger SpO_2

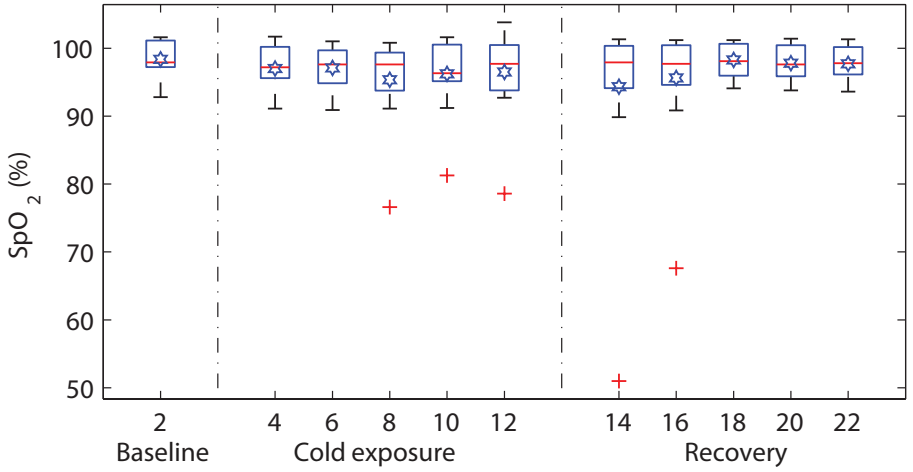

(b) Boxplot of the mean ear canal SpO_2

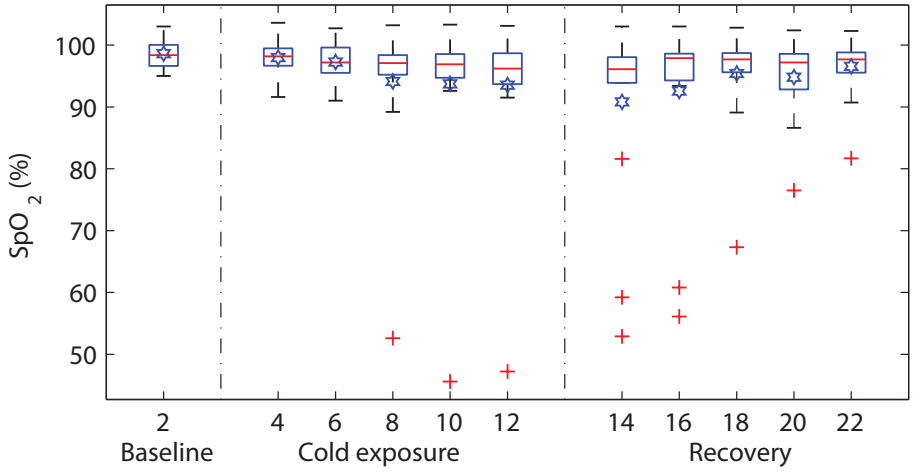

(c) Boxplot of the mean earlobe SpO_2

FIGURE 11.16: Box and whiskers plots demonstrating the change in mean SpO_2 measured for every two minutes of the study in (a) the finger and (b) the ear canal and (c) the earlobe. SpO_2 estimated from the finger have dropped significantly towards the end of the study when compared to the ear canal and the earlobe. The red line in each box shows the median value of the data, the ☆ shows the mean, and + shows the outliers.

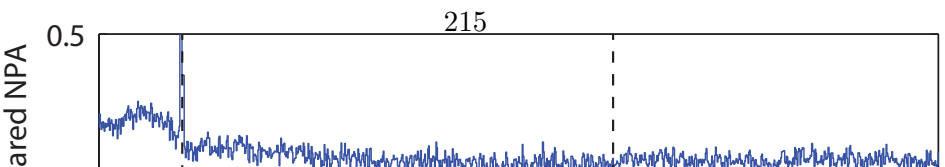

The mean SpO_2 values calculated for every two minutes of the study in all the volunteers is displayed in Figure 11.16 with the help of boxplots. The SpO_2 values estimated from all three uncalibrated probes during baseline were in the healthy adult oxygen saturation range (94% – 100%). The mean of the mean SpO_2 (±SEM) calculated for the entire group during baseline was 95 ± 0.45% in the finger, 98 ± 0.7% in the ear canal and 99 ± 0.6% in the earlobe.

During the cold exposure, the mean of the mean SpO_2 (represented by ☆ in Figure 11.16(a)) estimated from the finger probe had dropped with time, particularly in the last 4 minutes of the cold exposure. The increase in variability (interquartile range) of the data with time and the relatively stable median, however, indicate that the SpO_2 might have dropped significantly only in a few volunteers. Nonetheless, these low SpO_2 values would normally indicate hypoxia or even death in clinical circumstances, and hence are inaccurate. The mean of the mean SpO_2, the interquartile range and the median of the SpO_2 values calculated from the RECAP probe have remained relatively constant throughout the cold exposure, with the exception of one outlier towards the end of the stimulus (Figure 11.16(b)). The mean of the mean SpO_2 estimated from the earlobe probe reduced by the end of the cold stimuli. However, with the exception of the two or three outliers, the values generally are in the limits (Figure 11.16(c)). This is confirmed by the rather constant median and interquartile range.

During the recovery period, the mean of the mean SpO_2 estimated from the finger has recovered with time. Similarly, the mean of the mean earlobe SpO_2 has improved with time. However, SpO_2 estimated from the earlobe of two volunteers has remained significantly low in the first few minutes of the recovery period. The ear canal SpO_2, on the other hand, has remained relatively constant with the exception of the one outlier.

Since blood oxygenation is a global variable which does not change in healthy volunteers from site to site, the differences observed in mean SpO_2 amongst the sensors was further investigated. To differentiate the volunteers in whom any of the pulse oximeters had

TABLE 11.2: Summary of the pulse oximeter failure during the cold exposure and the recovery period in 15 volunteers

No. of volunteers with $SpO_2 < 90\%$										
Sensor	Cold exposure					Recovery				
	4	6	8	10	12	14	16	18	20	22
Finger	4	2	3	4	5	4	3	3	2	2
Ear canal	0	0	1	1	1	1	1	0	0	0
Earlobe	0	0	2	1	2	3	2	2	2	1

failed (i.e., inaccurate SpO_2) from the others, the percentage drop in SpO_2 for every 2 min of the study was calculated in each volunteer. The number of instances in which the SpO_2 estimated from a particular probe had dropped to a value <90% was calculated and considered as a failure. Table 11.2 shows the number of volunteers in whom the estimated SpO_2 has dropped to a value <90% during the cold exposure and the recovery period. From the table, the finger probe produced erroneous SpO_2 readings in four volunteers as soon as they were exposed to cold air, and by the end of the cold stimulus, 5 volunteers had SpO_2 below the 90% mark. The ear canal pulse oximeter, on the other hand, had failed in one volunteer towards the end of the cold exposure. Similarly, the earlobe pulse oximeter has failed to estimate accurate SpO_2 in 3 volunteers.

The high failure rate in the finger sensor was not due the reduction in blood oxygenation but is merely due to the quality of the signals acquired. As observed in Figure 11.9, the mean NPA of the red and infrared PPG signals dropped significantly towards the end of the cold exposure. In some volunteers, the amplitude of the PPG signals diminished so significantly that the peak detection algorithms could not distinguish between noise and PPG signal peaks. Hence in these volunteers, the amplitude of the noise is being measured instead of the PPG signal. Since the amplitude of noise in both the red and infrared channels is approximately similar, the absorbance ratio (R_{OS}) will drive towards 1, resulting in a SpO_2 close to 85% (i.e., a failure). To demonstrate this, the red finger AC

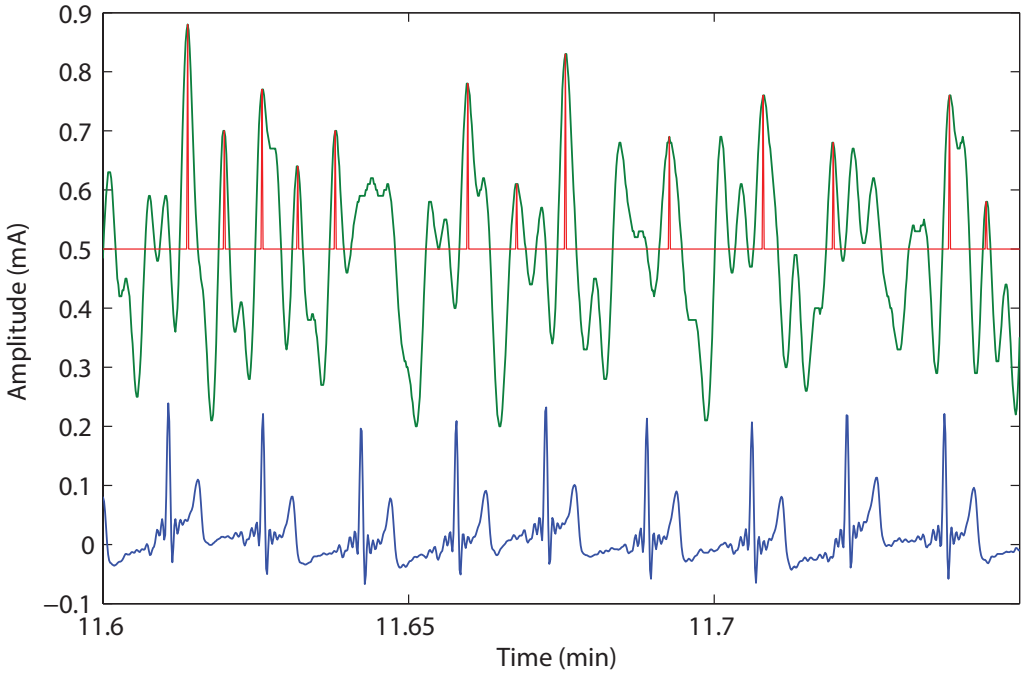

FIGURE 11.17: Depicts the red finger PPG signal (green trace) and the ECG signal (blue trace) acquired from a volunteer towards the end of the cold exposure, along with the peaks detected (red trace) by the peak detection algorithm. The amplitude of the red finger PPG signals was sometimes so small that the peak detection algorithm could not distinguish between the heart beat peaks and the noise peaks.

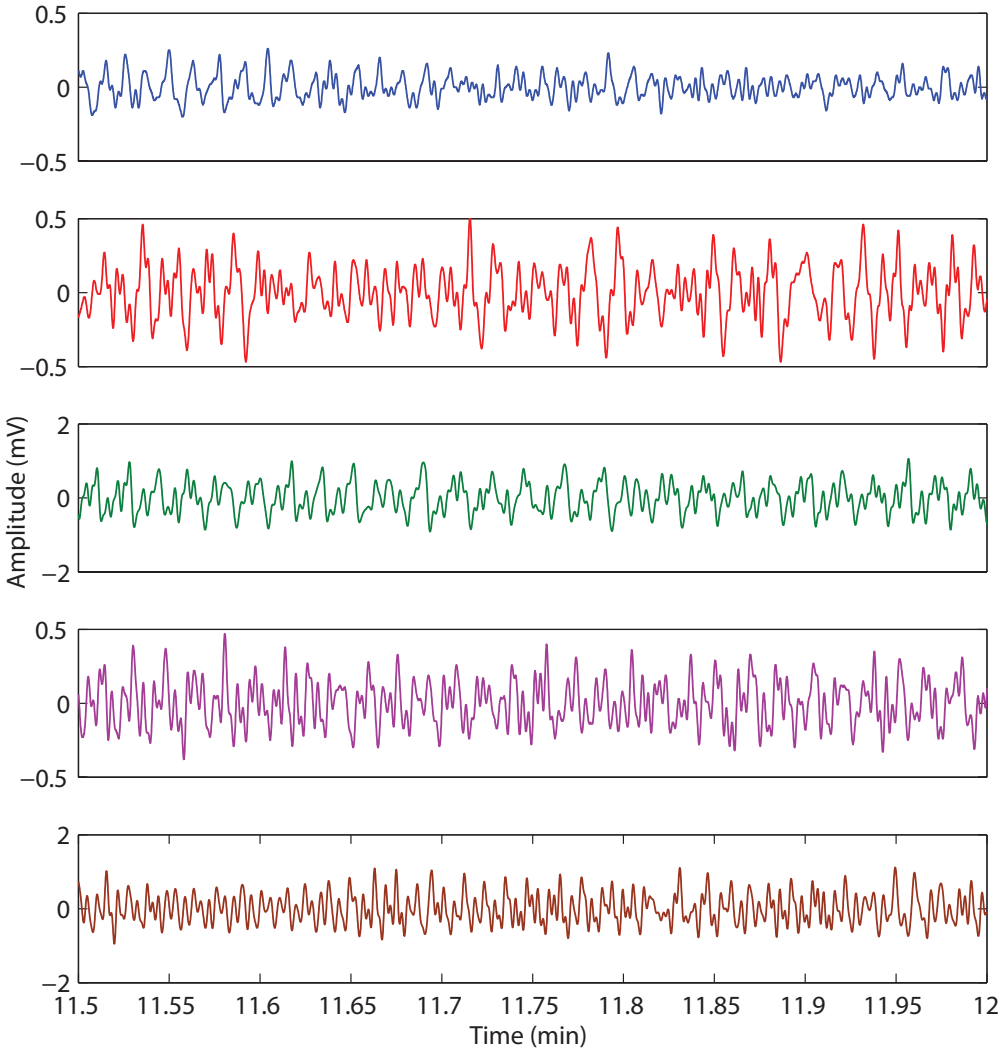

FIGURE 11.18: Red PPG signals acquired form the fingers of the volunteers in whom accurate estimation of SpO_2 was not possible during the cold exposure. The PPG signal is indistinguishable from noise in these cases.

PPG signal acquired from a volunteer during the cold exposure is shown in Figure 11.17, along with the peaks detected by the algorithm and the ECG signal. The quality of the red finger PPG signals acquired from the five volunteers in whom accurate SpO_2 estimation was not possible is shown in Figure 11.18.

From the results acquired in this study so far, it is fair to say that the SpO_2 measurements made from the finger are susceptible to poor peripheral perfusion and are heavily dependent on the thermal state of the site. This limitation really weakens the ability of the pulse oximeters in conditions when they are most needed. The newly developed RECAP probe on the other side offers reliable SpO_2 measurements even under the influence of the cold temperatures or profound vasoconstriction.

11.3.4 Sympathetic and parasympathetic activity

When the human body is exposed to low ambient temperatures (as in the case of this experiment), the thermoregulatory mechanism of the body initiates the activation of the sympathetic nervous system to counter the heat loss and maintain homeothermy. This activation causes a change in peripheral blood flow through the intense constriction of cutaneous blood vessels and a marked increase in the heart rate and the blood pressure. The degree of the sympathetic control over blood vessels is, however, known to be more

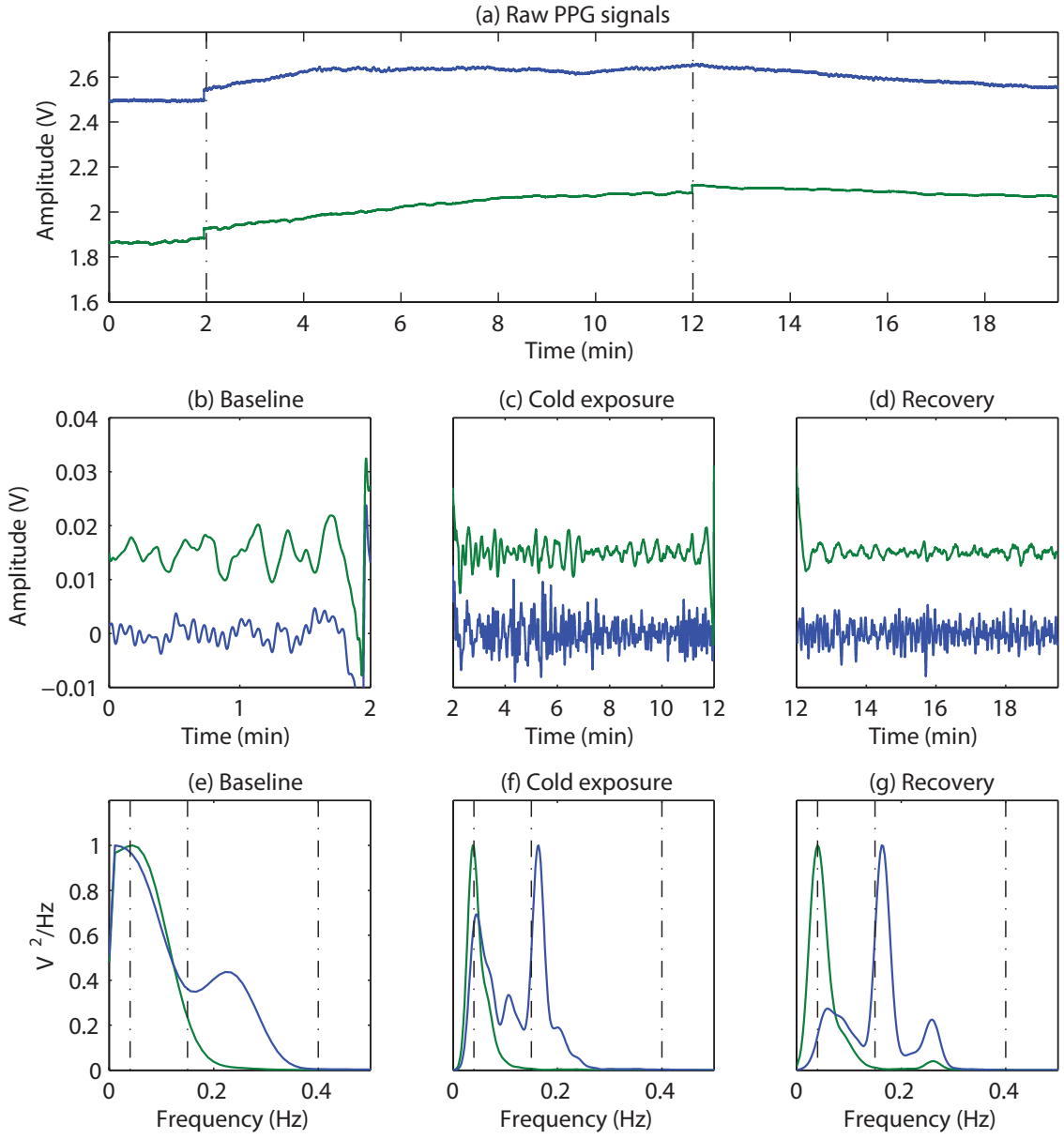

FIGURE 11.19: An example of the sympathetic activity estimation; (a) The raw PPG signals acquired from the ear canal (blue trace) and the finger (green trace) were first bandpass filtered and then divided into three segments, each containing data from (b) baseline, (c) cold exposure and (d) recovery; The power spectrum of the corresponding signals was then acquired (e), (f) and (g).

prominent in the periphery than the core vasculature. Hence, the significant drop in finger PPG amplitude compared to the earlobe or ear canal PPG signals. To quantify the differences in the degree of sympathetic nerve activation between the periphery and the core and supplement the above statement, low-frequency spectral analysis was performed on the raw PPG signals acquired from the finger and the ear canal. Two volunteers were exempt from this analysis, as the raw PPG signals acquired from these volunteers contained some noise.

The power spectrum of the ear canal (blue trace) and the finger (green trace) PPG signals acquired from a volunteer during (c) baseline, (d) cold exposure and (e) recovery periods is shown in Figure 11.19, along with (a) the raw and (b) the filtered PPG signals. Note that the power spectrum acquired at each stage was normalised to the component with the maximum power to facilitate easy comparison between the two locations. Therefore, the power of the highest component in each sub-plot is at 1. During baseline, the component with the maximum peak in both the finger and the ear canal was the LF component. During the cold exposure, the component with the maximum peak in the finger was the LF component, whereas in the ear canal it was the HF component. Hence, the ratio of LF to HF will be very high in the finger compared to the ear canal, suggesting a higher degree of sympathetic activity. The LF/HF ratio of the finger has increased to 86.4 during the cold exposure from 19.2 at the baseline. While the ear canal LF/HF ratio has decreased to 1.38 during the cold exposure from 1.62 at baseline. These results indicate the differences in the degree of sympathetic activation between the two locations. The LF/HF power ratio estimated from the finger and the ear canal PPG signals during baseline, cold exposure and recovery are graphically displayed in Figure 11.20.

Statistical tests were performed on the data to check if the changes occurring in the LF/HP

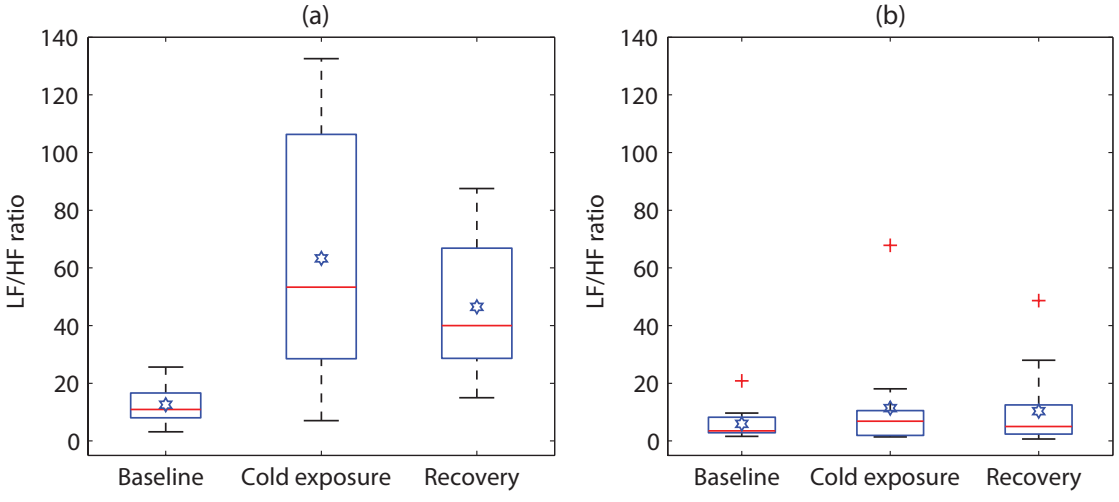

FIGURE 11.20: Box plot showing the changes in LF/HF ratio during the cold exposure in (a) finger and (b) the ear canal.

TABLE 11.3: Statistical test results obtained from non-parametric analysis performed on the LF/HF ratio measured from the finger and the ear canal PPGs.

Location	Comparison	Statistical significance	P-value
Finger	Baseline vs Cold	Yes	0.002
	Cold vs Recovery	No	
	Recovery vs Baseline	Yes	
Ear canal	Baseline vs Cold	No	0.781
	Cold vs Recovery	No	
	Recovery vs Baseline	No	

ratio are significantly different between any of the two stages in the study. Before the statistical analysis, the normality of the data was tested using the Kolmogorov-Smirnov test with Lilliefors' correction. As most of the data included in the study were not normally distributed, a non-parametric test (Kruskal-Wallis One Way Analysis of Variance on Ranks) was used for statistical analysis. A comparison between data acquired from two different stages of the experiment was recognised as significantly different if the computed P-value by Kruskal-Wallis test was < 0.05. To isolate the group or groups that differ from the others, all pairwise multiple comparison procedures (Student-Newman-Keuls Method) was used. The results of the statistical tests together with the corresponding P-value are shown in Table 11.3. A significant difference was found when the LF/HF power ratio computed from the finger was compared between baseline and the cold exposure, while no significant differences were found in the ear canal LF/HF ratio in any of the comparisons. These results prove that the sympathetic control of the blood vessels in the periphery is significantly higher than the core regions.

11.4 Summary

The newly developed ear canal PPG probe, the finger PPG probes, and a commercial ear clip pulse oximetry sensor were used along with the acquisition system in an *in-vivo* study investigating the effect of whole body the cold exposure on the quality of the PPG signals acquired from both the periphery (the finger and earlobe) and the core (the ear canal). The study aimed to prove the hypothesis that the ear canal remains sufficiently perfused and accurate SpO_2 estimation will be possible in conditions of compromised peripheral perfusion where the finger sensor will commonly fail due to the diminishing peripheral pulse. The study was carried out in 15 healthy volunteers with no history of cardiovascular disease. During the study, all volunteers were exposed to 10 minutes of low ambient temperatures (10°C). The red and infrared PPG signals acquired from all three

sensors during the study were analysed and compared with respect to their normalised amplitude (AC/DC) and the SpO_2 estimated. The measured parameters were averaged for every two minutes of the study, and the baseline 2-minute mean was compared with every two minutes mean of the cold exposure and recovery periods. The PPG signals between the ear canal and the finger were also analysed for their sympathetic modulation.

The PPG signals acquired from all the volunteers were generally of good quality. The morphology of the AC PPG signals acquired from the ear canal were different to the finger and the earlobe PPG signals. The morphological differences between the finger and the ear canal signals were expected due to the large distance between the heart to the finger than to the ear canal. However, the differences in the earlobe and the ear canal PPG signals were not expected. Especially since the earlobe is very close to the ear canal. The morphological difference between these sites is possibly due to the dissimilarity in the vasculature. The earlobe is supplied by the auricular branches (capillaries) of the superficial temporal artery while the ear canal gets rich blood supply from the deep auricular artery, a branch of the internal maxillary artery.

The NPA of the finger PPG signals has reduced significantly as soon as the volunteers were exposed to cold. The drop in NPA of red and infrared PPG signals was $> 80\%$ by the end of the cold exposure. The NPA of the earlobe PPG signals has also dropped considerably, but not as significantly as the finger. The mean drop in the NPA of earlobe PPGs was 20% and 26% at red and infrared wavelengths. On the contrary to both these sensors, the ear canal PPG signals remained relatively unchanged. During the recovery period, the NPA measured from both the finger and the earlobe sensors has increased with time. The earlobe NPA was close to the baseline value by the end of the recovery period. However, the NPA of the finger PPGs has not recovered to the baseline value by the end of the 10 min recovery period. The finger NPA was approximately 45% lower than the baseline value by the end of the study. The statistical tests carried out to measure the differences between the groups (baseline vs. every 2 min mean) have shown that a statistically significant difference (P-value: red– 0.002, infrared– <0.001) exists between the NPA of the finger PPG signals measured during baseline and the NPA of finger measured during the cold exposure. Similar results were found when finger NPA from baseline was compared with the recovery period. On the other hand, no significant difference was found between the groups when NPA of the earlobe (P-value: red– 0.926, infrared– 0.654) and the ear canal was compared (P-value: red– 0.993, infrared– 0.847).

The NPA of infrared PPG signals acquired from the ear canal and the finger during the study were compared with the nTHI measurements acquired from the forehead and the forearm to indirectly validate the acquired results. The results show that the NPA from the finger follows the nTHI during the study in both locations. This indicates that the arterial blood volume in the finger reduces significantly during the cold exposure while the

ear canal remains relatively constant. However, minor differences were observed between nTHI from the forehead and NPA from the ear canal. This could be due to the anatomical differences between sites and the penetration depth of the NIRS system.

The mean SpO_2 estimated from all three sensors during baseline was between 95% and 99%, i.e., in the healthy oxygen saturation range. During the cold exposure, the mean SpO_2 measured from the finger probe has dropped significantly in the last 4 minutes. The sensor has failed ($SpO_2 < 90\%$) to estimate accurate SpO_2 in 5 volunteers by the end of the cold exposure (a 33.3% failure rate). The SpO_2 estimated from the earlobe sensor has failed in 20% of the volunteers. Compared to both these sensors the SpO_2 estimated from the ear canal has only failed in 1 volunteer. The failure in SpO_2 of the finger sensor or the ear lobe sensor is not due to the drop in oxygen saturation but is due to the quality of the PPG signals acquired.

The degree of sympathetic control over peripheral and core vasculature was quantified through low-frequency spectral analysis. The frequency spectrum of the infrared finger and the ear canal PPG signals was acquired, and the power of the LF and HF component was calculated. The ratio of LF to HF power was then calculated and compared between the sites. The results show that the LF/HF ratio in the finger has increased significantly ($p= 0.002$) during the cold exposure. While the ear canal LF/HF ratio has stayed relatively constant compared to the finger ($p=0.781$).

From these results, it is reasonable to conclude that the ear canal is a superior site compared to the finger and the ear lobe in providing good quality PPG signals and accurate SpO_2 in condition of compromised perfusion.

— Any sufficiently advanced technology is indistinguishable from magic.

Arthur C Clarke, Hazards of Prophecy: The Failure of Imagination, 1973

12

Discussion and conclusions

Continuous assessment of arterial oxygenation (SpO_2) by pulse oximetry has become widespread during anaesthesia, in the peri-operative period, and in the critically ill. It is now an ASA standard for intraoperative monitoring during all anaesthetics. However, commercial pulse oximeter probes placed on the finger may fail to provide a valid reading in conditions of poor peripheral perfusion caused by hypotension, hypothermia, and vasoconstriction. Hence, this project aimed to develop an ear canal pulse oximeter, on the hypothesis that this central site will remain sufficiently perfused in order to enable accurate and reliable measurements of SpO_2 in conditions of poor peripheral perfusion.

A novel earphone shaped optoelectronic reflectance ear canal photoplethysmography probe *(RECAP II)*, small enough to fit inside the ear canal was successfully developed (Chapter 7) to acquired red (658 nm) and infrared (870 nm) PPG signals from the posterior surface of the outer ear canal. Two optically identical peripheral PPG sensors were also developed to obtain PPG signals from the fingers or toes, and hence allow for quantitative and qualitative analysis of the PPG signals obtained at both the periphery and the ear canal. To pre-process and acquire the ear canal and the finger PPG signals, a novel dual-wavelength PPG processing system was developed (ZenPPG). A modular design approach was implemented in the system's design, whereby the electronic circuitry in the system was divided into multiple modules, which were connected by a system bus. Through this modular approach, various functions in the system were kept independent of each other,

allowing for easy debugging and incremental improvement. The developed system comprised of two identical PPG processing channels and an ECG processing channel. The PPG instrumentation system was developed to operate in conjunction with a virtual acquisition and control instrument designed in LabVIEW. The virtual instrument allowed for the continuous acquisition and display of all signals from the instrumentation system and consisted of various filters and algorithms to reduce the bandwidth of the acquired signals and estimate parameters such as SpO_2 and heart rate.

During the design and developmental phase of the technology mentioned above, two *in vivo* investigations, a participant survey and several other performance verification experiments were conducted in the laboratory to aid the design of the ear canal PPG sensor, and to evaluate and optimise the performance of the ZenPPG system. Firstly, an *in-vivo* study was carried out in 7 healthy volunteers to investigate the quality of PPG signals that can be obtained from different depths of the ear canal (i.e., outer ear canal, inner ear canal). Two RECAP-I probes with different dimensions (10 mm and 15 mm in length and 7 and 8 mm in diameter) were used in this investigation. The results of this investigation showed that good quality red and infrared PPG signals can be acquired from both locations in the ear canal. However, two key differences were observed between the sites: (1) the amplitude of the PPG signals acquired from the outer ear canal were found to be marginally smaller than those acquired from deep inside the ear canal (infrared: $P = 0.07$, red: $P = 0.26$), (2) the PPG signals acquired from the deeper auditory canal are slightly noisy and contained high respiratory modulation. The noisy PPG signals in the deeper region of the ear canal were however expected since the Eustachian tube induces respiratory and jaw movements to the middle ear and deeper regions of the outer ear. These initial measurements have given the necessary confidence for the further development of the sensor and have shown the feasibility of the ear canal as a monitoring site for PPGs and blood oxygen saturation.

The volunteers participating in this study were asked to fill in a survey that was designed to aid the further development of the sensor technology. From the participants' responses, it was determined that (1) the size of the designed probe needs to be minimized, as some of the volunteers have expressed discomfort during prolonged usage; (2) thermal safety tests need to be carried out to establish if the light emitted by the LEDs could result in any undesirable thermal effects, especially as a couple of the volunteers have complained about warm sensation after prolonged use. Taking these observations into consideration, it was decided that the outer ear canal is used as the optimal site for monitoring PPG signals in future investigations.

Prior to any further development of the sensor, another *in-vivo* study was carried out in the same set of volunteers to determine the surface along the circumference of the ear canal from which the acquired PPG signals will be of the best possible quality. This investigation was focused only on the outer region of the ear canal. Anterior (top), ventral

(right), posterior (bottom) and dorsal (left) surfaces of the outer ear canal were investigated during this study. The PPG signals acquired from all four surfaces of the ear canal were of good quality. However, the posterior surface of the outer ear canal was found to be the best possible surface for the acquisition of high amplitude and undistorted PPG signals. Statistically, significant differences were found when the amplitude of PPG signals acquired from the anterior and posterior surfaces of the ear canal (Red: P= 0.008, infrared: P= 0.006) were compared. From these findings, it was decided that the posterior surface of the outer ear canal will be used as the location for PPG signal monitoring in the ear canal.

The above encouraging results have prompted the development of the second prototype probe (RECAP–II) with smaller dimensions. Preceding the design and development of the RECAP–I probe, a thermal safety test was carried out on the first prototype to determine the effect of the thermal radiation emitted by the LEDs on the surrounding tissue. The LEDs have reached a maximum temperature of 28.7°C in the first 15 min of on-time (i.e. a 3.2°C raise from baseline) and then stayed relatively constant for the rest of the test period. The minimum temperature at which the human skin might receive a shallow burn is at 44°C. Since the maximum temperature of the probe is well below the shallow burn range, it was concluded that there was no risk of thermal injury from the optical components used. Additionally, the size of the probe does not affect the amount of heat generated by the LEDs. Hence, the same optical components were used in the design of the second prototype. The RECAP–II probe was designed to look like a small earphone. The prototype probe was successfully tested in 3 volunteers. The amplitude of the infrared PPG signals recorded from the probe was between 200 and 400 mV. However, the smaller dimensions of the probe meant a higher susceptibility to motion artefacts in users with large ears, due to the loose fit. To provide more effective fixing and comfort, an interchangeable ear hook and an ear fin were incorporated into the probes design.

Similar to the prototype probes, the performance of each module in the ZenPPG system was thoroughly tested. Several simulations and experiments were conducted to fine-tune the current source, the transimpedance amplifier, the sample and hold amplifier and the analogue filters. As a result, a high SNR of 101.31 dB was achieved. The low power consumption (1.07 W) of the system also meant that it could be used continuously for more than 2 hours when powered by batteries.

Following these experimental investigations and the finalisation of the developed technology, sufficient confidence was acquired to commence a systematic *in vivo* evaluation of the ear canal probe in conditions of comprised peripheral perfusion for the first time. The City University Senate Research Ethics Committee has given the approval to conduct PPG measurements in 15 healthy volunteers undergoing a cold pressor test (CPT) (30 sec right hand into an ice bath). Red and infrared PPG signals were acquired from the ear canal

(EC), the right index finger (RIF) and the left index finger (LIF) of the volunteers during the study. Offline analysis was conducted on all acquired signals to examine the variations in the amplitude of AC and DC PPG signals. The results show that good quality red and infrared PPG signals can be obtained from the human auditory canal and the periphery using the custom built sensors. The ear canal PPG signals were found to be morphologically different to the finger PPG signals (Figure 10.9). PPG pulse features such as the dicrotic notch in the diastolic phase, arrive earlier in ear canal signals when compared to the finger PPG signals. The ear canal PPG signals bear a high resemblance to the arterial pressure pulse recorded from the aortic arch. These physiological features were suppressed in the finger PPG signals due to the increased vascular compliance of peripheral blood vessels. The ear canal PPG signals also contained pronounced respiratory modulations when compared to the left and right index finger PPGs. Hence, by further decomposing the ear canal PPG signal, valuable clinical information regarding the cardiovascular function might be extracted.

During the CPT, the amplitude of the AC PPG signals from the RIF have reduced significantly ($P < 0.05$), which is expected due to the profound vasoconstriction resulting from immersion of the right hand into ice water. However, the amplitude of the LIF has also reduced significantly, although the skin temperature of the left hand has remained constant. The effect of the right-hand immersion on the amplitude of the LIF PPGs is probably due to the activation of the sympathetic nervous system. The sudden change in temperature of the right-hand forces the thermoregulatory centre to stimulate the sympathetic nervous system, in order to maintain homoeostasis. This leads to an increase in vessel wall stiffness of peripheral blood vessels, which in turn causes the blood pressure and heart rate to increase (as seen in Figure 10.18). Hence, during ice water immersion most of the peripheral body parts are affected, as it has in this case with the left finger. On the contrary to the periphery, the amplitude of the AC ear canal PPG signals has remained relatively constant. These findings show that with induction of vasoconstrictive stimulus in the right hand, other peripheral parts such as the left hand are prominently affected while central areas such as the ear canal remain reasonably immune. During the recovery period, the amplitude of the AC PPG signals increased with temperature. No significant differences were found between the amplitude of the LIF PPGs during the baseline and the recovery periods (From Table 10.5). However, significant differences were found in the RIF, when the baseline and recovery periods were compared. This indicates that the amplitude of the RIF PPG signals has not increased to a greater extent by the end of the study, although the temperature of the right hand has increased to a minimum temperature of 24°C in all the volunteers.

The baseline mean SpO_2 estimated from the ear canal pulse oximeter was in good agreement with both the finger pulse oximeters. During the cold pressor test, the mean SpO_2

from both the finger pulse oximeters dropped considerably. However, SpO_2 is a global variable, and would not change from site to site in healthy volunteers. Therefore, the drop in SpO_2 of pulse oximeters is purely due to the reduction in amplitude and quality of PPG signals, resulting from vasoconstriction of peripheral blood vessels. A drop in SpO_2 higher than 5% was found in 34% of the volunteers in the RIF pulse oximeter while 27% of the volunteers experienced a similar drop in the LIF pulse oximeter. Compared to the finger pulse oximeters, the ear canal pulse oximeter has only failed in one volunteer. These results show the durability of the ear canal for SpO_2 monitoring.

One of the shortcomings of this study was the duration of applied stimulus. The short duration of cold immersion has not allowed for low-frequency spectral analysis which could have helped determine the extent of the sympathetic activity in each location. Nonetheless, the extent of vasoconstriction at each site during the ice immersion was indirectly quantified by calculating the PTT from the PPG signals acquired from the respective locations. The mean PTT measured during baseline from the EC was smaller than the RIF and LIF PTT, this was expected since the distance from the heart to the ear canal is smaller than that of the finger. However, this proves that the ear canal offers a faster desaturation response time than the periphery. The mean PTT measured from the EC, the RIF and the LIF has dropped during the ice water immersion. This indirectly indicates a general rise in blood pressure. However, the percentage drop in PTT varied across all three locations. The PTT in the EC and the LIF has dropped by 3% and 7% while the RIF PTT has dropped significantly by 12%. These differences in the drop of PTT across the three locations indicates the disparity in the strengths of local vasoconstriction in the respective areas. From all these findings it was concluded that the ear canal is a reliable site for monitoring PPGs and SpO_2 in conditions of compromised peripheral perfusion.

Since the ear canal was successfully shown to be an adequate site for monitoring PPGs and estimating SpO_2 in conditions of locally induced hypothermia, the next practical step was to test the sensors performance in a more realistic hypothermic situation (i.e., in patients or volunteers experiencing a mild form of hypothermia). Hence with the consent of City University Senate Research Ethics Committee, a study was carried in 15 healthy volunteers undergoing whole body cold exposure. The volunteers participating in this study were exposed to ambient temperature of about 10°C for 10 min, as the blood flow to the periphery is known to be minimal (less than 1 ml/min) at this temperature [277, 278]. Red and infrared PPG signals were acquired from the finger, the earlobe and the ear canal of the volunteer during the study. The PPG signals acquired from all the volunteers were generally of very good quality. The morphology of the AC PPG signals acquired from the ear canal were different to the finger and the earlobe PPG signals. The differences between the finger and the ear canal signals are expected due to the reasons mentioned earlier, however, the PPGs acquired from the ear lobe bore more resemblance to the finger

PPGs than the ear canal PPGs although being closer to the ear canal. This is perhaps due to the differences in the vasculature of the tissue in the respective areas. The earlobe is supplied by a capillary network originating from the superficial temporal artery while the ear canal is supplied mainly by the arterioles originating from the deep auricular artery and the internal maxillary artery.

During the cold exposure, the changes in NPA of the PPG signals has varied across all three locations. The NPA of the red and infrared PPG signals from the finger was significantly reduced as soon as the volunteer was exposed to cold temperature and has further decreased with time. By the end of the cold exposure, a mean drop in NPA of red and infrared finger PPGs greater than 70% was found in two thirds of the volunteers. Statistically, significant differences were found in the mean NPA of the red and infrared finger PPG signals (P-value: red– 0.002, infrared– < 0.001) when the baseline measurement was compared with every 2 min mean of cold exposure. The NPA of the earlobe PPGs was also affected, however, the magnitude of change was much smaller compared to the finger. A mean drop in NPA of earlobe PPGs greater than 70% was found only in one volunteer. No significant difference was found (P-value: red– 0.926, infrared– 0.654) between any of the groups when the mean NPA of baseline PPGs was compared with those acquired during cold exposure (every 2 min mean). In contrast with the finger and the earlobe, the NPA of the ear canal PPGs has remained relatively constant throughout the study, and none of the volunteers had a drop in NPA $> 70\%$. The mean drop in the red and infrared NPA of the ear canal PPGs was only 0.2% and 13% respectively. Similar to the earlobe, no significant difference was found (P-value: red– 0.993, infrared– 0.847) between any of the groups when the NPA of the ear canal PPGs from baseline was compared with cold exposure. However, judging from the P-value, the variations in ear canal PPGs were much smaller than the ear lobe PPGs. During the recovery period, the NPA of the PPG signals measured from all three locations has increased with time. However, the NPA of the finger PPGs was significantly ($P< 0.05$) lower than the baseline value by the end of the study.

The disparities in NPA of PPG signals acquired from the finger, the earlobe and the ear canal (or, in other words, the variations in the effect of cold exposure on the blood supply) are due to the thermal adaptation of the body. When the human body is exposed to cold, the efferent sympathetic nerves descending from the posterior hypothalamus (the body's thermostat) produce intense constriction of the skin resistance vessels and closure of the arteriovenous anastomoses. This innervation reduces the heat transfer from the body's core to the body's surface and subsequently the heat loss to the environment but at the expense of further cooling the extremities [278, 279]. Hence, appendages such as the finger, which are part of the peripheral circulation are more affected by the cold than the central areas such as the ear canal. The differences between the NPA of the ear canal and the

earlobe PPGs is explained by the dissimilarity in the vasculature of respective areas and the passive cooling of the skin surrounding the auricle and lobule during cold exposure.

To verify the measurements made from the custom built probes, the NPA changes measured from the finger and the ear canal probes were compared with the nTHI measurements from the forearm and the forehead. The NPA measured from the finger PPGs and the nTHI measured from the forearm followed the same trend throughout the measurement period. Both the parameters decrease rapidly during cold exposure due to profound vasoconstriction. Similarly, the NPA from the ear canal PPGs and the nTHI from the forehead followed the same trend. However, the parameters stayed relatively constant throughout the study in this region. However, minor differences were observed between the parameters measured in this region (see Figure 11.14). This is expected due to the anatomical differences between the forehead and the ear canal and the fundamental differences in the information provided by the parameters. nTHI is an indicator of changes in total blood volume while NPA is an indicator of changes only in arterial blood volume. These results show that the ear canal is recognisably resistant to profound vasoconstriction resulting from cold exposure.

To demonstrate the effect of the cold exposure on the SpO_2 estimated by the pulse oximeters, mean SpO_2 values were calculated from the PPGs acquired from all three probes, for every two minutes of the study. During baseline, the SpO_2 estimated from all three probes were in the healthy adult oxygen saturation range (94% – 100%). During the cold exposure, the mean of the mean SpO_2 measured from the finger has dropped significantly with time, particularly in the last 4 minutes of the cold exposure (see Figure 11.16). The mean of the mean SpO_2 calculated from the ear canal probe and the earlobe probe has remained relatively constant throughout the study, with the exception of three outliers. The failure rate of each probe was quantified by calculating the number of volunteers in whom the estimated SpO_2 had dropped to a value $< 90\%$. The finger probe produced erroneous SpO_2 readings in a maximum of 5 volunteers during the cold exposure. The earlobe pulse oximeter has failed to estimate accurate SpO_2 in a maximum of 3 volunteers during the course of the study. The ear canal pulse oximeter, on the other hand, had failed only in one volunteer.

The high failure rate in the finger sensor does not actually mean a reduction in the blood oxygenation of the volunteers. The failure of the pulse oximeter in these healthy volunteers is due to the quality of the signals acquired. When the body is exposed to ambient temperatures of 10°C, the blood flow through the hand is minimal (less than 1ml/min). Hence, the recorded AC PPG signals are very low in amplitude. In some cases, the amplitude diminishes so significantly that the peak detection algorithms cannot distinguish between noise and PPG signal peaks. In these instances, the amplitude being measured is of the noise. Since the amplitude of noise in both the red and infrared channels is

approximately similar, the absorbance ratio (R_{OS}) will drive towards 1, resulting in a SpO_2 close to 85%.

As mentioned earlier, the activation of the sympathetic nervous system by the thermoregulatory mechanism leads to a profound vasoconstriction. This innervation is, however, more prominent in the periphery than the core vasculature. In fact, the skin vessels of the human hand constrict so effectively that the ratio of maximum-to-minimum blood flow in the hand can be 60 to 1 whereas the same ratio in the body's core is about 6 to 1 [280]. Hence, to quantify the differences in the degree of sympathetic nerve activation between the periphery and the core during the cold exposure, the low-frequency spectral analysis was performed on the raw PPG signals acquired from the finger and the ear canal. The ratio of LF to HF power was calculated during this analysis and was compared at different stages of the study. A significant difference (P= 0.002) was found when the LF/HF power ratio computed from the finger was compared between baseline and the cold exposure while no significant differences were found in the ear canal LF/HF ratio (P= 0.781).

In summary, a new and clinically useful ear canal pulse oximetry system was successfully designed and developed. The system allowed for the first time the detailed investigation of PPG signals acquirable from the ear canal. The observations from both the *in vivo* investigations support the hypothesis that the ear canal can be used as an adequate site for monitoring blood oxygen saturation in conditions of poor peripheral perfusion where conventional pulse oximetry fails. However, more trials need to be conducted in more healthy volunteers and patients in order to assess this hypothesis.

The proposed future work is focused on conducting additional *in vivo* investigations in patients undergoing elective general and cardiothoracic surgery (ASA II-IV). As compromised peripheral perfusion is most likely to occur in this patient group. The goal of the further efforts is to develop a smaller, more robust and smart ear canal probe with added features such as core temperature measure. If developed, such a probe would have the potential to be the only technology capable of measuring heart rate, SpO_2, respiration rate, and core temperature. More emphasis will be made in future developments of the novel ZenPPG processing system. Work will be carried out in three different streams, (1) in making the system a multi-wavelength and multi-channel analogue system, (2) in developing a digital front end with adaptive DC correction, and adaptive LED intensity control, and (3) in implementing a high resolution ADC within the system, which would make the ZenPPG independent from LabVIEW DAQ cards. Finally, as the current system is un-calibrated, efforts will be made to calibrate the developed technology against the gold standard CO-Oximeter during a controlled hypoxic study.

A

Appendix

The schematic diagrams of the core module, the power supply module, the current source module, the transimpedance amplifier module and the vital sign module are depicted here. The 3D models showing the architecture of the ZenPPG system, and the microcontroller (MCU) control code are also presented.

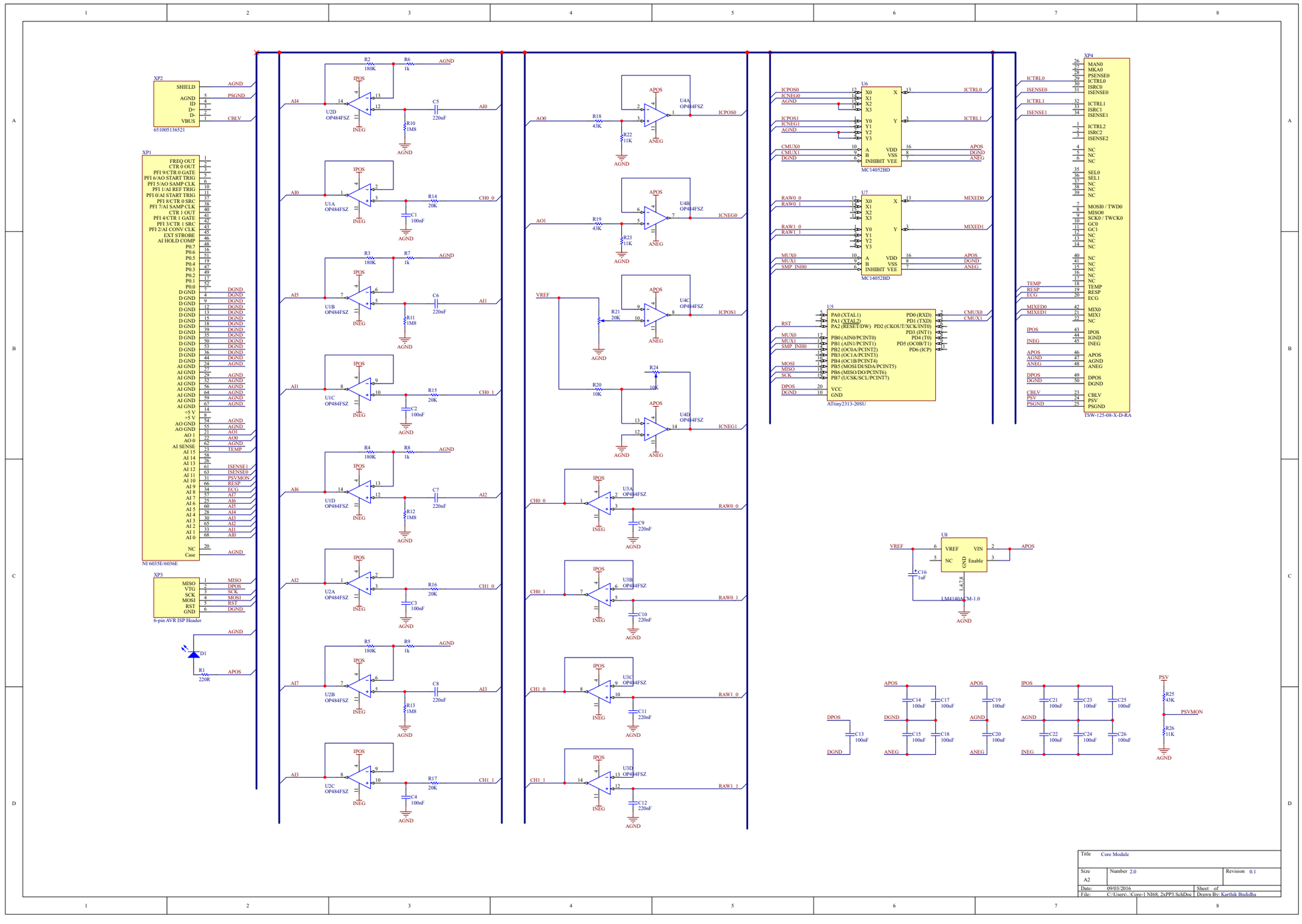

Title: Core Module
Size: A2
Number: 2.0
Revision: 0.1
Date: 09/03/2016
Sheet of
File: C:\Users\...\Core-1 NI68, 2xPP3.SchDoc
Drawn By: Karthik Budidha

FIGURE A.1: Schematic diagram of the core module

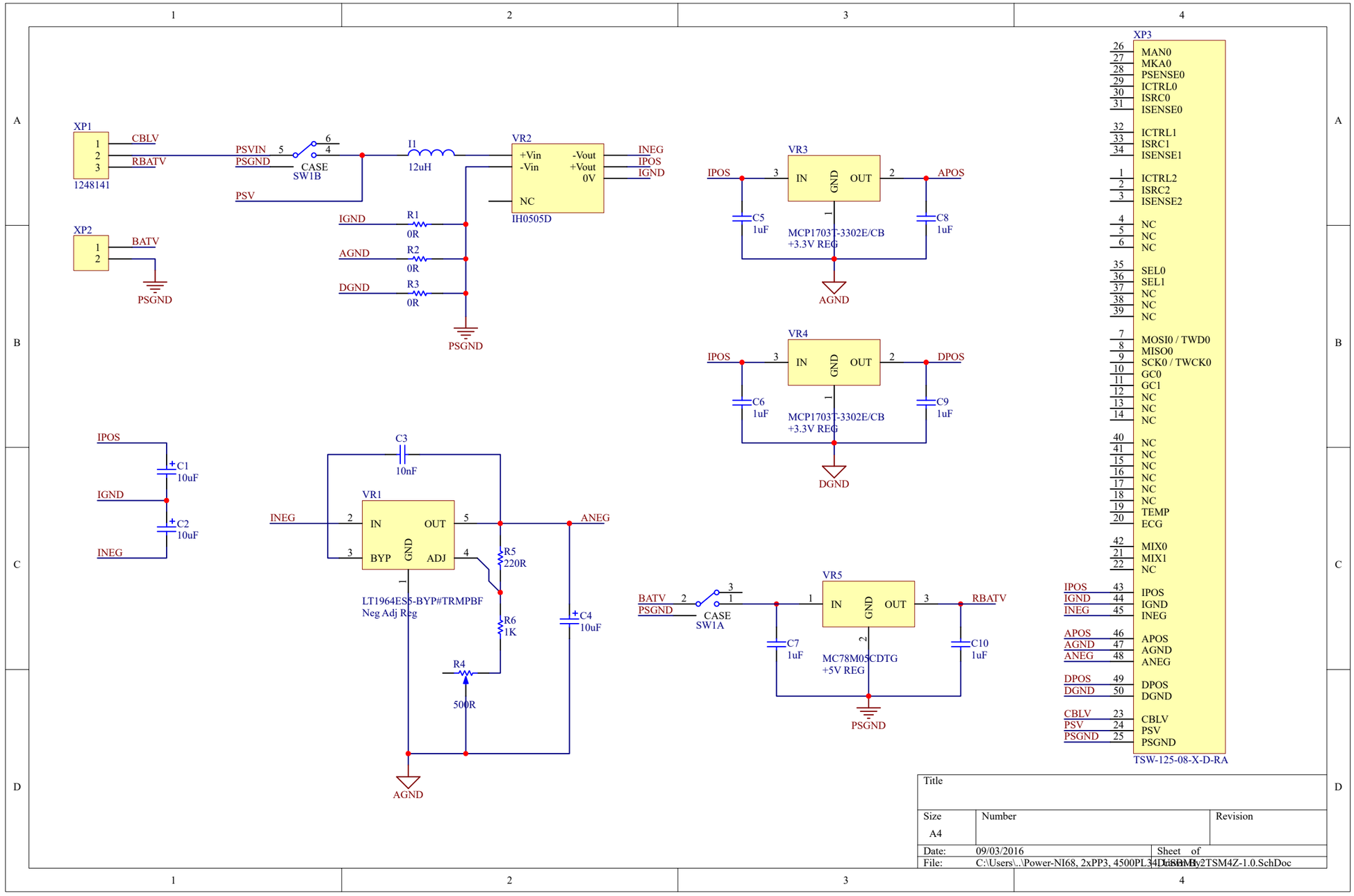

FIGURE A.2: Schematic diagram showing the circuitry in the power supply module

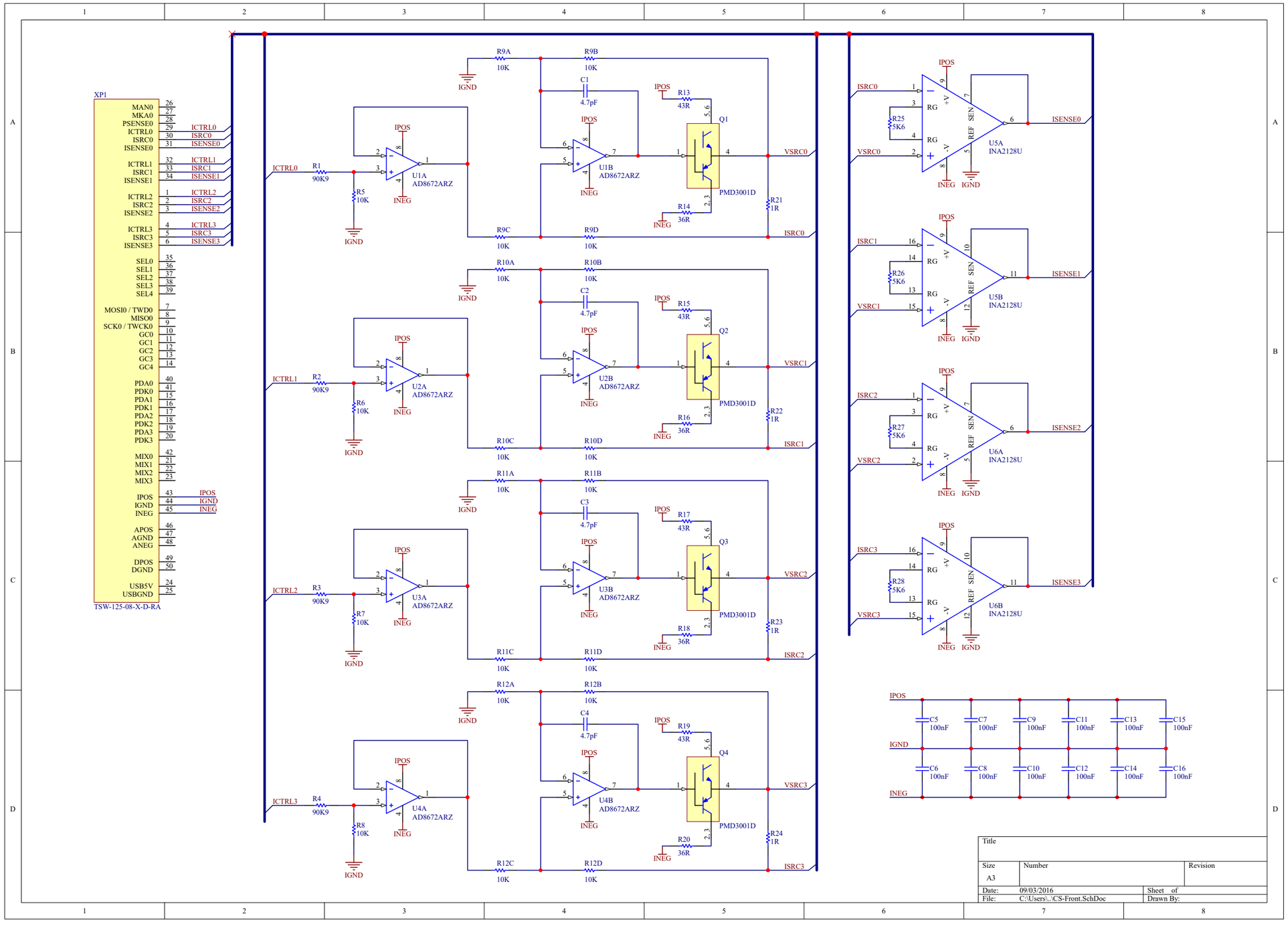

FIGURE A.3: Schematic diagram of the current source module

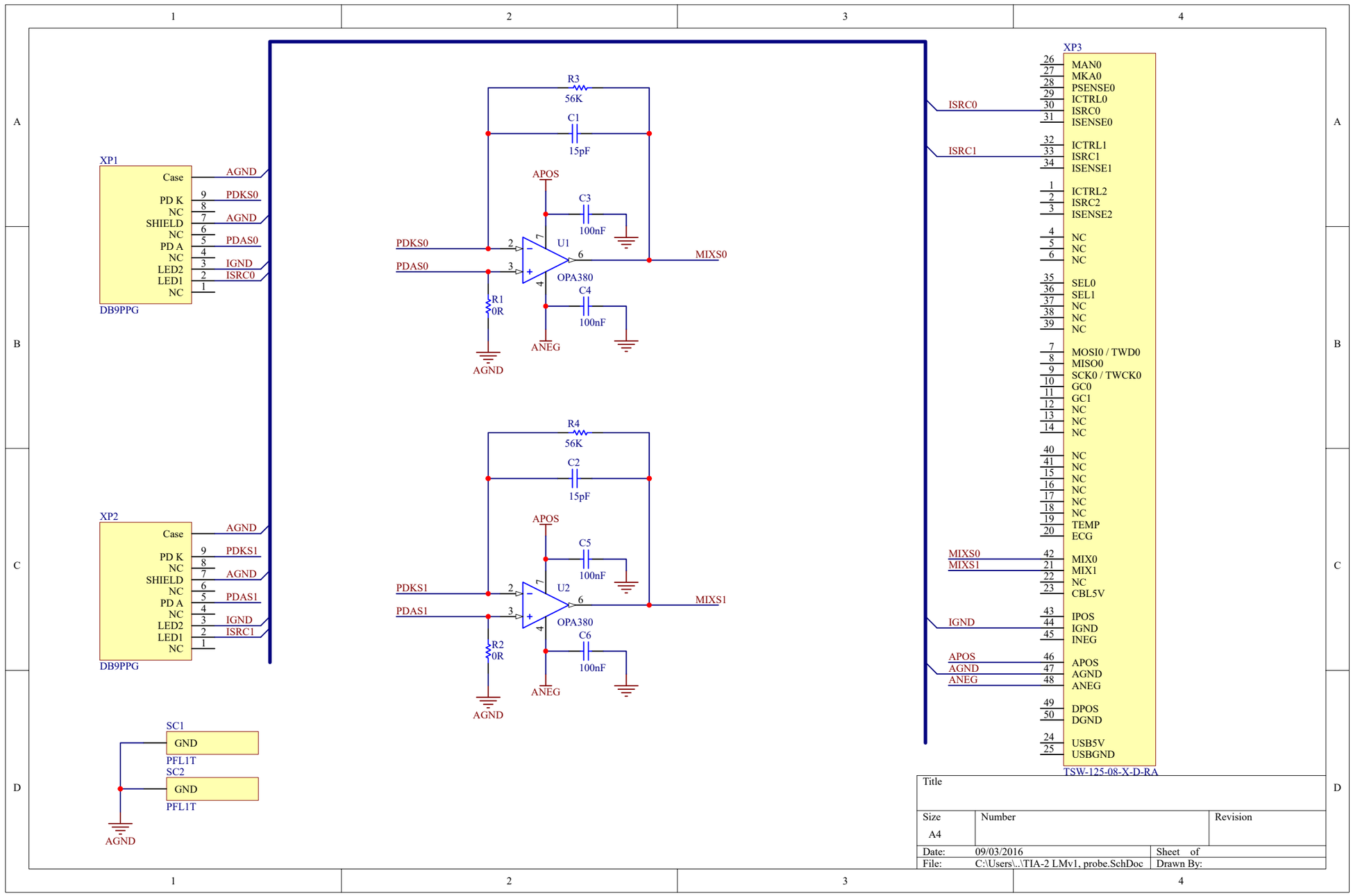

FIGURE A.4: Schematic diagram showing the circuitry in the transimpedance amplifier module

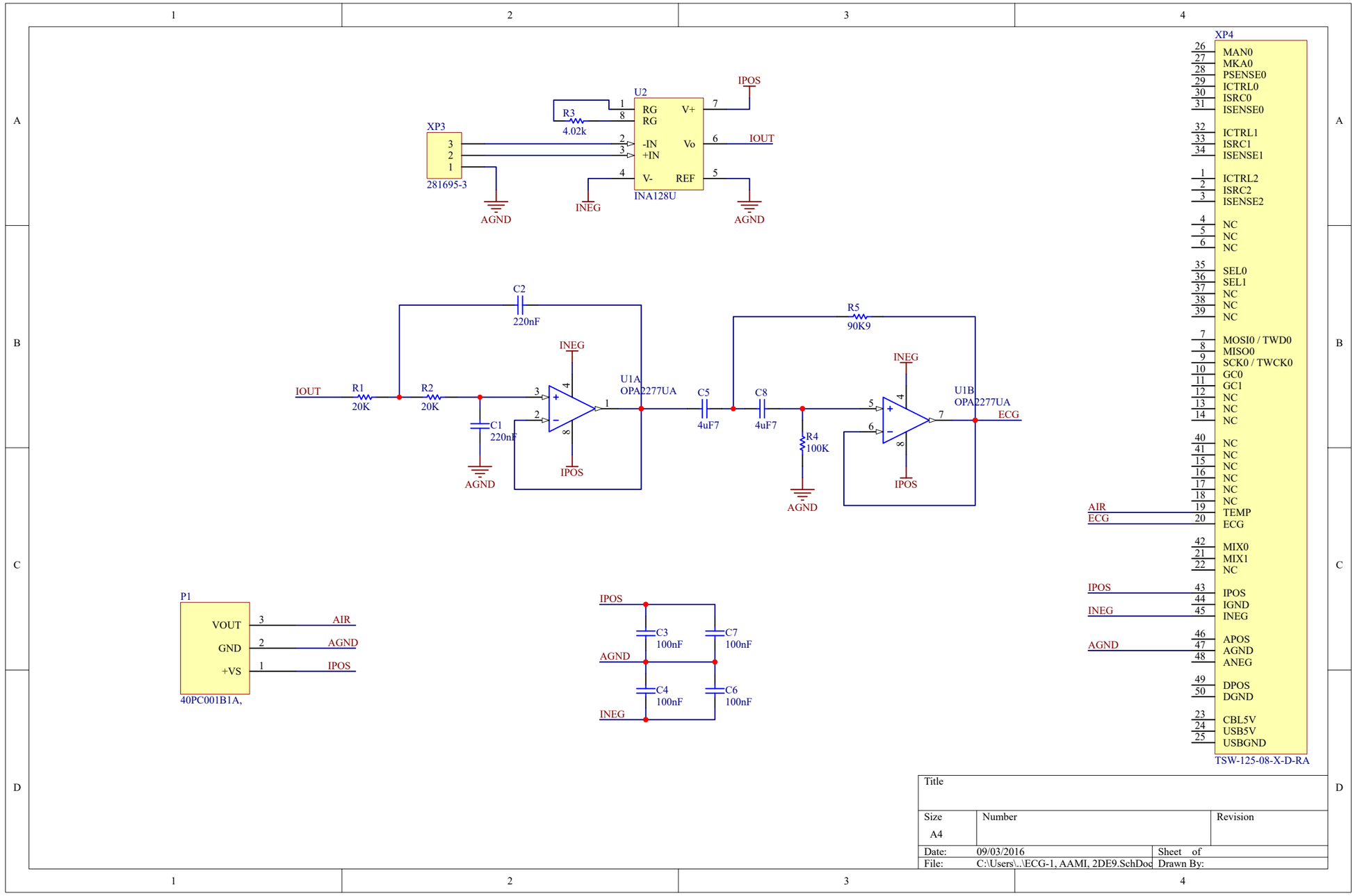

FIGURE A.5: Schematic diagram of the vital sign monitoring module

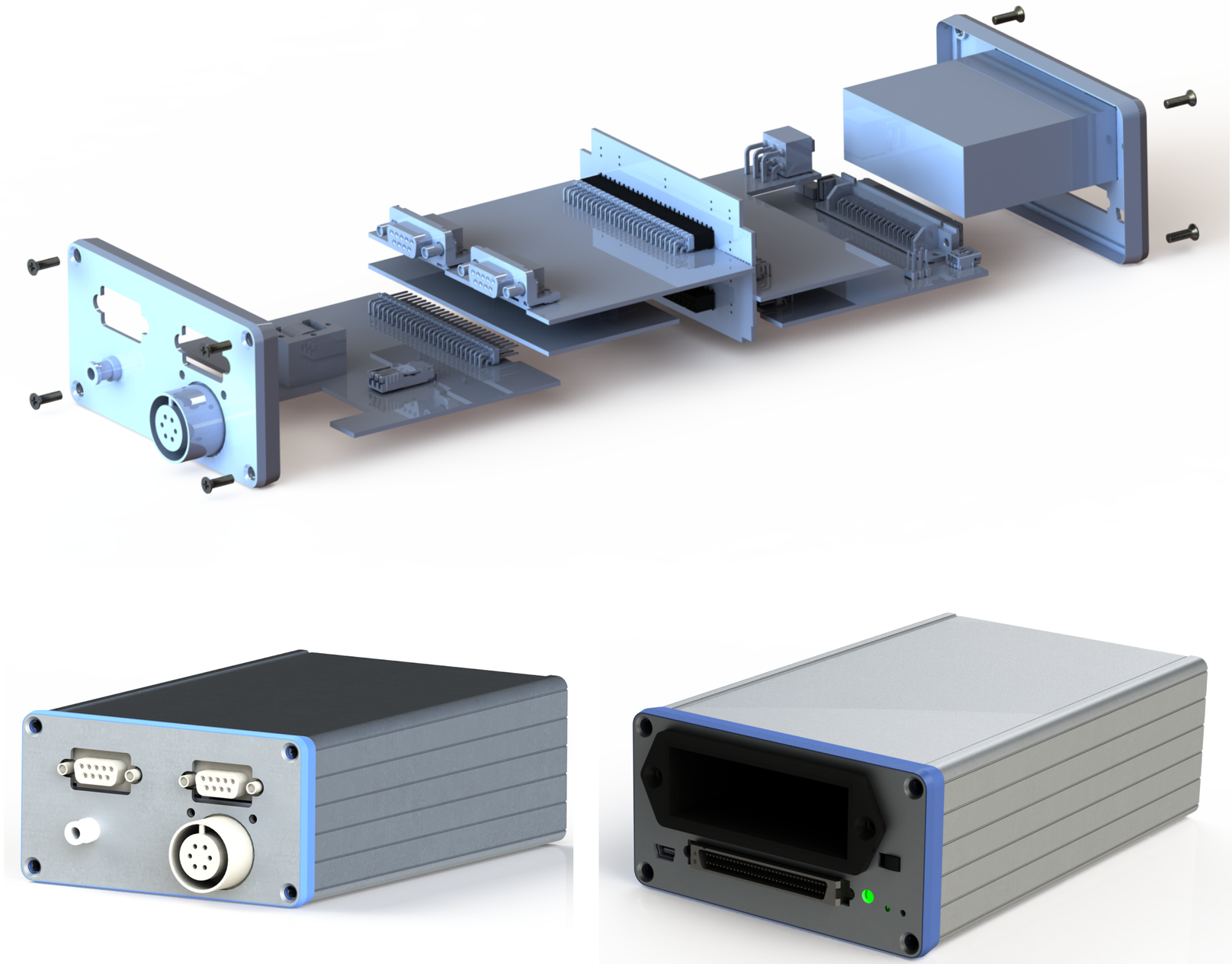

FIGURE A.6: 3D rendering showing the exploded view of the ZenPPG system along with the front and back panels

```
#include    <avr / io . h>
#include    <util   / delay  . h>

#define MUX PORTB
#define CMUX PORTD

// const unsigned char MUX      0  =  PB0;
// const unsigned char MUX      1  =  PB1;
// const unsigned char MUX      _INH  =  PB2;

const uint    8_t IR    = 0;
const uint    8_t RED   = 1;

inline void init        ()   {
      DDRB =  _BV( DDE2)  |_  BV( DDE1)  |_  BV( DDE0) ;
      DDRD =  _BV( DDE1)  |_  BV( DDE0) ;
}

inline void muxSel      ( uint  8_t n )  {
      uint  8_t tmp   = MUX;
      tmp  &= 0b11111100 ;
      tmp  |= n  &  0b00000011 ;
      MUX =  tmp;
}

inline void muxOn     ()   {
      MUX &= 0b11111011 ;
}

inline void muxOff      ()   {
      MUX |= 0b00000100 ;
}

inline void ledOn       ( uint  8_t n )  {
      uint  8_t tmp   = CMUX;
      tmp  &= 0b11111100 ;
      tmp  |= n  &  0b00000011 ;
      CMUX =  tmp;
}

inline void ledMuxSel       ( uint  8_t n )  {
      ledOn ( n) ;
      muxSel ( n) ;
}

inline static void qdelay           ( uint  8_t n )  {
      for  ( int i    =0;   i <n;   i ++)  {
            _delay  _us ( 125) ;
      }
}

inline static void ledMuxTrack            ()   {
      qdelay  ( 1) ;
      muxOn() ;
      qdelay  ( 2) ;
      muxOff () ;
      qdelay  ( 1) ;
}

int main   ( void )  {
      init   () ;

      while  ( 1)  {
            ledMuxSel  ( RED) ;
            ledMuxTrack   () ;
            ledMuxSel  ( IR ) ;
            ledMuxTrack   () ;
            }
}
```

References

[1] John TB Moyle. *Pulse oximetry*. BMJ Books, 2002.

[2] Thomas A Neff. Routine oximetry: A fifth vital sign? *Chest*, 94:227, 1988.

[3] SJ Barker, N Le, J Hyatt, et al. Failure rates of transmission and reflectance pulse oximetry for various sensor sites. *J Clin Monit*, 7:102–103, 1991.

[4] MI Bierman, KL Stein, and JV Snyder. Pulse oximetry in the postoperative care of cardiac surgical patients. a randomized controlled trail. *CHEST Journal*, 102(5): 1367–1370, 1992.

[5] Kazuo Irita, Yoichiro Kai, Kozaburo Akiyoshi, Yukako Tanaka, and Shosuke Takahashi. Performance evaluation of a new pulse oximeter during mild hypothermic cardiopulmonary bypass. *Anesthesia & Analgesia*, 96(1):11–14, 2003.

[6] H. Paelve. Reflection and transmission pulse oximetry during compromised peripheral perfusion. *J Clin Monit*, 8(1):12–15, Jan 1992.

[7] M. Shafique, P. A. Kyriacou, and S. K. Pal. Investigation of photoplethysmographic signals and blood oxygen saturation values on healthy volunteers during cuff-induced hypoperfusion using a multimode ppg/spo2 sensor. *Med Biol Eng Comput*, 50(6): 575–583, Jun 2012. doi: 10.1007/s11517-012-0910-z. URL http://dx.doi.org/10.1007/s11517-012-0910-z.

[8] M Shafique, PA Kyriacou, and SK Pal. Investigation of pulse oximeter failure rates during artificial hypoperfusion utilising a custom made multimode pulse oximetery sensor. In *Engineering in Medicine and Biology Society, EMBC, 2011 Annual International Conference of the IEEE*, pages 4352–4355. IEEE, 2011.

[9] David B Wax, Philip Rubin, and Steven Neustein. A comparison of transmittance and reflectance pulse oximetry during vascular surgery. *Anesthesia & Analgesia*, 109 (6):1847–1849, 2009.

[10] J. W. Severinghaus and MJ Spellman, Jr. Pulse oximeter failure thresholds in hypotension and vasoconstriction. *Anesthesiology*, 73(3):532–537, Sep 1990.

[11] E Barnett, A Duck, and R Barraclough. Effect of recording site on pulse oximetry readings. *Nursing times*, 108(1-2):22–23, 2011.

[12] Keith J Barrington, C Anthony Ryan, and Neil N Finer. Pulse oximetry during hemorrhagic hypotension and cardiopulmonary resuscitation in the rabbit. *Journal of Critical Care*, 1(4):241–246, 1986.

[13] DG Clayton, RK Webb, AC Ralston, D Duthie, and WB Runciman. Pulse oximeter probes- a comparison between finger, nose, ear and forehead probes under conditions of poor perfusion. *Anaesthesia*, 46(4):260–265, 1991.

[14] Jyotirmoy Das, Amit Aggarwal, and Naresh Kumar Aggarwal. Pulse oximeter accuracy and precision at five different sensor locations in infants and children with cyanotic heart disease. *Indian journal of anaesthesia*, 54(6):531, 2010.

[15] William W Hay, Jr, Donna J. Rodden, Shannon M. Collins, Diane L. Melara, Kathy A. Hale, and Lucy M. Fashaw. Reliability of conventional and new pulse oximetry in neonatal patients. *J Perinatol*, 22(5):360–366, 2002. doi: 10.1038/sj.jp.7210740. URL http://dx.doi.org/10.1038/sj.jp.7210740.

[16] Joshua Hofman, Marietta DePerio, Steven N Konstadt, and Tuula Kurki. Predictors of pulse oximetry data failure. *Anesthesiology*, 84(4):859–64, 1996.

[17] K Holroyd, M Lui, and C Beattie. Intraarterial vasodilator administration to restore pulse oximeter function. *Anesthesiology*, 79(2):388–390, 1993.

[18] Cordovi de Armas L and Costa Hidalgo T Vallongo Menendez MB. Espinaco Valdes J, Jimenez Paneque RE. Improved detection of the pulse oximeter signal with a digital nerve block in patients in poor health status. *Rev Esp Anestesiol Reanim*, 55(8):481–486, Oct 2008.

[19] D. L. Bourke and R. F. Grayson. Digital nerve blocks can restore pulse oximeter signal detection. *Anesth Analg*, 73(6):815–817, Dec 1991.

[20] M. E. Gentili, E. Chevaleraud, and E. Viel. Digital block of the flexor tendon sheath can restore pulse oximeter signal detection. *Reg Anesth*, 20(1):82–83, 1995.

[21] J Rosenberg and MH Pedersen. Nasal pulse oximetry overestimates oxygen saturation. *Anaesthesia*, 45(12):1070–1071, 1990.

[22] Panayiotis A Kyriacou. Pulse oximetry in the oesophagus. *Physiological measurement*, 27(1):R1, 2006.

[23] Valerie C Scanlon and Tina Sanders. *Essentials of anatomy and physiology*. FA Davis, 2010.

[24] Gerard J Tortora and Bryan H Derrickson. *Principles of anatomy and physiology*. John Wiley & Sons, 2008.

[25] Deborah Roiger. *Anatomy & Physiology: Foundations for the Health Professions*. McGraw-Hill Science/Engineering/Math, New York, NY, 1 edition edition, January 2012. ISBN 9780073402123.

[26] John G Webster. *Design of pulse oximeters*. CRC Press, 2002.

[27] Eric Wong. Breathing during exercise - some research. URL http://ericwongmma.com/breathing-during-exercise/.

[28] Richard M Schwartzstein and Michael J Parker. *Respiratory physiology: a clinical approach*. Lippincott Williams & Wilkins, 2006.

[29] Tommy Boone. *Introduction to Exercise Physiology*. Jones & Bartlett Publishers, 2013.

[30] John E Hall. *Guyton and Hall Textbook of Medical Physiology: Enhanced E-book*. Elsevier Health Sciences, 2010.

[31] Sylvia S Mader and Patrick L Galliart. *Understanding human anatomy & physiology*. McGraw-Hill Company, 1997.

[32] Walter F Boron and Emile L Boulpaep. *Medical Physiology, 2e Updated Edition: with student consult Online Access*. Elsevier Health Sciences, 2012.

[33] Inc BioDigital. The biodigital human, 2014. URL https://www.biodigital.com.

[34] SA McLellan and TS Walsh. Oxygen delivery and haemoglobin. *Continuing Education in Anaesthesia, Critical Care & Pain*, 4(4):123–126, 2004.

[35] Elaine Nicpon Marieb and Katja Hoehn. *Human anatomy & physiology*. Pearson Education, 2007.

[36] AJ Crerar-Gilbert, PA Kyriacou, DP Jones, and RM Langford. Assessment of photoplethysmographic signals for the determination of splanchnic oxygen saturation in humans. *Anaesthesia*, 57(5):442–445, 2002.

[37] Cindy L. Stanfield and William J. Germann. *Principles of Human Physiology*. Pearson Education, 1 edition edition, August 2007. ISBN 9781405887489.

[38] Stuart Ira Fox. *Fundamentals of human physiology*. McGraw-Hill, 2009.

[39] Heart: function and structure - access revision. URL https://sites.google.com/site/accessrevision/biology/respiratory-and-circulatory-systems/heart-function-and-structure.

[40] Human anatomy and physiology ii lab, 2010. URL http://www.highlands.edu/academics/divisions/scipe/biology/labs/cartersville/2122/2122.htm.

[41] William D McArdle, Frank I Katch, and Victor L Katch. *Exercise physiology: Nutrition, energy, and human performance*. Lippincott Williams & Wilkins, 2010.

[42] Jean Foret Giddens. *Concepts for Nursing Practice (with Pageburst Digital Book Access on VST)*. Mosby/Elsevier, March 2012. ISBN 9780323083768.

[43] Meir Nitzan and Haim Taitelbaum. The measurement of oxygen saturation in arterial and venous blood. *Instrumentation & Measurement Magazine, IEEE*, 11(3):9–15, 2008.

[44] Alton L Thygerson, Benjamin Gulli, and Jon R Krohmer. *First aid, CPR, and AED*. Jones & Bartlett Learning, 2007.

[45] J. P. Nolan and R. Pullinger. Hypovolaemic shock. *BMJ*, 348(mar07 1):bmj.g1139–bmj.g1139, March 2014. ISSN 1756-1833. doi: 10.1136/bmj.g1139. URL http://www.bmj.com/content/348/bmj.g1139.

[46] Arthur Guyton and John Hall. Textbook of medical physiology, 11th. 2006.

[47] John A. Kaufman MD MS FSIR FCIRSE and Michael J. Lee MSc FRCPI FRCR FFR FSIR EBIR. *Vascular and Interventional Radiology: The Requisites, 2e*. Saunders, 2 edition, August 2013. ISBN 9780323045841.

[48] Sharon L. Lewis RN PhD FAAN, Linda Bucher RN PhD CEN, and Margaret M. Heitkemper RN PhD FAAN. *Medical-Surgical Nursing: Assessment and Management of Clinical Problems, Single Volume, 9e*. Mosby, St. Louis, Missouri, 9 edition edition, January 2014. ISBN 9780323086783.

[49] Neil R Sims and Hakan Muyderman. Mitochondria, oxidative metabolism and cell death in stroke. *Biochimica et Biophysica Acta (BBA)-Molecular Basis of Disease*, 1802(1):80–91, 2010.

[50] Alex Dyson, Ray Stidwill, Val Taylor, and Mervyn Singer. Tissue oxygen monitoring in rodent models of shock. *American Journal of Physiology-Heart and Circulatory Physiology*, 293(1):H526–H533, 2007.

[51] Muhammad Shafique. *Investigation of photoplethysmography and arterial blood oxygen saturation during artificially induced peripheral hypoperfusion utilising multimode photometric sensors*. Ph.d., City University, 2011. URL http://ethos.bl.uk/OrderDetails.do?uin=uk.bl.ethos.531784.

[52] Kenneth Gerard Humphreys. *An investigation of remote non-contact photoplethysmography and pulse oximetry*. phd, National University of Ireland Maynooth, August 2007. URL http://eprints.maynoothuniversity.ie/1494/.

[53] Barry A Shapiro, Ronald A Harrison, and John R Walton. *Clinical application of blood gases*. Year Book Medical Publishers Chicago, 1989.

[54] Sundararajan V Madihally. *Principles of Biomedical Engineering*. Artech House, 2010.

[55] John W Severinghaus and Poul B Astrup. History of blood gas analysis. iv. leland clark's oxygen electrode. *Journal of clinical monitoring*, 2(2):125–139, 1986.

[56] John Enderle and Joseph Bronzino. *Introduction to Biomedical Engineering*. Academic Press, 3 edition, April 2011. ISBN 0123749794.

[57] John Webster. *Medical instrumentation: application and design*. John Wiley & Sons, 2009.

[58] Kevin Vo. Spectrophotometry. URL http://chemwiki.ucdavis.edu/Physical_Chemistry/Kinetics/Reaction_Rates/Experimental_Determination_of_Kinetcs/Spectrophotometry.

[59] Albert Huch, Renate Huch, Volker König, MichaelR Neuman, Dawood Parker, John Yount, and Dietrich Lubbers. Limitations of pulse oximetry. *The Lancet*, 331(8581): 357–358, 1988.

[60] H Franklin Bunn and Bernard G Forget. Hemoglobin–molecular, genetic, and clinical aspects. 1986.

[61] Howard Franklin Bunn, Bernard G Forget, and Helen M Ranney. *Human hemoglobins*. Saunders Philadelphia, PA;, 1977.

[62] Neil Townsend and M Term. Pulse oximetry. *Medical Electronics, Michaelmas Term*, 2001.

[63] Sonnia Maria Lopez Silva, Maria Luisa Dotor Castilla, and Juan Pedro Silveira Martin. Near-infrared transmittance pulse oximetry with laser diodes. *Journal of biomedical optics*, 8(3):525–533, July 2003. ISSN 1083-3668. doi: 10.1117/1.1578495.

[64] J A Wahr, K K Tremper, and M Diab. Pulse oximetry,. *Respiratory care clinics of North America*, 1(1):77–105, September 1995. ISSN 1078-5337.

[65] A Zwart, A Buursma, B Oeseburg, and W G Zijlstra. Determination of hemoglobin derivatives with IL 282 CO-oximeter as compared with a manual spectrophotometric five-wavelength method. *Clinical chemistry*, 27(11):1903–1907, November 1981. ISSN 0009-9147.

[66] Brenda Morgan. Svo2 (mixed venous oxygen saturation) or scvo2 (central venous oxygen saturation), July 2012. URL http://www.lhsc.on.ca/Health_Professionals/CCTC/edubriefs/svo2.htm.

[67] Jan M Headley. Understanding continuous mixed venous oxygen saturation (svo2) monitoring with the edwards swan-ganz oximetry td system. Edwards Lifesciences LLC. One Edwards way, Irvine, CA 92614 USA., 2002. URL http://ht.edwards.com/resourcegallery/products/swanganz/pdfs/svo2edbook.pdf.

[68] John Frazier. Theory and clinical application of continuous fiberoptic central venous oximetry (scvo2) monitoring. Edwards Lifesciences LLC. One Edwards way, Irvine, CA 92614 USA., 2011. URL http://ht.edwards.com/scin/edwards/sitecollectionimages/products/mininvasive/ar06578-pediasattheoryclinicalapp_1lr.pdf.

[69] Jan M Headley. Invasive hemodynamic monitoring: Physiological principles and clinical applications. Edwards Lifesciences LLC. One Edwards way, Irvine, CA 92614 USA., 2002. URL http://ht.edwards.com/resourcegallery/products/swanganz/pdfs/invasivehdmphysprincbook.pdf.

[70] John Moyle. *Principles and Practice Series: Pulse Oximetry, Revised Edition*. John Wiley & Sons, December 1998. ISBN 9780727912350.

[71] James P Payne and John Wendell Severinghaus. *Pulse Oximetry: Symposium on Clinical Applications of Oximetry: Papers*. Springer, 1986.

[72] Amal Jubran. Pulse oximetry. *Crit Care*, 3(2):R11–R17, 1999.

[73] Kamat Vijaylakshmi. Pulse oximetry. *Indian Journal of anaesthesia*, 46(4):261–268, 2002.

[74] H Owen-Reece, M Smith, CE Elwell, and JC Goldstone. Near infrared spectroscopy. *British journal of anaesthesia*, 82(3):418–426, 1999.

[75] David A Hampton and Martin A Schreiber. Near infrared spectroscopy: clinical and research uses. *Transfusion*, 53(S1):52S–58S, 2013.

[76] Stephen M Cohn. Near-infrared spectroscopy: potential clinical benefits in surgery. *Journal of the American College of Surgeons*, 205(2):322–332, 2007.

[77] TWL Scheeren, P Schober, and LA Schwarte. Monitoring tissue oxygenation by near infrared spectroscopy (nirs): background and current applications. *Journal of clinical monitoring and computing*, 26(4):279–287, 2012.

[78] Adelina Pellicer and María del Carmen Bravo. Near-infrared spectroscopy: a methodology-focused review. In *Seminars in Fetal and Neonatal Medicine*, volume 16, pages 42–49. Elsevier, 2011.

[79] Akke Bakker, Brianne Smith, Philip Ainslie, and Kurt Smith. Near-infrared spectroscopy. In Philip Ainslie, editor, *Applied Aspects of Ultrasonography in Humans*. InTech, April 2012. ISBN 978-953-51-0522-0. URL http://www.intechopen.com/books/applied-aspects-of-ultrasonography-in-humans/near-infrared-spectroscopy.

[80] P Van der Zee, M Cope, SR Arridge, M Essenpreis, LA Potter, AD Edwards, JS Wyatt, DC McCormick, SC Roth, EOR Reynolds, et al. Experimentally measured optical pathlengths for the adult head, calf and forearm and the head of the newborn infant as a function of inter optode spacing. In *Oxygen Transport to Tissue XIII*, pages 143–153. Springer, 1992.

[81] Arlene Duncan, Judith H Meek, Matthew Clemence, Clare E Elwell, Lidia Tyszczuk, Mark Cope, and D Delpy. Optical pathlength measurements on adult head, calf and forearm and the head of the newborn infant using phase resolved optical spectroscopy. *Physics in medicine and biology*, 40(2):295, 1995.

[82] JS Wyatt, M Cope, DT Delpy, P Van der Zee, S Arridge, AD Edwards, and EOR Reynolds. Measurement of optical path length for cerebral near-infrared spectroscopy in newborn infants. *Developmental neuroscience*, 12(2):140–144, 1990.

[83] Thomas Jue and Kazumi Masuda. *Application of near infrared spectroscopy in biomedicine*. Springer, 2013.

[84] D. T. Delpy and M. Cope. Quantification in tissue near-infrared spectroscopy. *Philosophical Transactions of the Royal Society B: Biological Sciences*, 352(1354): 649–659, June 1997. ISSN 0962-8436. doi: 10.1098/rstb.1997.0046. URL http://www.ncbi.nlm.nih.gov/pmc/articles/PMC1691964/.

[85] Peter Rolfe. In vivo near-infrared spectroscopy. *Annual review of biomedical engineering*, 2(1):715–754, 2000.

[86] John W Severinghaus. Takuo aoyagi: discovery of pulse oximetry. *Anesthesia & Analgesia*, 105(6):S1–S4, 2007.

[87] John Allen. Photoplethysmography and its application in clinical physiological measurement. *Physiological measurement*, 28(3):R1, 2007.

[88] Meir Nitzan, Yair Adar, Ellie Hoffman, Eran Shalom, Shlomo Engelberg, Iddo Z Ben-Dov, and Michael Bursztyn. Comparison of systolic blood pressure values obtained

by photoplethysmography and by korotkoff sounds. *Sensors*, 13(11):14797–14812, 2013.

[89] J De Trefford and K Lafferty. What does photoplethysmography measure? *Medical and biological engineering and computing*, 22(5):479–480, 1984.

[90] John G Webster. *Prevention of pressure sores: engineering and clinical aspects*. CRC Press, 1991.

[91] AVJ Challoner. Photoelectric plethysmography for estimating cutaneous blood flow. *Non-invasive physiological measurements*, 1:125–51, 1979.

[92] EK McGough and PG Boysen. Benefits and limitations of pulse oximetry in the icu. *J Crit Illness*, 4:23, 1989.

[93] Yitzhak Mendelson and Burt D Ochs. Noninvasive pulse oximetry utilizing skin reflectance photoplethysmography. *Biomedical Engineering, IEEE Transactions on*, 35(10):798–805, 1988.

[94] L. S. D'Agrosa and A. B. Hertzman. Opacity pulse of individual minute arteries. *Journal of Applied Physiology*, 23(5):613–620, November 1967. ISSN 8750-7587, 1522-1601. URL http://jap.physiology.org/content/23/5/613.

[95] JA Nijboer, JC Dorlas, and HF Mahieu. Photoelectric plethysmography-some fundamental aspects of the reflection and transmission methods. *Clinical Physics and Physiological Measurement*, 2(3):205, 1981.

[96] Alrick B Hertzman. Photoelectric plethysmography of the fingers and toes in man. *Experimental Biology and Medicine*, 37(3):529–534, 1937.

[97] John W Severinghaus and Poul B Astrup. History of blood gas analysis. vi. oximetry. *Journal of clinical monitoring*, 2(4):270–288, 1986.

[98] John W Severinghaus and Poul B Astrup. History of blood gas analysis. v. oxygen measurement. *Journal of clinical monitoring*, 2(3):174–189, 1986.

[99] Joseph F Kelleher. Pulse oximetry. *Journal of clinical monitoring*, 5(1):37–62, 1989.

[100] John W Severinghaus and Yoshiyuki Honda. History of blood gas analysis. vii. pulse oximetry. *Journal of clinical monitoring*, 3(2):135–138, 1987. URL http://link.springer.com/article/10.1007/BF00858362.

[101] Yitzhak Mendelson. Pulse oximetry: theory and applications for noninvasive monitoring. *Clinical chemistry*, 38(9):1601–1607, 1992.

[102] Scott Prahl. Tabulated molar extinction coefficient for hemoglobin in water, March 1998. URL http://omlc.org/spectra/hemoglobin/summary.html.

[103] RC Gupta, SS Ahluwalia, and SS Randhawa. Design and development of pulse oximeter. In *Engineering in Medicine and Biology Society, 1995 and 14th Conference of the Biomedical Engineering Society of India. an International Meeting, Proceedings of the First Regional Conference., IEEE*, pages 1–13. IEEE, 1995.

[104] LG Lindberg, T Tamura, and PÅ Öberg. Photoplethysmography. *Medical and Biological Engineering and Computing*, 29(1):40–47, 1991.

[105] Michael W Wukitsch, Mr Michael T Petterson, David R Tobler, and Jonas A Pologe. Pulse oximetry: analysis of theory, technology, and practice. *Journal of Clinical Monitoring*, 4(4):290–301, 1988.

[106] Clare Elwell. A practical users guide to near infrared spectroscopy. 1995.

[107] StevenJ Barker and Kevin K Tremper, K K. Pulse oximetry: applications and limitations. *International anesthesiology clinics*, 25(3):155–175, 1987.

[108] Panayiotis A. Kyriacou. *Investigation of new electro optical techniques for monitoring patients with compromised peripheral perfusion in anaesthesia*. Ph.d., Queen Mary, University of London, 2001. URL http://ethos.bl.uk/OrderDetails.do?uin=uk.bl.ethos.251876.

[109] Oliver Wieben. Light absorbance in pulse oximetry. *Design of pulse oximeters*, 4: 40–55, 1997.

[110] Justin Paul Phillips. *New optical methods for the measurement of oxygen saturation in cerebral tissue*. Ph.d., Queen Mary, University of London, 2009. URL http://ethos.bl.uk/OrderDetails.do?did=1&uin=uk.bl.ethos.515511.

[111] Kevin K Tremper. Pulse oximetry. *CHEST Journal*, 95(4):713–715, 1989.

[112] Stephen M Kennedy. An introduction to pulse oximeters: Equations and theory, 2009. URL http://www.google.co.uk/url?sa=t&rct=j&q=&esrc=s&source=web&cd=1&ved=0CCgQFjAA&url=http%3A%2F%2Fphp.iai.heig-vd.ch%2F~lzo%2Fbiomed%2Frefs%2FPulse%2520oximetry%2Fpulseoximetersequationsandtheory-stephenkennedy.doc&ei=BMrcVNqiNMfXariogcAM&usg=AFQjCNG3iKxm2vHcnn-rEImFvzFvASa3JA&sig2=O70cggRX4vel1Jy-AXqyEw&bvm=bv.85761416,d.d2s.

[113] Simon M Sze and Kwok K Ng. *Physics of semiconductor devices*. John Wiley & Sons, 2006.

[114] John N Amoore. Pulse oximetry: an equipment management perspective. 1996.

[115] Heikki Paelve. Reflection and transmission pulse oximetry during compromised peripheral perfusion. *Journal of clinical monitoring*, 8(1):12–15, 1992.

[116] Santiago Lopez and RTAC Americas. Pulse oximeter fundamentals and design. *Freescale Semiconductor, Inc., application note document number: AN4327 Rev*, 1(09), 2011.

[117] M Hickey and PA Kyriacou. Optimal spacing between transmitting and receiving optical fibres in reflectance pulse oximetry. In *Journal of Physics: Conference Series*, volume 85, page 012030. IOP Publishing, 2007.

[118] Jonas A Pologe. Pulse oximetry: technical aspects of machine design. *International anesthesiology clinics*, 25(3):137–153, 1987.

[119] Christian M Alexander, Lynn E Teller, and Jeffrey B Gross. Principles of pulse oximetry: theoretical and practical considerations. *Anesthesia & Analgesia*, 68(3): 368–376, 1989.

[120] Meir Nitzan, Amikam Patron, Zehava Glik, and Abraham T Weiss. Automatic noninvasive measurement of systolic blood pressure using photoplethysmography. *Biomedical engineering online*, 8(1):1–8, 2009.

[121] Zachary D Walton, Panayiotis A Kyriacou, David G Silverman, and Kirk H Shelley. Measuring venous oxygenation using the photoplethysmograph waveform. *Journal of clinical monitoring and computing*, 24(4):295–303, August 2010. ISSN 1573-2614. doi: 10.1007/s10877-010-9248-y.

[122] P Leonard, TF Beattie, PS Addison, and JN Watson. Standard pulse oximeters can be used to monitor respiratory rate. *Emergency medicine journal*, 20(6):524–525, 2003.

[123] J Spigulis. Biophotonic technologies for non-invasive assessment of skin condition and blood microcirculation. *Latvian Journal of Physics and Technical Sciences*, 49 (5):63–80, 2012.

[124] John Allen, Crispian P Oates, Timothy A Lees, and Alan Murray. Photoplethysmography detection of lower limb peripheral arterial occlusive disease: a comparison of pulse timing, amplitude and shape characteristics. *Physiological measurement*, 26 (5):811, 2005.

[125] Igor Alexandre Côrtes de Menezes, Márcio Roberto Viana Santos, and Cláudio Leinig Pereira da Cunha. Evaluation of endothelial function on atherosclerosis using perfusion index from pulse oximeter. *Arquivos brasileiros de cardiologia*, 102(3):237–244, 2014.

[126] Kirk H Shelley, W Bosseau Murray, and David Chang. Arterial–pulse oximetry loops: A new method of monitoring vascular tone. *Journal of Clinical monitoring*, 13(4):223–228, 1997.

[127] Sotirios Fouzas, Kostas N Priftis, and Michael B Anthracopoulos. Pulse oximetry in pediatric practice. *Pediatrics*, 128(4):740–752, 2011.

[128] Michael T Petterson, Valerie L Begnoche, and John M Graybeal. The effect of motion on pulse oximetry and its clinical significance. *Anesthesia & Analgesia*, 105 (6):S78–S84, 2007.

[129] James E Sinex. Pulse oximetry: principles and limitations. *The American journal of emergency medicine*, 17(1):59–66, 1999.

[130] Hartmut Gehring, Christoph Hornberger, Holger Matz, Ewald Konecny, and Peter Schmucker. The effects of motion artifact and low perfusion on the performance of a new generation of pulse oximeters in volunteers undergoing hypoxemia. *Respiratory Care*, 47(1):48–60, 2002.

[131] Christian F Poets and David P Southall. Noninvasive monitoring of oxygenation in infants and children: practical considerations and areas of concern. *Pediatrics*, 93 (5):737–746, 1994.

[132] Sergio Fanconi. Reliability of pulse oximetry in hypoxic infants. *The Journal of pediatrics*, 112(3):424–427, 1988.

[133] D Seidler, MM Hirschl, and G Roeggla. Limitations of pulse oximetry. *The Lancet*, 341(8860):1600–1601, 1993.

[134] C P F. O'Donnell, C O F. Kamlin, P. G. Davis, and C. J. Morley. Obtaining pulse oximetry data in neonates: a randomised crossover study of sensor application techniques. *Arch Dis Child Fetal Neonatal Ed*, 90(1):F84–F85, Jan 2005. doi: 10.1136/adc.2004.058925. URL http://dx.doi.org/10.1136/adc.2004.058925.

[135] Duncan Young, Claire Jewkes, Murray Spittal, Colin Blogg, James Weissman, and David Gradwell. Response time of pulse oximeters assessed using acute decompression. *Anesthesia & Analgesia*, 74(2):189–195, 1992.

[136] F Verhoeff and MK Sykes. Delayed detection of hypoxic events by pulse oximeters: computer simulations. *Anaesthesia*, 45(2):103–109, 1990.

[137] A. L. Ries, L. M. Prewitt, and J. J. Johnson. Skin color and ear oximetry. *Chest*, 96(2):287–290, Aug 1989.

[138] John R Feiner, John W Severinghaus, and Philip E Bickler. Dark skin decreases the accuracy of pulse oximeters at low oxygen saturation: the effects of oximeter probe type and gender. *Anesthesia & Analgesia*, 105(6):S18–S23, 2007.

[139] John W Salyer. Neonatal and pediatric pulse oximetry. *Respiratory care*, 48(4): 386–398, 2003.

[140] Mark S Scheller, Richard J Unger, and Michael J Kelner. Effects of intravenously administered dyes on pulse oximetry readings. *Anesthesiology*, 65(5):550–552, 1986.

[141] MR Kessler, Thoraas Eide, Bharathi Humayun, and PJ Poppers. Spurious pulse oximeter desaturation with methylene blue injection. *Anesthesiology*, 65(4):435–436, 1986.

[142] Avner Sidi, David A Paulus, William Rush, Nikolaus Gravenstein, and Richard F Davis. Methylene blue and indocyanine green artfactually lower pulse oximetry readings of oxygen saturation. studies in dogs. *Journal of clinical monitoring*, 3(4): 249–256, 1987.

[143] Hou-Chuan Lai, Huan-Ming Hsu, Chen-Hwan Cherng, Shinn-Long Lin, Ching-Tang Wu, Jyh-Cherng Yu, and Chun-Chang Yeh. Interference of patent blue dye with pulse oximetry readings, methemoglobin measurements, and blue urine in sentinel lymph node mapping: a case report and review of the literature. *Acta Anaesthesiol Taiwan*, 49(4):162–164, Dec 2011. doi: 10.1016/j.aat.2011.11.004. URL http://dx.doi.org/10.1016/j.aat.2011.11.004.

[144] David L. McDonagh, Matthew R. McDaniel, and Terri G. Monk. The effect of intravenous indigo carmine on near-infrared cerebral oximetry. *Anesth Analg*, 105 (3):704–706, Sep 2007. doi: 10.1213/01.ane.0000271917.20429.50. URL http://dx.doi.org/10.1213/01.ane.0000271917.20429.50.

[145] WG Zijlstra, A Buursma, and WP Meeuwsen-Van der Roest. Absorption spectra of human fetal and adult oxyhemoglobin, de-oxyhemoglobin, carboxyhemoglobin, and methemoglobin. *Clinical chemistry*, 37(9):1633–1638, 1991.

[146] Steven J. Barker, Jeremy Curry, Daniel Redford, and Scott Morgan. Measurement of carboxyhemoglobin and methemoglobin by pulse oximetry: a human volunteer study. *Anesthesiology*, 105(5):892–897, Nov 2006.

[147] N. B. Hampson. Pulse oximetry in severe carbon monoxide poisoning. *Chest*, 114 (4):1036–1041, Oct 1998.

[148] George Mardirossian and Roland E Schneider. Limitations of pulse oximetry. *Anesthesia progress*, 39(6):194, 1992.

[149] Ed Uthman. *Understanding anemia*. Univ. Press of Mississippi, 2009.

[150] John W Severinghaus and Shin O Koh. Effect of anemia on pulse oximeter accuracy at low saturation. *Journal of clinical monitoring*, 6(2):85–88, 1990.

[151] S Lee, KK Tremper, and SJ Barker. Effects of anemia on pulse oximetry and continuous mixed venous hemoglobin saturation monitoring in dogs. *Anesthesiology*, 75 (1):118–122, 1991.

[152] Gregory D Jay, Lori Hughes, and Francis P Renzi. Pulse oximetry is accurate in acute anemia from hemorrhage. *Annals of emergency medicine*, 24(1):32–35, 1994.

[153] KG Stewart and SJ Rowbottom. Inaccuracy of pulse oximetry in patients with severe tricuspid regurgitation. *Anaesthesia*, 46(8):668–670, 1991.

[154] JM Kim and HS Mathewson. Venous congestion affects arterial hemoglobin saturation measured by the pulse oximeter. *Anesthesiology*, 63(3a):A174, 1985.

[155] Hafez M Sami, Bruce S Kleinman, and Vassyl A Lonchyna. Central venous pulsations associated with a falsely low oxygen saturation measured by pulse oximetry. *Journal of clinical monitoring*, 7(4):309–312, 1991.

[156] Kirk H Shelley, Doris Tamai, Denis Jablonka, Michael Gesquiere, Robert G Stout, and David G Silverman. The effect of venous pulsation on the forehead pulse oximeter wave form as a possible source of error in spo2 calculation. *Anesthesia & Analgesia*, 100(3):743–747, 2005.

[157] T. B. Sloan. Finger injury by an oxygen saturation monitor probe. *Anesthesiology*, 68(6):936–938, Jun 1988.

[158] J. Wille, R. Braams, W. H. van Haren, and C. van der Werken. Pulse oximeter-induced digital injury: frequency rate and possible causative factors. *Crit Care Med*, 28(10):3555–3557, Oct 2000.

[159] C. W. Lin, H. Z. Wang, and K. S. Hsieh. Pulse oximeter-associated toe injuries in a premature neonate: a case report. *Zhonghua Yi Xue Za Zhi (Taipei)*, 62(12): 914–916, Dec 1999.

[160] Medicines and Healthcare products Regulatory Agency (MHRA). Pulse oximetry top tips. 2010. URL http://webarchive.nationalarchives.gov.uk/20141205150130/http://www.mhra.gov.uk/Publications/Postersandleaflets/CON100224.

[161] Matthew Clavey. Raynaud's phenomenon, Jan 2015. URL http://www.wellcomeimageawards.org/2016/raynauds-disease.

[162] Jerry A Dorsch. *Understanding anesthesia equipment*. Lippincott Williams & Wilkins, 2012.

[163] Jakob T Moller, NW Johannessen, K Espersen, O Ravlo, BD Pedersen, PF Jensen, NH Rasmussen, LS Rasmussen, T Pedersen, and JB Cooper. Randomized evaluation of pulse oximetry in 20,802 patients: Ii. perioperative events and postoperative complications. *Anesthesiology*, 78(3):445–453, 1993.

[164] Jakob T Moller, T Pedersen, LS Rasmussen, PF Jensen, BD Pedersen, O Ravlo, NH Rasmussen, K Espersen, NW Johannessen, and JB Cooper. Randomized evaluation of pulse oximetry in 20,802 patients: I. design, demography, pulse oximetry failure rate, and overall complication rate. *Anesthesiology*, 78(3):436–444, 1993.

[165] Peter R Freund, Patrick T Overand, Jeremy Cooper, Lawrence Jacobson, Stan Bosse, Brad Walker, Karen L Posner, and Frederick W Cheney. A prospective study of intraoperative pulse oximetry failure. *Journal of clinical monitoring*, 7(3):253–258, 1991.

[166] Bruce S Gillies, Karen Posner, Peter Freund, and Frederick Cheney. Failure rate of pulse oximetry in the postanesthesia care unit. *Journal of clinical monitoring*, 9(5): 326–329, 1993.

[167] DL Reich, A Timcenko, C Bodian, J Kraidin, J Hoffman, M DePerio, and SN Konstadt. Pulse oximetry failure rate is higher in cardiac surgery. *Anesthesia & Analgesia*, 80(4):SCA87, 1995.

[168] M. Shafique and P. A. Kyriacou. Photoplethysmographic signals and blood oxygen saturation values during artificial hypothermia in healthy volunteers. *Physiol Meas*, 33(12):2065–2078, Dec 2012. doi: 10.1088/0967-3334/33/12/2065. URL http://dx.doi.org/10.1088/0967-3334/33/12/2065.

[169] Helmut D. Hummler, Anja Engelmann, Frank Pohlandt, Josef Högel, and Axel R. Franz. Decreased accuracy of pulse oximetry measurements during low perfusion caused by sepsis: Is the perfusion index of any value? *Intensive Care Med*, 32(9): 1428–1431, Sep 2006. doi: 10.1007/s00134-006-0254-y. URL http://dx.doi.org/10.1007/s00134-006-0254-y.

[170] Steven J. Barker. Problems with forehead reflectance pulse oximetry. *Respir Care*, 51(7):715–716, Jul 2006.

[171] Shigekazu Sugino, Noriaki Kanaya, Masahito Mizuuchi, Masayasu Nakayama, and Akiyoshi Namiki. Forehead is as sensitive as finger pulse oximetry during general anesthesia. *Canadian Journal of Anesthesia*, 51(5):432–436, 2004.

[172] J Brimacombe and C Keller. Successful pharyngeal pulse oximetry in low perfusion states. *Canadian journal of anaesthesia*, 47(9):907–909, 2000.

[173] JM May, PA Kyriacou, M Honsel, and AJ Petros. Investigation of photoplethysmographs from the anterior fontanelle of neonates. *Physiological measurement*, 35(10): 1961, 2014.

[174] Michelle Hickey, Neal Samuels, Nilesh Randive, RM Langford, and PA Kyriacou. Investigation of photoplethysmographic signals and blood oxygen saturation values

obtained from human splanchnic organs using a fiber optic sensor. *Journal of clinical monitoring and computing*, 25(4):245–255, 2011.

[175] C. Lennmarken and M. Vegfors. Advances in pulse oximetry. *Curr Opin Anaesthesiol*, 11(6):639–644, Dec 1998.

[176] Rakesh Sahni. Noninvasive monitoring by photoplethysmography. *Clin Perinatol*, 39(3):573–583, Sep 2012. doi: 10.1016/j.clp.2012.06.012. URL http://dx.doi.org/10.1016/j.clp.2012.06.012.

[177] Kirk H. Shelley. Photoplethysmography: beyond the calculation of arterial oxygen saturation and heart rate. *Anesth Analg*, 105(6 Suppl):S31–6, tables of contents, Dec 2007. doi: 10.1213/01.ane.0000269512.82836.c9. URL http://dx.doi.org/10.1213/01.ane.0000269512.82836.c9.

[178] Masimo Corporation. Clinical applications of perfusion index. Technical bulletin, Masimo Corporation, 40 parker, irvine, CA, 92618, 2007. URL http://www.masimo.co.uk/pdf/whitepaper/LAB3410F.pdf.

[179] Maxime Cannesson and Pekka Talke. Recent advances in pulse oximetry. *F1000 medicine reports*, 1, 2009.

[180] Claudio De Felice, Giuseppe Latini, Paola Vacca, and Robert J. Kopotic. The pulse oximeter perfusion index as a predictor for high illness severity in neonates. *European Journal of Pediatrics*, 161(10):561–562, October 2002. ISSN 0340-6199. doi: 10.1007/s00431-002-1042-5.

[181] Y. Ginosar, C. F. Weiniger, Y. Meroz, V. Kurz, T. Bdolah-Abram, A. Babchenko, M. Nitzan, and E. M. Davidson. Pulse oximeter perfusion index as an early indicator of sympathectomy after epidural anesthesia. *Acta Anaesthesiologica Scandinavica*, 53 (8):1018–1026, September 2009. ISSN 00015172, 13996576. doi: 10.1111/j.1399-6576.2009.01968.x. URL http://doi.wiley.com/10.1111/j.1399-6576.2009.01968.x.

[182] H Hagar, Susan Church, Goutham Mandadi, Debra Pulley, and Andrea Kurz. The perfusion index measured by a pulse oximeter indicates pain stimuli in anesthetized volunteers. *Anesthesiology*, 101(A514):A514, 2004.

[183] Helmut Hager, Dayakar Reddy, and Andrea Kurz. Perfusion index-a valuable tool to assess changes in peripheral perfusion caused by sevoflurane. *Anesthesiology*, 99: A593, 2003.

[184] Alexandre Pinto Lima, Peter Beelen, and Jan Bakker. Use of a peripheral perfusion index derived from the pulse oximetry signal as a noninvasive indicator of perfusion. *Critical Care Medicine*, 30(6):1210–1213, June 2002. ISSN 0090-3493.

[185] L-G Lindberg, H Ugnell, and PÅ Öberg. Monitoring of respiratory and heart rates using a fibre-optic sensor. *Medical and Biological Engineering and Computing*, 30 (5):533–537, 1992.

[186] RONALD E De Meersman, ADRIENNE S Zion, SUSAN Teitelbaum, JOSEPH P Weir, JAMES Lieberman, and JOHN Downey. Deriving respiration from pulse wave: a new signal-processing technique. *American Journal of Physiology-Heart and Circulatory Physiology*, 270(5):H1672–H1675, 1996.

[187] Maxime Cannesson, Cyril Besnard, Pierre G Durand, Julien Bohé, and Didier Jacques. Relation between respiratory variations in pulse oximetry plethysmographic waveform amplitude and arterial pulse pressure in ventilated patients. *Critical Care*, 9(5):R562, 2005.

[188] Paul A Leonard, J Graham Douglas, Neil R Grubb, David Clifton, Paul S Addison, and James N Watson. A fully automated algorithm for the determination of respiratory rate from the photoplethysmogram. *Journal of Clinical Monitoring and Computing*, 20(1):33–36, 2006.

[189] Lena Nilsson, Anders Johansson, and Sigga Kalman. Respiration can be monitored by photoplethysmography with high sensitivity and specificity regardless of anaesthesia and ventilatory mode. *Acta anaesthesiologica scandinavica*, 49(8):1157–1162, 2005.

[190] Kirk H Shelley, Denis H Jablonka, Aymen A Awad, Robert G Stout, Hoda Rezkanna, and David G Silverman. What is the best site for measuring the effect of ventilation on the pulse oximeter waveform? *Anesthesia & Analgesia*, 103(2):372–377, 2006.

[191] K. Shafqat, R. M. Langford, S. K. Pal, and P. A. Kyriacou. Estimation of venous oxygenation saturation using the finger photoplethysmograph (ppg) waveform. *Conf Proc IEEE Eng Med Biol Soc*, 2012:2905–2908, 2012. doi: 10.1109/EMBC.2012.6346571. URL http://dx.doi.org/10.1109/EMBC.2012.6346571.

[192] A. J. Wilson, C. I. Franks, and I. L. Freeston. Algorithms for the detection of breaths from respiratory waveform recordings of infants. *Med Biol Eng Comput*, 20 (3):286–292, May 1982.

[193] Laura Mason. *Signal processing methods for non-invasive respiration monitoring*. PhD thesis, Department of Engineering Science, University of Oxford, 2002.

[194] Masimo Corporation. Pleth variability index: A dynamic measurement to help assess physiology and fluid responsiveness. Technical bulletin, Masimo Corporation, 40 parker, irvine, CA, 92618, 2013. URL http://www.masimo.co.uk/pdf/whitepaper/LAB7698A.pdf.

[195] O. Broch, B. Bein, M. Gruenewald, J. Höcker, J. Schöttler, P. Meybohm, M. Steinfath, and J. Renner. Accuracy of the pleth variability index to predict fluid responsiveness depends on the perfusion index. *Acta Anaesthesiol Scand*, 55(6):686–693, Jul 2011. doi: 10.1111/j.1399-6576.2011.02435.x. URL http://dx.doi.org/10.1111/j.1399-6576.2011.02435.x.

[196] Thibault Loupec, Hodanou Nanadoumgar, Denis Frasca, Franck Petitpas, Leila Laksiri, Didier Baudouin, Bertrand Debaene, Claire Dahyot-Fizelier, and Olivier Mimoz. Pleth variability index predicts fluid responsiveness in critically ill patients*. *Critical care medicine*, 39(2):294–299, 2011.

[197] Anne Sebastiani, Larissa Philippi, Stefan Boehme, Dorothea Closhen, Irene Schmidtmann, Anton Scherhag, Klaus Markstaller, Kristin Engelhard, and Gunther Pestel. Perfusion index and plethysmographic variability index in patients with interscalene nerve catheters. *Can J Anaesth*, 59(12):1095–1101, Dec 2012. doi: 10.1007/s12630-012-9796-3. URL http://dx.doi.org/10.1007/s12630-012-9796-3.

[198] Yinan Yu, Jing Dong, Zifeng Xu, Hao Shen, and Jijian Zheng. Pleth variability index-directed fluid management in abdominal surgery under combined general and epidural anesthesia. *J Clin Monit Comput*, 29(1):47–52, Feb 2015. doi: 10.1007/s10877-014-9567-5. URL http://dx.doi.org/10.1007/s10877-014-9567-5.

[199] Marek Malik. Heart rate variability- standards of measurement, physiological interpretation, and clinical use. *Eur Heart J, Task Force of the European Society of Cardiology and the North American Society of Pacing and Electrophysiology.*, 17(3):354–381, Mar 1996.

[200] K. Shafqat, S. K. Pal, S. Kumari, and P. A. Kyriacou. Empirical mode decomposition (emd) analysis of hrv data from locally anesthetized patients. *Conf Proc IEEE Eng Med Biol Soc*, 2009:2244–2247, 2009. doi: 10.1109/IEMBS.2009.5335000. URL http://dx.doi.org/10.1109/IEMBS.2009.5335000.

[201] E Gil, M Orini, R Bailón, JM Vergara, L Mainardi, and P Laguna. Photoplethysmography pulse rate variability as a surrogate measurement of heart rate variability during non-stationary conditions. *Physiological Measurement*, 31(9):1271, 2010.

[202] Axel Schäfer and Jan Vagedes. How accurate is pulse rate variability as an estimate of heart rate variability?: A review on studies comparing photoplethysmographic technology with an electrocardiogram. *International journal of cardiology*, 166(1):15–29, 2013.

[203] Kamran Shafqat, SK Pal, and PA Kyriacou. Evaluation of two detrending techniques for application in heart rate variability. In *Engineering in Medicine and Biology*

Society, 2007. EMBS 2007. 29th Annual International Conference of the IEEE, pages 267–270. IEEE, 2007.

[204] Ashok K Jaryal, Nandakumar Selvaraj, Jayashree Santhosh, Sneh Anand, and Kishore K Deepak. Monitoring of cardiovascular reactivity to cold stress using digital volume pulse characteristics in health and diabetes. *Journal of clinical monitoring and computing*, 23(2):123–130, 2009.

[205] Bruno M Pannier, Alberto P Avolio, Arnold Hoeks, Giuseppe Mancia, and Kenji Takazawa. Methods and devices for measuring arterial compliance in humans. *American journal of hypertension*, 15(8):743–753, 2002.

[206] Steven J Barker and John J Badal. The measurement of dyshemoglobins and total hemoglobin by pulse oximetry. *Current Opinion in Anesthesiology*, 21(6):805–810, 2008.

[207] Masimo Corporation. accuracy of noninvasive carbonmonoxide detection by spco: the rainbow set technology platform. Technical bulletin, Masimo Corporation, 40 parker, irvine, CA, 92618, 2009. URL http://www.masimo.co.uk/pdf/whitepaper/LAB5317A.pdf.

[208] Takuo Aoyagi and Katsuyuki Miyasaka. The theory and applications of pulse spectrophotometry. *Anesthesia and analgesia*, 94(1 Suppl):S93–5, 2002.

[209] Takuo Aoyagi, Masayoshi Fuse, Naoki Kobayashi, Kazuko Machida, and Katsuyuki Miyasaka. Multiwavelength pulse oximetry: theory for the future. *Anesthesia & Analgesia*, 105(6):S53–S58, 2007.

[210] Eisei Noiri, Naoki Kobayashi, Yoshiaki Takamura, Takehiko Iijima, Toshiyuki Takagi, Kent Doi, Akihide Nakao, Tokunori Yamamoto, Sunao Takeda, and Toshiro Fujita. Pulse total-hemoglobinometer provides accurate noninvasive monitoring. *Critical care medicine*, 33(12):E2831, 2005.

[211] Aristomenis Exadaktylos, Christian Tasso Braun, and Mairi Ziaka. Pulse co-oximetry–clinical impact in the emergency department. *Trends in Anaesthesia and Critical Care*, 4(5):152–158, 2014.

[212] M Coulange, A Barthelemy, F Hug, AL Thierry, and L De Haro. Reliability of new pulse co-oximeter in victims of carbon monoxide poisoning. 2008.

[213] Brooks D Enjeti S Layne T, Snyder C. Evaluation of a new pulse co-oximeter: Noninvasive measurement of carboxyhemoglobin in the outpatient pulmonary lab and emergency departments. *The Science Journal of the American Association for Respiratory Care*, 2006.

URL http://www.masimo.com/pdf/clinical/carboxyhemoglobin/layne-evaluation-of-a-new-pulse-co-oximeter-nov-2006.pdf.

[214] Wael Awada. Continuous and noninvasive hemoglobin monitoring reduces red blood cell transfusion during neurosurgery: A prospective cohort study. In *Qatar Foundation Annual Research Conference*, number 2013, 2013.

[215] Boreom Lee, Jonghee Han, Hyun Jae Baek, Jae Hyuk Shin, Kwang Suk Park, and Won Jin Yi. Improved elimination of motion artifacts from a photoplethysmographic signal using a kalman smoother with simultaneous accelerometry. *Physiological measurement*, 31(12):1585, 2010.

[216] H Lee, J Lee, W Jung, and Gun-Ki Lee. The periodic moving average filter for removing motion artifacts from ppg signals. *INTERNATIONAL JOURNAL OF CONTROL AUTOMATION AND SYSTEMS*, 5(6):701, 2007.

[217] Rasoul Yousefi, Mehrdad Nourani, Sarah Ostadabbas, and Issa Panahi. A motion-tolerant adaptive algorithm for wearable photoplethysmographic biosensors. *Biomedical and Health Informatics, IEEE Journal of*, 18(2):670–681, 2014.

[218] Qian Wang, Ping Yang, and Yuanting Zhang. Artifact reduction based on empirical mode decomposition (emd) in photoplethysmography for pulse rate detection. *Conf Proc IEEE Eng Med Biol Soc*, 2010:959–962, 2010. doi: 10.1109/IEMBS.2010.5627581. URL http://dx.doi.org/10.1109/IEMBS.2010.5627581.

[219] Rasoul Yousefi, Mehrdad Nourani, and Issa Panahi. Adaptive cancellation of motion artifact in wearable biosensors. In *Engineering in Medicine and Biology Society (EMBC), 2012 Annual International Conference of the IEEE*, pages 2004–2008. IEEE, 2012.

[220] Julian M Goldman, Michael T Petterson, Robert J Kopotic, and Steven J Barker. Masimo signal extraction pulse oximetry. *Journal of Clinical Monitoring and Computing*, 16(7):475–483, 2000.

[221] Masimo Corporation. Signal extraction technology. Technical bulletin, Masimo Corporation, 40 parker, irvine, CA, 92618, 2008. URL http://www.masimo.co.uk/pdf/whitepaper/LAB1035R.pdf.

[222] Nellcor Technical staff. A technology overview of the nellcor oximax^{TM} pulse oximetry system. Technical bulletin, 6135 Gunbarrel Avenue, Boulser, CO, 80301, 2003. URL http://www.covidien.com/imageServer.aspx/doc226941.1.2.3_OxiMax%20whitepaper.pdf?contentID=25496&contenttype=application/pdf.

[223] R Neumann et al. Fourier artifact suppression technology provides reliable spo_2. In *Abstracts A*, volume 11, page S105, 2002.

[224] Steven J. Barker. "motion-resistant" pulse oximetry: a comparison of new and old models. *Anesth Analg*, 95(4):967–72, table of contents, Oct 2002.

[225] Masimo. Selection of independent and objective studies comparing masimo and nellcor technology. 2012.

[226] Karen K. Giuliano and Thomas L. Higgins. New-generation pulse oximetry in the care of critically ill patients. *Am J Crit Care*, 14(1):26–37; quiz 38–9, Jan 2005.

[227] Kazuo Irita, Yoichiro Kai, Kozaburo Akiyoshi, Yukako Tanaka, and Shosuke Takahashi. Performance evaluation of a new pulse oximeter during mild hypothermic cardiopulmonary bypass. *Anesth Analg*, 96(1):11–4, table of contents, Jan 2003.

[228] Ryan E R. Forde, Frederic M. DeBros, Emily L. Guimaraes, and Warren S. Sandberg. Misleading behavior of masimo pulse oximeter tone during profound bradycardia. *Anesthesiology*, 107(6):1038–9; discussion 1039–40, Dec 2007. doi: 10.1097/01.anes.0000290621.03797.37. URL http://dx.doi.org/10.1097/01.anes.0000290621.03797.37.

[229] Toshiya Kawagishi, Noriaki Kanaya, Masayasu Nakayama, Saori Kurosawa, and Akiyoshi Namiki. A comparison of the failure times of pulse oximeters during blood pressure cuff-induced hypoperfusion in volunteers. *Anesth Analg*, 99(3):793–6, table of contents, Sep 2004. doi: 10.1213/01.ANE.0000130343.66453.37. URL http://dx.doi.org/10.1213/01.ANE.0000130343.66453.37.

[230] B. Bohnhorst, C. S. Peter, and C. F. Poets. Pulse oximeters' reliability in detecting hypoxemia and bradycardia: comparison between a conventional and two new generation oximeters. *Crit Care Med*, 28(5):1565–1568, May 2000.

[231] Helmut D. Hummler, Anja Engelmann, Frank Pohlandt, Josef Högel, and Axel R. Franz. Accuracy of pulse oximetry readings in an animal model of low perfusion caused by emerging pneumonia and sepsis. *Intensive Care Med*, 30(4):709–713, Apr 2004. doi: 10.1007/s00134-003-2116-1. URL http://dx.doi.org/10.1007/s00134-003-2116-1.

[232] James May. *Investigation of fontanelle photoplethysmographs and oxygen saturations in intensive care neonates and infants utilising miniature photometric sensors*. PhD thesis, City University London, 2013.

[233] T Zaman, PA Kyriacou, and SK Pal. Free flap pulse oximetry utilizing reflectance photoplethysmography. In *Engineering in Medicine and Biology Society (EMBC), 2013 35th Annual International Conference of the IEEE*, pages 4046–4049. IEEE, 2013.

[234] Sung Wu Sun, Bhavi Patel, Wanda Gangoo, and Zev Carrey. Reliability of forehead pulse oximetry in critically ill patients. *CHEST Journal*, 124(4_MeetingAbstracts): 178S–c, 2003.

[235] M Nuhr, K Hoerauf, A Joldzo, N Frickey, R Barker, L Gorove, T Puskas, and A Kober. Forehead spo2 monitoring compared to finger spo2 recording in emergency transport. *Anaesthesia*, 59(4):390–393, 2004.

[236] Helmut Hager, Goutham Mandadi, Dayakar Reddy, Debra Pulley, and Andrea Kurz. Clinical experiences with a new forehead reflectance pulse oximetry sensor in asa iii patients during surgery. *Anesthesiology*, 101:A564, 2004.

[237] Eugene Y Cheng, Margaret B Hopwood, and Jonathan Kay. Forehead pulse oximetry compared with finger pulse oximetry and arterial blood gas measurement. *Journal of clinical monitoring*, 4(3):223–226, 1988.

[238] Howard A Smithline, Ned Rudnitzky, Sandy Macomber, and Fidela SJ Blank. Pulse oximetry using a disposable finger sensor placed on the forehead in hypoxic patients. *The Journal of emergency medicine*, 39(1):121–125, 2010.

[239] Geeta S Agashe, Joseph Coakley, and Paul D Mannheimer. Forehead pulse oximetry: Headband use helps alleviate false low readings likely related to venous pulsation artifact. *Anesthesiology*, 105(6):1111–1116, 2006.

[240] Melissa Lee and James B Eisenkraft. Forehead pulse oximeter-associated pressure injury. *A&A Case Reports*, 2(2):13–15, 2014.

[241] Karin Faisst, Whitney Hannon, Jan S Jorgensen, Volker Konig, Hans U Bucher, Albert Huch, and Renate Huch. Reflectance pulse oximetry in neonates. *European Journal of Obstetrics & Gynecology and Reproductive Biology*, 61(2):117–122, 1995.

[242] PA Kyriacou, SL Powell, DP Jones, and RM Langford. Evaluation of oesophageal pulse oximetry in patients undergoing cardiothoracic surgery*. *Anaesthesia*, 58(5): 422–427, 2003.

[243] P. A. Kyriacou, S. Powell, R. M. Langford, and D. P. Jones. Investigation of oesophageal photoplethysmographic signals and blood oxygen saturation measurements in cardiothoracic surgery patients. *Physiol Meas*, 23(3):533–545, Aug 2002.

[244] Panayiotis A. Kyriacou, Sarah Powell, Richard M. Langford, and Deric P. Jones. Esophageal pulse oximetry utilizing reflectance photoplethysmography. *IEEE Trans Biomed Eng*, 49(11):1360–1368, Nov 2002. doi: 10.1109/TBME.2002.804584. URL http://dx.doi.org/10.1109/TBME.2002.804584.

[245] P. A. Kyriacou, A. R. Moye, D. M. Choi, R. M. Langford, and D. P. Jones. Investigation of the human oesophagus as a new monitoring site for blood oxygen saturation. *Physiol Meas*, 22(1):223–232, Feb 2001.

[246] P. A. Kyriacou, A. R. Moye, A. Gregg, D. M. Choi, R. M. Langford, and D. P. Jones. A system for investigating oesophageal photoplethysmographic signals in anaesthetised patients. *Med Biol Eng Comput*, 37(5):639–643, Sep 1999.

[247] Guo Chen, Zhaoqiong Zhu, Jin Liu, and Wei Wei. Esophageal pulse oximetry is more accurate and detects hypoxemia earlier than conventional pulse oximetry during general anesthesia. *Frontiers of medicine*, 6(4):406–410, 2012.

[248] Panayiotis A. Kyriacou, Deric P. Jones, Richard M. Langford, and Andy J. Petros. A pilot study of neonatal and pediatric esophageal pulse oximetry. *Anesth Analg*, 107(3):905–908, Sep 2008. doi: 10.1213/ane.0b013e31817e67d1. URL http://dx.doi.org/10.1213/ane.0b013e31817e67d1.

[249] Michelle Hickey and PA Kyriacou. Development of a new splanchnic perfusion sensor. In *Engineering in Medicine and Biology Society, 2007. EMBS 2007. 29th Annual International Conference of the IEEE*, pages 2952–2955. IEEE, 2007.

[250] Michelle Hickey, Neal Samuels, Nilesh Randive, Richard M Langford, and Panayiotis A Kyriacou. An in vivo investigation of photoplethysmographic signals and preliminary pulse oximetry estimation from the bowel using a new fiberoptic sensor. *Anesthesia & Analgesia*, 112(5):1104–1109, 2011.

[251] Michelle Hickey, Neal Samuels, Nilesh Randive, Richard M Langford, and Panayiotis A Kyriacou. Measurement of splanchnic photoplethysmographic signals using a new reflectance fiber optic sensor. *Journal of biomedical optics*, 15(2):027012–027012, 2010.

[252] J. P. Phillips, R. M. Langford, S. H. Chang, K. Maney, P. A. Kyriacou, and D. P. Jones. Cerebral arterial oxygen saturation measurements using a fiber-optic pulse oximeter. *Neurocrit Care*, 13(2):278–285, Oct 2010. doi: 10.1007/s12028-010-9349-y. URL http://dx.doi.org/10.1007/s12028-010-9349-y.

[253] Sylvia S Mader. Understanding human anatomy and physiology. 1994.

[254] Adolf Faller, Michael Schünke, Gabriele Schünke, and Ethan Taub. *The human body: an introduction to structure and function*. Thieme, 2004.

[255] Brockmann Chittka L, 04 2009. URL https://commons.wikimedia.org/wiki/File:Anatomy_of_the_Human_Ear_en.svg.

[256] Keith L Moore, Arthur F Dalley, and Anne MR Agur. *Clinically oriented anatomy*. Lippincott Williams & Wilkins, 2013.

[257] Peter W Alberti. The anatomy and physiology of the ear and hearing. *Occupational exposure to noise: Evaluation, prevention, and control*, pages 53–62, 2001.

[258] Anthony F Jahn and Joseph Santos-Sacchi. *Physiology of the Ear*. Taylor & Francis US, 2001.

[259] Lynn S Alvord and Brenda L Farmer. Anatomy and orientation of the human external ear. *JOURNAL-AMERICAN ACADEMY OF AUDIOLOGY*, 8:383–390, 1997.

[260] Marko Hiipakka. *Measurement apparatus and modelling techniques of ear canal acoustics*. PhD thesis, HELSINKI UNIVERSITY OF TECHNOLOGY, 2008.

[261] Richard Wasicky and Michael L Pretterklieber. The human anterior tympanic artery. *Cells Tissues Organs*, 166(4):388–394, 2000.

[262] van de T Water and H Staecker. Otolaryngology, basic science and clinical revie, ed, 2006.

[263] Arthur Tucker. Thermogram of a close-up of a human ear, May 2013. URL http://fineartamerica.com/featured/1-thermogram-of-a-close-up-of-a-human-ear-dr-arthur-tucker.html.

[264] Olaf Brodersen, D Römhild, D Starke, A Steinke, and Stefan Vogel. In-ear acquisition of vital signs discloses new chances for preventive continuous cardiovascular monitoring. In *4th International Workshop on Wearable and Implantable Body Sensor Networks (BSN 2007)*, pages 189–194. Springer, 2007.

[265] Stefan Vogel, M Hulsbusch, Thomas Hennig, Vladimir Blazek, and Steffen Leonhardt. In-ear vital signs monitoring using a novel microoptic reflective sensor. *Information Technology in Biomedicine, IEEE Transactions on*, 13(6):882–889, 2009.

[266] Stefan Vogel, S Leonhardt, M Hulsbusch, and D Starke. In-ear heart rate monitoring using a micro-optic reflective sensor. In *Engineering in Medicine and Biology Society, 2007. EMBS 2007. 29th Annual International Conference of the IEEE*, pages 1375–1378. IEEE, 2007.

[267] Boudewijn Venema, Nikolai Blanik, Vladimir Blazek, Hartmut Gehring, Alexander Opp, and Steffen Leonhardt. Advances in reflective oxygen saturation monitoring with a novel in-ear sensor system: results of a human hypoxia study. *Biomedical Engineering, IEEE Transactions on*, 59(7):2003–2010, 2012.

[268] Boudewijn Venema, Hartmut Gehring, Ina Michelsen, Nikolai Blanik, Vladimir Blazek, and Steffen Leonhardt. Robustness, specificity, and reliability of an in-ear pulse oximetric sensor in surgical patients. *Biomedical and Health Informatics, IEEE Journal of*, 18(4):1178–1185, 2014.

[269] Jerald G Graeme. *Amplifier applications of op amps*, volume 1. McGraw-Hill/TAB Electronics, 1999.

[270] Jerald G. Graeme. *Photodiode Amplifiers: OP-AMP Solutions*. McGraw-Hill Professional. ISBN 007024247X.

[271] Akshay Bhat. Stabilize your transimpedance amplifier. (1):1–11, 2012. URL http://www.maximintegrated.com/app-notes/index.mvp/id/5129.

[272] Analog Devices. Sample-and-hold amplifiers. *Analog Devices Tutorials*, page 21, October 2008.

[273] Transimpedance circuit output noise-voltage calculator, Aug 2012. URL http://www.jensign.com/noise/noisecalculator.html.

[274] Jeffrey Travis and Jim Kring. *LabVIEW for everyone*. Prentice-Hall, 2007.

[275] George E Billman. Heart rate variability–a historical perspective, 2011.

[276] M Pagani, F Lombardi, S Guzzetti, G Sandrone, O Rimoldi, G Malfatto, S Cerutti, and A Malliani. Power spectral density of heart rate variability as an index of sympatho-vagal interaction in normal and hypertensive subjects. *Journal of hypertension. Supplement: official journal of the International Society of Hypertension*, 2 (3):S383–5, 1984.

[277] Alan Chadburn Burton, Otto Gustaf Edholm, et al. Man in a cold environment. physiological and pathological effects of exposure to low temperatures. *Man in a cold environment. Physiological and pathological effects of exposure to low temperatures.*, 1955.

[278] Hanna Kaciuba-Uscilko and John E Greenleaf. Acclimatization to cold in humans. 1989.

[279] GE Folk. Climatic change and acclimatization. *Biometeorology, thermal physiology and comfort*, pages 157–168, 1981.

[280] GE Thompson. Physiological effects of cold exposure. *International review of physiology*, 15:29, 1977.